AN ANALYSIS OF WIND-FORCED, SEASONAL TRANSPORT VARIABILITY AT THE FLORIDA STRAITS USING LINEAR MODELS OF THE NORTH ATLANTIC

CENTRE FOR NEWFOUNDLAND STUDIES

TOTAL OF 10 PAGES ONLY
MAY BE XEROXED

(Without Author's Permission)

AUGUSTUS F. FANNING

AN ANALYSIS OF WIND-FORCED, SEASONAL TRANSPORT VARIABILITY AT THE FLORIDA STRAITS USING LINEAR MODELS OF THE NORTH ATLANTIC

by

©Augustus F. Fanning, BSc. (Hons.)

A thesis submitted to the School of Graduate Studies in partial fulfillment of the requirements for the degree of

Master of Science

Department of Physics

Memorial University of Newfoundland

1993

St. John's Newfoundland

ABSTRACT

Two linear models of the North Atlantic, a linear barotropic model and a linear two-density layer model, are employed to investigate the effect of using different wind stress climatologies on the model-calculated transport. Particular emphasis is placed on the model-calculated response at the Florida Straits. The model domains extend from 10^0S to 65^0N and 100^0W to 15^0E at $1^o \times 1^o$ resolution. The wind stress climatologies are those of da Silva et al.(1993a; hereafter DS), Hellerman and Rosenstein (1983; hereafter HR), Isemer and Hasse (1987; hereafter IH) and Trenberth et al. (1990; hereafter TR). Comparing the results at the Florida Straits, we find that for each climatology, the barotropic model shows maximum northward transport in the summer and minima in the fall and late winter, in general agreement with transport measurements from cable data (Larsen, 1992). However, the amplitude of the model response differs considerably between the climatologies. In the case of DS the range (maximum transport minus minimum transport) is 2.8 Sv; HR, 3.6 Sv; TR, 5.2 Sv and IH, 5.9 Sv, compared to a range of 4.6 ± 0.4 Sv derived from cable data. When the JEBAR (Joint Effect of Baroclinicity And Relief; Sarkisyan and Ivanov, 1971) forced transport is also considered, using the two-layer model, the amplitude of the model-calculated response changes slightly in each case, with ranges of $3.3Sv$, $3.9Sv$, $5.8Sv$ and $6.1Sv$ for each of DS, HR, TR, and IH respectively.

We have also conducted experiments using a $1/3^o \times 1/3^o$ version of the model applied to the region extending from 5^0N to 42^0N, and 100^0W to 70^0W. The Bahama/Antilles Island Arc are resolved in this model. Transport through the boundary at 70^0W is specified from the 1^0 x 1^0 calculations referred to above. The details of the model-calculated response

are particularily sensitive to the precise choice of grid point used to represent the offshore boundary of the Florida Straits. If we choose the Grand Bahama Islands, the cases with transport specified on the eastern boundary yield ranges of $1.3Sv$, $2.8Sv$, $3.0Sv$ and $3.1Sv$ for each of DS, HR, TR, and HI respectively. If instead, we choose a region between the Grand Bahama Island, and Andros Island (the Providence Channel area) the $1/3^{o} \times 1/3^{o}$ model calculated results agree quite well with our $1^{o} \times 1^{o}$ results. This is a consequence of the fact that even at $1/3^{o} \times 1/3^{o}$ resolution, we still do not properly resolve the Florida Straits. In fact, in the model the Straits are much too shallow (roughly half the depth of the true Florida Straits), and hence, does not receive as much information along f/H contours as in the 1^{0} x 1^{0} case, or as the grid-point in the vicinity of the Providence Channel.

The increased range in the HI case compared to HR in our $1^{o} \times 1^{o}$ case is in general agreement with the finding of Böning et al.(1991b) using the Kiel version of the model that forms the WOCE Community Modelling Effort. However, whereas Böning et al. claim that winds north of $35^{o}N$ have little influence on the seasonal response of their model at the Florida Straits, we find that winds north of $35^{o}N$ play an important role in our model. The reason for the behaviour of the Community Model is not clear but may be associated with advection by the western boundary current. In our model, we show the importance of forcing by the meridional component of the wind, although forcing through the zonal component also plays some role in explaining the differences between the cases run under the different climatologies. We also show the importance of forcing associated with the meridional component of the wind along the continental slope region north of the Straits.

TABLE OF CONTENTS

LIST OF FIGURES

CHAPTER 6: MODEL RESPONSE AT THE FLORIDA STRAITS

LIST OF TABLES

Acknowledgements

I cannot possibly name all of those who have contributed to my work in Graduate studies at Memorial University, but several people deserve special mention: Brad deYoung, Alex Hay and Kevin Lamb, whose comments helped improve the work presented here. I am also grateful to my internal examiner, Brad deYoung, and external examiner Andrew Weaver for their patient review of this thesis. Their comments and suggestions certainly improved the work presented here.

I am also grateful to Arlindo Moraes da Silva for providing me with several of the wind stress fields I have utilized here, and for his encouragement through this project. Allan Goulding, Helmut Roth, Todd Wareham, and Ying Ren provided assistance in dealing with computer problems. Indeed, without the help of Allan and Helmut, whose computing expertise and knowledge I frequently drew on, the model results presented in this work would not have been possible.

I also wish to thank my parents, Augustus and Verna Fanning, whose love, support and encouragement, kept me going through the tough times and enabled me to see this work to fruition. The same can be said for all of my close friends in the Physics department and elsewhere.

Finally, and most importantly, I extend my greatest thanks to Richard Greatbatch. Richard has guided me through both my graduate and undergraduate career here at Memorial University, and was willing to take a chance and supervise my work. Over these years, he has become more to me than just my supervisor, and I count him as one of my closest

friends. Indeed, virtually all I know of Oceanography, research, and scientific discipline, he has taught me. I only hope that I can maintain the high standards he has tried to instill in me in all my future endeavors. I know I can never repay him for the time and effort he has invested in me. I can only say with the deepest sincerity,

Thank you Richard.

This work has been carried out with support from the NSERC Collobarative Research Initiative Programme in support of Canadian university activities in the World Ocean Circulation Experiment (WOCE), research grants from the Atlantic Accord Career Development Award's programme, and Memorial University of Newfoundland Graduate Studies Fellowships.

CHAPTER 1: INTRODUCTION

The Florida Current is a major contributor to the circulation of the North Atlantic and the transport of heat from the equatorial regions to higher latitudes; as such it plays an important role in the climate variability of the North Atlantic. The Florida Current passes between the southern tip of the Florida coast and Cuba, at which point it turns northeast into the Florida Straits, a natural bottleneck bounded on the west by the Florida coast and on the east by the Bahamas island arc (Andros Island, Grand Bahama Island, Great Abaco etc), see Fig.1.1. This natural bottleneck provides an excellent region within which the transport at the core of the Florida Current can be measured, without the problems associated with meanders in the flow.

The pioneering work of Niiler and Richardson(1973) indicated the Florida Current had a mean transport of roughly 30 Sv, ($1\ Sv = 10^6 m^3 s^{-1}$) and suggested an annual range (*maximum transport minus minimum transport*) of roughly 8.2 Sv. These authors fitted an annual cycle to their data, indicating that maximum northward transport occurs in summer, and minimum transport in the fall and late winter. Figure 1.2 shows the monthly anomalies of Niiler and Richardson's data; that is, monthly means with the annual mean removed. Note also the transport measurements of Brooks(1979) are included with the Niiler and Richardson data to fill the gaps in their data set. These transport estimates were based on a series of dropsonde measurements (a total of 3682 dropsonde measurements from 13 transects from Miami to Bimini Island). Each set of transect measurements lasted a few weeks, over a period of several years (a total of 85 days of measurements spanning 1964-1970), and were not corrected for tidal transport variations. The fact that the measurements

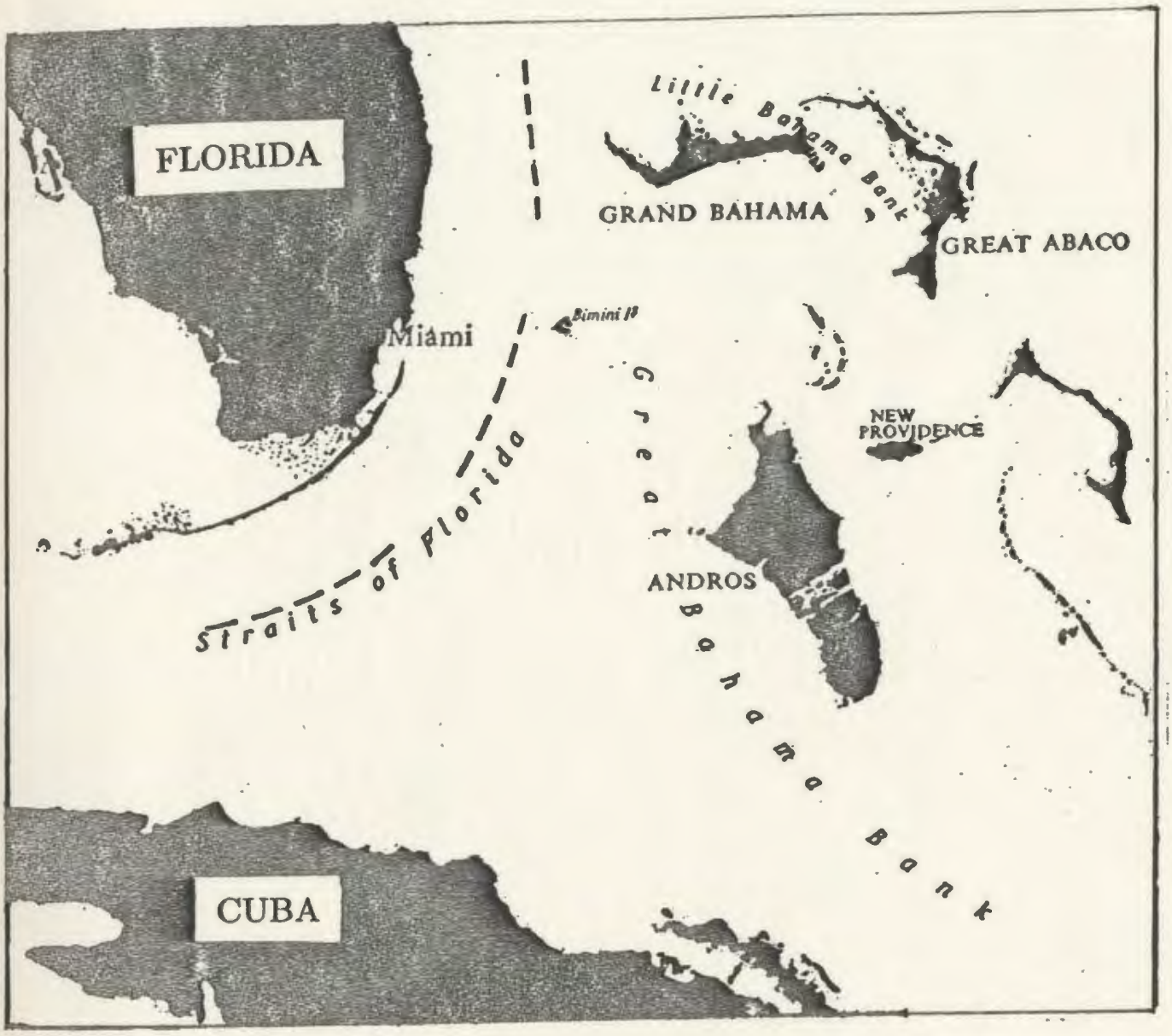

Figure 1.1: *Schematic of the Florida Straits indicating the axis of the Florida Current (the dashed line) and the major islands bounding this region.*

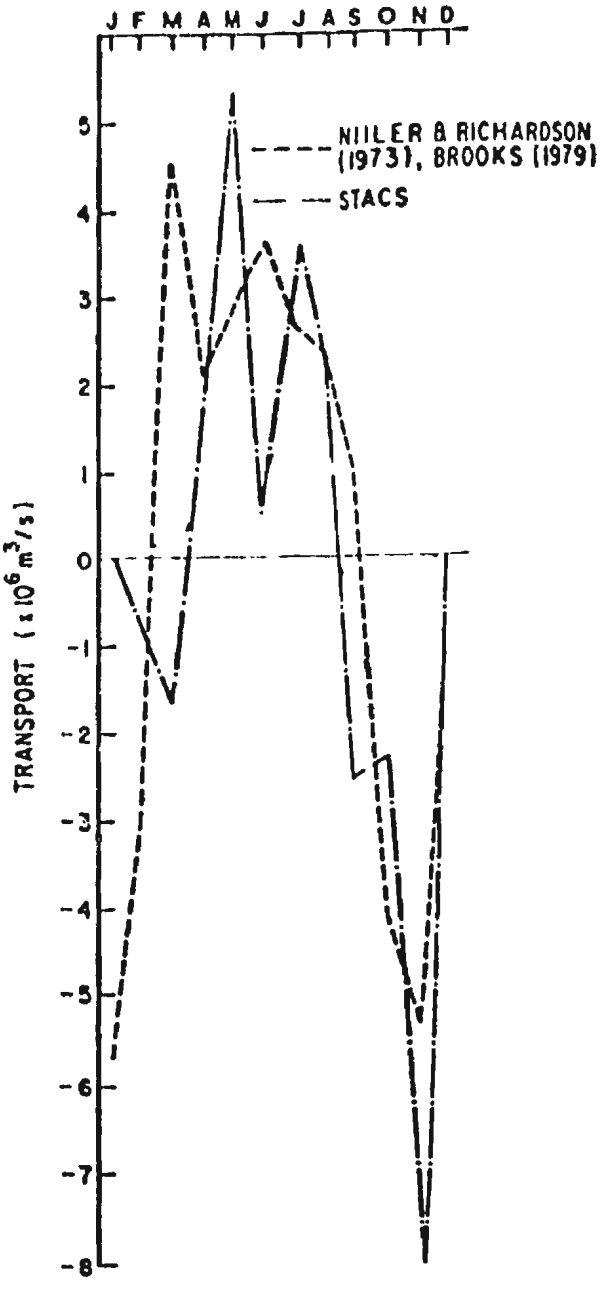

Figure 1.2: *Comparison of monthly anomalies (monthly means with the annual mean removed) of transport measurements through the Florida Straits as measured by Niiler and Richardson(1973) with Brooks(1979) and STACS PEGASUS cruises (after Leaman et al., 1987).*

were not distributed uniformly over the year, combined with high frequency fluctuations, makes it difficult to accurately define the seasonal cycle and distinguish interannual, and tidal variability present in the transport measurements.

Subsequent measurements by the STACS (Subtropical Atlantic Climate Studies) program which utilized PEGASUS profiler measurements, indicated a similar seasonal cycle to that described by Niiler and Richardson, with a much higher annual range of roughly 13 Sv (Leaman et al.; 1987). The STACS transport measurements, corrected for tidal variations, indicate an absolute maximum occurring in May, and minimum occurring in November, with a secondary maximum and minimum in August and March respectively, see Fig.1.2. The STACS data set, although comprehensive (a total of 19 cruises, lasting 130 days over the period 1982-84) is not long enough to produce a long-term-mean picture of the Florida Straits seasonal transport cycle owing to interannual variability of the Florida Current. Taken together, however, a general picture does emerge, with a Florida Current showing maximum northward transport in the summer months with a minimum in the fall and late winter.

Recently Larsen(1992) has produced a comprehensive time series of transport measurements at $27°N$ based on the voltage drop across an abandoned communications cable between a point 16 km east of Jupiter Inlet, Florida, and Settlement Point, Grand Bahama Island, see Fig.1.3. The method which allows this measurement, although quite ingenious, is not new, and was first suggested by Faraday in 1832. Faraday noted that an electromotive force (EMF) would be induced in a conductor which moves across a magnetic field (motional induction). In the present case, seawater acts as the conductor, and as it moves

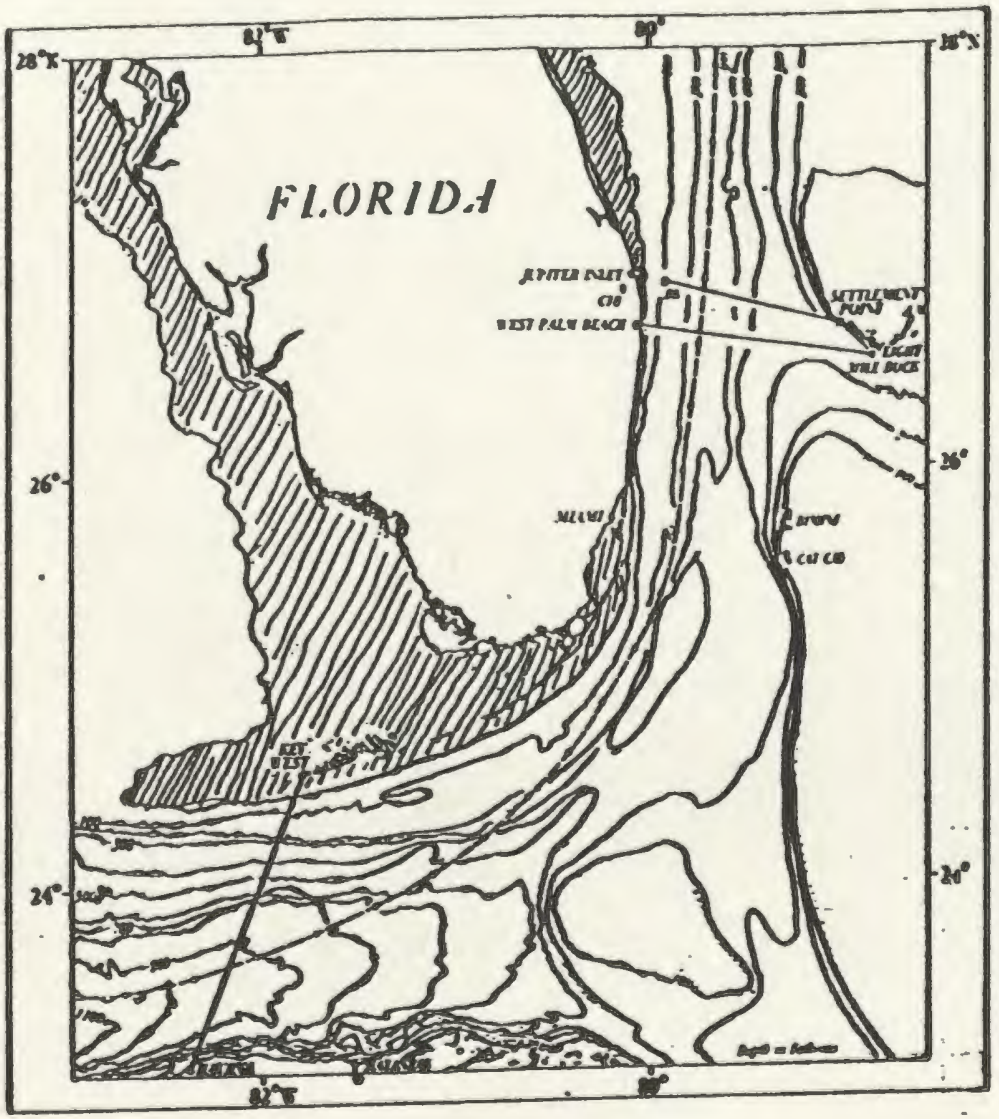

Figure 1.3: *The geometry of the Florida Straits indicating the axis of the Florida Current (the dashed/arrowed line) and the placement of submarine telecommunication cables considered by Larsen. Depth units are in Fathoms, (from Larsen, 1992).*

across the lines of force created by the earth's magnetic field, an EMF is produced, defined by

$$E = B \cdot L \cdot v$$

with v being the current speed, L the width of the current, and B the strength of the earth's magnetic field component mutually perpendicular to both v and L. Faraday attempted to apply this idea to measure flow of the Thames river in England, but was unsuccessful because of problems associated with the copper electrodes he utilized. Young et al.(1920) were, however, able to successfully measure the tidal currents in the English Channel using this technique. Several sources of error inherent to this method (e.g. geomagnetically induced voltage variations, instability of cable-ocean contacts, and others) are discussed in detail by Larsen. Perhaps the greatest limiting factor is the need to determine the voltage calibration factor, which must be specified to convert the measured voltages into transport measurements. The voltage-transport equation for the Florida Straits, reduces to the simple linear equation;

$$\Psi(t) = C_o \Delta\Phi_V(t)$$

where C_o is the voltage calibration factor, $\Delta\Phi_V$ is the motionally induced voltage, and Ψ is the corresponding volume transport. The STACS program provided an excellent means of defining the necessary voltage calibration factor since cable voltage measurements and PEGASUS profile measurements were recorded simultaneously. Based on 137 days of daily mean profiling derived transport values, Larsen defines the voltage calibration as C_o =

$24.42 \pm 0.56\ Sv V^{-1}$, yielding an estimated error in cable derived transport measurements of $10.8 Sv$.

Based upon this analysis, and a total of 4862 daily mean voltage values spanning 1969-1990 (1969 1974 and 1981-1990), Larsen found the annual mean Florida Straits transport to be $32 Sv$, consistent with Niiler and Richardson's 30 Sv. The seasonal cycle, produced by removing the annual mean from the monthly means (see Larsen's table 12.), exhibits a broad maximum northward transport occurring in July-August followed by a sharp drop to a minimum in October-November, with an annual range of $4.6\ Sv$. Utilizing the data contained in Larsen's Table 12, we can estimate the error associated with the calculation of the seasonal cycle to be roughly $\pm 0.2\ Sv$ for each monthly mean (this is obtained by taking the standard deviation given by Larsen and dividing by the square root of the number of daily measurements). Note that since the majority of measurements were collected in the period 1981-1990, there is the possibility that Larsen's seasonal anomalies reflect interdecadal circulation changes. The upper layer return flow of the thermohaline cell transports roughly $12\ Sv$ through the Florida Straits (Schmitz et al. 1992). Recent analysis of historical hydrographic data (Levitus, 1989a,b,c;1990) indicates that major changes have occured in the thermohaline structure of the North Atlantic. In the idealised studies of Weaver and Sarachik(1991) the modelled thermohaline circulation undergoes oscillations on decadal time scales indicating that the thermohaline flow through the Florida Straits may undergo oscillations on similar time scales. There is, therefore the possibility that Larsen's data may overestimate or underestimate the seasonal Florida Current transport variation.

Nonetheless, Larsen's cable data set is the most comprehensive set of measurements made to date and serves as a standard against which to compare the results in this thesis.

Leetmaa et al. (1977) claimed consistency between the flat-bottomed Sverdrup transport at the latitude of the Florida Straits when the wind stress curl of Bunker(1976) is integrated across this latitude (see also Leetmaa and Bunker, 1978).

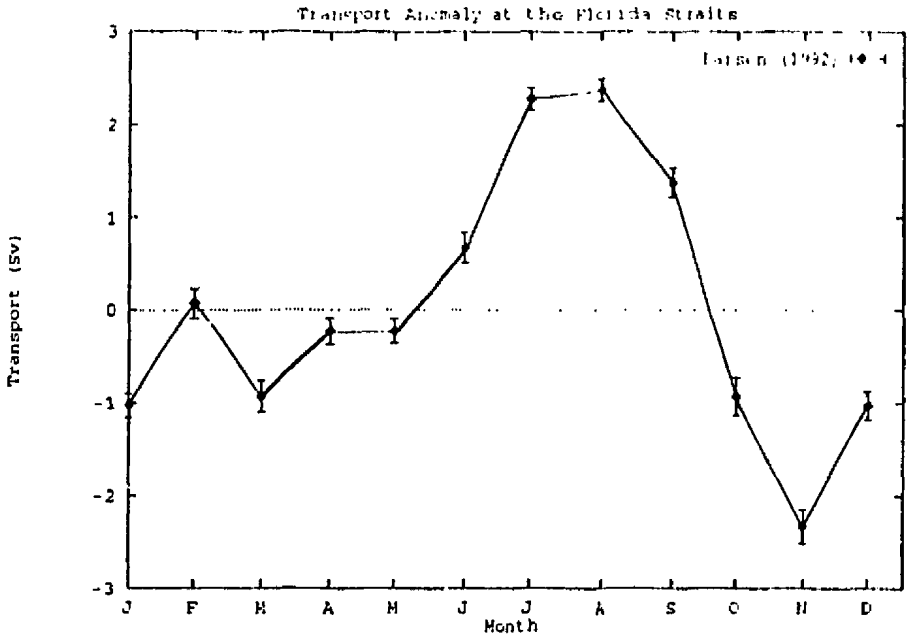

Figure 1.4: *The seasonal variation of transport through the Florida Straits, as derived from cable data by Larsen(1992). It should be noted that the annual mean has been removed and that the units are Sverdrups* ($1 Sv = 10^6 m^3 s^{-1}$).

In Chapter 4 we find remarkable differences in the amplitude of transport produced in this manner, by merely applying different wind stress climatologies. Wunsch and Roemmich (1985) also cast considerable doubt as to whether the flat-bottomed Sverdrup balance can ever hold in the ocean. Further discussion of the validity of the flat-bottomed Sverdrup

balance at the latitude of the Florida Straits can be found in Roemmich and Wunsch (1985), and Schmitz et al. (1992). At seasonal time scales, integrating the wind stress across this latitude suggests a Florida Current with a seasonal range of approximately 25 *Sv*, and maximum northward transport in February-March, and minimum in October-November. The fact that neither the amplitude nor phase predicted by flat-bottomed Sverdrup theory are consistent with observations suggests that dynamics responsible for the mean flow are different from those governing the seasonal response.

Veronis and Stommel(1956) studied the midlatitude response of a continuously stratified, flat-bottomed ocean, to seasonal wind stress variations. These authors show the response should consist of both barotropic and baroclinic forced variations (by barotropic we mean the response associated with the vertically integrated velocities, while baroclinic refers to the remainder). Indeed, Veronis and Stommel found weak, but significant currents in the deep ocean, suggesting a possible role for the effects of bottom topography. This was confirmed in a later study by Gill and Niiler(1973) who showed that in the ocean interior, the barotropic response at midlatitudes due to seasonally varying wind stress forcing should be described by the topographic Sverdrup relation. This is an equilibrium response which neglects the density stratification of the ocean, and balances transport variations by the combined effect of windstress over topography. These authors also suggest the baroclinic response should be a purely local one with no significant role for baroclinic Rossby waves on seasonal time scales.

Anderson and Corry (1985a) have investigated the dynamics of seasonal variations in western boundary currents. They showed that the flat-bottomed Sverdrup balance was

unlikely to hold at the annual period for the North Atlantic. This is because for periods much less than the time taken for wind-generated baroclinic Rossby waves to completely compensate for the effect of variable bottom topography (see Anderson and Killworth, 1977, Anderson et al. 1979) the ocean response is primarily that for a homogeneous ocean and thus strongly affected by the bottom topography, a result consistent with the conclusions of Veronis and Stommel, and Gill and Niiler discussed above. Anderson and Corry indicate that at midlatitudes, on seasonal time scales, within the context of linear theory, variations in the transport of western boundary currents can be due to *barotropic* Rossby waves, with an additional response associated with the passage of internal Kelvin waves over realistic bottom topography.

In a companion paper, Anderson and Corry (1985b; hereafter AC) investigated the seasonal transport variation through the Florida Straits utilizing a linear two density layer model of the North Atlantic. Their model employed dynamics linearized about a state of rest, incorporated realistic coastlines and bottom topography, extending from $10°S$ to $50°N$ and $100°W$ to $0°W$, and was forced by seasonal anomalies of windstress prepared by Hellerman from the Bunker and Goldsmith(1979) data. It should be noted that since their model was linear they removed the annual mean windstress and drove the model with the seasonal anomalies (monthly means of windstress with the annual mean removed). AC successfully reproduced the observed phase of the seasonal cycle through the Florida Straits, but underestimated the amplitude.

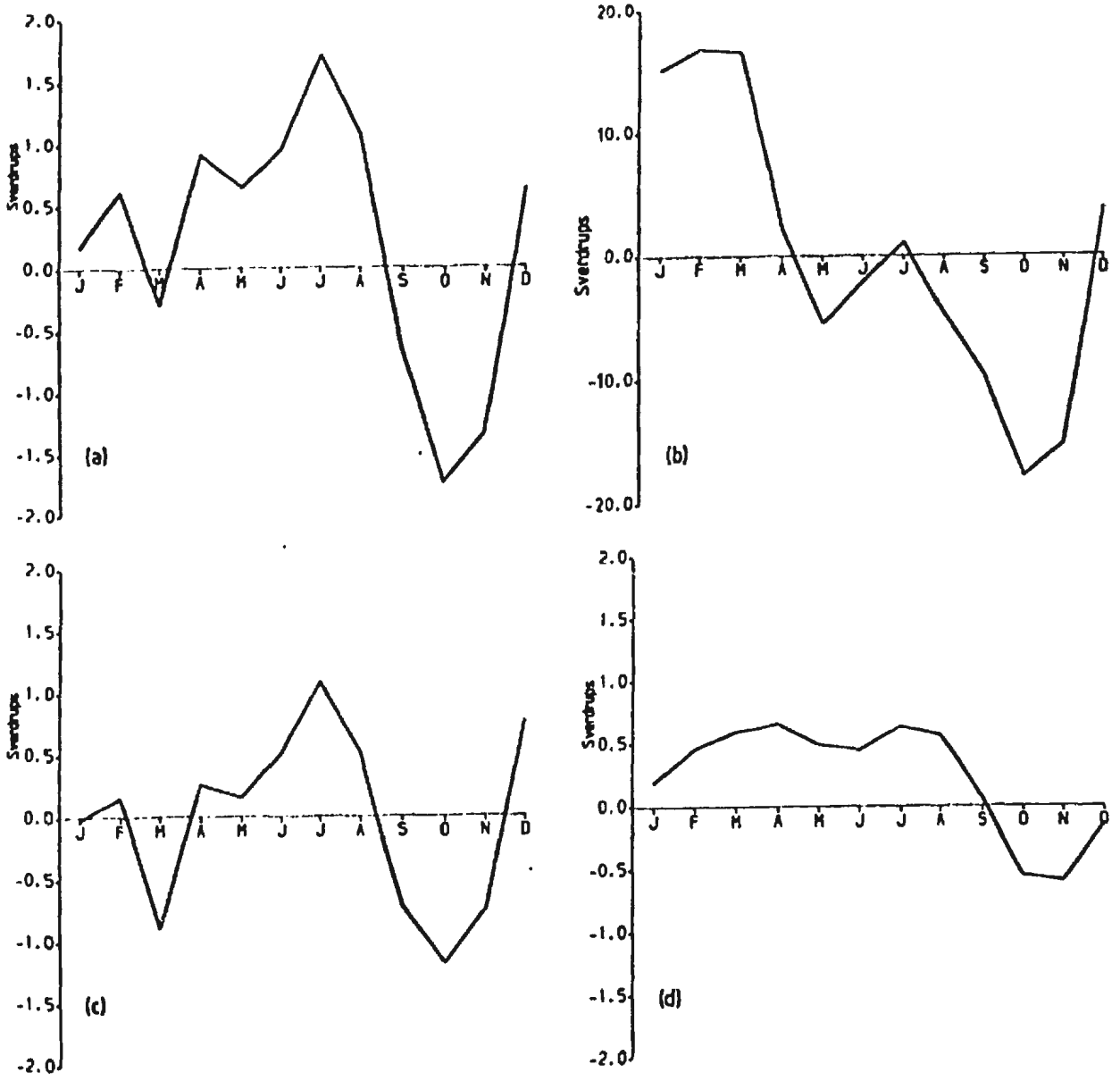

Figure 1.5: *Transport (Sv) through the Florida Straits as predicted by Anderson and Corry(1985b) for (a) their two-density-layer model including realistic bottom topography when forced by seasonal anomalies of wind stress; (b) as in (a) but for a homogeneous flat-bottomed ocean; (c) as in (a) but using a homogeneous ocean; (d) the contribution to (a) due to JEBAR (see text). (from Anderson and Corry, 1985b).*

Figure 1.5 indicates their model response associated with (*a*) the two density layer model response at the Florida Straits, (*b*) the flat-bottomed Sverdrup transport, (*c*) the response associated with a homogeneous ocean including realistic topography, and (*d*) the contribution to Fig.1.5(*a*) of baroclinic effects over realistic topography (JEBAR, Sarkisyan and

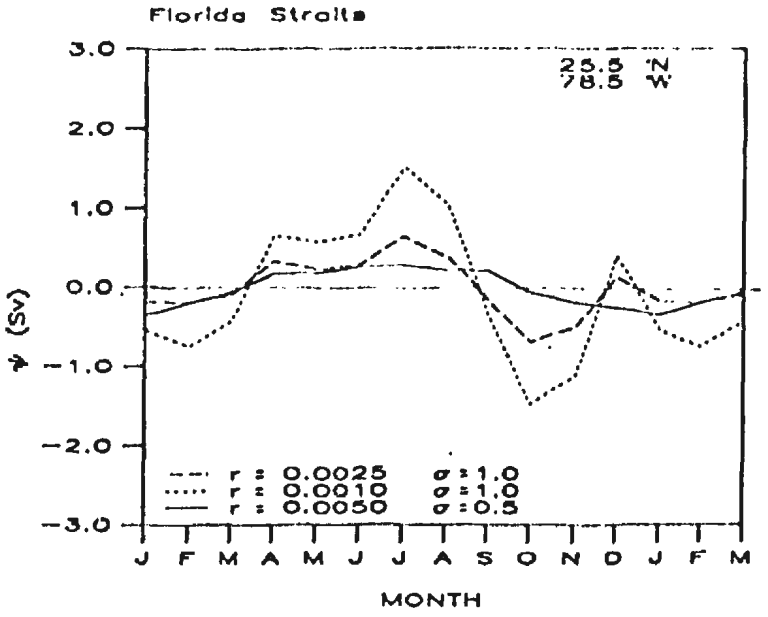

Figure 1.6: *The seasonal transport variation through the Florida Straits as predicted by Greatbatch and Goulding(1989) for three of their model experiments. Here r is the linear bottom friction coefficient, while σ denotes the length scale (in degrees) used in their Gaussian smoother of topography. (from Greatbatch and Goulding, 1989).*

Ivanov, 1971).The noted effects due to JEBAR were attributed to the passage of a Kelvin wave, generated to the north of the Florida Straits, as it passed over the realistic topography in the shelf region. The seasonal transport variation predicted by AC's model achieves a

range of 3.5 *Sv* slightly lower than Larsen's cable derived transport. The phase, however indicates a maximum northward transport in July-August dropping abruptly to a minimum in October-November, consistent with Larsen(1992), (compare Fig.1.5(*a*) and Fig.1.4).

Encouraged by AC's results, particularily the ability of a homogeneous ocean including realistic topography to capture much of the two-density-layer model's results (compare Fig.1.5(*a*) and Fig.1.5(*c*)), Greatbatch and Goulding(1989; hereafter GG) considered the response of a linear, single-layer barotropic model of the North Atlantic. GG's model utilized realistic coastlines and topography, and extended from 10°*S* to 80°*N* and 100°*W* to 0°W. GG utilized the seasonal anomalies of Hellerman and Rosenstein(1983; hereafter HR). Figure 1.6 indicates the seasonal transport variation produced by GG for several values of friction they used. Again, these authors captured the correct phase of the observed seasonal transport through the Florida Straits, (compare Fig.1.6 and Fig.1.4), although they also underestimated the seasonal range compared to Larsen. (Compare their lowest friction case with a range 3.1 *Sv* with Larsen's 4.6 *Sv*). Furthermore, while the model of AC extended to only 50°*N*, GG's model extended to 80°*N* and indicated that wind forcing north of 50°*N* significantly influenced their model-calculated transport variation at the location of the Florida Straits.

More recently, Böning et al. (1991b) have discussed output from the Kiel version of the WOCE-CME (the World Ocean Circulation Experiment, Community Modelling Effort; Bryan and Holland, 1989). This is an eddy resolving model of the North Atlantic driven by seasonally varying surface forcing. Two different wind stress climatologies were used, those of HR and Isemer and Hasse (1987; hereafter IH). In common with AC, the model captures

the observed phase of the seasonal transport variation through the Straits. However, the model results obtained using IH have a seasonal range of $6.3Sv$ compared with only $3.4Sv$ using HR; indicating that with IH wind forcing the model-calculated range is too high and with HR wind forcing it is too low compared to Larsen(1992). Indeed, this indicates a strong dependence of the model-calculated seasonal signal on the wind stress climatology used to drive the model (see Fig.1.7).

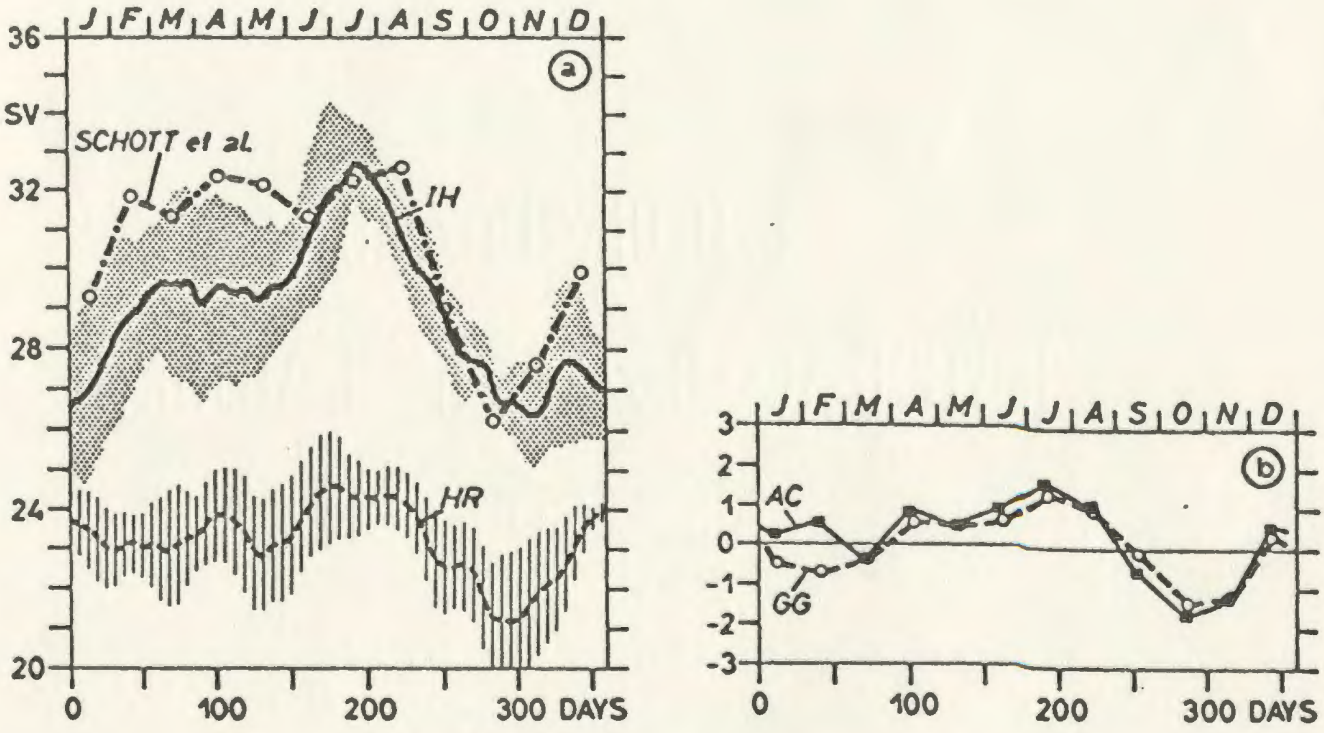

Figure 1.7: *(a)The annual cycle of transport through the Florida Straits as calculated by Böning et al.(1991b) using 5 years of output from the Kiel version of the WOCE-CME under each of HR and IH forcing. Stippling indicates the standard deviation from the 5 year mean; dash-dot indicates observed transports from Schott et al.(1988). (b) Transport anomaly at the Florida Straits as calculated by GG and AC. (from Böning et al. (1991b)).*

The model results discussed by Böning et al.(1991b) were averaged over the last 5 years of integration. Including a further 3 years of integration in this average (Böning, personal communication) leads to results using the HI climatology that are closer to the cable derived measurements of Larsen (see Fig.1.8), with a range of $4.6Sv$. This is still larger than the range found under HR, but indicates a dependence on the averaging period used. It also suggests that estimates of the seasonal signal from observations are likely to depend, in a similar way, on the length of the measurement period, as we have already discussed.

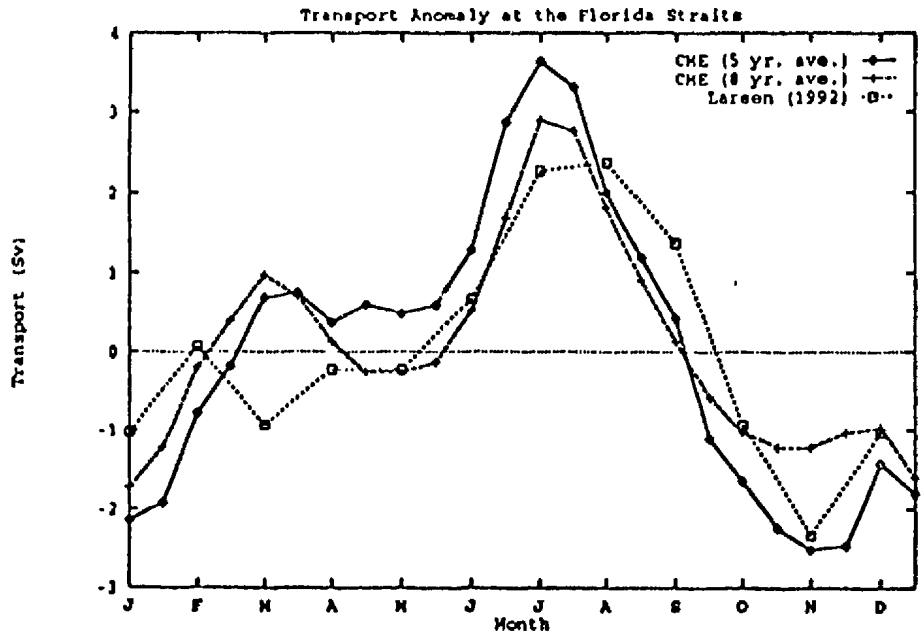

Figure 1.8: *The annual cycle of transport through the Florida Straits as calculated by the Kiel version of the WOCE-CME under HI forcing using:*

(i) 5 years of output (Böning et al.(1991);

(ii)including an additional 3 years, making 8 years output in total.

Also shown is the cable derived annual cycle from Larsen(1992).

Böning et al. (1991b) also compared their model solutions with those obtained by AC and GG. As seen in Fig.1.7, the WOCE-CME under HR wind forcing agrees well with GG and AC. This suggests that model-calculated transport variability through the Straits is more sensitive to the wind forcing applied than the model configuration, and further suggests that linear barotropic dynamics is playing a fundamental role in the CME model results.

Given the sensitivity of the CME results to the wind stress climatology used, and the apparent agreement between the linear models and the CME when run under HR wind forcing, the question arises as to whether a linear model will exhibit similar sensitivity to the CME when driven with different wind stress climatologies. It may then be possible to use these models and model intercomparisons to assess the importance of linear, barotropic dynamics in determining the CME results. In the present work, we follow AC and GG in utilizing a simple, linear, barotropic model of the North Atlantic, similar to that of GG, and a linear two-density-layer model similar to that of AC, extending from 10^0S to 65^0N and 100^0W to 15^0E. The models are forced using various wind stress climatologies. In particular we extend the work of Böning et al. (1991a) by investigating not only HR (1983) and HI (1987) wind forcing, but also the climatologies of Trenberth et al. (1990; hereafter TR), and da Silva et al. (1993a; hereafter DS). Each of these climatologies utilize different data sources and methodologies in the production of the wind stresses. The present work will concentrate on the impact using these different climatologies has on the model-calculated seasonal transport variations through the Florida Straits and over the North Atlantic as a whole.

The organization of this thesis is as follows. Chapter 2 outlines the models employed, and details the parameters used. Chapter 3 briefly outlines the wind stress data sets and points out the major differences in the way they were compiled. Chapter 4 provides a comparison of the flat-bottomed Sverdrup transports calculated for each climatology, while Chapter 5 presents results obtained from each model for the North Atlantic as a whole. In Chapter 6, attention is concentrated on the model-calculated transports through the Florida Straits when realistic bottom topography is included, while Chapter 7 presents some high-resolution model results for the Florida Straits area. Finally, Chapter 8 presents a summary and discussion.

CHAPTER 2: THE MODELS

2.1: The Barotropic Model

The barotropic model is the same as that described by Greatbatch and Goulding (1989), except that we now include lateral mixing of momentum and solve the governing equations in the time domain rather than the frequency domain. The vertically integrated equations of motion for an ocean of uniform density and linearized about a state of rest, can be written in spherical coordinates as:

$$\frac{\partial u}{\partial t} - fv = -\frac{g}{a\cos\phi}\frac{\partial \eta_1}{\partial \lambda} + \frac{\tau^\lambda}{\rho_0 H} - \frac{ru}{H} + A_H \mathcal{L}^\lambda \tag{2.1.1}$$

$$\frac{\partial v}{\partial t} + fu = -\frac{g}{a}\frac{\partial \eta_1}{\partial \phi} + \frac{\tau^\phi}{\rho_0 H} - \frac{rv}{H} + A_H \mathcal{L}^\phi \tag{2.1.2}$$

$$\frac{\partial}{\partial \lambda}(Hu) + \frac{\partial}{\partial \phi}(Hv\cos\phi) = 0 \tag{2.1.3}$$

where

$$\mathcal{L}^\lambda = \left[\nabla_h^2 u + \left(\frac{1-\tan^2\phi}{a^2}\right)u - \frac{2\sin\phi}{a^2\cos^2\phi}\frac{\partial v}{\partial \lambda}\right]$$

$$\mathcal{L}^\phi = \left[\nabla_h^2 v + \left(\frac{1-\tan^2\phi}{a^2}\right)v + \frac{2\sin\phi}{a^2\cos^2\phi}\frac{\partial u}{\partial \lambda}\right]$$

are the horizontal Laplacian terms representing the horizontal mixing of momentum, ∇_h^2 is the horizontal Laplacian operator in spherical coordinates,

$$\nabla_h^2 A = \frac{1}{a^2\cos^2\phi}\frac{\partial^2 A}{\partial \lambda^2} + \frac{1}{a^2\cos\phi}\frac{\partial}{\partial \phi}\left(\cos\phi\frac{\partial A}{\partial \phi}\right)$$

and A_H is the horizontal mixing coefficient; $H = H(\lambda,\phi)$ is the realistic bottom topography for the domain; λ is longitude, ϕ is latitude and (u,v) are the (λ,ϕ) components of velocity respectively; $f = 2\Omega\sin\phi$ is the Coriolis parameter, Ω the Earth's rotation rate, a is the

radius of the Earth; $(\tau^{\lambda}, \tau^{\phi})$ are the eastward and northward components of the surface wind stress respectively; g is the acceleration due to gravity; ρ_0 is a representative density for sea water, and r is a linear bottom friction coefficient.

In writing (2.1.3) the rigid-lid approximation has been made. This is achieved by requiring the vertical velocity at the surface to be zero. Effects due to the variation in sea level, η, will arise as the equivalent pressure distribution on the rigid, level, upper surface of the model. Employing scale analysis of the continuity equation indicates that the local time derivative of the sea level term is order f^2L^2/gH_0 with the velocity terms scaling as order 1. Therefore, we neglect the sea level variations provided

$$\left(\frac{fL}{c}\right)^2 \ll 1$$

clearly the case for typical values at midlatitudes (*ie.* where $L = 10^6 m$, $f = 10^{-5} s^{-1}$, $c = \sqrt{gH_0} = 100 m s^{-1}$, with $H_0 = 10^3 m$). Note, however, that we have implicitly assumed time scales, $T \geq O(1/f)$, so that employing the rigid-lid approximation filters out higher frequency motions, eg. tides, barotropic Kelvin waves, etc. Employing the rigid-lid approximation, does allow us to utilize the non-divergent nature of the flow and define a volume transport streamfunction Ψ with

$$\Psi_{\phi} = -auH \qquad \Psi_{\lambda} = avH\cos\phi \tag{2.1.4}$$

Taking the vertical component of the curl of the momentum equations,

$$\frac{\partial}{\partial\lambda}(2.1.2) - \frac{\partial}{\partial\phi}(\cos\phi(2.1.1))$$

and making use of (2.1.4) we obtain the following equation for the barotropic streamfunction:

$$\frac{\partial}{\partial\lambda}\left\{\left(\frac{\partial}{\partial t}+\frac{r}{H}\right)\frac{\Psi_\lambda}{H\cos\phi}\right\}+\frac{\partial}{\partial\phi}\left\{\left(\frac{\partial}{\partial t}+\frac{r}{H}\right)\frac{\Psi_\phi\cos\phi}{H}\right\}+J\left(\Psi,\frac{f}{H}\right)$$
$$=\frac{a}{\rho_0}\left\{\tau^\lambda\cos\phi\frac{H_\phi}{H^2}-\tau^\phi\frac{H_\lambda}{H^2}\right\}+\frac{a}{\rho_0 H}\left\{\frac{\partial}{\partial\lambda}\left(\tau^\phi\right)-\frac{\partial}{\partial\phi}\left(\tau^\lambda\cos\phi\right)\right\}$$
$$+aA_H\left\{\frac{\partial}{\partial\lambda}\mathcal{L}^\phi-\frac{\partial}{\partial\phi}(\cos\phi\mathcal{L}^\lambda)\right\} \tag{2.1.5}$$

where $J(A, B)$ is the Jacobian operator defined as

$$J(A,B)=\frac{\partial A}{\partial\lambda}\frac{\partial B}{\partial\phi}-\frac{\partial A}{\partial\phi}\frac{\partial B}{\partial\lambda} \tag{2.1.6}$$

2.1.1 : Physical Interpretation of the Governing Equations

Equation (2.1.5) is a vorticity equation and has a simple interpretation. The first group of terms represent the time rate of change of relative vorticity and its dissipation by bottom friction, the second represents flow across lines of planetary potential vorticity, f/H. The vorticity input is provided by the first two terms on the right hand side. The first is the vorticity input by the wind stress in conjunction with gradients of topography; the second is the vorticity generated by the curl of the wind stress. The final term in (2.1.5) is the dissipation of vorticity through the lateral mixing of momentum.

Gill and Niiler (1973) indicate that in the ocean interior, away from boundaries, the response associated with the vertically integrated horizontal currents due to seasonally varying wind stress should be described by the topographic Sverdrup relation,

$$\left\{\frac{\partial}{\partial\phi}\left(\frac{f}{H}\Psi_\lambda\right)-\frac{\partial}{\partial\lambda}\left(\frac{f}{H}\Psi_\phi\right)\right\}=\frac{a}{\rho_0}\left\{\tau^\lambda\cos\phi\frac{H_\phi}{H^2}-\tau^\phi\frac{H_\lambda}{H^2}\right\}$$
$$+\frac{a}{\rho_0 H}\left\{\frac{\partial}{\partial\lambda}\left(\tau^\phi\right)-\frac{\partial}{\partial\phi}\left(\tau^\lambda\cos\phi\right)\right\} \tag{2.1.7}$$

so that gradients of transport ($\nabla\Psi$), and gradients of planetary potential vorticity ($\nabla(f/H)$) are parallel. The planetary potential vorticity contours (f/H) for the North Atlantic are strongly affected by the shelf/slope topography along the eastern seaboard of Canada and the United States, (see Fig.2.1), indicating that transport Ψ will be guided along the continental boundary of the eastern seaboard, an effect we will return to in Chapters 6 and 7. Information in this model propagates along f/H contours from east to west, as in Stommel's model for western intensification (Stommel, 1948). In the case of the Florida Straits this means that the important f/H contours are those to the north and east, along the continental slope, as discussed above. It also indicates that the Florida Straits transport in our model will be strongly affected by wind forcing along these f/H contours, i.e. to the north and east.

Dissipation arises in our model in two forms: a linear bottom stress term (the terms r/H^2 in (2.1.5)) and a horizontal mixing of momentum term (the A_H term in (2.1.5)). Parameterizing the bottom stress in terms of the vertically averaged velocities (u, v) is strictly only valid for the case we consider here, that of a weakly stratified or barotropic ocean. The effect of friction in our model is the same as in Csanady's theory on the arrested topographic wave (Csanady, 1978), that is, in the form of diffusion analagous to the heat conduction equation. Here, transport, Ψ, is diffused across planetary potential vorticity contours, (f/H contours), with the direction of long wave propagation playing the role of the time coordinate in the analagous heat conduction equation. Ideally we would prefer to use realistic values for our friction parameter, r; however, we need friction to control computational instabilities arising from grid point noise. The use of bottom

to which (2.1.5) reduces in the inviscid, steady state limit. In (2.1.7), wind forcing causes Ψ contours to cross f/H contours by the vorticity imparted by the wind. Note further, that in the absence of wind forcing (2.1.7) reduces to

$$\left\{\frac{\partial}{\partial\phi}\left(\frac{f}{H}\Psi_\lambda\right) - \frac{\partial}{\partial\lambda}\left(\frac{f}{H}\Psi_\phi\right)\right\} = 0 \tag{2.1.8}$$

which can be rewritten as

$$\nabla\Psi \times \nabla\frac{f}{H} = 0 \tag{2.1.9}$$

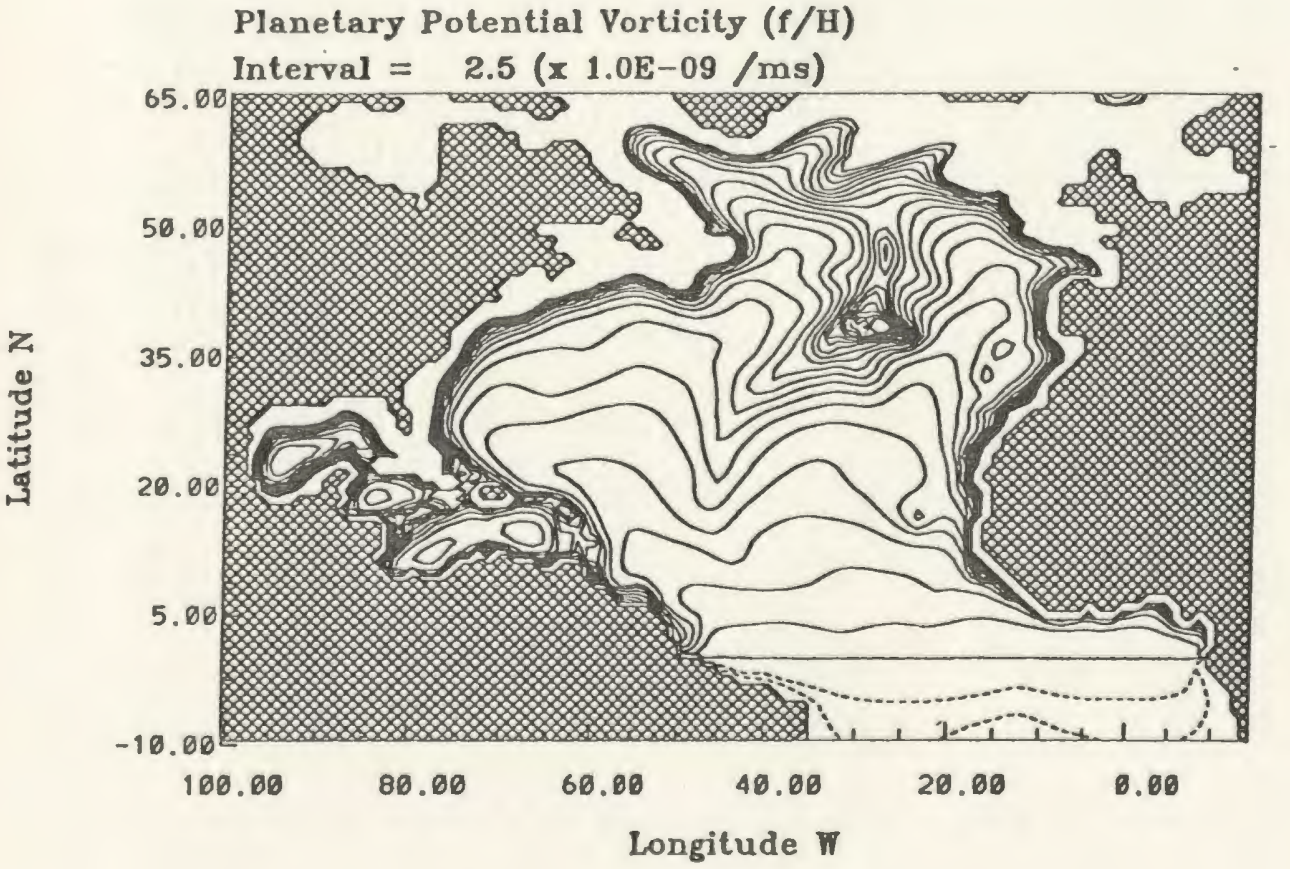

Figure 2.1: *Planetary potential vorticity, f/H, contours. The topography has been smoothed using a Laplacian smoother as outlined in the text. The contour interval is* $2.5 \times 10^{-9} s^{-1} m^{-1}$.

friction does, however, damp all scales of motion indiscriminately, reducing the amplitude of the model predicted results. We therefore use the smallest value of the linear bottom friction coefficient, r, that allows the model to retain computational stability, and include lateral friction, (the lateral mixing of momentum terms in (2.1.1) to (2.1.5)), which tends primarily to damp smaller scale features. In general the lateral mixing coefficient, A_H can vary a great deal in the ocean (cf. Webster, 1965). Its precise form is unknown, so for simplicity a constant value of A_H is employed. We now proceed to discuss the manner in which (2.1.5) is solved numerically.

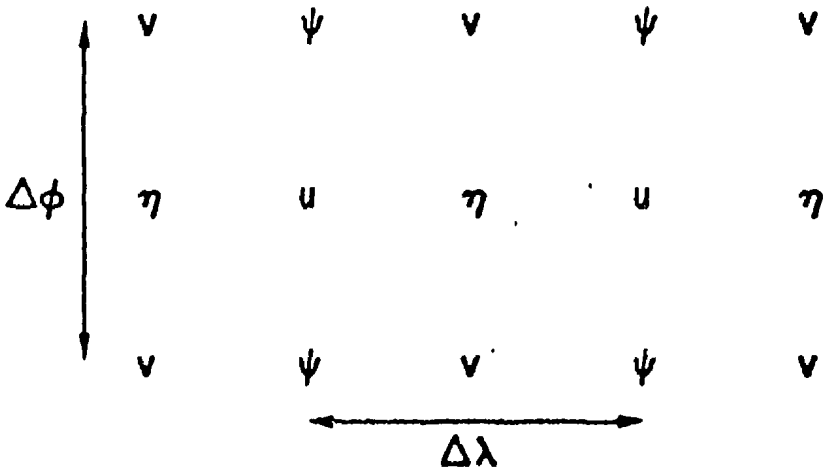

Figure 2.2: *The Arakawa C-Grid*

2.1.2 : Numerical Solution Technique

To solve (2.1.5) we use centered differencing to rewrite (2.1.5) in finite difference form on the staggered C-grid of Mesinger and Arakawa(1976). The wind stress $(\tau^\lambda, \tau^\phi)$, and topography are stored at η points, while the streamfunction is calculated at Ψ points (see Fig.2.2). The formulation of (2.1.5) is completely implicit except for the lateral mixing of

momentum which is explicitly calculated. This can be written as;

$$\left(\frac{\partial}{\partial\lambda}\left\{\frac{\Psi_\lambda^{n+1}}{H\cos\phi}\right\}+\frac{\partial}{\partial\phi}\left\{\frac{\Psi_\phi^{n+1}\cos\phi}{H}\right\}\right)-\left(\frac{\partial}{\partial\lambda}\left\{\frac{\Psi_\lambda^{n}}{H\cos\phi}\right\}+\frac{\partial}{\partial\phi}\left\{\frac{\Psi_\phi^{n}\cos\phi}{H}\right\}\right)$$

$$+\triangle t\left(\frac{\partial}{\partial\lambda}\left\{\frac{r\Psi_\lambda^{n+1}}{H^2}\right\}+\frac{\partial}{\partial\phi}\left\{\frac{r\cos\phi\Psi_\phi^{n+1}}{H^2}\right\}\right)+\triangle t J\left(\Psi^{n+1},\frac{f}{H}\right)$$

$$=\frac{a\triangle t}{\rho_0}\left\{\frac{\partial}{\partial\lambda}\left(\frac{\tau^{\lambda,n+1}}{H}\right)-\frac{\partial}{\partial\phi}\left(\frac{\tau^{\phi,n+1}}{H}\right)\right\}+a\triangle t A_H\left\{\frac{\partial}{\partial\lambda}\zeta^{\phi,n}-\frac{\partial}{\partial\phi}(\cos\phi\zeta^{\lambda,n})\right\} \quad (2.1.10)$$

with $\triangle t$ representing the time step, $n+1$ denoting the current time-step, and n denoting the last time-step. Once Ψ^{n+1} is known from (2.1.5), (2.1.4) can be used to solve for (u,v) which in turn are used to calculate the horizontal mixing of momentum term in (2.1.5) required for the next time step. The method of solution relies on the tridiagonality of the resulting matrix equation for (2.1.10) to perform Gaussian elimination and invert the matrix equation to solve for Ψ^{n+1}.

The implicit treatment of the friction and Coriolis terms can amount to a considerable saving of computer integration costs. To see this, consider the following simple example of the friction equation:

$$\frac{\partial u}{\partial t}+ru=\chi$$

where χ represents some forcing function. In the final steady state, the analytic solution is $u=\chi/r$. The friction equation can be finite differenced either implicitly as:

$$\frac{u^{n+1}-u^n}{\triangle t}+ru^{n+1}=\chi^{n+1}$$

or explicitly as

$$\frac{u^{n+1}-u^n}{\triangle t}+ru^n=\chi^{n+1}$$

If we consider the unforced implicit case first, we can write;

$$u^{n+1}(1 + r\Delta t) = u^n$$

Following Von Neumann's method we look for a solution of the form $u^n = A\lambda^n$, which upon simplifying reduces to

$$\lambda = \frac{1}{(1 + r\Delta t)}$$

The CFL (Courant, Friedrichs and Lewy, 1926) stability criterion stipulates that, in general, $|\lambda| \leq 1$, however, in this form, there is the possibility of allowing negative values for λ, which give rise to the computational mode (a steady oscillating grid point wave). Instead, we apply the more stringent criterion, $0 < \lambda < 1$ a condition clearly satisfied by this example for any $\Delta t > 0$. Note that for $\Delta t \gg 1$ the forced case reduces to

$$u^{n+1} = \frac{V^{n+1}}{r}$$

ie. the steady state solution. If we now consider the explicit case, following the above analysis we obtain the CFL criterion

$$0 < (\lambda = 1 - r\Delta t) < 1$$

which implies that $\Delta t \leq 1/r$. This simple example indicates the advantages of the implicit treatment of the friction and Coriolis terms. Indeed with A_H set to zero, (2.1.10) is stable for any time step. Ideally, we would like to treat the Laplacian mixing terms implicitly as well. However, treating the Laplacian mixing of momentum implicitly would change (2.1.5) from a second to a fourth order equation in Ψ and would require a computationally

more expensive solution technique than we employ here. Treating the Laplacian mixing of momentum explicitly does, however, present a limitation on the model's efficiency since it defines an upper bound on the allowable time-step. In order to describe the bound on the allowable time step imposed by the inclusion of the lateral mixing terms, we consider the two dimensional diffusion equation

$$\frac{\partial u}{\partial t} = A_H \left(\frac{\partial^2 u}{\partial x^2} + \frac{\partial^2 u}{\partial y^2} \right)$$

Using centered differencing, this can be rewritten as:

$$u_{i,j}^{n+1} = u_{i,j}^{n} + \frac{A_H \Delta t}{\Delta x^2} \left\{ u_{i+1,j}^{n} + u_{i-1,j}^{n} - 2u_{i,j}^{n} \right\} + \frac{A_H \Delta t}{\Delta y^2} \left\{ u_{i,j+1}^{n} + u_{i,j-1}^{n} - 2u_{i,j}^{n} \right\} \quad (2.1.11)$$

where i, j denote spatially where the point lies on the grid mesh; n denotes the last time step; $n+1$ denotes the current time step; Δx is analagous to $\Delta\lambda$ in Fig.2.2; and Δy is analagous to $\Delta\phi$ in Fig.2.2. Using Von Neumann's method we look for a solution of the form $u_{i,j}^{n} = U_n e^{Iik\Delta x} e^{Ijl\Delta y}$ (where $I = \sqrt{-1}$), substituting into (2.1.11) and simplifying, we obtain:

$$U^{n+1} = U^{n} \left\{ 1 + 2A_H \Delta t \left(\frac{\cos k\Delta x - 1}{\Delta x^2} + \frac{\cos l\Delta y - 1}{\Delta y^2} \right) \right\}$$

If we consider a grid-point wave, for which $k\Delta x = l\Delta y = \pi$, then this reduces to

$$U^{n+1} = U^{n} \left\{ 1 - 4A_H \Delta t \left(\frac{1}{\Delta x^2} + \frac{1}{\Delta y^2} \right) \right\}$$

If we look for a solution of the form $U^n = A\lambda^n$ as before, we obtain the CFL stability criterion which requires

$$4A_H \Delta t \left(\frac{1}{\Delta x^2} + \frac{1}{\Delta y^2} \right) < 1$$

Therefore, the time step for the barotropic model is limited only by the choice of the zonal and meridional grid spacings ($\triangle\lambda, \triangle\phi$) and choice of the lateral mixing of momentum coefficient, A_H, a point we return to in section 2.2.5.

Instead of taking proper account of the irregular coastline of the North Atlantic, we follow GG and work in a rectangular domain in (λ, ϕ) space, treating the land mass as shallow water. In particular, the continental margins are treated as land of $0.5m$ depth, while small islands (Cuba, Hispaniola) are treated as water of $1.0m$ depth. The wind forcing terms are set to zero over the land and the boundary condition $\Psi = 0$ is implemented at the regular boundary of the rectangular domain, equivalent to specifying no normal flow at the model domain boundaries. The relatively high friction over the land mass (note the terms in r/H^2 in (2.1.5)) ensures $\Psi \sim 0$ there. Since $\Psi \sim 0$ over the land, it follows from (2.1.4) that the velocities are small there as well. A more detailed description of the topography, grid resolution, and other parameters will be given in sections 2.2.4 and 2.2.5.

2.2: The Two Density Layer Model

The two density layer model is similar to that described and utilized by Anderson and Corry (1985a,b) (hereafter AC). The model is composed of two superposed layers of uniform density ρ_1 and ρ_2. The upper layer is assumed to be of uniform undisturbed depth H_1, while the undisturbed depth of the second layer is dependent on the depth of the ocean at that point (*ie.* $H_2 = H - H_1$), as portrayed in Fig.2.3. The finite jump in density between the two layers represents the ocean's thermocline/pycnocline, the downwards displacement of which is measured by η_2 as shown in Fig.2.3. In spherical coordinates, the linearized equations of motion for the upper and lower layers of the two density layer model are given as

Layer 1

$$\frac{\partial u_1}{\partial t} - fv_1 = \frac{-g}{a\cos\phi}\frac{\partial \eta_1}{\partial \lambda} + \frac{\tau^\lambda}{\rho_0 H_1} + A_H \mathcal{L}_1^\lambda \tag{2.2.1}$$

$$\frac{\partial v_1}{\partial t} + fu_1 = -\frac{g}{a}\frac{\partial \eta_1}{\partial \phi} + \frac{\tau^\phi}{\rho_0 H_1} + A_H \mathcal{L}_1^\phi \tag{2.2.2}$$

$$\frac{\partial \eta_2}{\partial t} + \frac{H_1}{a\cos\phi}\left\{\frac{\partial u_1}{\partial \lambda} + \frac{\partial}{\partial \phi}(v_1 \cos\phi)\right\} = 0 \tag{2.2.3}$$

Here, (2.2.1) and (2.2.2) are the momentum equations in the upper layer, while (2.2.3) is the continuity equation in the upper layer after having made the simplification of neglecting the sea-surface elevation term η_{1t} as compared to η_{2t}, since $\eta_{2t} \gg \eta_{1t}$. This is the form of

the rigid-lid approximation applicable to the baroclinic mode Note that we must also satisfy the rigid-lid approximation applicable to the barotropic mode as discussed in section 2.1.

Layer 2

$$\frac{\partial u_2}{\partial t} - f v_2 = \frac{-1}{a\cos\phi}\left\{ g\frac{\partial \eta_1}{\partial \lambda} - g'\frac{\partial \eta_2}{\partial \lambda}\right\} - \frac{r u_2}{H_2} + A_H \mathcal{L}_2^{\lambda} \tag{2.2.4}$$

$$\frac{\partial v_2}{\partial t} + f u_2 = \frac{-1}{a}\left\{ g\frac{\partial \eta_1}{\partial \phi} - g'\frac{\partial \eta_2}{\partial \phi}\right\} - \frac{r v_2}{H_2} + A_H \mathcal{L}_2^{\phi} \tag{2.2.5}$$

$$-\frac{\partial \eta_2}{\partial t} + \frac{1}{a\cos\phi}\left\{ \frac{\partial}{\partial \lambda}(H_2 u_2) + \frac{\partial}{\partial \phi}(H_2 v_2 \cos\phi)\right\} = 0 \tag{2.2.6}$$

(2.2.4) and (2.2.5) are the momentum equations for the lower layer, while (2.2.6) is the continuity equation for the lower layer. Here $(\mathcal{L}_q^{\lambda}\mathcal{L}_q^{\phi})$ are the horizontal Laplacian terms (as defined in section 2.1) representing the horizontal mixing of momentum in each layer, the subscript q referring to the layer in question. A_H is the horizontal mixing coefficient; $H = H(\lambda, \phi)$ is the realistic bottom topography for the domain; H_2 is the difference between this and the undisturbed depth of the upper layer H_1, (*ie.* $H_2 = H - H_1$); λ is longitude, ϕ is latitude and (u_q, v_q) are the (λ, ϕ) components of velocity in each layer respectively $(q = 1, 2)$; $f = 2\Omega \sin\phi$ is the Coriolis parameter, Ω the Earth's rotation rate, a is the radius of the Earth; $\tau^{\lambda}, \tau^{\phi}$ are the eastward and northward components of the surface wind stress respectively; g is the acceleration due to gravity; g' is the reduced gravity (defined as $g(\rho_2 - \rho_1)/\rho_2$); ρ_0 is a representative density for sea water; r is a linear bottom friction coefficient; η_1 is the sea level height measured upwards, and η_2 is the interface elevation (model thermocline/pycnocline) measured downwards.

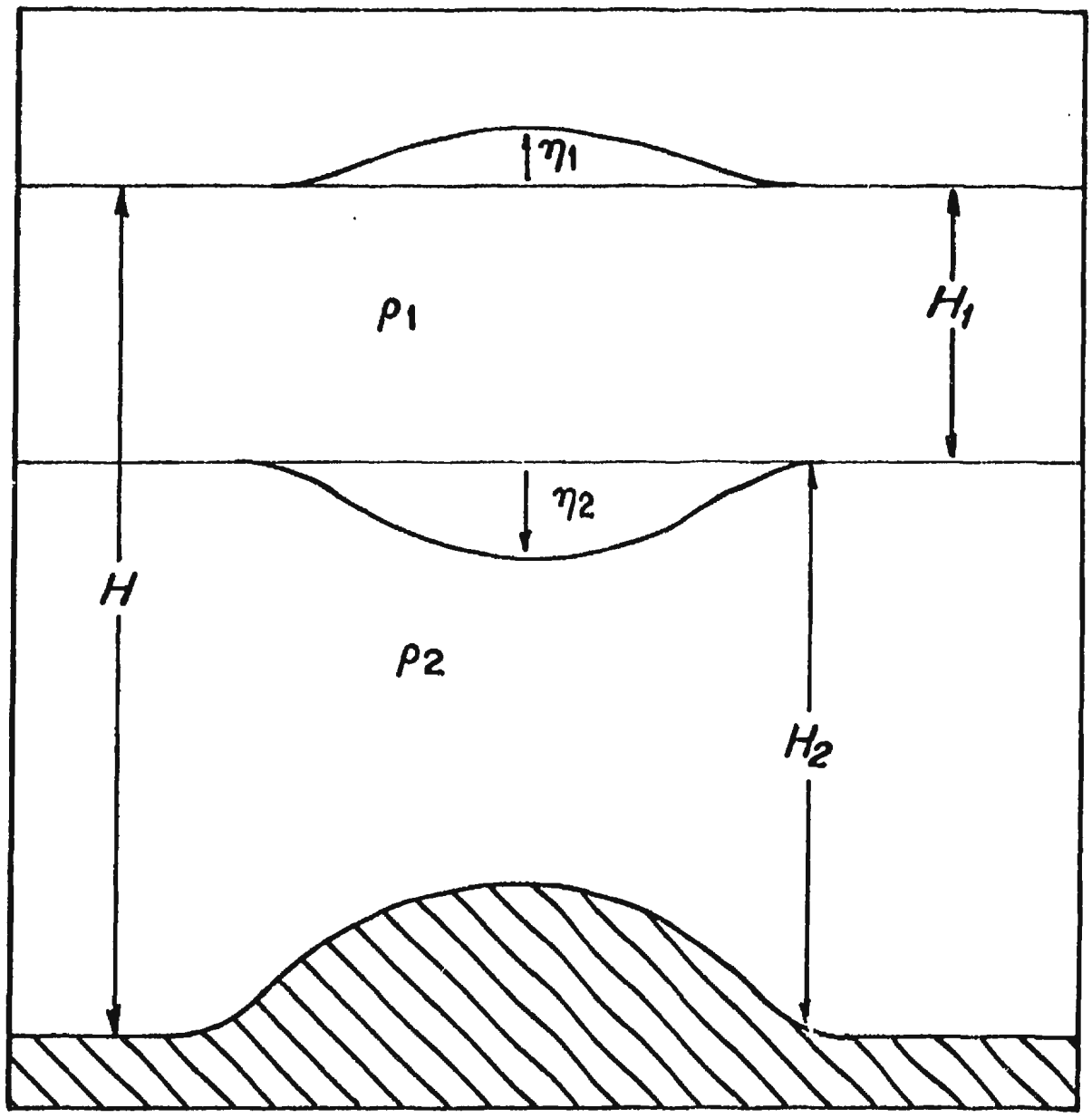

Figure 2.3: *Schematic diagram indicating the definition of variables used in the two-density-layer model.*

Combining (2.2.3) and (2.2.6) we can write;

$$\frac{1}{a\cos\phi}\left\{\frac{\partial}{\partial\lambda}(H_1u_1+H_2u_2)+\frac{\partial}{\partial\phi}\left[(H_1v_1+H_2v_2)\cos\phi\right]\right\}=0 \qquad (2.2.7)$$

which is analagous to (2.1.3) and allows the introduction of the barotropic streamfunction Ψ such that

$$auH=-\Psi_\phi \;;\; avH\cos\phi=\Psi_\lambda \qquad (2.2.8)$$

where

$$u=\frac{1}{H}(H_1u_1+H_2u_2) \quad ; \quad v=\frac{1}{H}(H_1v_1+H_2v_2) \qquad (2.2.9)$$

are the barotropic (vertically averaged) velocities. Forming the barotropic part of the solution, we take

$$\frac{[H_1(2.2.1)+H_2(2.2.4)]}{H}$$

and

$$\frac{[H_1(2.2.2)+H_2(2.2.5)]}{H}$$

which, employing the definition of the barotropic velocities (eq.(2.2.9)) yields the analagous forms of (2.1.1) and (2.1.2);

$$\frac{\partial u}{\partial t}-fv=\frac{-g}{a\cos\phi}\frac{\partial\eta_1}{\partial\lambda}+\frac{\tau^\lambda}{\rho_0H}+\frac{g'H_2}{a\cos\phi H}\frac{\partial\eta_2}{\partial\lambda}-\frac{ru_2}{H}+\mathcal{F}^\lambda \qquad (2.2.10)$$

$$\frac{\partial v}{\partial t}+fu=-\frac{g}{a}\frac{\partial\eta_1}{\partial\phi}+\frac{\tau^\phi}{\rho_0H}+\frac{g'H_2}{aH}\frac{\partial\eta_2}{\partial\phi}-\frac{rv_2}{H}+\mathcal{F}^\phi \qquad (2.2.11)$$

Here $(\mathcal{F}^\lambda,\mathcal{F}^\phi)$ are the terms arising from the horizontal mixing of momentum,$(\mathcal{L}_q^\lambda,\mathcal{L}_q^\phi)$ in the initial equations. Taking the vertical component of the curl:

$$\frac{\partial}{\partial\lambda}(2.2.11)-\frac{\partial}{\partial\phi}(\cos\phi(2.2.10))$$

and using the definition for the barotropic streamfunction, Ψ (see (2.2.8)), yields the following equation for the mass transport streamfunction

$$\frac{\partial}{\partial t}\left\{\frac{\partial}{\partial\lambda}\left(\frac{\Psi_\lambda}{H\cos\phi}\right)+\frac{\partial}{\partial\phi}\left(\frac{\Psi_\phi\cos\phi}{H}\right)\right\}+J\left(\Psi,\frac{f}{H}\right)=g'H_1J\left(\eta_2,\frac{1}{H}\right)$$
$$-ar\left\{\frac{\partial}{\partial\lambda}\left(\frac{v_2}{H}\right)-\frac{\partial}{\partial\phi}\left(\frac{u_2\cos\phi}{H}\right)\right\}+\frac{a}{\rho_0}\left\{\frac{\partial}{\partial\lambda}\left(\frac{\tau^\lambda}{H}\right)-\frac{\partial}{\partial\phi}\left(\frac{\tau^\phi\cos\phi}{H}\right)\right\}$$
$$+\left\{\frac{\partial\mathcal{F}^\phi}{\partial\lambda}-\frac{\partial}{\partial\phi}\left(\cos\phi\mathcal{F}^\lambda\right)\right\} \tag{2.2.12}$$

where $J(A, B)$ is the Jacobian operator defined by (2.1.6). In order to solve (2.2.12) we first require solutions of (u_2, v_2) and η_2, which are easily obtained by utilizing the definition of the baroclinic velocities $(\hat{u}, \hat{v})$, defined as

$$\hat{u}=u_2-u_1\ ;\ \hat{v}=v_2-v_1 \tag{2.2.13}$$

Utilizing (2.2.9) and (2.2.13) we may rewrite the lower layer velocities, (u_2, v_2), as

$$u_2=u+\frac{H_1}{H}\hat{u}\ ;\ v_2=v+\frac{H_1}{H}\hat{v} \tag{2.2.14}$$

(2.2.14) together with the definition of the barotropic streamfunction, allows us to recast (2.2.12) as

$$\frac{\partial}{\partial\lambda}\left\{\left(\frac{\partial}{\partial t}+\frac{r}{H}\right)\frac{\Psi_\lambda}{H\cos\phi}\right\}+\frac{\partial}{\partial\phi}\left\{\left(\frac{\partial}{\partial t}+\frac{r}{H}\right)\frac{\Psi_\phi\cos\phi}{H}\right\}+J\left(\Psi,\frac{f}{H}\right)$$
$$=g'H_1J\left(\eta_2,\frac{1}{H}\right)-arH_1\left\{\frac{\partial}{\partial\lambda}\left(\frac{\hat{v}}{H^2}\right)-\frac{\partial}{\partial\phi}\left(\frac{\hat{u}\cos\phi}{H^2}\right)\right\}$$
$$+\frac{a}{\rho_0}\left\{\tau^\lambda\cos\phi\frac{H_\phi}{H^2}-\tau^\phi\frac{H_\lambda}{H^2}\right\}+\frac{a}{\rho_0H}\left\{\frac{\partial}{\partial\lambda}\left(\tau^\phi\right)-\frac{\partial}{\partial\phi}\left(\tau^\lambda\cos\phi\right)\right\}$$
$$+aA_H\left\{\frac{\partial\mathcal{F}^\phi}{\partial\lambda}-\frac{\partial}{\partial\phi}\left(\cos\phi\mathcal{F}^\lambda\right)\right\} \tag{2.2.15}$$

In order to obtain the equations necessary for solving the baroclinic velocities $(\hat{u}, \hat{v})$ we first form $\{(2.2.4) - (2.2.1)\}$ and $\{(2.2.5) - (2.2.2)\}$. These, together with (2.2.13) and (2.2.14) allow us to define the momentum and continuity equations for the baroclinic part as:

$$\frac{\partial \hat{u}}{\partial t} - f\hat{v} = \frac{g'}{a\cos\phi}\frac{\partial \eta_2}{\partial \lambda} - \frac{rH_1\hat{u}}{HH_2} - \frac{r\bar{u}}{H_2} - \frac{\tau^{\lambda}}{\rho_0 H_1} + A_h\mathcal{G}^{\lambda} \tag{2.2.16}$$

$$\frac{\partial \hat{v}}{\partial t} + f\hat{u} = \frac{g'}{a}\frac{\partial \eta_2}{\partial \phi} - \frac{rH_1\hat{v}}{HH_2} - \frac{r\bar{v}}{H_2} - \frac{\tau^{\phi}}{\rho_0 H_1} + A_h\mathcal{G}^{\phi} \tag{2.2.17}$$

where $(\mathcal{G}^{\lambda}, \mathcal{G}^{\phi})$ are the terms arising from the horizontal mixing of momentum,$(\mathcal{L}_q^{\lambda}, \mathcal{L}_q^{\phi})$ in the initial equations. Finally to obtain the equation governing the motion of the interface (or model pycnocline/thermocline), we form $\{(2.2.6) - (2.2.3)\}$ to obtain

$$\frac{\partial \eta_2}{\partial t} = \frac{H_1 H_2}{aH\cos\phi}\left\{\left(\frac{\partial \hat{u}}{\partial \lambda} + \frac{\partial}{\partial \phi}(\hat{v}\cos\phi)\right)\right\}$$

$$+\frac{H_1}{aH\cos\phi}\left\{\left(u + \frac{H_1\hat{u}}{H}\right)\frac{\partial H_2}{\partial \lambda} + \left(\bar{v} + \frac{H_1\hat{v}}{H}\right)\frac{\partial}{\partial \phi}(H_2\cos\phi)\right\} \tag{2.2.18}$$

Note that (2.2.15), (2.2.16), (2.2.17) and (2.2.18) completely specify the solution for the two density layer model.

2.2.1: Physical Interpretation of the Governing Equations

Note that comparing (2.2.15) with (2.1.5), the primary differences are the additional terms involving η_2 and $(\hat{u}, \hat{v})$ which arise due to the baroclinic nature of the two density layer model. Indeed, one can decompose the transport streamfunction, Ψ, of (2.2.15) into a part driven solely by the barotropic dynamics (that defined by (2.1.5)) and that part driven solely by the baroclinic nature of the model, Ψ_J. The barotropic response will be that described in section 2.1.2, while the additional transport due to the inclusion of the

baroclinic structure can be examined in terms of Ψ_J. We can solve for Ψ_J by subtracting (2.1.5) from (2.2.15) to yield:

$$\frac{\partial}{\partial\lambda}\left\{\left(\frac{\partial}{\partial t}+\frac{r}{H}\right)\frac{\Psi_{J\lambda}}{H\cos\phi}\right\}+\frac{\partial}{\partial\phi}\left\{\left(\frac{\partial}{\partial t}+\frac{r}{H}\right)\frac{\Psi_{J\phi}\cos\phi}{H}\right\}+J\left(\Psi_J,\frac{f}{H}\right)$$

$$=g'H_1J\left(\eta_2,\frac{1}{H}\right)-arH_1\left\{\frac{\partial}{\partial\lambda}\left(\frac{\hat{v}}{H^2}\right)-\frac{\partial}{\partial\phi}\left(\frac{\hat{u}\cos\phi}{H^2}\right)\right\}+MIXING \qquad (2.2.19)$$

Equation (2.2.19) is a vorticity equation and has a simple interpretation along the lines of (2.1.5). The first group of terms on the right hand side represents the time rate of change of relative vorticity and its dissipation by bottom friction, the second represents flow across lines of planetary potential vorticity, f/H. Vorticity can be generated here by the JEBAR term (Sarkisyan and Ivanov, 1971), where

$$JEBAR=J\left(\eta_2,\frac{1}{H}\right)$$

The final terms in (2.2.19) are the terms involving $(\hat{u},\hat{v})$, which may represent either a source or sink of vorticity, and the lateral mixing of momentum. This term arises since the mixing term in (2.1.5) is not, in general, equal to that of (2.2.15). Note that JEBAR can also be written as

$$JEBAR=\hat{k}\cdot\left(\nabla\eta_2\times\nabla\frac{1}{H}\right) \qquad (2.2.20)$$

where $\hat{k}$ is a unit vector in the vertical upwards direction. It follows that if JEBAR is zero, then gradients of interface ($\nabla\eta_2$), and gradients of topography ($\nabla(1/H)$) are parallel. So that in order for JEBAR forcing to be present we must have contours of η_2 and H crossing one another at appreciable angles. Therefore, the manner with which gradients in the interface are produced also produce the baroclinically (JEBAR forced)

transport, Ψ_1, in the two density layer model. The sources that generate interface displacements, discussed further later, have been identified as being of two types, (1) that due to Ekman pumping by the windstress curl forcing (e.g. White(1977), Meyers(1979), White and Saur(1981)), and (2) that due to boundary influences induced either locally by the windstress (upwelling/downwelling) or associated with the propagation of coastally trapped internal Kelvin waves (e.g. White and Saur(1981), Mysak(1983), Johnson and O'Brien(1990)).

Anderson et al.(1979) indicate that inclusion of the baroclinic field will significantly modify the barotropic response over time scales of tens of years, while the barotropic response has an order $H_1/H_2 \ll 1$ weaker effect on the baroclinic response, so that there is much less adjustment in the baroclinic field as a result of barotropic forcing. Likewise, the direct topographic effect will be weak in the baroclinic response (although not totally negligable). In contrast, the effect on the barotropic case is order $H_2/H_1 \gg 1$ larger. Therefore, the barotropic mode shows response to topography on its own rapid time scale but will also change on the much slower time scale of the baroclinic mode, with the baroclinic mode essentially behaving as that for a flat-bottomed ocean. In a continuously stratified, flat-bottomed ocean, an infinite number of vertical modes exist. The horizontal structure associated with each mode is described by the shallow water equations. In the unforced, inviscid case in cartesian coordinates, these are:

$$\frac{\partial u_n}{\partial t} - f v_n = -g \frac{\partial \eta_n}{\partial x}$$

$$\frac{\partial v_n}{\partial t} + f u_n = -g \frac{\partial \eta_n}{\partial y}$$

$$\frac{\partial \eta_n}{\partial t} + H_n\left(\frac{\partial u_n}{\partial x} + \frac{\partial v_n}{\partial y}\right) = 0$$

where n is the number of the mode, f is the Coriolis parameter, g is the acceleration due to gravity, H_n is an equivalent depth that determines the mode wave speed $c_n = (gH_n)^{1/2}$, u_n and v_n are the velocities of each mode in the x and y directions, respectively, and η_n is the effective displacement representing the pressure in each mode. The $n = 0$ mode describes the barotropic case in which H_0 is the ocean depth, the subsequent n modes are defined by c_n. These have the property that $c_0 > c_1 > \cdots > c_{n-1} > c_n > c_{n+1} > \cdots$. The c_n for $n \geq 1$ depend on the stratification. c_n is usually in the range 0.5 to 3 ms^{-1} for the $n = 1$ (or primary) mode, the case we consider here. The total solution is obtained by summing over all n modes (see Gill, 1982, Chapter 6). For the primary mode, we rewrite the shallow water equations as:

$$\frac{\partial u}{\partial t} - fv = -g'\frac{\partial \eta_2}{\partial x}$$

$$\frac{\partial v}{\partial t} + fu = -g'\frac{\partial \eta_2}{\partial y}$$

$$\frac{\partial \eta_2}{\partial t} + H_1\left(\frac{\partial u}{\partial x} + \frac{\partial v}{\partial y}\right) = 0$$

These are the equivalent equations of (2.2.16) to (2.2.18), expressed in cartesian coordinates and neglecting the forcing terms, and topographic effects, for simplicity. It can readily be shown these equations give rise to a trapped Kelvin wave travelling along the coastal boundary with wave speed, $c = \sqrt{g'H_1}$ with the coast on the right when travelling in the northern hemisphere, the opposite is true for the southern hemisphere. The amplitude of the Kelvin wave is confined within an e-folding distance of the Rossby radius ($R_i = c/|f|$)

of the coast. These equations also give rise to baroclinic Rossby waves. If we consider the flow to be geostrophic to first order, then we may obtain the following;

$$\frac{\partial \eta_2}{\partial t} + \beta \frac{c^2}{f^2} \frac{\partial \eta_2}{\partial x} = 0$$

indicating a westward propagating baroclinic Rossby wave of wave speed $\beta c^2/f^2$ (typically $4 \times 10^{-2} ms^{-1}$ at midlatitudes).

The first baroclinic mode Rossby wave can cross the equatorial Atlantic in roughly 65 days, while at mid-latitudes, it can take decades. It follows that the baroclinic Rossby waves will have little or no effect on the seasonal response of the midlatitude North Atlantic. However, the coastal Kelvin wave can effect the seasonal signal in a number of ways. Coastal Kelvin waves travelling equatorward can effect the transport along the western boundary via the JEBAR term (Anderson and Corry, 1985a,b). Kelvin waves can also excite equatorial Kelvin waves which can modify the east-west pressure gradient along the equator as it passes. Upon reaching the eastern boundary, the Kelvin wave will in turn excite poleward propagating waves, and baroclinic Rossby waves (see Moore and Philander, 1977, Anderson and Rowlands, 1976), all of which can affect the transport via the JEBAR term. We now proceed to discuss the manner in which (2.2.15) is solved numerically.

2.2.2 : Numerical Solution Technique

Before proceeding to discussion of (2.2.15), we first consider the baroclinic equations (2.2.16) through (2.2.18). The model uses a method suggested by Sielecki (1968) for an E-grid and modified by Heaps (1971) to fit the C-grid. Note that in calculating the Coriolis term in (2.2.16), the 4 neighboring values of $\hat{v}$ are averaged. Likewise in Equation (2.2.17),

the 4 neighboring values of $\hat{u}$ are averaged to calculate the Coriolis term. We update (2.2.18) using forward-in-time differencing, then update (2.2.16) and (2.2.17) using η_2 at the new time level, with the terms involving $(r\bar{u}, r\bar{v})$ from the most recent solution of the barotropic equation. In solving for $(\hat{u}, \hat{v})$, (2.2.16) is utilized to update all $\hat{u}$ values first, and then all $\hat{v}$ values are updated using the most recent values of $\hat{u}$. That is, backward time differencing is used in (2.2.16) and (2.2 17), with the exception of the Coriolis term in (2.2.17), which uses forward time differencing. In this way, η_2, $\hat{u}$ and $\hat{v}$ are all known at the same time level. Treating the Coriolis parameter in this manner does, however, present a limitation on the allowable timestep we can employ in the model, a point we return to shortly.

The solution of (2.2.15) follows approximately the solution of the barotropic model. We again use centered differencing to rewrite (2.2.15) in finite difference form on the staggered C-grid, with variables stored as in the barotropic model. Again, (2.2.15) is completely implicit except for the lateral mixing of momentum, the frictional term arising from the baroclinic velocities $(\hat{u}, \hat{v})$, and the JEBAR term which are explicitly calculated. We again expect our time step to be bounded by the grid resolution, $(\Delta\lambda, \Delta\phi)$, and the magnitude of the lateral mixing of momentum, A_H as in section 2.1.3;

$$1 - 4A_H\Delta t\left(\frac{1}{\Delta x^2} + \frac{1}{\Delta y^2}\right) > 0$$

or;

$$\Delta t < \frac{1}{4A_H}\left(\frac{\Delta x^2 \Delta y^2}{\Delta x^2 + \Delta y^2}\right) \tag{2.2.21}$$

However, we also have baroclinic effects in the two density layer model which are bounded by two further CFL criterion. First that arising from the treatment of the Coriolis parameter in (2.2.16)

$$\Delta t \leq 1/f_{max}$$

where f_{max} is the Coriolis parameter at the northern boundary, and

$$\Delta t \leq \frac{\Delta x}{\sqrt{2}c}$$

due to the wave propagation in the model. Typically the limitation of the time step is much stonger by the baroclinic effects than by the momentum diffusion effects (at midlatiudes, for $1^o \times 1^o$ resolution, $1/f_{max} \sim 16000s$, while $\Delta x/\sqrt{2}c \sim 35000s$). By comparison, the momentum diffusion effects yields a typical value at midlatitudes (assuming $A_H = 10^4 m^2 s^{-1}$) of $\sim 10^5 s$. In order to retain computational efficiency, we simply take an integral number of baroclinic time steps, m, to each barotropic time step bounded by (2.2.21); that is, (2.2.16)-(2.2.18) are each solved (time stepped) m times for every one time step (solution) to (2.2.15). In this form the finite difference form of (2.2.15) can be written as;

$$\left(\frac{\partial}{\partial\lambda}\left\{\frac{\Psi_\lambda^{n+1}}{H\cos\phi}\right\}+\frac{\partial}{\partial\phi}\left\{\frac{\Psi_\phi^{n+1}\cos\phi}{H}\right\}\right)-\left(\frac{\partial}{\partial\lambda}\left\{\frac{\Psi_\lambda^{n}}{H\cos\phi}\right\}+\frac{\partial}{\partial\phi}\left\{\frac{\Psi_\phi^{n}\cos\phi}{H}\right\}\right)$$

$$+m\Delta t\left(\frac{\partial}{\partial\lambda}\left\{\frac{r\Psi_\lambda^{n+1}}{H^2}\right\}+\frac{\partial}{\partial\phi}\left\{\frac{r\cos\phi\Psi_\phi^{n+1}}{H^2}\right\}\right)+m\Delta tJ\left(\Psi^{n+1},\frac{f}{H}\right)$$

$$=m\Delta tg'H_1J\left(\eta_2^{n+1},\frac{1}{H}\right)+\frac{am\Delta t}{\rho_0}\left\{\frac{\partial}{\partial\lambda}\left(\frac{\tau^{\lambda,n+1}}{H}\right)-\frac{\partial}{\partial\phi}\left(\frac{\tau^{\phi,n+1}}{H}\right)\right\}$$

$$+am\Delta tA_H\left\{\frac{\partial}{\partial\lambda}\mathcal{L}^{\phi,n}-\frac{\partial}{\partial\phi}(\cos\phi\mathcal{L}^{\lambda,n})\right\}-amr\Delta tH_1\left\{\frac{\partial}{\partial\lambda}\left(\frac{\hat{v}^n}{H^2}\right)-\frac{\partial}{\partial\phi}\left(\frac{\hat{u}^n\cos\phi}{H^2}\right)\right\}$$

We now continue to describe the choice of model parameters utilized in the following experiments.

2.2.3: The Model Domain

As has been previously mentioned, Kelvin waves are excited along meridional and zonal boundaries, and can travel along the equator giving rise to northward propagating waves which will in turn shed baroclinic Rossby waves.

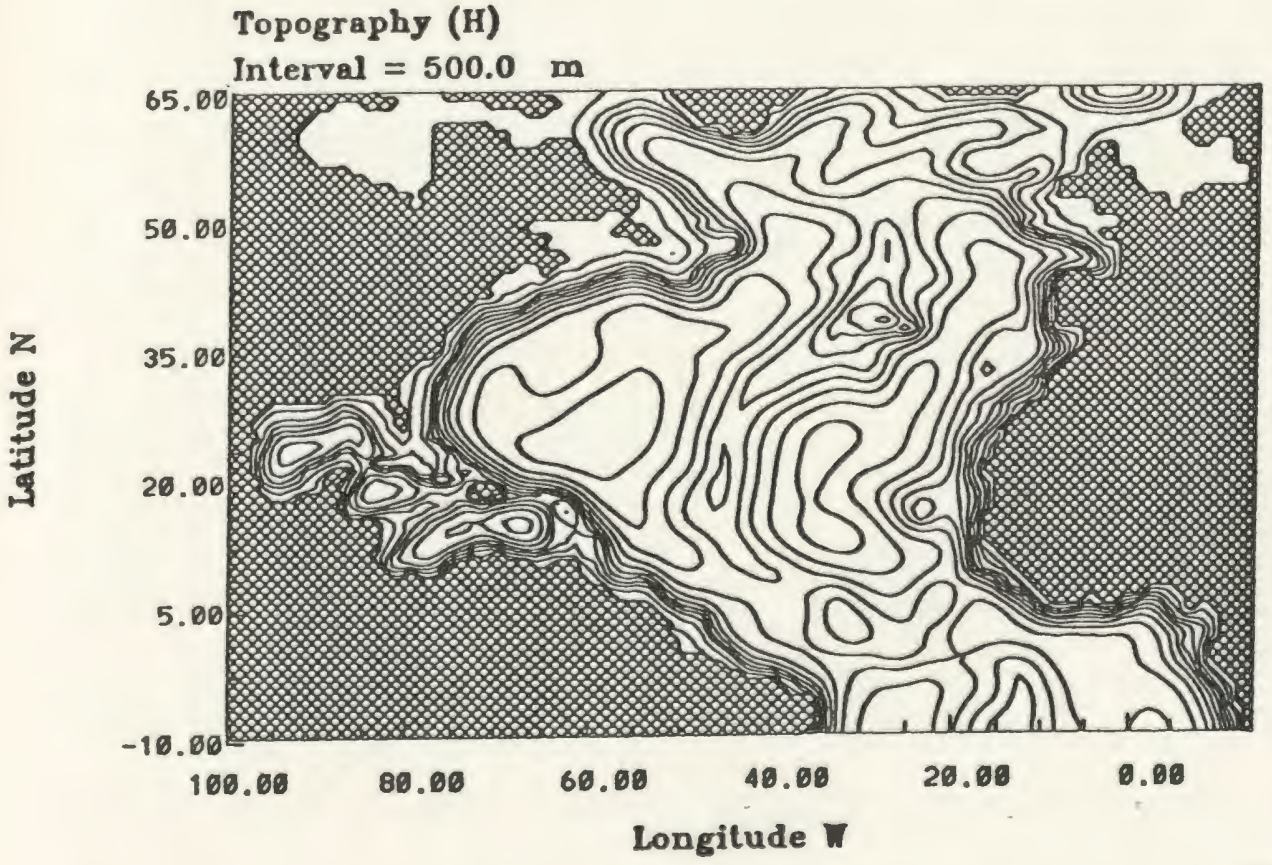

Figure 2.4: *The North Atlantic bottom topography, smoothed as outlined in the text. The contour interval is* $500m$.

To include this effect, it is necessary for the eastern and western continental boundaries,

and the equator, to be within the grid domain. The northern and southern boundaries of the model domain are placed at 65^0N, and 10^0S respectively. The choice of these boundaries resolves the region noted by GG as playing a role in their model results, (the Labrador/Irminger Sea) as well as supplies a partial northern land boundary due to Baffin Island, Greenland, and Iceland. Note, however, that the southern and northern boundaries occur in open ocean regions. It is therefore necessary to specify no wave propogation in from these areas, a point we return to in the next section.

The bottom topography was supplied on a $1^0 \times 1^0$ grid by the Geophysical Fluid Dynamics Laboratory (GFDL) at Princeton University, New Jersey, USA. As has been noted by previous authors (see for example AC, GG), the bottom topography must be smoothed to avoid the solution being contaminated by computational noise. Here, we follow AC (see their appendix A) and employ a Laplacian smoother defined by:

$$H^n_{i,j} = H^{n-1}_{i,j} + \sigma \mathcal{L} H^{n-1}_{i,j}$$

where

$$\mathcal{L} H^{n-1}_{i,j} = H^{n-1}_{i+1,j} + H^{n-1}_{i-1,j} + H^{n-1}_{i,j+1} + H^{n-1}_{i,j-1} - 4H^{n-1}_{i,j}$$

Here n denotes the number of times the Laplacian smoother has been applied to the topography data ($n = 1$ denotes 1 iteration). If one of the four neighbouring points is a land point, a value of $400m$ replaces that point in $\mathcal{L} H^{n-1}_{i,j}$. The extent of smoothing is dependent on depth through the value of σ chosen. Here we follow AC and define σ as

$$\sigma = \begin{cases} .1 & H_{i,j} \leq 1000m \\ .1 + (1500/4000)^2 & 1000m < H_{i,j} \leq 1500m \\ .1 + (H_{i,j}/4000)^2 & 1500m < H_{i,j} \end{cases}$$

The smoother is applied ten times (n=10). If any depths (not land) are still less than $400m$ depth after ten iterations, they are set to $400m$ depth. After each iteration of smoothing, the original coastline and islands are restored. The bottom topography produced in this manner is shown in Fig.2.4. At first sight this may appear to be an exceptionally strong smoothing function. However, since this is a Laplacian smoother, it will smooth grid point features stronger than large scale features. The amount that shallow regions become deeper is much less than the extent to which deep regions become shallow owing to the depth dependence of the smoothing parameter σ. A comparison of selected longitudinal sections at various latitudes of the raw and smoothed topography is shown in Fig.2.5. It is clear that the gross features of the bottom topography remain unchanged, while certain areas, (e.g. the Brownson Deep/Puerto Rico Trench, $25^{o}N$) have been strongly smoothed.

2.2.4: The Choice of Model Parameters

(i) Time Step:

The model experiments to be described use a linear bottom friction parameter of r $1.25 \times 10^{-3} ms^{-1}$ (corresponding to strong friction in a shelf region; Csanady, 1982) and the same horizontal mixing coefficient as utilized by AC of $A_H = 10^4 m^2 s^{-1}$. As mentioned, the model extends to $65^{o}N$, since $f = 2\Omega \sin\phi$, we have

$$\triangle t \leq \frac{1}{f} \sim 7500s$$

and since meridians converge as we move northward, the minimum longitudinal grid spacing is $\triangle x = 47km$ so

$$\triangle t \leq \frac{\triangle x}{\sqrt{2}c} \sim 15000s$$

where the choice of our value for $c = 2.17ms^{-1}$ is discussed in detail in (iii). At 65^oN, $\Delta y \sim 2.5\Delta x$ so that the CFL stability criterion for the barotropic part (with $A_H = 10^4 m^2 s^{-1}$) becomes

$$\Delta t \leq \frac{\Delta x^2}{4.64 A_H} \sim 45000s$$

indicating that we can take 6 baroclinic time steps to every one barotropic time step. In order for the model output to be calculated exactly at the middle of each month, we actually use a baroclinic time step of $\Delta t = 6574.5s$ with a barotropic time step of $\Delta t = 39447s$, in this way, each month requires 400 baroclinic time steps, while requiring only 66 barotropic time steps. This is a considerable savings since the elliptic inversion required at each time step to solve (2.2.15) is computationally much more expensive than the CPU cost of each baroclinic equation that requires solution.

(ii) The Kelvin Wave Damper:

In order to prevent the growth and propagation of spurious Kelvin waves in the model, a sponge boundary layer is constructed on the open ocean boundaries of the model domain. In their original work, AC applied a linear damping term, $-\gamma\alpha$ into the equations governing both the baroclinic velocities as well as the interface elevation (here α corresponds to each of $\hat{u}$, $\hat{v}$, or η_2). In this manner, the velocities as well as the interface decay to zero at the ocean boundaries of their domain. However, Greatbatch and Otterson (1991), carried out a number of experiments to determine the most favourable boundary conditions applicable for a reduced gravity model. These authors indicate sponging only the interface while leaving the velocities undamped yields results similar to applying a radiation boundary condition

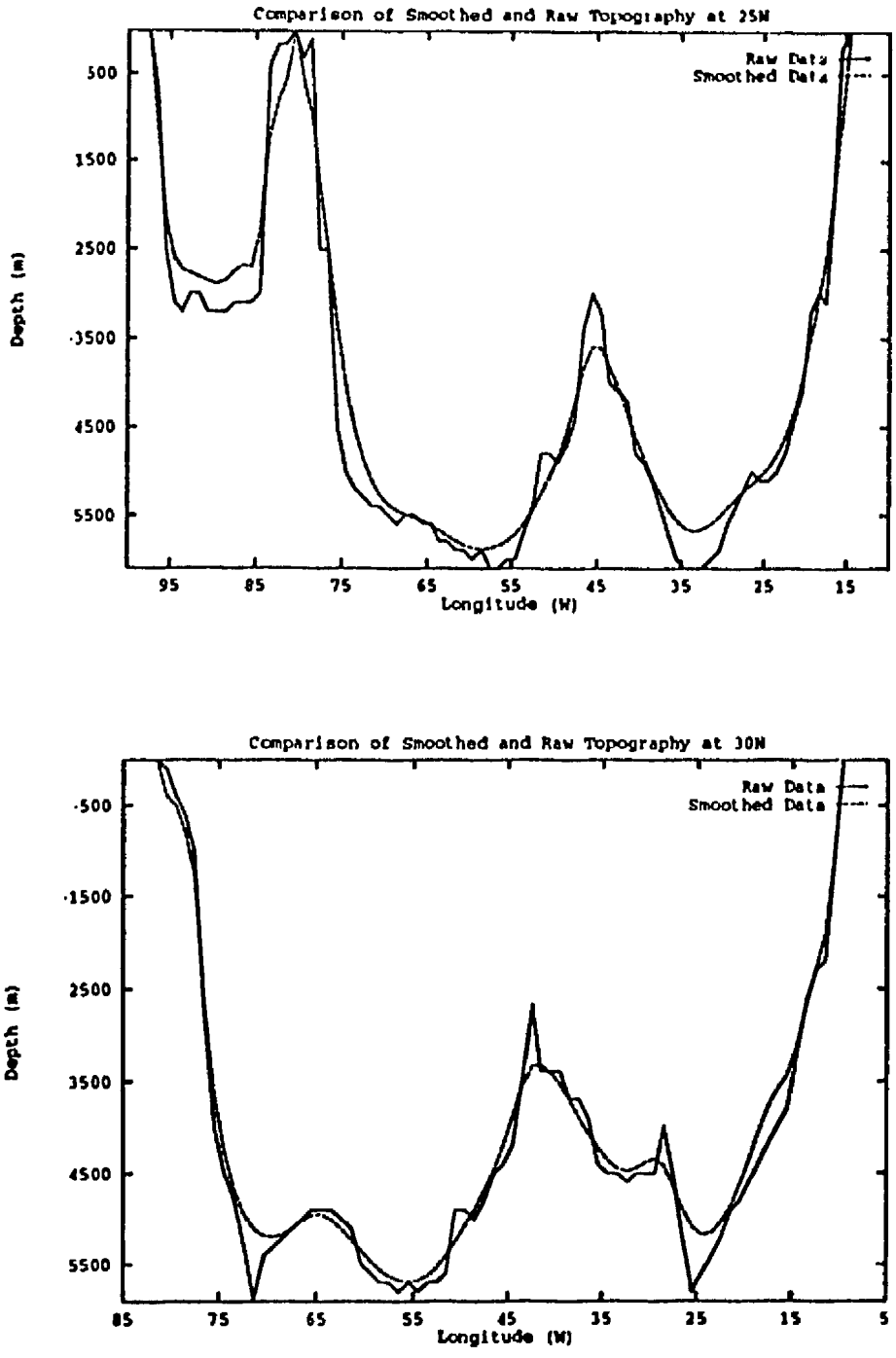

Figure 2.5: *Longitudinal sections of topography at selected latitude intervals comparing the bottom topography before (raw), and after (smoothed) the Laplacian filter has been applied (see text for details).*

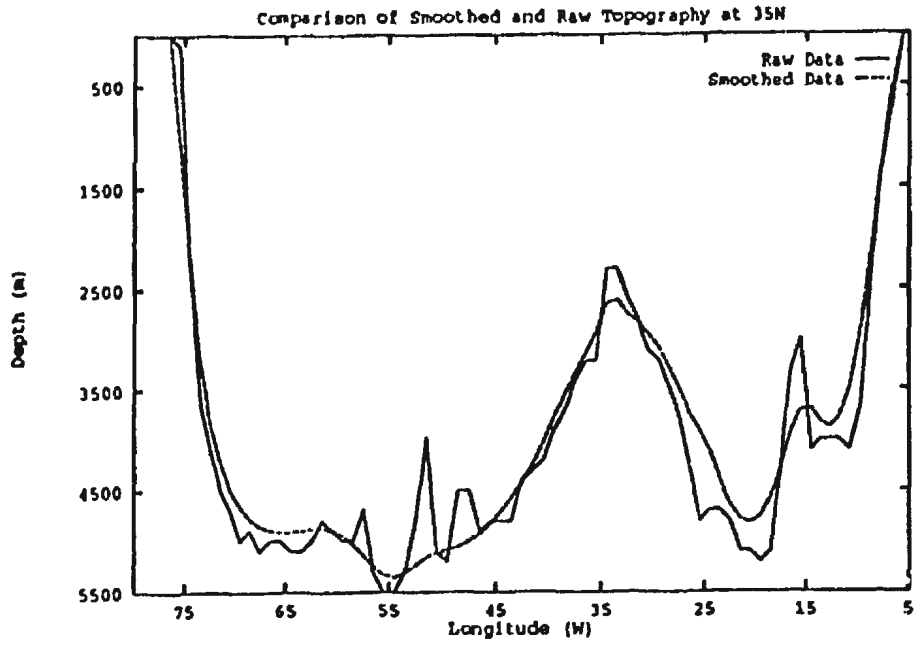

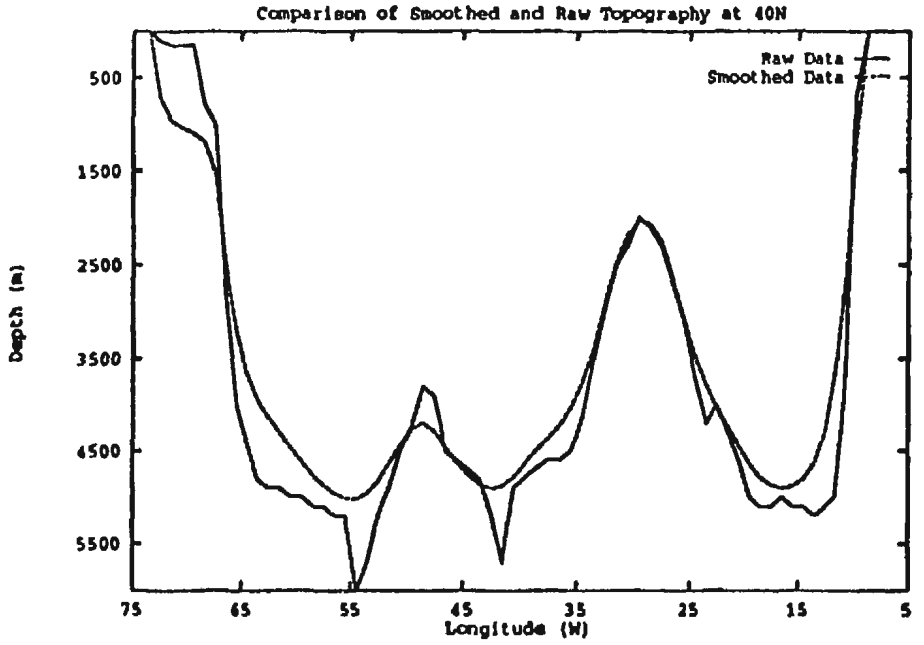

Figure 2.5: *continued*

at the open ocean boundaries, while sponging both interface and velocities is counterproductive. The sponge utilized in our model is introduced into the continuity equation as

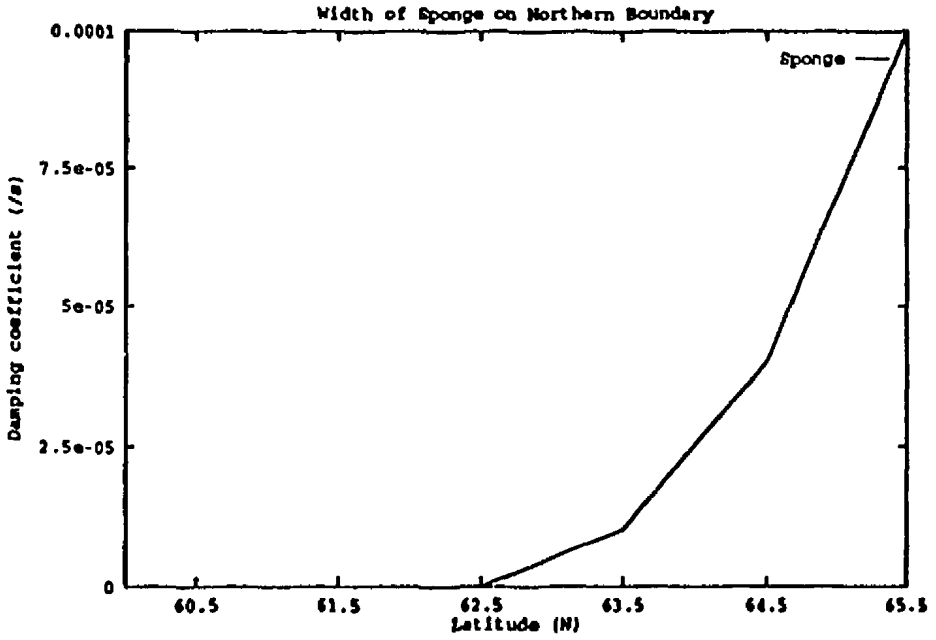

Figure 2.6: *The width of the sponge applied to the model's interface η_2 for the northern boundary.*

a linear damping term, that is a term $-\gamma\eta_2$ is added to equation (2.2.18) such that η_2 decreases exponentially to zero at the northern and southern ocean boundaries. The damping coefficient, γ is defined by:

$$\gamma = \gamma_0 \left(exp\left\{ \frac{\phi - \phi_n}{\alpha} \right\} + exp\left\{ \frac{\phi_s - \phi}{\alpha} \right\} \right)$$

where ϕ is latitude, ϕ_n is the latitude of the northern boundary, ϕ_s is the latitude of the southern boundary, α is an e-folding length scale (here 1^0) and γ_0 is a damping time scale, here we use $\gamma_0 = 10^{-4} s^{-1}$. The width of the sponge produced in this manner is indicated in Fig.2.6 for the northern boundary of our basin (the width is identical on the southern

boundary). Clearly the effect of this sponge is felt only within 3 grid points of the model boundaries and will not affect the interior solution.

(iii) Choice of Kelvin wave Speed:

For an immiscable two layer fluid of different densities ρ_1 and ρ_2 and undisturbed depths H_1 and H_2 respectively, and reduced gravity $g' = g(\rho_2 - \rho_1)/\rho_2$, the internal Rossby radius of deformation (R_i) is defined by

$$R_i = \frac{c}{|f|}$$

where

$$c = \left(\frac{g'(H_1 H_2)}{(H_1 + H_2)}\right)^{1/2}$$

For $H_2 \gg H_1$, (the case for the North Atlantic) this reduces to $c = \sqrt{g'H_1}$ where c is the wave speed, and f is the Coriolis parameter. In a continuously stratified fluid, the internal Rossby radius depends on the vertical stratification of the fluid column, the latitude, and the ocean depth. Seasonal fluctuations in R_i (due to seasonal stratification changes) are small (see Emery et al., 1984). To select c for the North Atlantic model we utilize the internal Rossby radii calculated by Emery et al. (1984). These authors utilized all density data contained in the NODC (National Oceanographic Data Center, Washington D.C., U.S.A) data files (up to the end of 1979) and the UNESCO (1980) equation of state to calculate the Brunt-Väisälä frequency, internal Rossby radii, and external Rossby radii for the North Atlantic and North Pacific for $5^0 \times 5^0$ squares. Figure 2.7 indicates the climatological annual mean internal (upper value) and external (lower value) Rossby radii for the North Atlantic.

The corresponding wave speed, c, produced from this analysis are contained in Fig.2.8 for each $5^0 \times 5^0$ square as in Fig.2.7, while Table 2.1 indicates the latitudinal average of the internal Kelvin wave speed, c, and baroclinic Rossby wave speed for each 5^o latitude band. The average over all 146 observations in the North Atlantic results in an average internal Kelvin wave speed of $2.17ms^{-1}$. Utilizing this value and the corresponding baroclinic Rossby wave speed, $(\beta c^2/f^2)$, Fig.2.9 indicates the comparison between the latitudinally averaged theoretical, and analysed baroclinic Rossby wave speed, showing excellent agreement for all latitudes.

At higher latitudes, due to weak stratification the internal Kelvin speed is small ($c = .94ms^{-1}$) however, the models wave speed is a constant value of $2.17ms^{-1}$. This may be considered a deficiency in the model since it allows internal Kelvin waves, and hence the baroclinic Rossby waves to propagate too fast at higher latitudes. There is a numerical compensating factor here. Anderson et al.(1979) considered the effect of north-south propogation speed errors associated with internal Kelvin waves travelling along an eastern or western boundary (see their appendix B) due to their coarse grid resolution (see also Hsieh et al., 1983). These authors indicate that as the numerical radius of deformation decreases with increasing latitude, so does the speed of the coastal wave, even though the numerical value should be constant. In this sense, the modelled internal Kelvin waves will actually slow down as they move northward as they should, while they will speed up to a maximum of $c = 2.17ms^{-1}$ as they move southward. Having now defined the internal Kelvin wave speed, the reduced gravity, as well as densities in each layer are fully specified

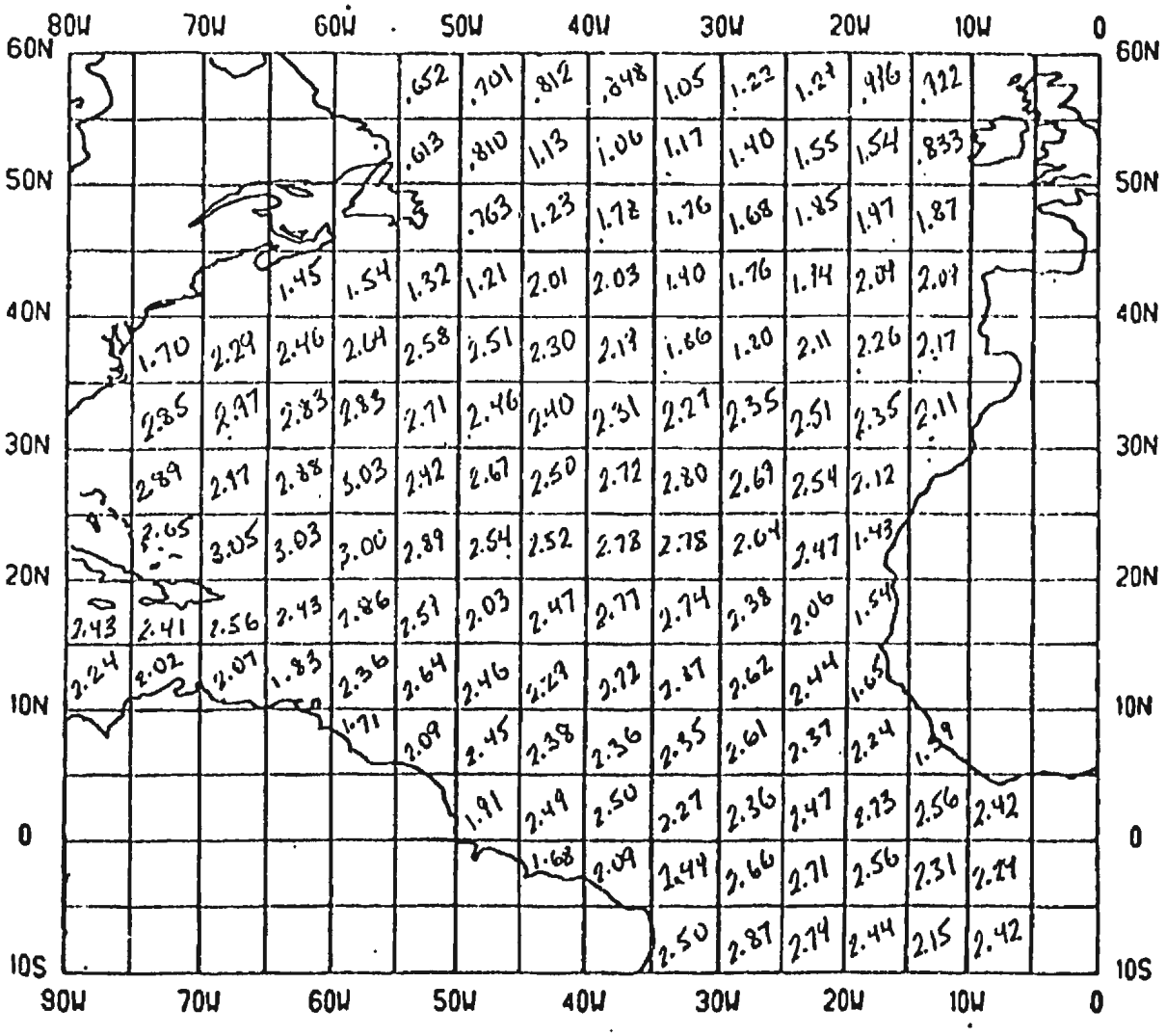

Figure 2.8: *Annual mean Kelvin wave speeds (ms^{-1}) for $5° \times 5°$ squares in the North Atlantic, based on the data of Emery et al. (1984).*

by the value of H_1 utilized in the model. Here, we follow AC and choose $H_1 = 100m$, yielding; $g' = 4.70890 \times 10^{-2} ms^{-2}$.

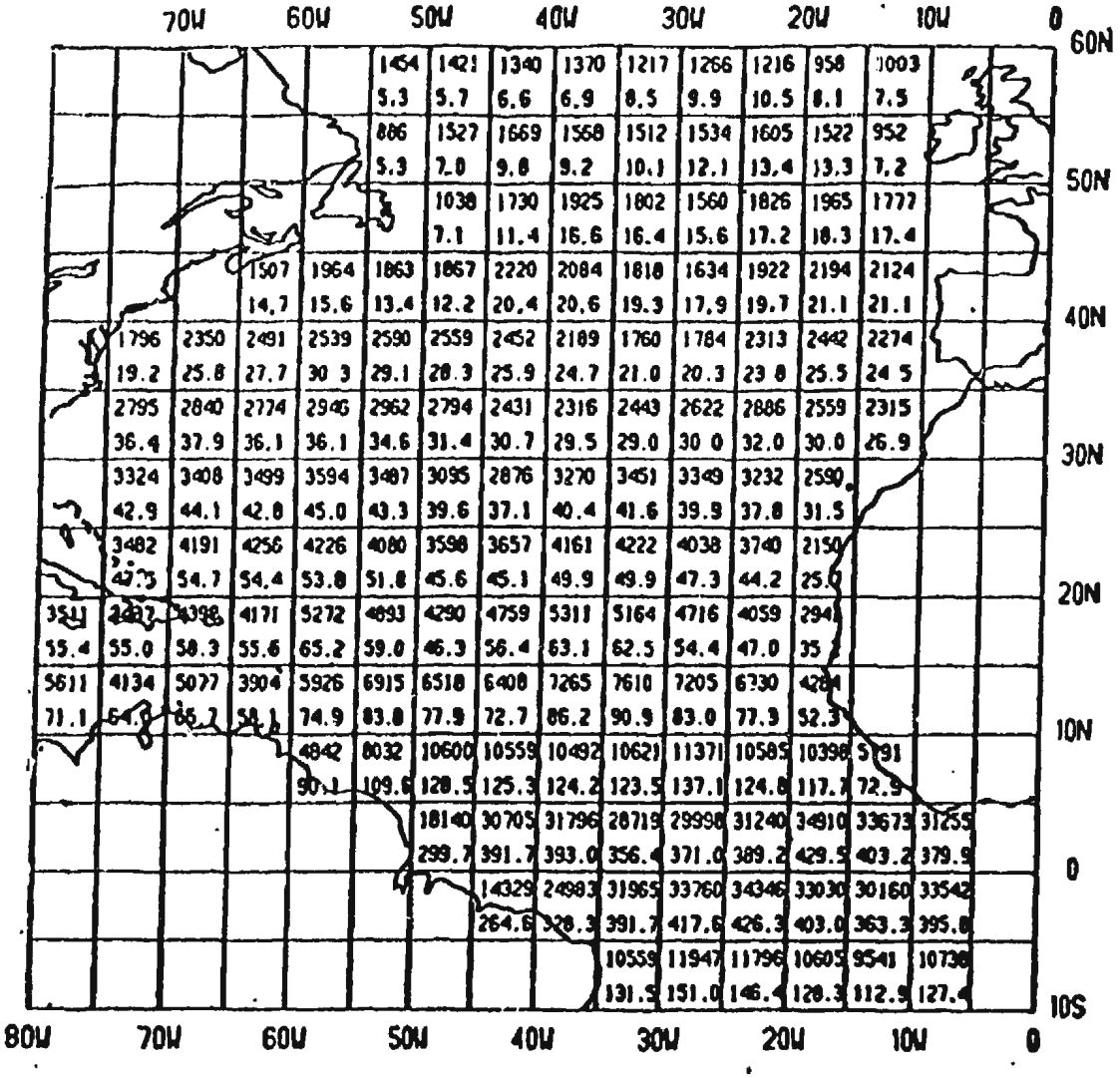

Figure 2.7: *Annual mean external (upper number) and internal (lower number) Rossby radii (in km) for 5° × 5° squares in the North Atlantic. (from Emery et al. (1984).*

Latitude Range	c (ms^{-1})	$\beta c^2/f^2$ (ms^{-1})
$5-10°S$	2.53	4.01×10^{-1}
$0-5°S$	2.35	3.12
$0-5°N$	2.41	3.28
$5-10°N$	2.20	3.03×10^{-1}
$10-15°N$	2.32	1.21×10^{-1}
$15-20°N$	2.41	6.60×10^{-2}
$20-25°N$	2.65	4.77×10^{-2}
$25-30°N$	2.73	3.34×10^{-2}
$30-35°N$	2.53	2.01×10^{-2}
$35-40°N$	2.22	1.14×10^{-2}
$40-45°N$	1.76	5.39×10^{-3}
$45-50°N$	1.61	3.48×10^{-3}
$50-55°N$	1.13	1.31×10^{-3}
$55-60°N$	0.94	7.24×10^{-4}

Table 2.1: *Summary of longitudinally averaged Kelvin and Baroclinic Rossby wave speeds for the North Atlantic.*

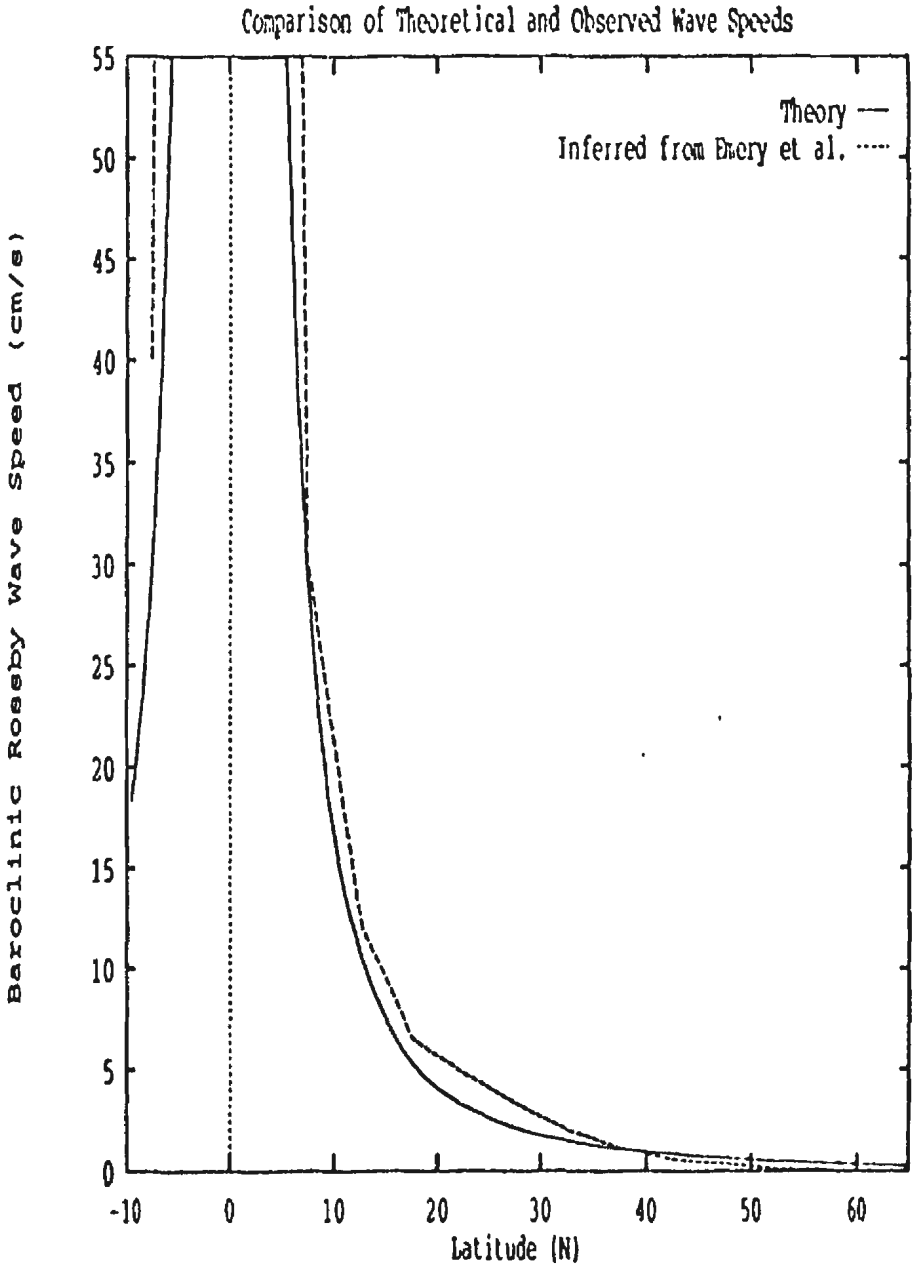

Figure 2.9: *Comparison of baroclinic Rossby wave speeds (cms $^{-1}$) for the North Atlantic (see text for details).*

CHAPTER 3: THE WIND STRESS CLIMATOLOGIES

The wind stress fields used to drive the model are those of da Silva, Young and Levitus(1993a; hereafter DS), Hellerman and Rosenstein(1983: hereafter HR), Isemer and Hasse (1987; hereafter IH), and Trenberth, Large and Olson (1990; hereafter TR). Estimates of the surface wind stress $\vec{\tau}$ are commonly based on the bulk aerodynamic formula

$$\vec{\tau} = \rho_a C_D \left(|\mathrm{U}|, \frac{Z}{L} \right) |\mathrm{U}|(u, v)$$

where the stress vector is assumed to be parallel to the surface wind (nominally at 10 m), (u, v) are the eastward and northward vector components of the surface wind; $|U|$ the wind speed; ρ_a the density of air at the surface; C_D is the drag coefficient dependent on wind speed and an atmospheric stability factor, (Z/L), with Z the height above the sea surface ($10\,m$), and L is the Monin-Obukhov length. L gives the height at which the magnitude of the buoyant kinetic energy produced in a non-neutral air column equals the purely mechanical kinetic energy in the equivalent neutral case. (Z/L) is a function of the air temperature, sea surface temperature, and relative humidity. Prior to the 1970's, the majority of wind speed estimates were based on ship observations of the sea state, and had to be converted to wind speed through the Beaufort equivalent scale. Systematic errors in this estimation are a primary source of error associated with individual estimates predating the wide-spread use of ship anemometers. Another source of error arises due to the choice of a value for the drag coefficient, C_D.

As has already been mentioned, the climatologies employed here differ in terms of the methodology used to produce them and the data sources employed in their production.

Here we give a brief overview of the analysis used in each. A more detailed description can be found in the original references.

(*i*) **DS:**

The DS wind stress fields are based on individual ship observations given in the COADS Compressed Marine Reports 5 (CMR-5), Product 10 (Slutz et al. 1985). About 70 million surface marine observations from the period 1945-89 are used to produce a global climatology and anomalies. The wind stress is computed for each individual ship observation using the Large and Pond (1981) formulation of the drag coefficient. Wind estimates based on sea state are converted to ms^{-1} using the Kaufeld(1981) scientific Beaufort scale. In addition, a stability dependent procedure is employed to convert wind speeds from the average ship anemometer height of 20 m to the standard 10 m reference level, required for the evaluation of the wind stress. The wind stress estimates have been averaged into 1° by 1° boxes, and objectively analyzed by the same procedure described in Levitus' Climatological Atlas of the World Oceans (1982). A detailed discussion of the effect of these corrections over the global oceans can be found in da Silva et al.(1993a,b).

We believe the DS wind stress climatology to be the most representative of the actual wind stress over the ocean of all the climatologies used here. This is because of the way the DS climatology has been constructed: taking account of the scientific Beaufort scale (Kaufeld, 1981) and a correction for ship anemometer height, before calculating the stress. Furthermore, unlike III, these corrections were made to the individual ship observations, in an effort to reduce bias in the calculated momentum fluxes.

(*ii*) **IIR :**

The IIR wind stress climatology employed over 35 million ship observations catalogued between 1870-1976. Wind estimates based on sea state were converted to ms^{-1} using the old WMO (1970) Beaufort equivalent scale which has been shown to introduce biases in climatological wind speeds (Isemer and Hasse 1991, da Silva et al. 1993b). IIR then employed a second-degree polynomial fit of Bunker's (1976) drag coefficients to create the wind stress on a $2° \times 2°$ grid over the entire globe. The wind stress fields were then interpolated and heavily smoothed to fill data deficient boxes. The resulting monthly mean wind stress fields were obtained on a $1° \times 1°$ grid from the Geophysical Fluid Dynamics Laboratory at Princeton University, New Jersey, USA.

(*iii*) **III :**

III returned to the Bunker(1976) data set, and in order to make them consistent with Kaufeld's(1981) Beaufort equivalent scale, corrected Bunker's monthly mean wind speeds using a two parameter Weibull distribution. Subsequent to the Beaufort correction, the monthly mean wind speeds were converted to a standard reference height of $10m$ using a constant 93% reduction factor typical of neutral conditions. The monthly mean wind speeds were then converted to monthly mean wind stresses through use of a "step function" drag coefficient formulation based on Bunker's (1976) drag coefficients which had been reduced by a constant factor of 21%. The drag coefficients reduced by this amount, are slightly larger than those of Large and Pond (1981) for wind speeds between 10-20 m s^{-1} and slightly smaller in other ranges (see Böning et al. 1991a, Fig.2). III also use additional information from Bunker's data set to account for the fact that they work with

mean values instead of individual observations. da Silva et al.(1993a,b) have shown that although HH's procedure gives accurate wind speed corrections (assuming an appropriate Weibull distribution is used), significant error can occur in the calculation of wind stress. In particular, the nonlinearity in the bulk aerodynamic formula for wind stress ultimately requires the consideration of individual observations and a detailed stability correction. Consequently, we believe HH overestimates the Beaufort scale correction for most of the North Atlantic. Since our grid domain extends from $10°S$ to $65°N$ we follow Böning et al.(1991a) and merge the HH wind stress field (defined from $0°N$ to $65°N$) into the HR wind stress field between $5°N$ and the equator, using a linear weighted average.

(*iv*) **TR :**

TR took a somewhat different approach and employed seven years of wind speeds computed from wind analyses provided by ECMWF (the European Centre for Medium Range Weather Forecasting) for the period 1980-86. The wind speeds were individually computed from twice daily $1000mb$ wind analyses, produced by ECMWF. TR then employed the Large and Pond (1981) drag coefficients utilizing the climatological monthly mean COADS air sea temperature and humidity differences to compute the stability correction. The twice daily wind stress fields were then averaged to compute monthly means. By using twice daily data, TR ameliorate the spatial/temporal sampling problem that plagues most data sets based on surface marine observations. However, because of the large interannual variability of surface winds in the North Atlantic, the question remains to what extent this seven year average is representative of the climatology. The TR climatological monthly mean wind stresses were obtained on a $2.5° \times 2.5°$ grid over the globe from the National Center for

Atmospheric Research (NCAR), Boulder, Colorado, U.S.A.. These data were then interpolated to a regular $1^\circ \times 1^\circ$ grid over the globe using the interpolation scheme of Akima (1978). Akima's scheme employs quintic polynomials to place the $2.5^\circ \times 2.5^\circ$ gridded data on a $1^\circ \times 1^\circ$ grid while preserving the global shape and properties of the field. In particular, this interpolation scheme ensures that the first derivative is continuous and consistent with the original data, thereby ensuring that the curl of the wind stress remains equivalent to the curl of the wind stress on the original grid.

Since our models are linear, we follow other authors (AC, GG) and drive them with seasonal anomalies of wind stress: that is, monthly means of wind stress with the annual mean removed. Linear interpolation between the middle of each month is used to provide the wind stress fields at a given time step.

CHAPTER 4: EVALUATION OF THE FLAT-BOTTOMED SVERDRUP RESPONSE

A measure of the representativeness of each wind stress climatology can be gained by calculating the flat-bottomed Sverdrup transport for each case. The conventional Sverdrup balance is a linear vorticity balance expressed as

$$\beta V = \hat{k} \cdot \nabla \times \vec{\tau} - f w(z_o) \tag{4.1}$$

where $\hat{k}$ is a unit vector in the vertical upwards direction, $\vec{\tau}$ is the surface wind stress, f is the Coriolis parameter, w is the vertical velocity at the reference depth z_o β is the latitudinal derivative of the Coriolis parameter, and V is the meridional vertically integrated transport above depth z_o, given as

$$V = \int_{-z_o}^{0} v dz$$

If we assume that z_o can be chosen so the motion becomes so weak below this depth that $w(z_o) = 0$,

$$\beta V = \hat{k} \cdot \nabla \times \vec{\tau} \tag{4.2}$$

This is the flat-bottomed Sverdrup balance, which holds for a flat-bottomed ocean, with z_o taken to be the total depth. Equation (4.2) is equivalent to assuming the wind stress is the only force acting on the ocean, and motion due to the wind stress is confined to the upper ocean. The work of Anderson and Killworth(1977) provides a mechanism for the ability of the flow to be isolated from the bottom topography, and hence allow the flat-bottomed Sverdrup balance to exist in an ocean with realistic bottom topography. Anderson and Killworth (1977) investigated the spin-up of a two-layered ocean under an applied steady

wind stress. Model results indicated that as more wind-generated baroclinic Rossby waves cross the basin, the flow becomes increasingly isolated from the bottom topography, until all flow is confined to the upper ocean. At midlatitudes this compensation effect takes decades, while at subpolar regions, it may never exist. This effect was subsequently confirmed in the three-dimensional studies performed by Anderson et al.(1979).

In the classical theories of the wind-driven ocean circulation (Stommel, 1948; Munk 1950) the transport associated with the flat-bottomed Sverdrup flow is balanced by an opposite flowing, frictional western boundary current. At the latitude of the Florida Straits, Leetmaa et al.(1977) showed that this transport, when computed from the climatological annual mean wind stress field of Bunker(1976), compares well with the annual mean transport through the Straits and is $\sim 30Sv$ (compare with 32 Sv, Larsen, 1992). Wunsch and Roemmich (1985), however, cast considerable doubt as to whether the flat-bottomed Sverdrup balance (as distinct from the linear vorticity balance of (4.1)) can ever hold in the ocean. Following Holland(1973), and taking z_o as the depth of the ocean, H, we can rewrite (4.1) as

$$\beta V = \frac{1}{\rho_0}\left[\hat{k}\cdot\nabla\times(p_b\nabla H) + \hat{k}\cdot\nabla\times(\vec{\tau})\right] \tag{4.3}$$

where we have used the kinematic boundary condition

$$w|_{z=-H} = \frac{1}{a\cos\phi}\left(u\frac{\partial H}{\partial\lambda} + v\cos\phi\frac{\partial H}{\partial\phi}\right)$$

and the geostrophic approximation to the momentum equations so that

$$J(p_b, H) = f\rho_o w|_{z=-H}$$

$\left[\hat{k} \cdot \nabla \times (p_b \nabla H)\right]$ is the bottom pressure torque, and p_b is the bottom pressure. It is apparent that if the bottom pressure torque is everywhere zero, then (4.3) again reduces to the flat-bottomed Sverdrup relation, (4.2). In Holland (1973), it was the interaction between the thermohaline circulation and the bottom topography that lead to the bottom pressure torques responsible for enhancing the gyre circulation above that of the flat-bottomed case. A further discussion of the validity of (4.2) can be found in Roemmich and Wunsch (1985) and Schmitz et al. (1992).

Here we consider the Sverdrup transport mainly to serve as a measure of the curl of the wind stress to the east of the Florida Straits and use it to indicate the differences in the curl associated with each climatological annual mean wind stress field. To compute the flat-bottomed Sverdrup transport we note that equ.(2.1.7), for a flat-bottomed ocean, reduces to the spherical equivalent of (4.2),

$$\left(\frac{\partial f}{\partial \phi}\right) \Psi_\lambda = \frac{a}{\rho_0} \left\{ \frac{\partial}{\partial \lambda}(\tau^\phi) - \frac{\partial}{\partial \phi}(cos\,\phi \tau^\lambda) \right\} \tag{4.4}$$

We therefore compute Ψ by integrating the wind stress curl from the eastern boundary, where $\Psi = 0$, along f/H contours (lines of latitude) to the western boundary, to obtain

$$\left(\frac{\partial f}{\partial \phi}\right) \Psi_W = -\frac{a}{\rho_0} \int_E^W \left\{ \frac{\partial}{\partial \lambda}(\tau^\phi) - \frac{\partial}{\partial \phi}(cos\,\phi \tau^\lambda) \right\} d\lambda \tag{4.5}$$

Ψ_W specifies the required transport across a given latitude due to the curl of the wind stress.

Figure 4.1 indicates the flat-bottomed Sverdrup transports obtained by integrating (4.4) with $\Psi = 0$ at the eastern boundary and using the curl of the climatological annual mean wind stresses of (a) DS, (b) HR, (c) HI, and (d) TR. Each exhibits a similar structure

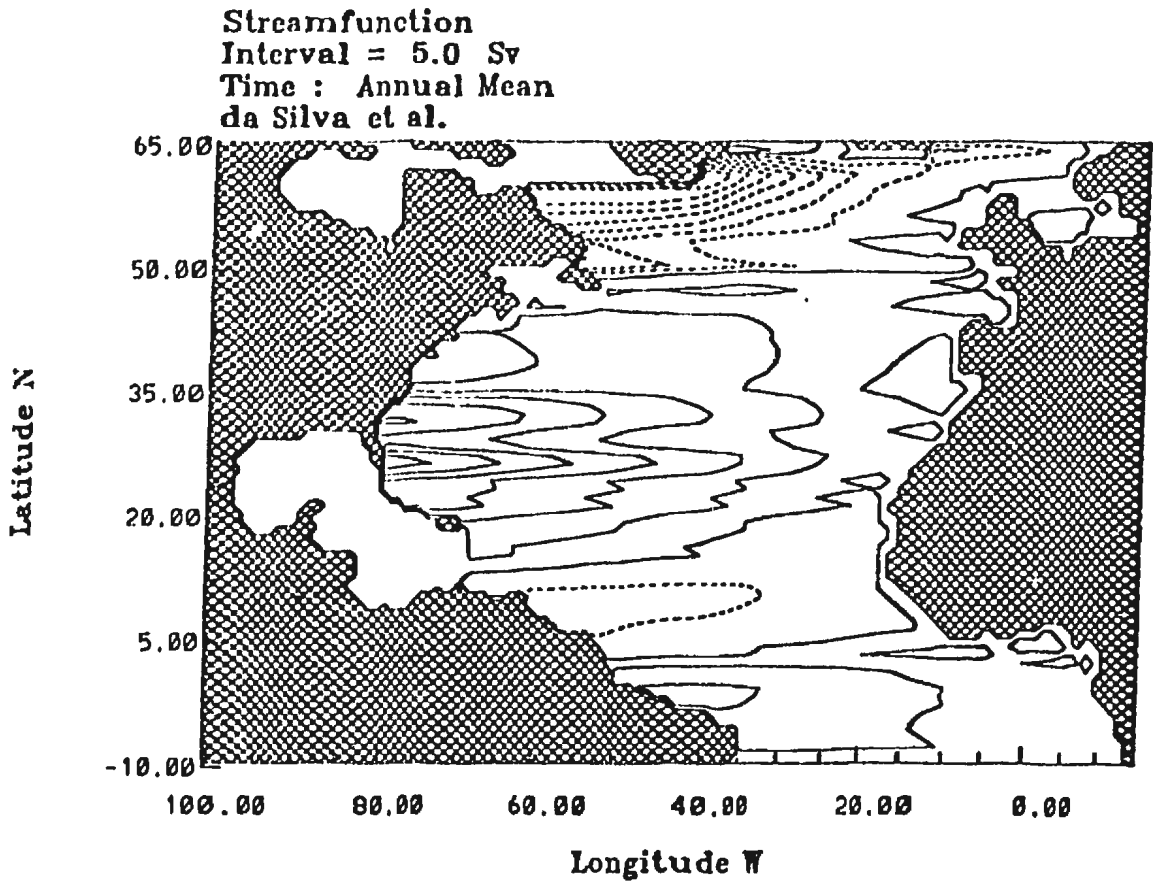

Figure 4.1: *The flat-bottomed Sverdrup transport calculated from the annual mean wind stress of (a) DS; (b) HR; (c) HI; and (d) TR. The contour interval is 5Sv, with dashed contours indicating negative values.*

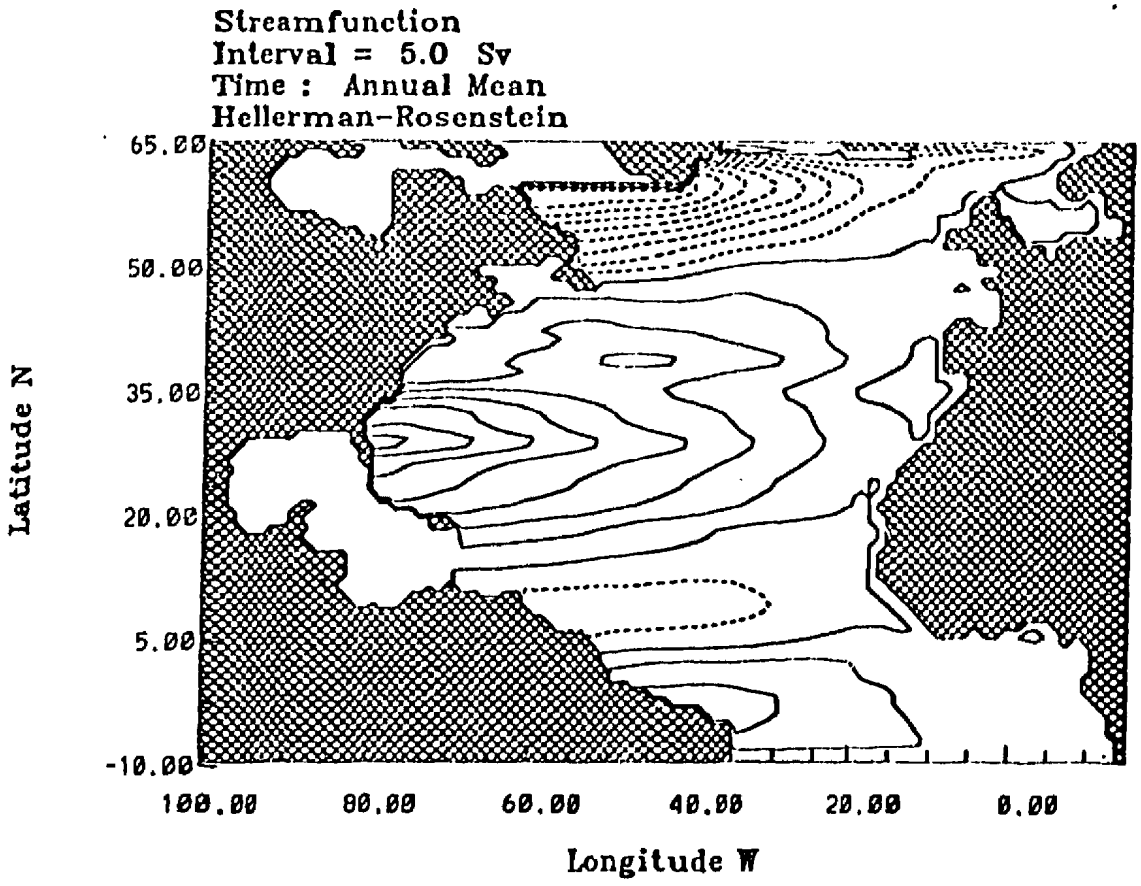

Figure 4.1: *continued*

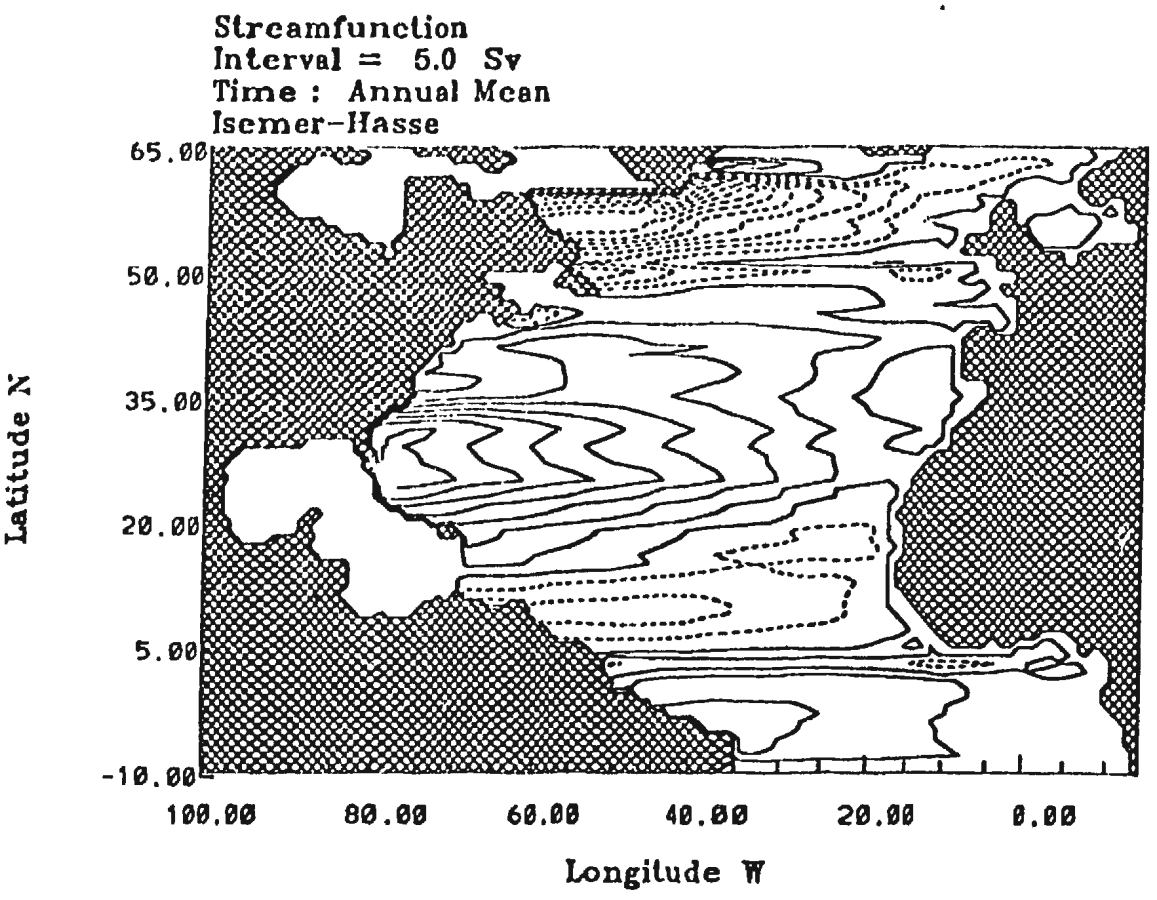

Figure 4.1: *continued*

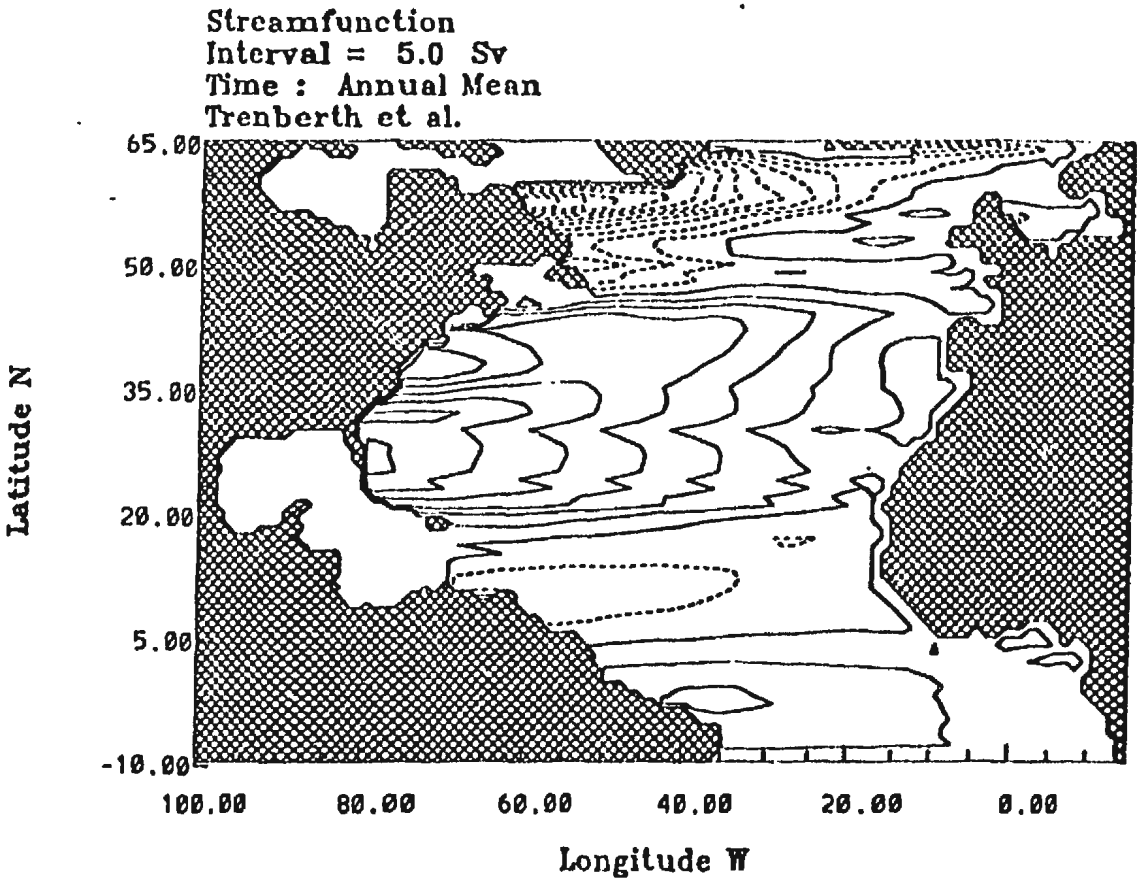

Figure 4.1: *continued*

to that of Leetmaa and Bunker (1978) (see their Fig.3) with a subtropical gyre separating from the coast near Cape Hatteras and a subpolar gyre in the northern part of the basin.

In the case of HR forcing (Fig. 4.1(b)), the subtropical gyre transport is $\sim 35Sv$ and the subpolar gyre $\sim 10Sv$. DS on the other hand (Fig.4.1(a)), exhibits a somewhat weaker subtropical and subpolar gyre of $\sim 30Sv$ and $\sim 35Sv$ respectively. TR (Fig.4.1(d)) wind forcing gives a subtropical gyre of $\sim 30Sv$ and a subpolar gyre of $\sim 55Sv$. The larger subpolar gyre transport in this case is also a feature of the HI case (Fig.4.1(c)) which exhibits somewhat intensified subtropical and subpolar gyres of $\sim 40Sv$ and $\sim 60Sv$ respectively. Note that DS, HI and TR each exhibit two maxima near Florida. The intervening dip has perhaps been lost due to the smoothing used by HR to produce their wind stress field.

Figure 4.2 compares the western boundary transports, Ψ_W defined by eqn.(4.5), in each case (these results are also summarized in Table 4.1 for each 5^0 latitude). We see that the Sverdrup transports agree reasonably well below 20^0N. However, north of 20^0N major departures occur. For example, at the latitude of the Florida Straits (25.5^0N), HR gives $24.9Sv$, DS $19.6Sv$, TR $27.0Sv$ and HI $32.9Sv$, (the CME mean transport at the Florida Straits shows similar behaviour with HR giving 24.3 Sv, and HI giving 29.1 Sv) indicating differences of more than $10Sv$. Differences of this magnitude are common further north. At $\sim 47^0N$ all climatologies begin their transition to the subpolar regime, with HI differing from DS and TR by some $10Sv$ and from HR by $\sim 15Sv$. The final major departure occurs at $\sim 55 - 60^0N$ where both HI and TR differ from HR and DS by $\sim 20Sv$.

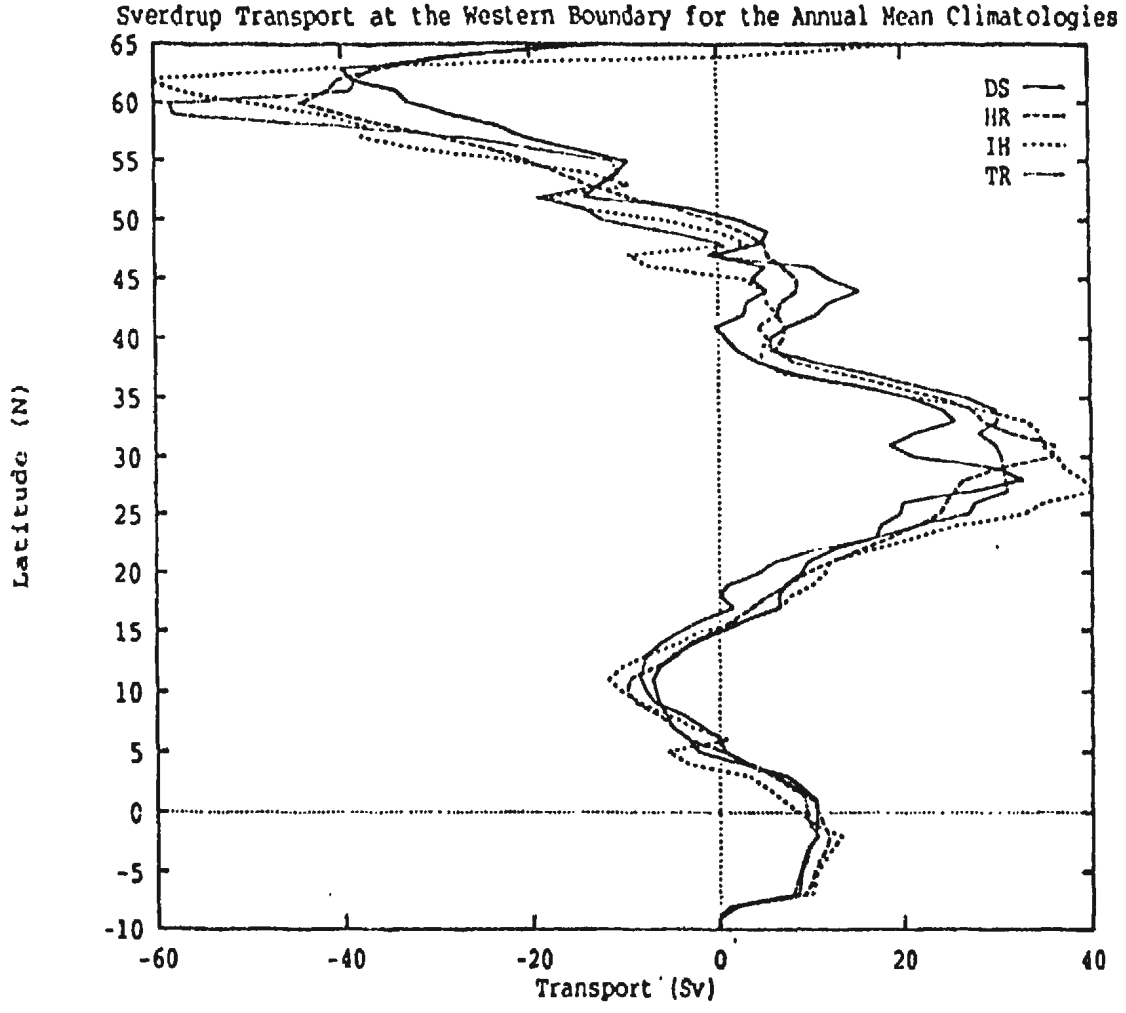

Figure 4.2: *Latitudinal profile of the flat-bottomed Sverdrup transport at the western boundary calculated from the annual mean wind stress fields of DS, HR, IH, and TR.*

Latitude	Wind Stress Climatology			
(^0N)	DS	HR	IH	TR
65.5	-11.9	-10.8	21.1	-14.0
60.5	-33.2	-44.3	-49.9	-58.8
55.5	-9.6	-20.1	-21.6	-11.3
50.5	2.2	0.0	-5.7	-12.3
45.5	3.7	8.4	2.7	12.1
40.5	0.7	6.9	5.2	5.5
35.5	20.8	24.0	21.7	26.9
30.5	30.2	35.9	36.4	30.6
25.5	19.6	23.9	32.9	27.0
20.5	8.8	9.4	11.5	4.2
15.5	0.3	-0.4	-1.7	-3.8
10.5	-6.8	-10.0	-10.6	-7.8
5.5	-2.1	0.5	-5.5	0.6
EQ.	10.4	10.2	10.1	9.5
-5.5	8.7	10.5	10.5	8.7
-9.5	1.0	1.8	1.8	1.1

Table 4.1: Ψ_W, *at* 5^0 *latitude intervals, calculated from the annual mean climatologies of DS, HR, IH and TR. Units are in Sv.*

The flat-bottomed Sverdrup relation is unlikely to hold at seasonal time scales. The time required for baroclinic Rossby waves, emanating from the eastern boundary, to completely compensate for the effect of variable bottom topography can be many decades at mid-latitudes (Anderson and Corry, 1985a).

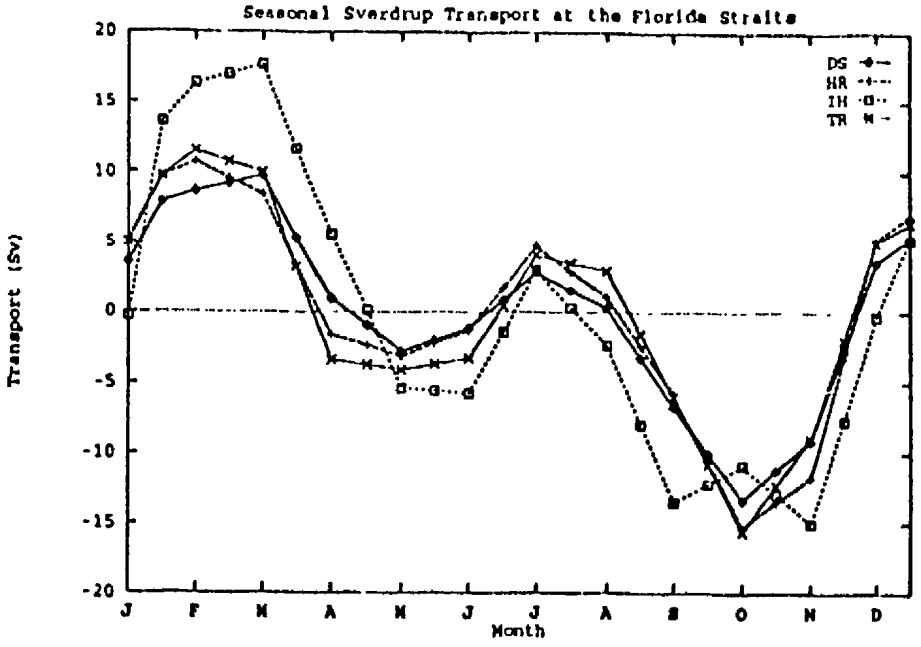

Figure 4.3: *Flat-bottomed Sverdrup transport at the Florida Straits calculated from the seasonal wind stresses of DS, HR, IH, TR.*

Niiler and Richardson (1973) noted that the seasonal transport variation observed at the Florida Straits is out of phase with that predicted by flat-bottomed Sverdrup theory. This is illustrated by comparing Fig.4.3 with Fig.1.4. Figure 4.3 depicts the flat-bottomed seasonal transport variation at the Florida Straits (that is with the annual mean removed) for each of the climatologies, and indicates, in each case, a seasonal transport variation of much greater magnitude and with a different phase from that observed. For each climatology, the

maximum transport now occurs in February-March while the minimum occurs in October-November. Note the DS, HR and TR transports are quite similar (to within $5Sv$). The HI case differs most from these in the early part of the year, but also exhibits two minima in the fall (in September and November) rather than the single minimum in October seen in the other cases. There are also some differences to be found in the annual range (maximum minus minimum), HR and TR giving $25Sv$, DS $21Sv$, while HI gives $31Sv$. The large differences between Fig.1.3 and Fig.1.4 indicate the importance of including realistic bottom topography at seasonal time scales.

CHAPTER 5: THE NORTH ATLANTIC RESPONSE

In this section we describe the large-scale North Atlantic results obtained from the barotropic model (see eqn.2.1.5), as well as that part forced by the baroclinic terms in the two-density layer model (see eqn.2.2.19), obtained utilizing realistic topography and the seasonal anomalies of wind stress. Each model begins from a state of rest. Appendix A shows the model-calculated transport streamfunction fields produced by the barotropic model from the second year of integration, at a time corresponding to the middle of each month. Appendix B shows the baroclinically forced part of the transport streamfunction fields produced by the two-density layer model from the third year of integration, at a time corresponding to the middle of each month. In the following description, it should be noted that "cyclonic" corresponds to counter-clockwise rotation and "anticyclonic" to clockwise rotation, with cyclonic(anticyclonic) circulation about negative(positive) anomalies of streamfunction. (The opposite is true in the Southern hemisphere.)

Figure 5.1 is thought to represent the long time mean annual circulation of the North Atlantic as inferred originally by Mellor et al.(1982) from historical hydrographic data. In the present text, we include this figure to allow an interpretation of the seasonal changes which occur in the large scale features of the North Atlantic. Figure 5.1 was produced by the diagnostic calculations of Greatbatch et al.(1991) using Mellor et al.'s model and the mean HR wind stress fields, with Levitus'(1982) mean density data as inputs. In particular, th diagnosed Gulf Stream separates from the American coast at Cape Hatteras and reaches a maximum transport to the south of the Grand Banks of Newfoundland of ~ 80 *Sv*. As an example, this compares, with the 93 *Sv* estimate of Gulf Stream transport near 55^0W given

by Richardson (1985)(this was obtained using long-term current measurements made with surface drifters, SOFAR floats and current meters). The model also diagnoses a subpolar gyre with a maximum westward transport to the south of Greenland of over 40 *Sv*, comparing favourably with the estimate of 33.5 *Sv* given by Clarke (1984).

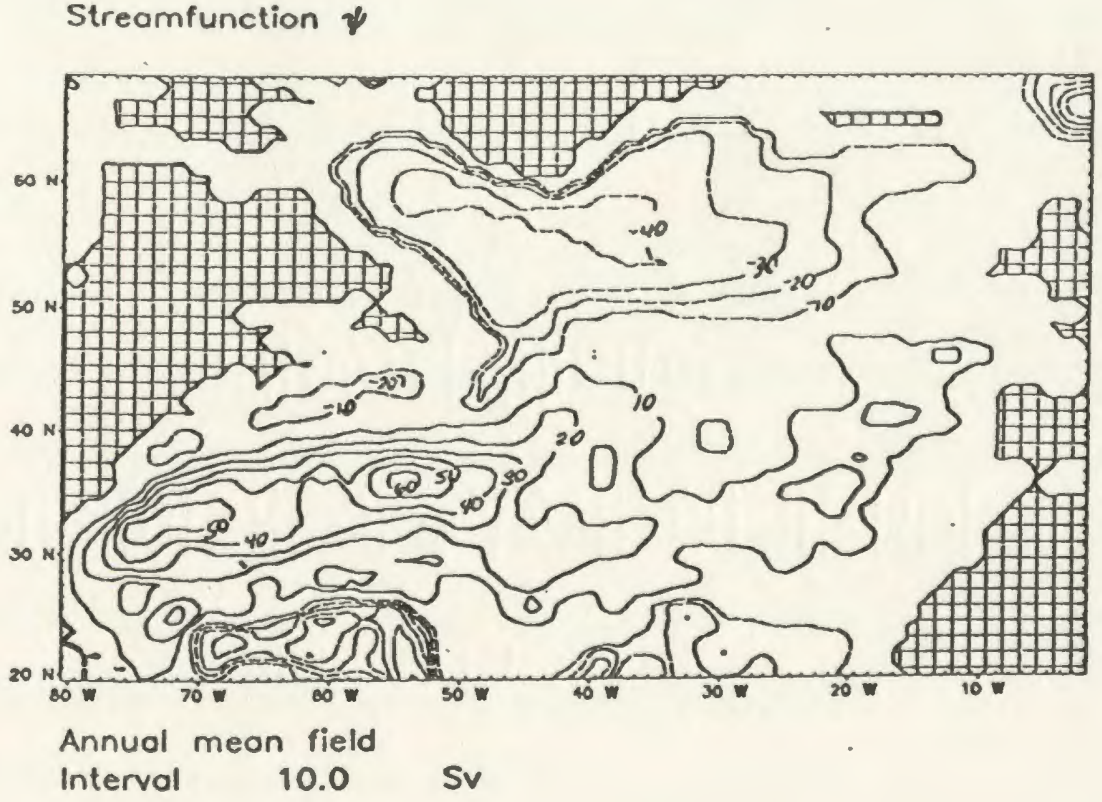

Figure 5.1: *Transport streamfunction calculated using climatological annual mean wind and density data. The contour interval is* $10Sv$. *Dashed contours indicate negative values, solid contours positive values. The zero contour is not drawn. (From Greatbatch et al., 1991)*

5.1 : The Large Scale Barotropic Ocean Response

Appendix A indicates the large scale ocean response produced by integrating eqn.2.1.5,

that is;

$$\frac{\partial}{\partial\lambda}\left\{\left(\frac{\partial}{\partial t}+\frac{r}{H}\right)\frac{\Psi_\lambda}{H\cos\phi}\right\}+\frac{\partial}{\partial\phi}\left\{\left(\frac{\partial}{\partial t}+\frac{r}{H}\right)\frac{\Psi_\phi\cos\phi}{H}\right\}+J\left(\Psi,\frac{f}{H}\right)$$

$$=\frac{a}{\rho_0}\left\{\tau^\lambda\cos\phi\frac{H_\phi}{H^2}-\tau^\phi\frac{H_\lambda}{H^2}\right\}+\frac{a}{\rho_0 H}\left\{\frac{\partial}{\partial\lambda}\left(\tau^\phi\right)-\frac{\partial}{\partial\phi}\left(\tau^\lambda\cos\phi\right)\right\}$$

$$+aA_H\left\{\frac{\partial}{\partial\lambda}\mathcal{L}^\phi-\frac{\partial}{\partial\phi}(\cos\phi\mathcal{L}^\lambda)\right\}$$

driven by each of the wind stress climatologies of da Silva, Young and Levitus(1993a; DS), Hellerman and Rosenstein(1983; HR), Isemer and Hasse (1987; IH), and Trenberth, Large and Olson (1990; TR). In the following analysis, we will concentrate on the subpolar gyre defined by the cyclonic gyre extending roughly 45^oN to 65^oN, (see Fig.5.1) and the subtropical gyre defined by the anticyclonic gyre extending roughly 15^oN to 45^oN (see Fig.5.1) independently. Recall that the wind stress fields used to drive the model are seasonal anomalies, or departures from the long time mean. It follows that the results presented here are transport anomalies, or departures from the long time mean.

(i) The DS barotropic response

The barotropic model, when driven under the seasonal wind stress anomalies of DS exhibits a cyclonic circulation in the subpolar regime of roughly 2 *Sv* in January, which expands without intensifying into February. By March, the cyclonic anomaly has shifted somewhat southward and weakens, before collapsing in April. Note the appearance of a weak 'tongue' of cyclonic transport extending beyond the Flemish Cap in January; by February this tongue has expanded along the shelf/slope region on the eastern seaboard of the United States. It intensifies slightly in March, before weakening in April and collapsing

in May. In June, a weak anticyclonic anomaly begins to form in the Labrador Sea, which becomes enhanced slightly and extends along the shelf/slope in July and August, before collapsing in September, and reforming only slightly in October and December.

In the subtropical regime, the DS case exhibits a rather intense anticyclonic anomaly ranging from 7 *Sv* in January, to its maximum value of 8 *Sv* in February, and weakening to 6 *Sv* in March. In April this anticyclonic anomaly weakens considerably, before completely collapsing in May. By June, a weak cyclonic anomaly begins to form, this intensifies through July and August, reaching a maximum of 8 *Sv* in September-October. In November the cyclonic feature weakens slightly to roughly 5 *Sv* before reversing completely to an anticyclonic transport anomaly in December.

(ii) The HR barotropic response

Not surprisingly, these results and those of GG, and AC compare favourably for those regions where the model domains overlap. Here, however, the transport values are slightly lower in some months, possibly due to the inclusion of the extra frictional effects in this model arising from the lateral mixing of momentum, as well as the different smoothing techniques employed in the treatment of topography as compared to GG.

The HR driven model results indicate a somewhat enhanced cyclonic anomaly in the subpolar gyre of roughly 3 *Sv* in January. This cyclonic anomaly intensifies to over 5 *Sv* in February, then weakens slightly and shifts southward in March, before collapsing in April-May. Note a tongue of cyclonic anomaly also extends along the shelf/slope margin in February and March carrying roughly 2-3 *Sv* along the east coast, which also collapses

in April-May. In June, a weak anticyclonic anomaly begins to form in the subpolar gyre region, this intensifies in July to roughly 3 *Sv* and extends along the shelf/slope region as a tongue of anticyclonic transport. The anticyclonic feature then weakens in August September, before collapsing in October-November, while in December this intensifies to over 4 *Sv* in the subpolar gyre and across the Mid Atlantic Ridge (MAR).

In the subtropical regime, an anticyclonic circulation of 9 to 11 *Sv* exists from January through to March. This feature weakens in April to 3 *Sv* and collapses, being replaced by a cyclonic anomaly which begins to form in May. In June-July-August, this cyclonic anomaly intensifies to over 5 *Sv* before reaching its maximum of 10 *Sv* in September October. By November, this feature weakens slightly before undergoing a complete reversal in December, being replaced by an anticyclonic anomaly.

(iii) The III barotropic response

The III driven model results indicate a rather intense anomalous cyclonic circulation in the subpolar gyre of over 5 *Sv* in January, with a tongue of cyclonic transport anomaly extending along the shelf/slope with a maximum off Cape Hatteras ($35°N$) of 4 *Sv*. These features intensify considerably in February to over 8 *Sv*, while in March, the subpolar cyclonic anomaly shifts southward and weakens to 5 *Sv*, before collapsing in April May when it is replaced by the formation of a weak anticyclonic anomaly. This anticyclonic anomaly begins intensifying in June-July to over 2 *Sv* in the Labrador/Irminger Sea, and 5 *Sv* east of Cape Hatteras, in the shelf/slope region. In August-September the anticyclonic feature in the subpolar gyre weakens slightly before undergoing a complete reversal in

October to a cyclonic anomaly of roughly 5 *Sv*, which in turn collapses in November. In December, a rather intense anticyclonic anomaly forms with over 6 *Sv* contained in the subpolar gyre and over the MAR.

In the subtropical regime, an anticyclonic transport anomaly ranging from 7 to 12 *Sv* exists from January to March. In May, this feature reverses to a cyclonic anomaly of roughly 2 *Sv* which exists in this state through to July when it begins to intensify. The intensification proceeds until a maximum cyclonic anomaly exists in the subtropical regime of roughly 10 *Sv* from September through to November, at which time a complete reversal occurs to an anticyclonic anomaly of 4 *Sv* in December.

(iv) The TR barotropic response

The model-results, when driven under the seasonal wind stress anomalies of TR exhibits a cyclonic circulation in the Labrador Sea region of roughly 3 *Sv* in January. The overall picture of the North Atlantic in January resembles the December circulation anomaly of the other cases. The cyclonic anomaly intensifies to over 7 *Sv* in February, with a tongue of streamfunction anomaly in the shelf/slope region of roughly 3 *Sv*. The cyclonic anomaly reverses to an anticyclonic anomaly in March of roughly 3 *Sv*, with the cyclonic anomaly off Cape Hatteras indicating roughly 3 *Sv*. These features continue into April before collapsing completely in May. In June-July-August, an anticyclonic anomaly is formed and begins to intensify to 4 *Sv* before undergoing a complete reversal in September to a cyclonic anomaly which intensifies into November to roughly 7 *Sv* before weakening to 4 *Sv* in December.

In the subtropical gyre, an anticyclonic anomaly of roughly 5 Sv appears in January, before intensifying to 10 Sv in February and March. This weakens considerably to 2 Sv in April, May, and June, while a 5 Sv cyclonic anomaly covers much of the latitude band 30°N to 50°N. In July, a cyclonic anomaly of 3 Sv forms and begins to intensify in August before reaching a maximum of 9-10 Sv in September-October, this reduces slightly in November to roughly 6 Sv, before undergoing a complete reversal into December when an intense (9 Sv) anticyclonic anomaly forms over the western subtropical gyre region.

In general, the above results, together with Fig.5.1 indicate an enhanced subpolar gyre in the fall (September, October, November) and late winter (January, February, and March), with a somewhat reduced transport in the spring (April, May) and greater reduction in summer (June, July, August). The subtropical gyre indicates an enhanced transport in winter (January, February, March) with a reduced transport beginning in summer (June-July) and reaching a minimum in fall (September-November). These results, however, like those of GG and AC are unable to explain the observed annual cycle of transport in the Gulf Stream off Cape Hatteras (Halkin and Rossby, 1985) which seems to be baroclinic in nature. In a related study, Fanning(1991) was unable to ascertain whether these effects were due to the seasonal changes in the density stratification of the North Atlantic. In that study, Fanning attempted to diagnose the seasonal JEBAR-driven transport variation in the North Atlantic using the climatological monthly mean Levitus (1982) density data. However, due to the appearance of "bull's eyes" in the potential energy field with length scales approximately that of Levitus' smoothing function, this was unsuccessful.

second year of integration, here we consider model output from the third year of integration. High energy baroclinic Kelvin and first-mode Rossby waves have a tremendous effect on the transport in the equatorial regime. This tends to mask the response at midlatitudes, so we exclude that region in the present analysis. It is important to note that the transport depicted in Appendix B is exceptionally weak (compare 0.3 *Sv* contour interval with that of Appendix A's 1 *Sv* contour interval), and have little effect on the North Atlantic's transport as compared to the barotropic model's response. Here we will discuss the baroclinically forced transport in very general terms since the particular details are relatively unimportant. We point out only the similarities and differences, the reader is referred to the figures in Appendix B for more details. Recall that the wind stress fields used to drive the model are seasonal anomalies, or departures from the long time mean, it follows that the results presented here are transport anomalies, or departures from the long time mean.

The subpolar regime in January contains a cyclonic anomaly in all cases except for DS which indicates a collapsed state at this time of year. By February a cyclonic anomaly begins forming in the DS case, while the HR and TR cyclonic anomalies intensify slightly, and the IH case collapses. In March the IH case's cyclonic anomaly has reformed, while the DS, HR and TR cases' cyclonic anomalies are expanding. Expansion continues through April in the DS, HR and IH cases, while the TR cyclonic anomaly begins to collapse. By May, the DS and TR cases indicate collapsed anomalous subpolar gyres, while the HR cyclonic anomaly begins to collapse and an anticyclonic anomaly begins forming. In June, all cases exhibit a collapsed anomalous subpolar gyre, except for IH which exhibits a cyclonic anomaly in the Labrador Sea, and an anticyclonic feature forming below Greenland. The DS and TR

In comparison, Fig.A.5 shows the seasonal anomalies produced by the WOCE-CME (the World Ocean Circulation Experiment, Community Modelling Effort; Bryan and Holland, 1989) when HR wind forcing is employed. As has been previously mentioned, this is an eddy resolving model of the North Atlantic driven by seasonally varying surface forcing. The model results shown here, were obtained from Frank Bryan (personal communication) and are averaged over the last 5 years of model integration. The general features noted when analysing the HR response, also apply to the CME results. Note, however, that even averaging over the last five years of model integration has not removed the strong eddy activity in the CME. Nevertheless, the general agreement between our model and the CME in the HR case does suggest that linear dynamics plays a role in determining the seasonal response of the CME.

5.2 : The Large Scale Baroclinic Ocean Response

Appendix B indicates the large scale ocean response produced by integrating (2.2.15) and removing the response associated with (2.1.5) to obtain the baroclinically forced transport field for the North Atlantic, that is, the transport defined by;

$$\frac{\partial}{\partial\lambda}\left\{\left(\frac{\partial}{\partial t}+\frac{r}{H}\right)\frac{\Psi_{J\lambda}}{H\cos\phi}\right\}+\frac{\partial}{\partial\phi}\left\{\left(\frac{\partial}{\partial t}+\frac{r}{H}\right)\frac{\Psi_{J\phi}\cos\phi}{H}\right\}+J\left(\Psi_J,\frac{f}{H}\right)$$

$$=g'H_1J\left(\eta_2,\frac{1}{H}\right)-arH_1\left\{\frac{\partial}{\partial\lambda}\left(\frac{\hat{v}}{H^2}\right)-\frac{\partial}{\partial\phi}\left(\frac{\hat{u}\cos\phi}{H^2}\right)\right\}+MIXING \qquad (2.2.19)$$

Following the previous analysis, we concentrate on the subpolar gyre extending from roughly $45°N$ to $65°N$, and subtropical gyre extending from roughly $15°N$ to $45°N$ independently, (see Fig.5.1). Since the two layer model's response does not change significantly beyond the

cases each exhibit an anticyclonic feature forming in the subpolar region in July, while the III and IIR cases contain both cyclonic and anticyclonic features in the subpolar gyre at this time of year. The anticyclonic anomalies in each case expand and intensify through to October when they begin to weaken. By November the anticyclonic features begin to collapse, and are fully collapsed in the DS, IIR for December, while the III case exhibits a cyclonic anomaly beginning to form in the Labrador Sea, and TR exhibits an anticyclonic anomaly at this time of year.

The subtropical gyre indicates a relatively enhanced anticyclonic anomaly in January in all cases (as compared to the subpolar gyre), these features begin to collapse in February when cyclonic anomalies begin to form. By April-May the cyclonic anomalies begin intensification, and by July-August, the cyclonic anomalies are collapsed and anticyclonic anoamlies begin spreading over the subtropical gyre in the IIR and III cases. These anticyclonic anomalies begin to weaken in the DS, IIR and III cases in September, while actually expanding in the TR case. The TR case exhibits an anticyclonic feature throughout the rest of the year, weakening only slightly in October and November. The DS, IIR and III anticyclonic anomalies continue weakening into October with cyclonic anomalies beginning to form in the DS and III cases. By November-December, each of DS, IIR and III exhibit cyclonic anomalies, with the DS anomaly almost fully collapsed.

These results are somewhat disappointing. As compared to the barotropic response, we see that inclusion of the first baroclinic mode alone, has very little effect on seasonal time scales, confirming the earlier studies of Veronis and Stommel(1956), Gill and Niiler(1973), Anderson et al.(1979), and Anderson and Corry (1985a,b). In Chapter 6 we examine the

models response at the Florida Straits. The discussion, and experiments in Chapter 6 concentrate on the barotropic model's response to the various wind stress climatoiogies owing to the much larger response in the barotropic transport field. However for completeness we do include the response associated with the baroclinically forced transport at the Florida Straits.

CHAPTER 6: MODEL RESPONSE AT THE FLORIDA STRAITS

At 1^0 x 1^0 resolution, the bottom topography as supplied by GFDL does not explicitly contain the Bahama Islands (see Fig.2.4), and unlike AC, we have not artificially constructed them here. In order to compare with observations and results from other models, we follow GG and consider the transport between the coast and a location at $25.5^0N, 78.5^0W$ (two grid points offshore of Miami) to correspond to that of the Florida Straits. This is equivalent to the region chosen by AC (see Rosenfeld et al., 1989, Fig.5). The depth of water at this

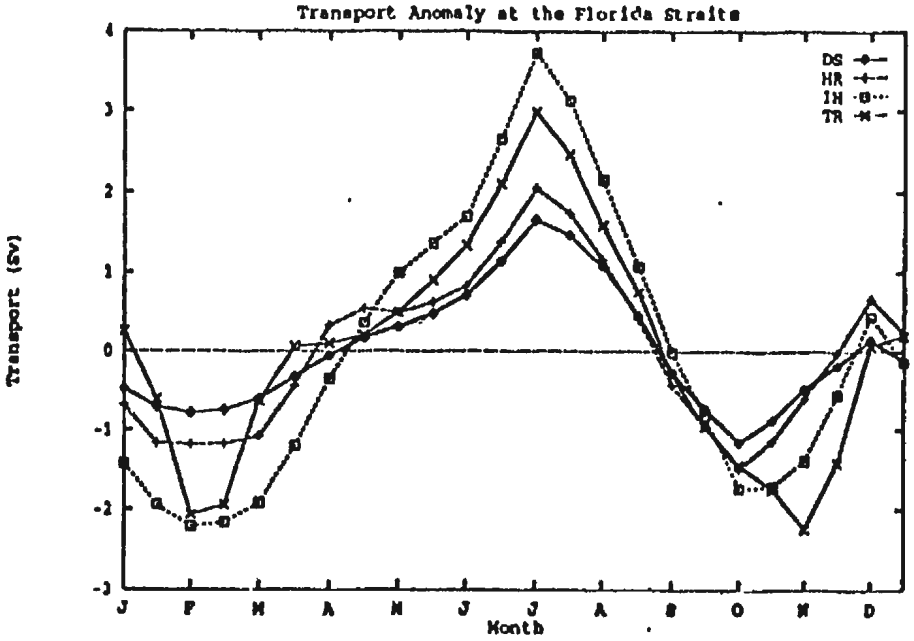

Figure 6.1: *The model-calculated seasonal cycle of transport (Sv) through the Florida Straits when realistic topography is considered.*

grid point is 939.5 m in our smoothed topography, a depth similar to that in the deepest part of the Straits. In order to test the sensitivity of our results to this choice, we shall also

show results obtained by choosing instead each of the three grid points further offshore (see Fig.6.3).

Month	Larsen	DS	HR	IH	TR
Jan.	-1.03	-0.49	-0.69	-1.44	0.25
Feb.	0.07	-0.78	-1.19	-2.22	-2.06
Mar.	-0.93	-0.61	-1.08	-1.92	-0.64
Apr.	-0.23	-0.05	0.33	-0.35	0.10
May	-0.23	0.31	0.49	0.99	0.49
Jun.	0.67	0.70	0.82	1.69	1.34
Jul.	2.27	1.65	2.05	3.72	2.98
Aug.	2.37	1.08	1.17	2.16	1.59
Sep.	1.37	-0.27	-0.43	-0.01	-0.29
Oct.	-0.93	-1.16	-1.50	-1.74	-1.45
Nov.	-2.33	-0.49	-0.60	-1.40	-2.25
Dec.	-1.03	0.14	0.66	0.44	0.08

Table 6.1: *Summary of observed (cable-derived) and model-calculated seasonal transport variations through the Florida Straits. Units are in Sv.*

Figure 6.1 shows the barotropic model-calculated seasonal transport anomaly through the Straits obtained from each of the different wind stress climatologies (see also Table 6.1). In each case, the seasonal variation in transport is quite similar to that observed (cf. Fig.1.4), with the maximum transport in July-August and a minimum in October-November (although the absolute minimum occurs in February in the IH case). The amplitude of the model-calculated response is quite different in each case, with ranges of $5.9Sv$, $5.2Sv$, $3.6Sv$ and $2.8Sv$ for each of IH, TR, HR and DS, respectively. In comparison to Fig.1.4, we see that the amplitudes predicted by HR and DS are too small, while IH and TR are too large. The range in the HR case is in excellent agreement with the results of AC, GG and the

WOCE-CME with HR wind forcing (Bryan and Holland, 1989; Böning et al., 1991b) and the IH case also agrees in range with the WOCE-CME under IH forcing (Böning et al., 1991b). These CME results are obtained from 5 year averages of

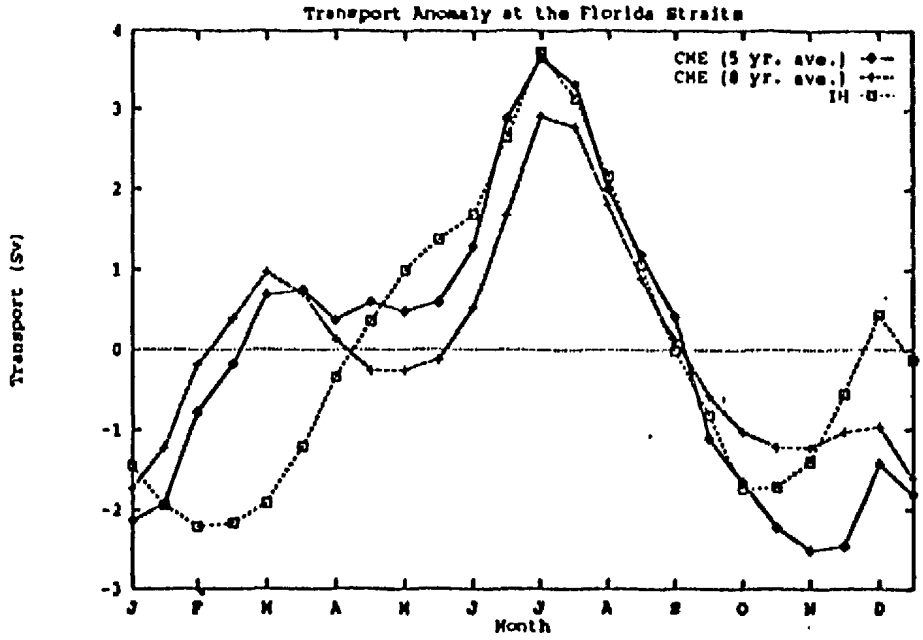

Figure 6.2: *Comparison of the model-calculated seasonal cycle of transport (Sv) with that of Böning et al. 1991b, when IH wind forcing is used.*

CME output. Figure 6.2 compares our IH case with the CME under IH forcing for both 5 year (Böning et al., 1991b) and 8 year averages (Böning, personal communication) of CME output. This shows that our linear model agrees quite well with the 5 year average (indeed, from June to October, the two model results are virtually identical) but that agreement is less good when incorporating a further 3 years of CME output. In the CME experiments, IH wind forcing was applied only for the 8 years over which these averages were taken (in the case of the 5 year average, this was over the first 5 years). It is possible, therefore,

that the baroclinic structure of the CME evolves over the 8 year period and that even the 8 year case may not be in statistical equilibrium. Of course, this also indicates a role for additional dynamics present in the CME but not in our barotropic model. For example, the baroclinic structure in the WOCE-CME can lead to transport being driven through the JEBAR term. This effect was noted by AC in their model (see Fig. 1.4(d)) and had the effect of enhancing northward transport in their model in the first 8 months of the year and reducing transport

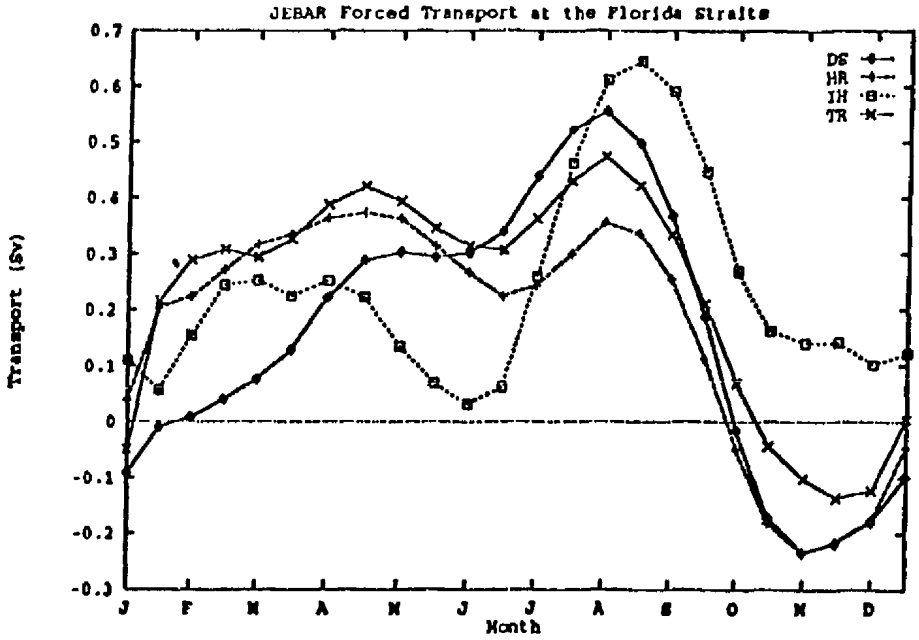

Figure 6.3: *The model-calculated seasonal cycle of transport (Sv) through the Florida Straits considering baroclinic effects over realistic topography (JEBAR) only. (see text for details).*

thereafter. This is broadly consistent with the difference between our barotropic model result and the 5 year average CME case in Fig.6.2; and indeed, when we consider the

JEBAR forced component of transport in our two-density layer model (see Fig.6.3) our results tend to agree with those of AC.

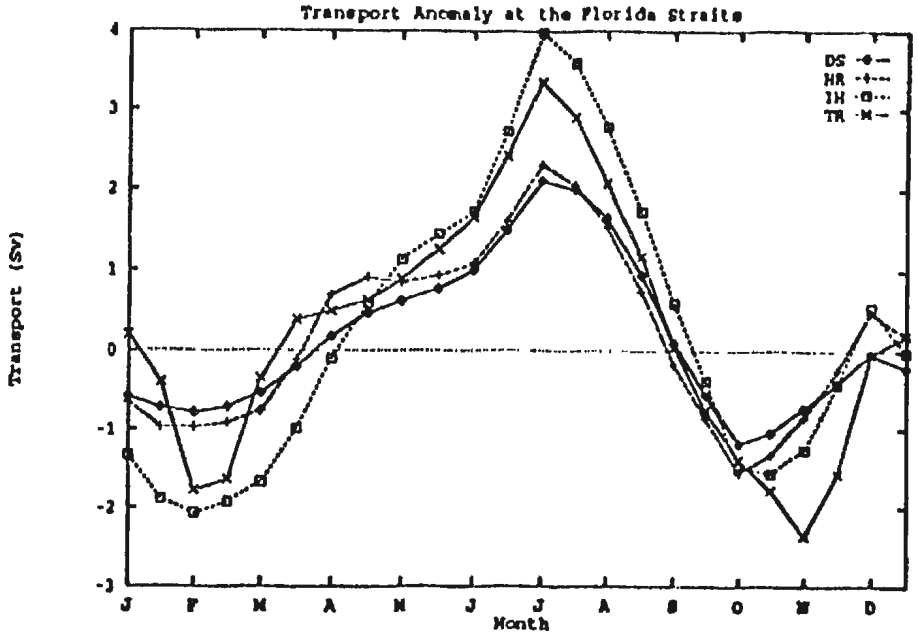

Figure 6.4: *The model-calculated seasonal cycle of transport (Sv) through the Florida Straits produced by the two-density layer model.*

Figure 6.3 indicates the transport at the Florida Straits obtained by removing the strictly barotropic part of the transport from the two-density layer model's transport field (see (2.2.19). In general, we see that the baroclinic structure of the two layer model leads to more northward transport in the summer (July-August), and reduced transport in the fall (October-November) compared to the barotropic case. The exception is the IH climatology for which there is more northward transport throughout the year. In particular, in the DS case there is an additional 0.56 *Sv* northward transport in July, with a reduction of 0.23 *Sv* in November. Similarily, in the HR case there is an additional 0.37 *Sv* in April and a

reduction of 0.24 Sv in October. On the other hand, in the HI case there is 0.64 Sv more northward transport in September, without any reduction in transport at any time in the course of the year. Finally the TR baroclinically forced transport indicates an increased transport of 0.47 Sv in August, with a reduced transport of 0.13 Sv in November compared to the barotropic model. When the baroclinically forced transport is taken into account, the amplitude of the model-calculated response changes slightly in each case (see Fig.6.4), with ranges of $6.1Sv$, $5.8Sv$, $3.9Sv$ and $3.3Sv$ for each of HI, TR, HR and DS, respectively. Note the range in the DS case is now in closer agreement with the results of AC, GG and the CME under HR forcing.

The general agreement between our model and the CME in the HR and HI cases (especially the 5 year average), and the ability of our model to capture the increase in range found when the CME is run with HI forcing, does suggest that linear dynamics plays an important role in determining the seasonal response of the CME at the Straits. As we shall see later, this conclusion is not supported by other experiments carried out using our model and the CME. The response associated with the JEBAR forcing in the two-density layer model does not appreciably alter our earlier results obtained from the barotropic model. Hence we now concentrate our analysis on the single layer, barotropic model.

Figure 6.5 shows the model-calculated seasonal transport between the coast and each of the three grid points further offshore from that used to produce Figure 6.1 (i.e. 25.5^0N : 77.5^0W, 76.5^0W and 75.5^0W). Considerable differences are again found between each case. At 25.5^0N, 77.5^0W, the results are quite similar to those in Fig.6.1. This shows that the differences in Figure 6.1 are not particular to our choice of grid point to represent the

offshore boundary of the Florida Straits in our model. As we move further offshore, the pattern begins to resemble more that obtained from the flat-bottomed Sverdrup relation (Fig.4.3) in all but the HI case (this too starts to look more like Fig.4.3 further offshore again). The DS case always has the smallest range, with the summer peak collapsing faster in the DS and HR cases, and the fall minimum deepening faster in the HR and TR cases.

Böning et al.(1991b) carried out a number of experiments designed to determine where the important wind forcing occurs that drives the seasonal transport variations through the Florida Straits (these are their experiments 2A,B,C). They concluded that wind forcing north of 35^0N was not important, but that wind forcing over the Caribbean/Florida Straits area was important. These results are NOT consistent with our model, as we shall now

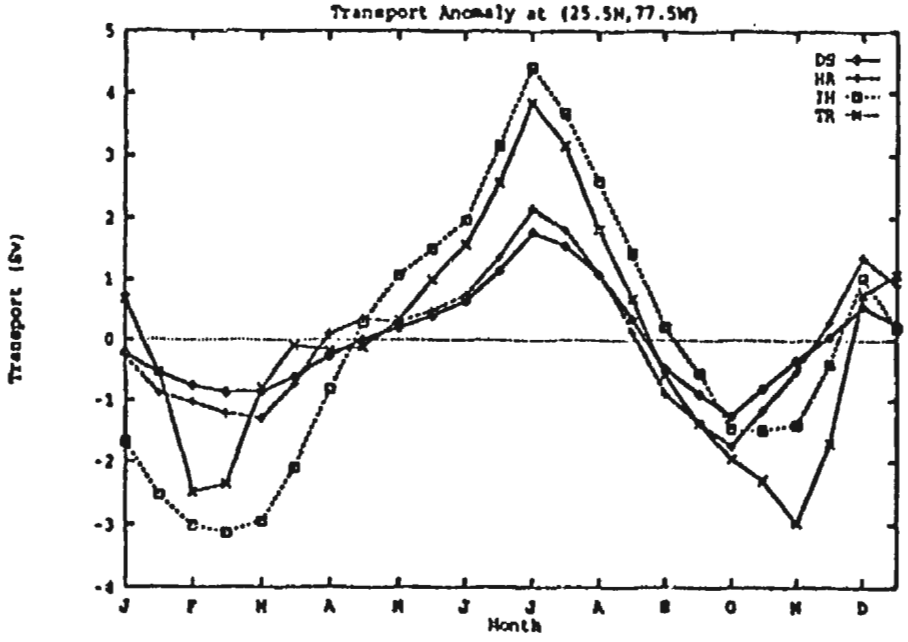

Figure 6.5: *As Figure 6.1, but showing the model-calculated seasonal cycle of transport between the coast and grid points along* $25.5°N$ *at* $77.5°W$, $76.5°W$ *and* $75.5°W$.

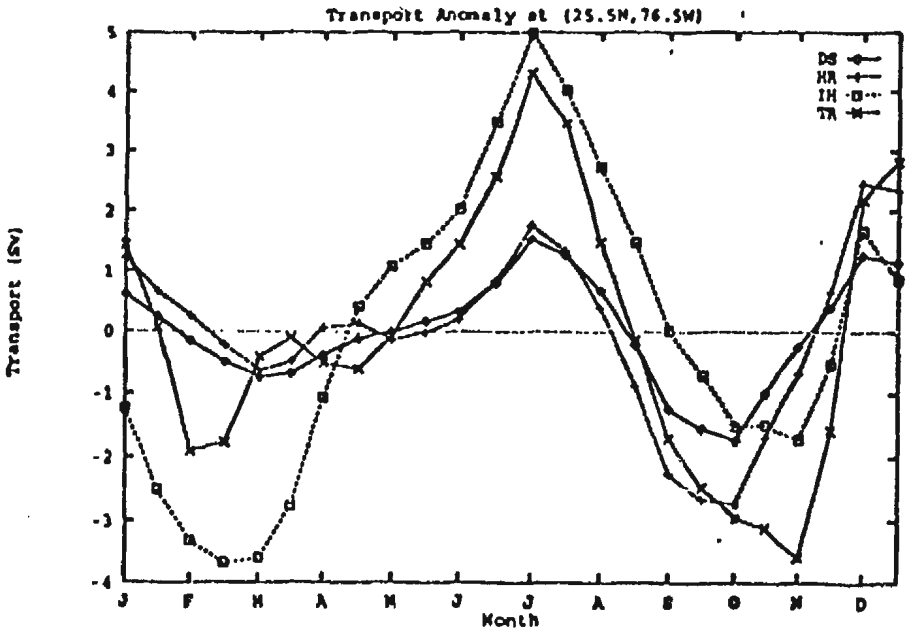

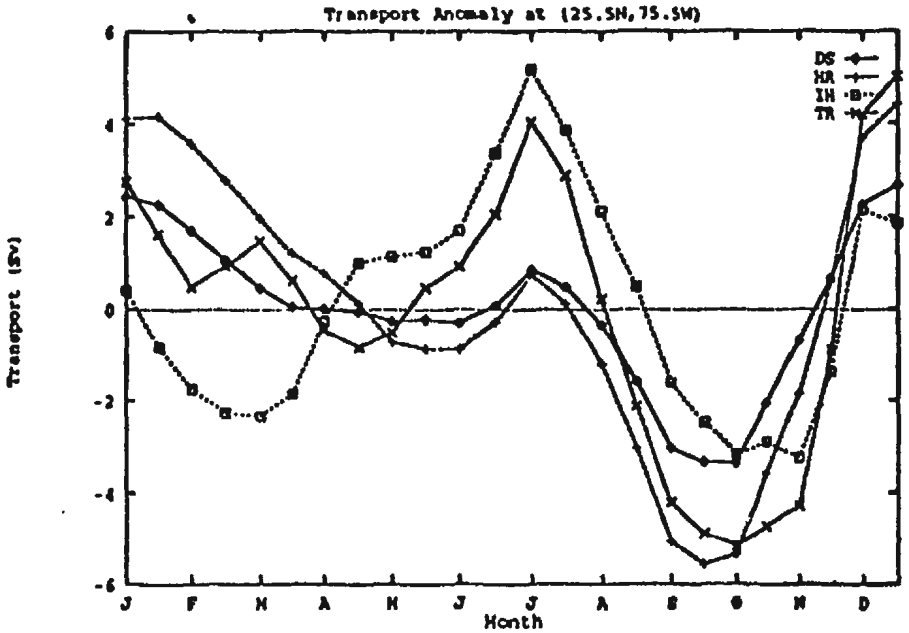

Figure 6.5: *continued*

illustrate (indeed, GG, who used a model essentially the same as ours, demonstrated a role for wind forcing north of $50^0 N$ in their model results). This is because in our linear, barotropic model, information propagates in the direction of long topographic wave propagation, implying that it is regions to the north and east of the Florida Straits, particularly along the continental slope region, that are important, as we noted when discussing eqn.(2.1.7), and (2.1.8). However, a difficulty arises with Böning et al.'s experiments. This is because the wind forcing is kept fixed in time in parts of their model domain and then merged in buffer zones (of 5^0 width) to regions where the full, seasonally varying wind forcing was maintained. However, within the buffer zones, a spurious forcing will occur through the curl of the wind stress term in eqn.(2.1.5) (this is the second group of terms on the right hand side). A better way to assess the importance of wind forcing in different regions is to simply zero out the forcing terms in (2.1.5) in certain parts of the model domain AFTER the curl has been calculated. In this way, the curl is the same where it is non zero, as it is in the experiments with the forcing applied everywhere. Unfortunately, once a model with baroclinic structure is used (such as the CME, or our two-density layer model), this procedure cannot be applied. However, we can use our barotropic model to assess the magnitude of the error introduced.

We therefore conducted three experiments using III wind forcing (the same as used by Böning et al.,1991b, in their experiments). In the first of these experiments, the forcing terms in (2.1.5) are as before, except that they are set to that of January north of $35^0 N$ (experiment I in Fig.6.6). In the second, a 5^0 buffer zone is applied between 30^0 - $35^0 N$ in

which the wind stress is linearly weight-averaged from the seasonally varying wind stress field below $30^{o}N$ to January's wind stress field north of $35^{0}N$ (experiment II in Fig.6.6).

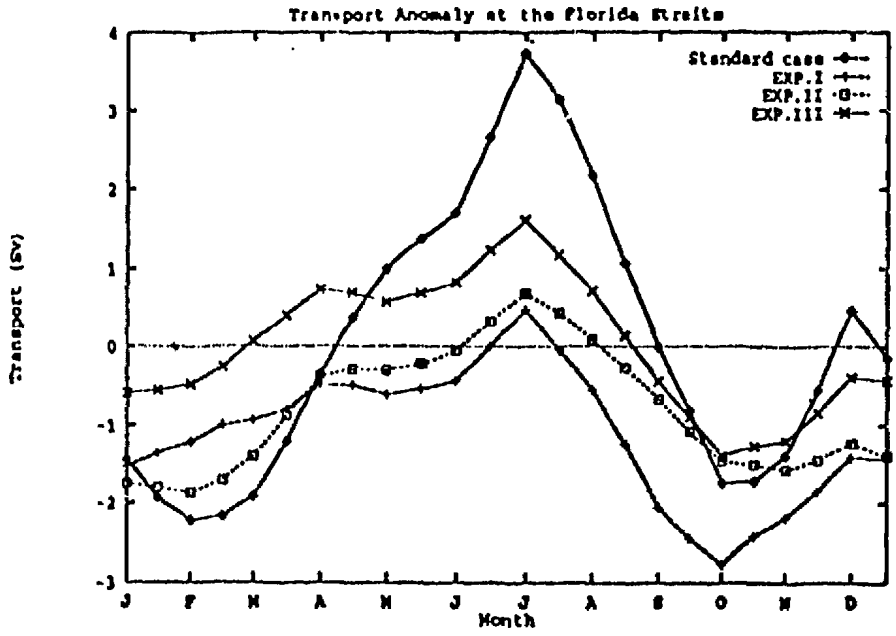

Figure 6.6: *Model-calculated transport through the Florida Straits using IH forcing when (i) forcing is applied over the entire model domain (standard case); (ii) the wind forcing terms in (2.1.5) are fixed at those of mid-January north of* $35^{0}N$ *(EXP.I); (iii) a* 5^{0} *buffer zone is used to merge the seasonally varying wind stress south of* $30^{0}N$ *with mid-January's wind stress north of* $35^{0}N$ *(EXP.II); and (iv) as EXP.1 but with the wind forcing terms set to zero north of* $35^{0}N$ *(EXP.III). See text for details.*

This experiment uses the same wind stress field as used by Böning et al. in their experiment 2B. The third experiment is the same as experiment I except that the forcing terms in (2.1.5) are set to zero north of $35^{0}N$ (experiment III in Fig.6.6). Each of the experiments exhibits a phase similar to that of our standard case (also depicted in Fig.6.6) in which the forcing

is applied over the entire domain. Exp.III is similar to that of AC shown in their Fig.9b (AC zeroed out the wind forcing north of 30^0N and west of 40^0W). Comparing with the

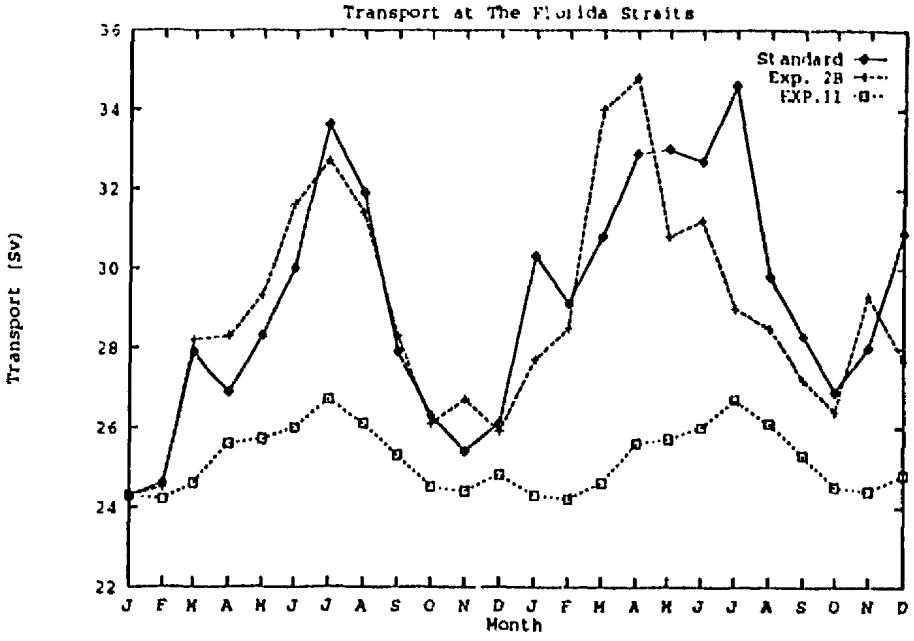

Figure 6.7: *Comparison of CME and barotropic model-calculated transport through the Florida Straits using IH forcing when (i) forcing is applied in the CME over the entire model domain (standard case); (ii) CME transport when a 5^0 buffer zone is used to merge the seasonally varying wind stress south of 30^0N with mid-January's wind stress north of 35^0N (Exp.2B); and (iii) as in (ii) except for the barotropic model (EXP.II). See text for details.*

standard case, it is clear that wind forcing north of 35^0N is an important part of our model response at the Florida Straits. Differences between Exp.I and Exp.II indicate the flow driven by the spurious curl which exists in the 5^0 buffer zone extending between 30^0N and 35^0N in Exp.II. The spurious curl drives a deeper minimum in winter (roughly $0.4Sv$

deeper) while driving more northward flow throughout the rest of the year (approximately $0.2 - 0.4 Sv$ more), except for September-October, when the spurious curl adds some $1.5 - 2.0 Sv$ northward transport.

Given the general agreement we found before between the CME and our simple, linear barotropic model, it is interesting that Exp.II in Fig.6.6 fails to show an increase in transport in the summer comparable to that in Böning et al.'s experiment 2B, since both experiments are driven under identical wind forcing (see Fig. 6.7). Clearly, dynamics not included in our linear model must be playing a role in maintaining the seasonal variation of transport in the CME. The equation governing the volume transport streamfunction in the CME can be written

$$\frac{\partial}{\partial t}\left\{\frac{\partial}{\partial \lambda}\left\{\frac{\Psi_\lambda}{H\cos\phi}\right\}+\frac{\partial}{\partial \phi}\left\{\frac{\Psi_\phi \cos\phi}{H}\right\}\right\}+\left\{\frac{\partial}{\partial \phi}\left(\frac{f}{H}\Psi_\lambda\right)-\frac{\partial}{\partial \lambda}\left(\frac{f}{H}\Psi_\phi\right)\right\}$$

$$=\frac{a}{\rho_0}\left\{\tau^\lambda \cos\phi \frac{H_\phi}{H^2}-\tau^\phi\frac{H_\lambda}{H^2}\right\}+\frac{a}{\rho_0 H}\left\{\frac{\partial}{\partial\lambda}\left(\tau^\phi\right)-\frac{\partial}{\partial\phi}\left(\tau^\lambda\cos\phi\right)\right\}$$

$$+ \text{JEBAR} + \text{ADVECTION} + \text{FRICTION}$$

JEBAR is the Joint Effect of Baroclinicity And Relief (Sarkisyan and Ivanov, 1971); ADVECTION refers to terms arising from the advection terms in the momentum equations; and FRICTION to the friction terms in the model. Compared to equation (2.1.5), the most important difference is the appearance of the JEBAR and ADVECTION terms on the right-hand side, (it is important to note that the CME's JEBAR term includes full density stratification, and should not be confused with the rather simple representation in the two-density layer model). Given that the CME is an eddy-resolving model, these will exhibit time fluctuations associated with mesoscale eddies. However, they also contain

longer time scales that could be important for driving the seasonal cycle in the model. For example, it is possible for advection of the density field by the mean flow of the western boundary current system to influence the barotropic transport through the JEBAR term. Greatbatch and Goulding(1992) give an example in which this effect allows information to be carried in the opposite direction to that of long-topographic wave propagation in an idealised model calculation. Also, Greatbatch and Li(1990) have discussed how the presence of a (barotropically stable) mean flow can modify wind-driven variability in an idealised, barotropic ocean model. They found that their solutions were influenced by both advection by the mean flow and the modification of the ambient potential vorticity field by the mean flow. It remains to be seen if these effects are important for determining Florida Straits transport variations, something that will have to be investigated using a model that includes a proper representation of the density field, and advective mechanisms.

Figure 6.6 indicates the importance of wind forcing to the north of 35^0N in our model. In a related experiment, we investigated the model's response to forcing south of the Florida Straits (25^0N) to assess the role, if any, wind forcing over the Caribbean has on our model results. To facilitate this, we ran the model with the forcing terms in (2.1.5) applied only to regions south of 25^0N and zero north of 25^0N. The results (not shown) show a very weak response at the Straits, with a range of only $0.15Sv$. This shows that in our model, wind forcing south of the Straits has an insignificant effect on the seasonal variation of transport through the Straits. This agrees with AC (see their Fig.9b, but note that in their experiment, non-zero wind forcing extended up to 30^0N).

Next we investigate the importance of wind forcing by each of the meridional and zonal components of the wind stress for each climatology. Figure 6.8 shows the model results in each case. As previously demonstrated by AC (see their Fig.7), the meridional component is the most important for determining the model-calculated seasonal transport variations at the Florida Straits (compare Fig.6.8 with Fig.6.1), although the zonal component does play some role in the winter months. Looking only at the meridional component (Fig.6.8b), we see that once again, DS wind forcing gives the smallest range (maximum minus minimum) and that in the summer months, HI gives the largest northward anomaly. We also see that, as far as the meridional component is concerned, HR and TR give rather similar behaviour - much greater differences are evident in the zonal component. It follows that most of the difference between HR and TR in Fig.6.1 can be attributed to differences in the zonal component of the wind stress (apart from January when it is the meridional component that leads to the difference). There are also large differences between the HI and HR cases due to forcing by the zonal component of the wind stress throughout the year (Fig.6.8a). It follows that although the meridional component is important in determining the overall shape of the model-calculated signal in Fig.6.1 (in particular, the summer maximum and fall minimum), much of the difference between the cases using the different wind stress climatologies can be attributed to forcing by the zonal component of the wind stress, with the meridional component also playing a role in the DS and HI cases.

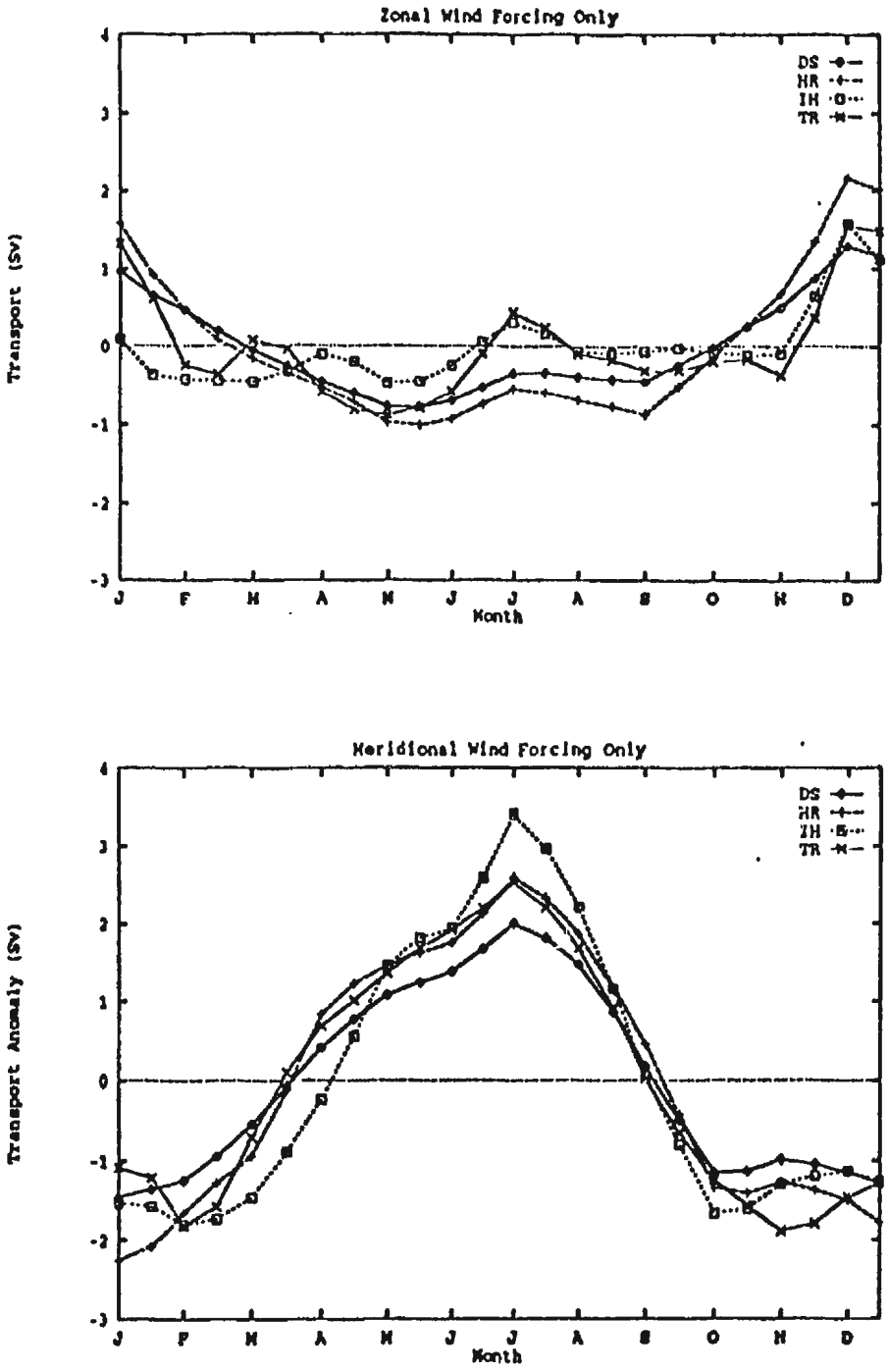

Figure 6.8: *Model-calculated seasonal cycle of transport (Sv) through the Florida Straits when (a) only the zonal component of wind stress is applied and (b) only the meridional component of wind stress is applied.*

We now decompose our model response at the Florida Straits into parts associated with each of the forcing terms in (2.1.5) *i.e.*

$(i)\frac{a}{\rho_o}\tau^\lambda \cos\phi \frac{H_\phi}{H^2}$

$(ii)\frac{-a}{\rho_o}\tau^\phi \frac{H_\lambda}{H^2}$

$(iii)\frac{a}{\rho_o}\frac{1}{H}\left\{\frac{\partial}{\partial\lambda}\left(\tau^\phi\right) - \frac{\partial}{\partial\phi}\left(\tau^\lambda \cos\phi\right)\right\}.$

The results are shown in Fig.6.9 (the standard case refers to forcing with all the forcing terms in (2.1.5) included). These indicate that for each wind stress climatology, the model-calculated transport from January through to August is driven by the meridional and curl terms (*(ii)* and *(iii)* above) with the term involving the zonal component (*(i)* above) giving a contribution of the opposite sign (the exception is the TR case in January and July). In the fall (from September to November), it is the zonal and meridional terms (*(i)* and *(ii)* above) which produce the fall minimum, with the curl forcing acting oppositely. The exception is the TR case in November for which the curl term also acts to produce the minumum. Finally, the northward transport indicated in December in the standard cases is completely dependent on the zonal forcing term for its existence, the curl and meridional forcing acting oppositely in that month.

It is important to note that the meridional component of wind stress in conjunction with longitudinal gradients of topography is capable of independently producing the bulk (on average, roughly 70%) of the standard model-calculated response. Clearly this term will be particularly large in the continental slope region where the east-west gradient of the topography is large. In light of this, we now consider a final set of experiments in which forcing using the III climatology is confined to the western shelf/slope region only; that is,

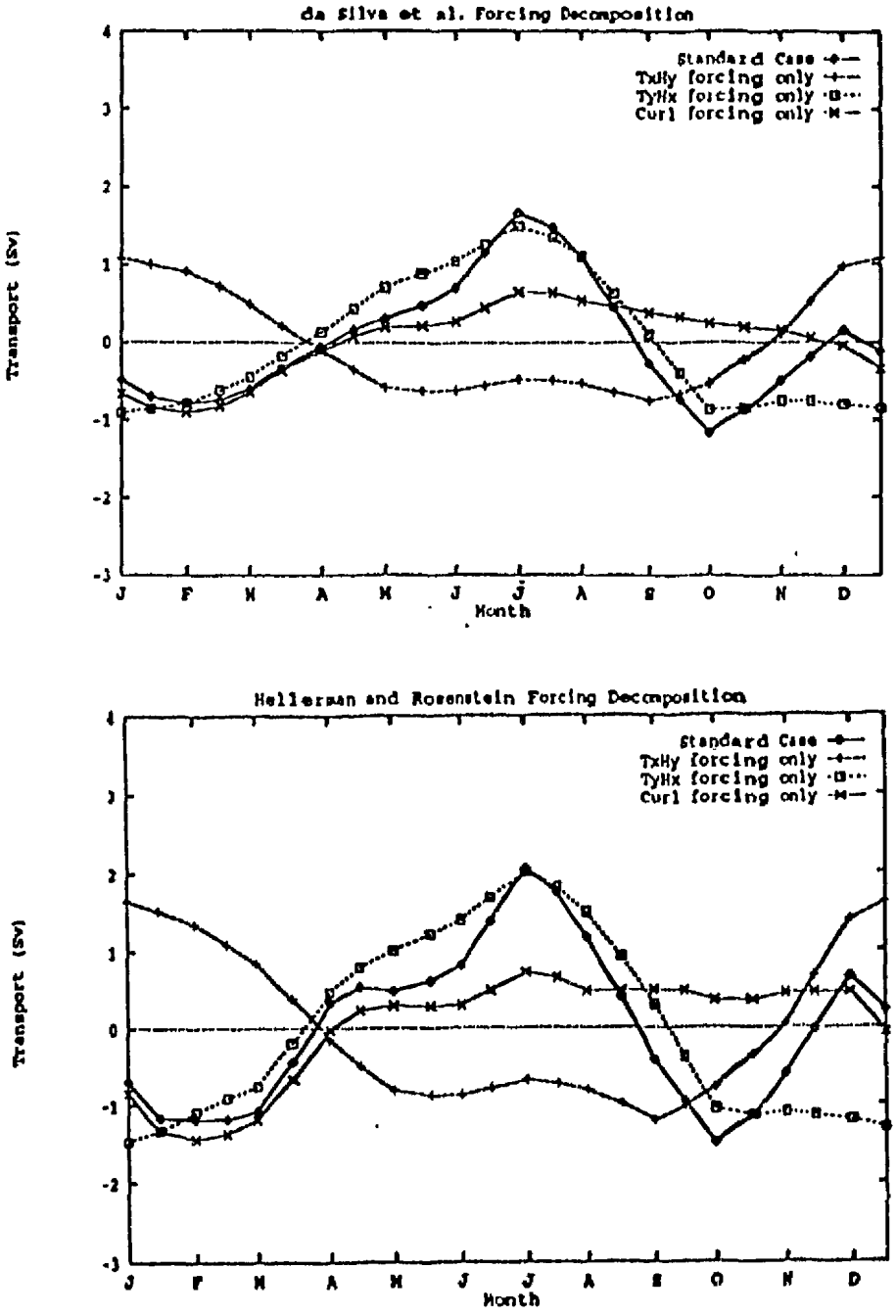

Figure 6.9: *That part of the model-calculated seasonal cycle attributable to each of the forcing terms in (2.1.5) for (a) DS; (b) HR; (c) HH; and (d) TR. "TxHy" refers to the* $\tau^{\lambda} \cos\phi \frac{H_{\phi}}{H^2}$ *term; "TyHx" to the* $\tau^{\phi} \frac{H_{\lambda}}{H^2}$ *term, and "curl forcing" to the* $\frac{1}{H}\left\{\frac{\partial}{\partial\lambda}\left(\tau^{\phi}\right) - \frac{\partial}{\partial\phi}\left(\tau^{\lambda}\cos\phi\right)\right\}$ *term. The standard case, in which all forcing terms are used to drive the model, is also shown.*

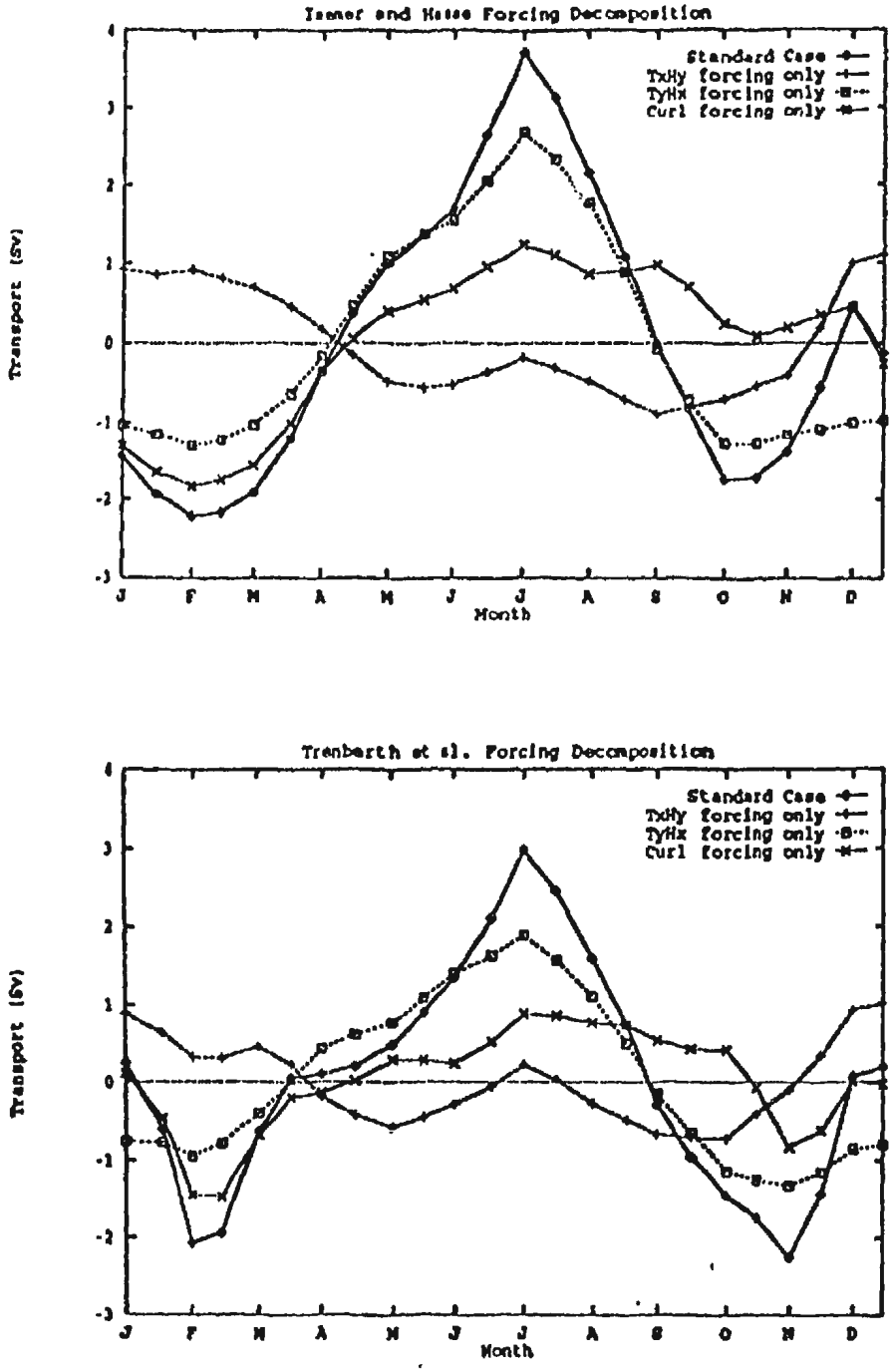

Figure 6.9: *continued*

the forcing terms in (2.1.5) are non-zero only in water of depth less than 3000m bounding the coast and north of 25^0N and west of 40^0W (see Fig.6.10). In the first of these experiments

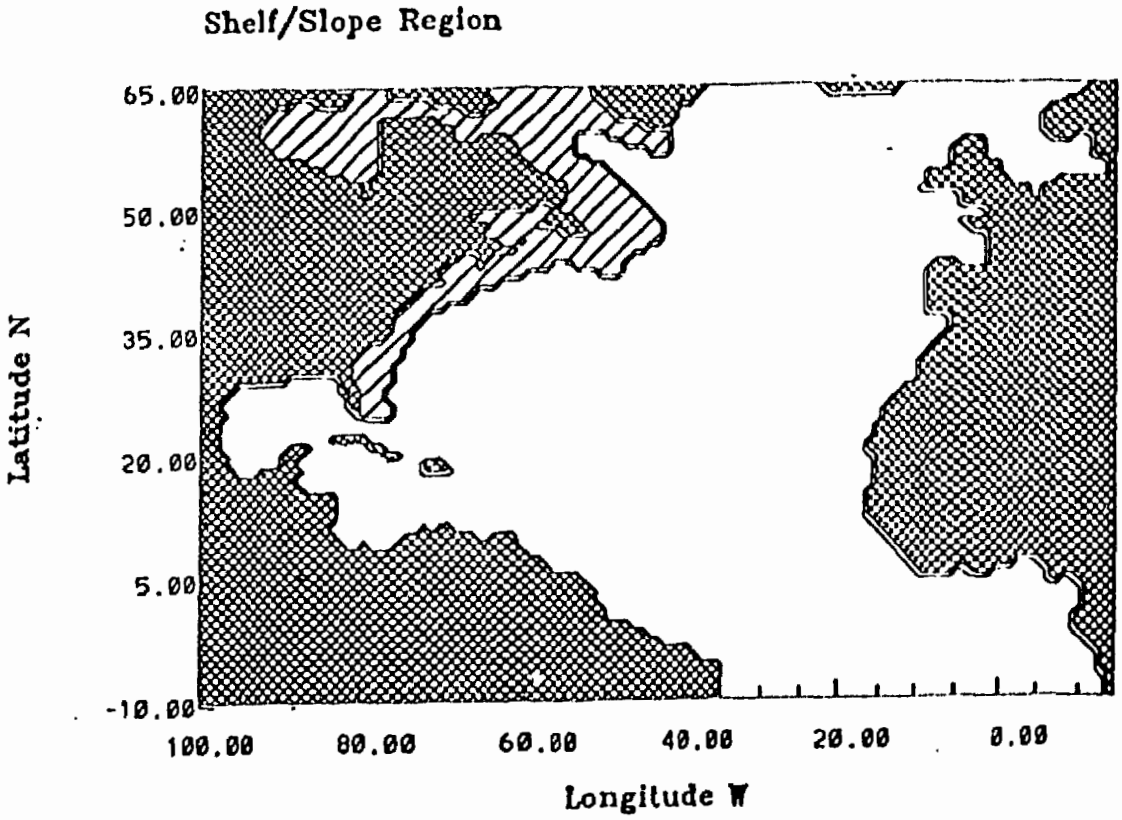

Figure 6.10: *The hatched region shows that part of the model domain in which the forcing terms are non-zero in the shelf/slope experiments (see Figure 6.11).*

(full forcing in Fig.6.11) we include all forcing terms in (2.1.5) over the shelf/slope region, while in the second, we consider only the forcing due to the term $r^{\phi}H_{\lambda}$ in (2.1.5) (the "Ty only" case in Fig.6.11). The results, shown in Fig.6.11, indicate that both these experiments are quite successful in reproducing not only the phase, but much of the annual range of the standard case. In particular, when all forcing terms are included over the shelf, the model captures roughly 70% of the standard case's annual range (cf. $4.1Sv$ for the shelf/slope

forced case with $5.0Sv$ for the standard case). Furthermore, the case considering only the meridional forcing term (*(ii)* above) over the shelf/slope does almost as well, indicating

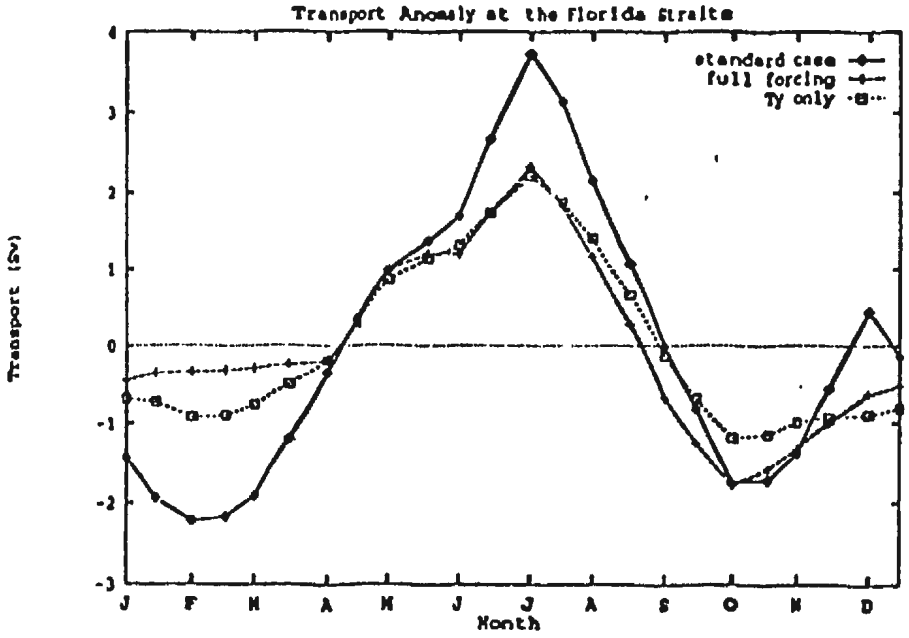

Figure 6.11: *The model-calculated response when III forcing is confined to the hatched region in Figure 6.10. "full forcing" refers to all forcing terms non-zero in this region; "Ty only" to having only the $\tau^{\phi}\frac{H_\lambda}{H^2}$ term non-zero in this region. Also shown is the standard case in which all forcing terms are applied throughout the entire model domain.*

the dominance of this term in this region. This result can be understood in terms of the inviscid, steady state solution to (2.1.5) (the topographic Sverdrup relation). Consider the eastern seaboard to be approximated by a latitudinally straight coastline, with the shelf/slope varying only in the longitudinal direction, and the surface wind stress to be

northward and spatially uniform. We can then write the topographic Sverdrup relation as

$$J\left(\Psi, \frac{f}{H}\right) = -\frac{H_\lambda}{H^2}\tau^\phi$$

Assuming an f-plane, this reduces to

$$\Psi_\phi = -\frac{\tau^\phi}{\rho_0 f}$$

which is simply the Ekman transport. It is clear therefore, that an increased northward wind stress (the case for the summer) will drive more flow across the shelf/slope. This will lead to a divergance of the flow from the coast, information about which will be carried southward, along the f/H contours to the Florida Straits region, by long topographic waves. The northward transport at the Straits must then increase to balance the net off-slope Ekman transport, with this transport occurring in the frictional boundary layer necessary to satisfy the coastal boundary condition. A similar situation exists in the fall and late winter when the wind stress anomaly is southward, in which case, the transport through the Straits must be reduced.

Figure 6.12 shows results from a further decomposition of this case. The forcing term *(ii)* is the only non-zero forcing term, and this is nonzero only in selected latitude ranges over the shelf/slope region. As with Fig.6.6, we again see that regions north of 35^0N (indeed, even north of 45^0N) contribute to the model response. The importance of forcing in the shelf/slope region to the north of the Straits is consistent with the linear, barotropic dynamics employed in our model. This is because, as was noted earlier when discussing

(2.1.5), and the CME, information in our model propagates in the direction of long, topographic wave propagation which in this case, is southward along the continental slope (cf. Csanady, 1978). We have also run similar cases in which we have used f/H contours to define the outer edge of the shelf/slope region. Choosing the f/H contour passing over the 3000 m isobath at the latitude of the Florida Straits (rather than the 3000m isobath itself as in Fig.6.10) gives results that differ little from those shown in Fig.6.11, even when the restriction to regions west of 40^0W is lifted. This shows the importance of "diffusion" across f/H contours from deep water, as in the model of Csanady(1978), for explaining the difference between the full forcing and standard cases in Fig.6.11.

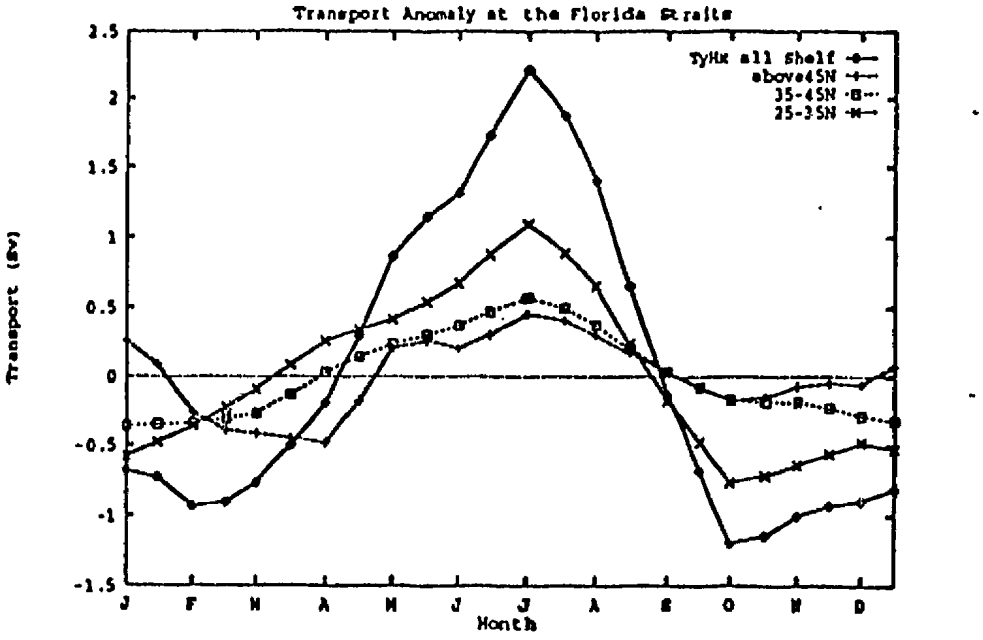

Figure 6.12: *As Figure 6.11, but when the* $\tau^{\phi}\frac{H_\lambda}{H^2}$ *is the only non-zero term.* $25^0N - 35^0N$ *means that this term is further restricted to be non-zero only in the latitude range* $25^0N - 35^0N$. *Similarly in the other cases.*

CHAPTER 7: HIGH RESOLUTION MODEL RESULTS

One feature of GG's model results we have previously noted was the sensitivity of their model to the smoothing of topography, and the value of the linear bottom friction coefficient (see Fig.1.5). Indeed, owing to the similarities between our models we expect the same to hold for our model results. Furthermore, owing to the sensitivity in our model to the forcing due to the meridional component of the wind stress in conjunction with longitudinal gradients in topography (the term $\tau^{\phi} H_{\lambda}$ in (2.1.5)) we expect that increased resolution of the model geometry should significantly increase the accuracy of our model results.

By increasing our model resolution, we can reduce the degree of smoothing of bottom topography necessary to maintain model stability since features are better resolved. Furthermore, this allows selection of a bottom friction coefficient, and lateral mixing of momentum coefficient more applicable to the shelf/slope regions. Finally, by moving to higher resolution, we obtain a more accurate representation of the Florida Straits, as well as the longitudinal gradients in topography which, as we have seen, play an important role in our model results.

Here we examine the robustness of our earlier $1^{\circ} \times 1^{\circ}$ results using a $1/3^{\circ} \times 1/3^{\circ}$ resolution, limited area version of our model as applied to the Florida Straits region. In addition to the seasonal wind stress anomalies of DS, HR, HI and TR, the model is driven by flow through the open eastern (ocean) boundary specified from the $1^{\circ} \times 1^{\circ}$ North Atlantic calculation described in Chapter 6.

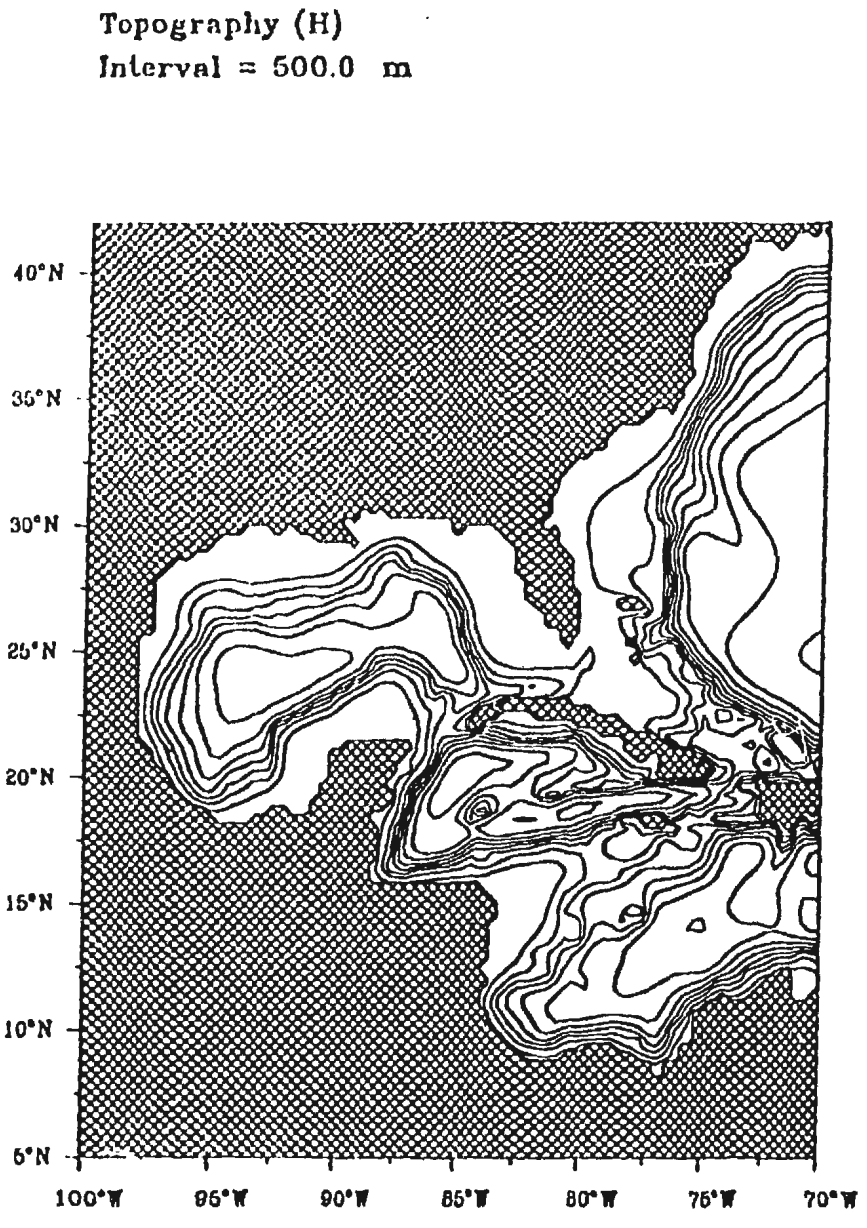

Figure 7.1: *The limited-area, 1/3° × 1/3° resolution bottom topography, smoothed as outlined in the text. The contour interval is 500m.*

We solve (2.1.5) on a $1/3^o \times 1/3^o$ grid bounded by latitudes 5^oN and 42^oN, and longitudes 100^oW and 70^oW. The western, northern, and southern boundaries are closed by requiring $\Psi = 0$ there as before. However, along the eastern boundary, Ψ is specified using output from the $r = 1.25 \times 10^{-3} ms^{-1}$; $A_H = 10^4 m^2 s^{-1}$ case described in Chapter 6. The eastern boundary transport data is linearly interpolated from our $1^o \times 1^o$ results to the $1/3^o \times 1/3^o$ grid employed here. Linear interpolation from the center of each month provides the necessary eastern boundary condition for each time step. In cases described as " no inflow ", $\Psi = 0$ along these boundaries.

The seasonal anomalies of wind stress (those of DS, HR, HI, and TR) are interpolated from $1^o \times 1^o$ to the $1/3^o \times 1/3^o$ grid employed here using the scheme of Akima(1978) which, as we mentioned when discussing the wind stresses of TR in Chapter 3, preserves the curl of the wind stress.

The topography employed here is smoothed using the Laplacian smoother as detailed in section 2.2.4. Here, however, we no longer impose the constraint of a minimum depth of 400 m during the application of the Laplacian filter. Furthermore, the continental boundaries, as well as islands are now treated as shallow water of 0.1 m depth. The topography produced in this manner is depicted in Fig.7.1. Note the model geometry now clearly resolves the Grand Bahamas Island, as well as Andros Island (see Fig.1).

The results to be described were obtained using a value of $r = 5 \times 10^{-4} ms^{-1}$ and $A_H = 10^3 m^2 s^{-1}$. For comparison, Csanady(1982) indicates values of r applicable to the shelf/slope regions within the range $2.5 \times 10^{-4} ms^{-1} \leq r \leq 10^{-3} ms^{-1}$ indicating the current value for r lies in the low to moderate friction range for a shelf/slope region.

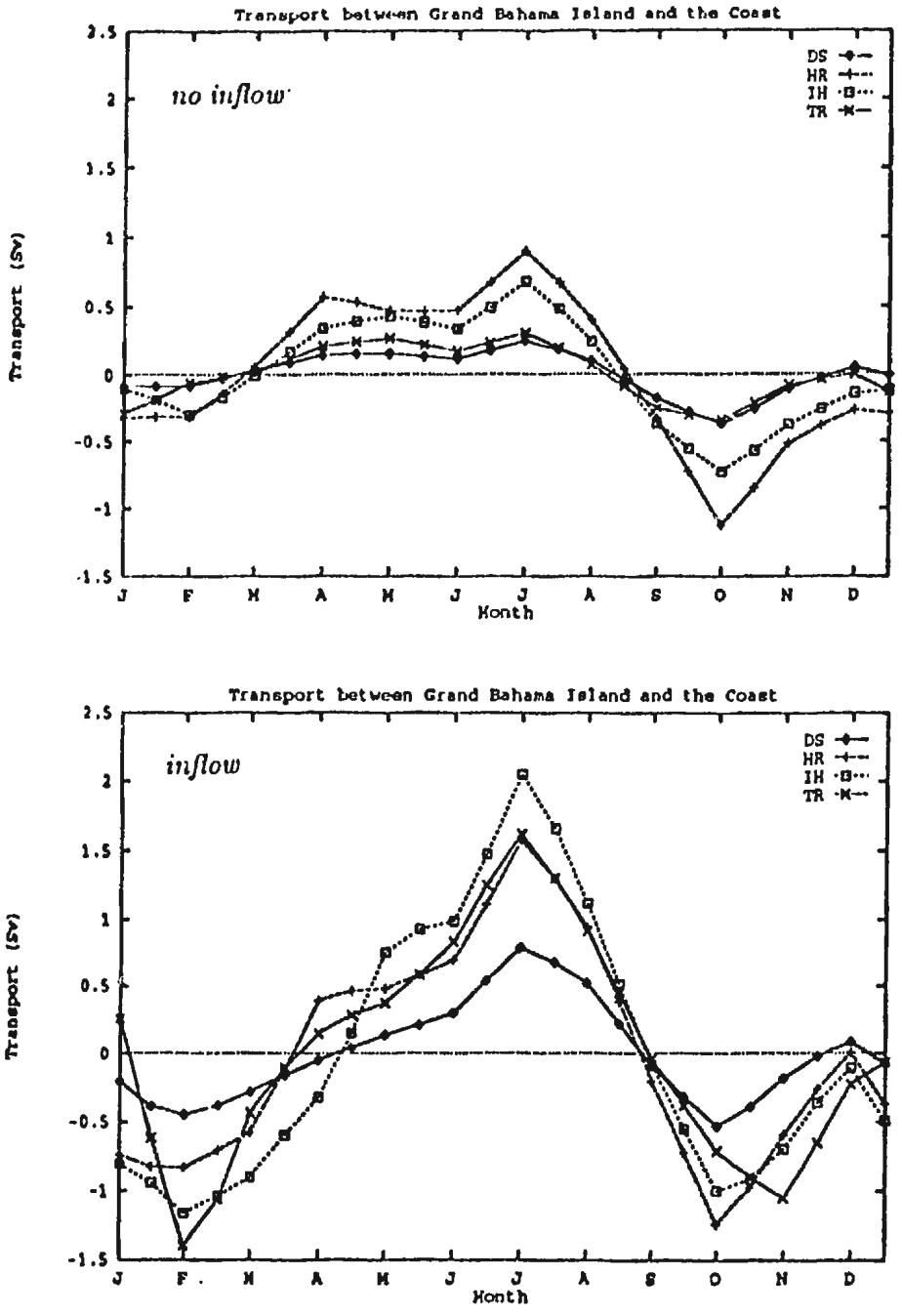

Figure 7.2: *The model-calculated seasonal cycle of transport (Sv) between the coast, and the Grand Bahama Island. (a) The "no inflow" cases refer to those with* $\Psi = 0$ *on the eastern boundary. (b) The "inflow" cases refer to those with* Ψ *specified from the* $1^\circ \times 1^\circ$ *model studies of Chapter 6 (see text for details).*

In order to perform a more direct comparison with Larsen's cable data, we first examine the transport between the model's Grand Bahama Island and the coast. Figure 7.2 indicates the model-calculated transport between the coast and the Grand Bahama Island for both (a) "no inflow" and (b) "inflow" cases, that is with Ψ specified from the $1^{\circ} \times 1^{\circ}$ model results, or set to zero along the eastern boundary. The curves for each climatology indicate a seasonal cycle similar to that of Larsen (Fig.1.1) and the $1^{\circ} \times 1^{\circ}$ model results, Fig.6.1. Note, however, the transport range is reduced in both cases as compared to the $1^{\circ} \times 1^{\circ}$ case of Fig.6.1.

In the "no inflow" cases the model-calculated seasonal ranges vary widely, with the DS and TR cases indicating the lowest range (0.60 *Sv* and 0.64 *Sv* respectively) while the IH and HR cases do much better (1.41 and 2.02 *Sv* respectively). The "no inflow" cases represent the importance of local (within the limited area model domain considered here) wind forcing, and seems to indicate that for the IH and HR cases, local forcing is much more important than for the TR and DS cases. The differences between the "inflow" and "no inflow" cases indicates the importance of wind forcing exterior to the model domain utilized here. Examination of Fig.7.2a-b indicates a much higher transport in all cases with "inflow" (in fact, twice as large in the DS and IH cases, while the TR case exhibits five times the model response compared with "no inflow"). Whereas, in our earlier experiments we found that the IH and TR transports were too large in the Florida Straits, we now find these climatologies exhibit transport ranges lower than Larsen's cable data. Compare the IH range of 3.12 *Sv* produced here, with the 5.9 *Sv* of Chapter 6, and Larsen's 4.6 *Sv*; also

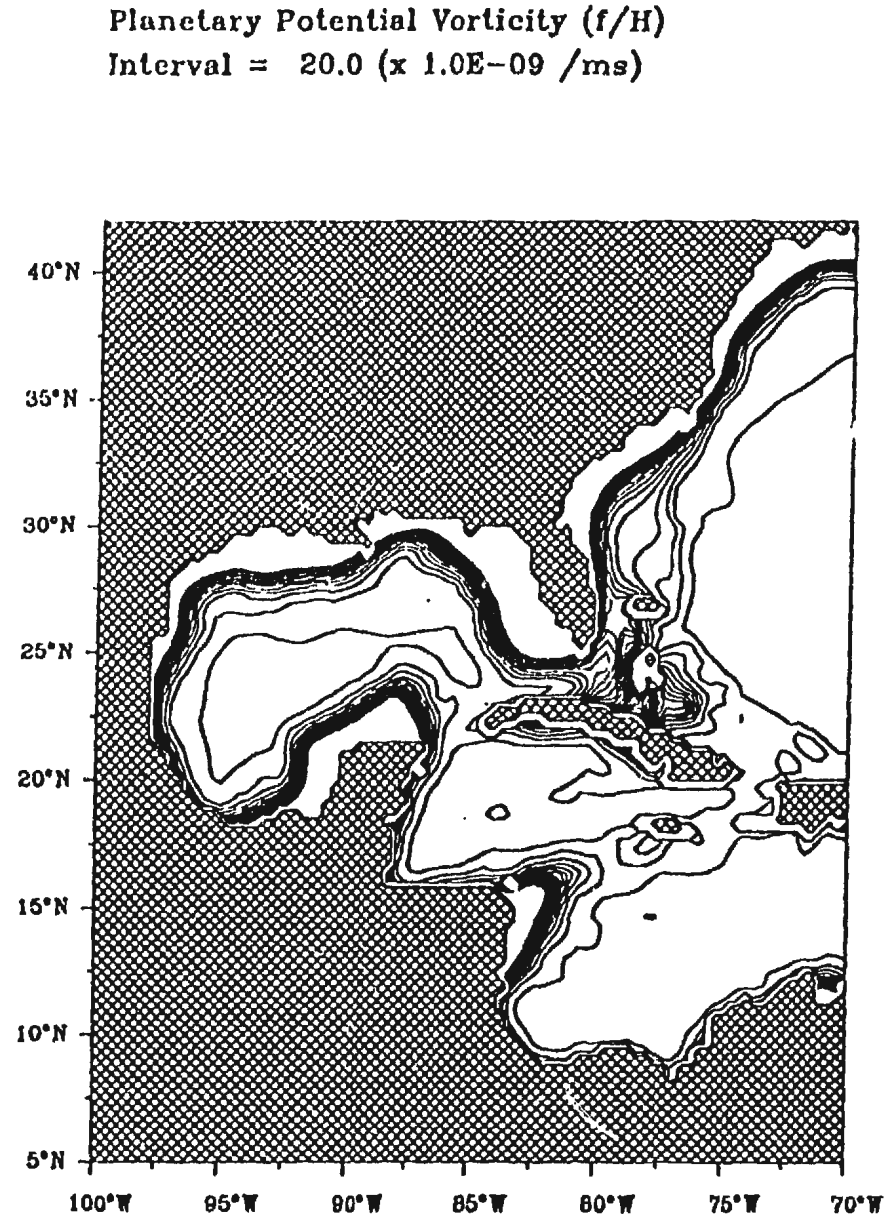

Figure 7.3: *Planetary potential vorticity, f/H, contours. The topography has been smoothed using a Laplacian smoother as outlined in the text. The contour interval is* $2.0 \times 10^{-8} s^{-1} m^{-1}$.

compare the TR range of 3.02 Sv produced here, with the 5.2 Sv of Chapter 6, and Larsen's data. The DS and HR cases with "inflow" fare the worst with transport ranges of only 1.32 Sv and 2.82 Sv respectively. This result can be understood in terms of the structure of the f/H contours in the area of the Grand Bahama Island. In our $1^\circ \times 1^\circ$ case, the Grand Bahama Island was unresolved, allowing information from a wider range of f/H contours to propagate to the model Florida Straits. In the $1/3^\circ \times 1/3^\circ$ case the proximity of the island with the coast shallows the Florida Straits during smoothing of the bottom topography, so that the maximum depth of the Florida Straits is just over 500 m, roughly half the depth of the $1^\circ \times 1^\circ$ case. This indicates that the range of f/H contours able to enter the $1/3^\circ \times 1/3^\circ$ model's Florida Straits is half that of the $1^\circ \times 1^\circ$ case and hence limits the information entering this area due to forcing to the north and east of the Straits. Indeed, examination of Fig.7.3, the f/H structure in this area, indicates the islands act to divert f/H contours out of the Florida Straits, to the east of the Grand Bahama and Andros Islands. Due to the convergence of planetary potential vorticity contours in this area, we see intense gradients in f/H and therefore also expect this region to be one of strong dissipation. Future work will have to address the problems associated with using smoothed, high resolution topography. That is, smoothing the topography in such a manner that a realistic depth for the Florida Straits is maintained, while at the same time removing grid scale features which can destroy computational stability.

Next, we note that when choosing a grid point corresponding to that utilized in Chapter 6 (ie/ $25.5^\circ N$, $78.5^\circ W$, see Fig.7.1) we find that the $1/3^\circ \times 1/3^\circ$ resolution model results ("inflow" cases) agree quite well with our earlier analysis, see Fig.7.4. Choice of other grid

points in this region yields similar results. This increased range arises from the fact that the current points lie further offshore as compared to the Grand Bahama Island, in a depth of 950 m (c.f. 939.5 m in the $1^o \times 1^o$ case), and hence are receiving information about wind forcing from a larger range of f/H contours. Furthermore, there is a role for the diffusion across f/H contours from deeper waters as we discussed in conjunction with Fig.6.9, an effect which also helps to account for the increased range at this grid-point.

To gain more insight into these results we now consider "plan-views" of the model-calculated streamfunction for the limited area model domain cases. Appendix C shows both "inflow" and "no inflow" boundary conditions, for each of the months of January, July, and October. In the "inflow" case for January (Fig.C.1a) there are large positive values of transport in the deep waters to the east of the Florida Straits, which implies an enhanced northward transport offshore of the Bahama/Antilles Island arc at this time of year. Note, with the exception of the TR case, the Florida Straits lies within a tongue of negative streamfunction anomaly which extends along the eastern seaboard of the model domain (see also the corresponding figures in Appendix A). The fact that this feature is virtually non-existent in the "no inflow" case (Fig. C.1b) indicates the reduced flow at this time of year in our model is a result of the inflow boundary condition applied on the eastern boundary. It follows that the response is associated with forcing to the north and east of the limited-area domain (north of 42^oN, east of 70^oW) and its presence accounts for the reduced transport in January from the "no inflow" to the "inflow" case of Fig.7.2. A similar situation exists for the October case (see Fig.C.2a,b). As well, in July an anticyclonic

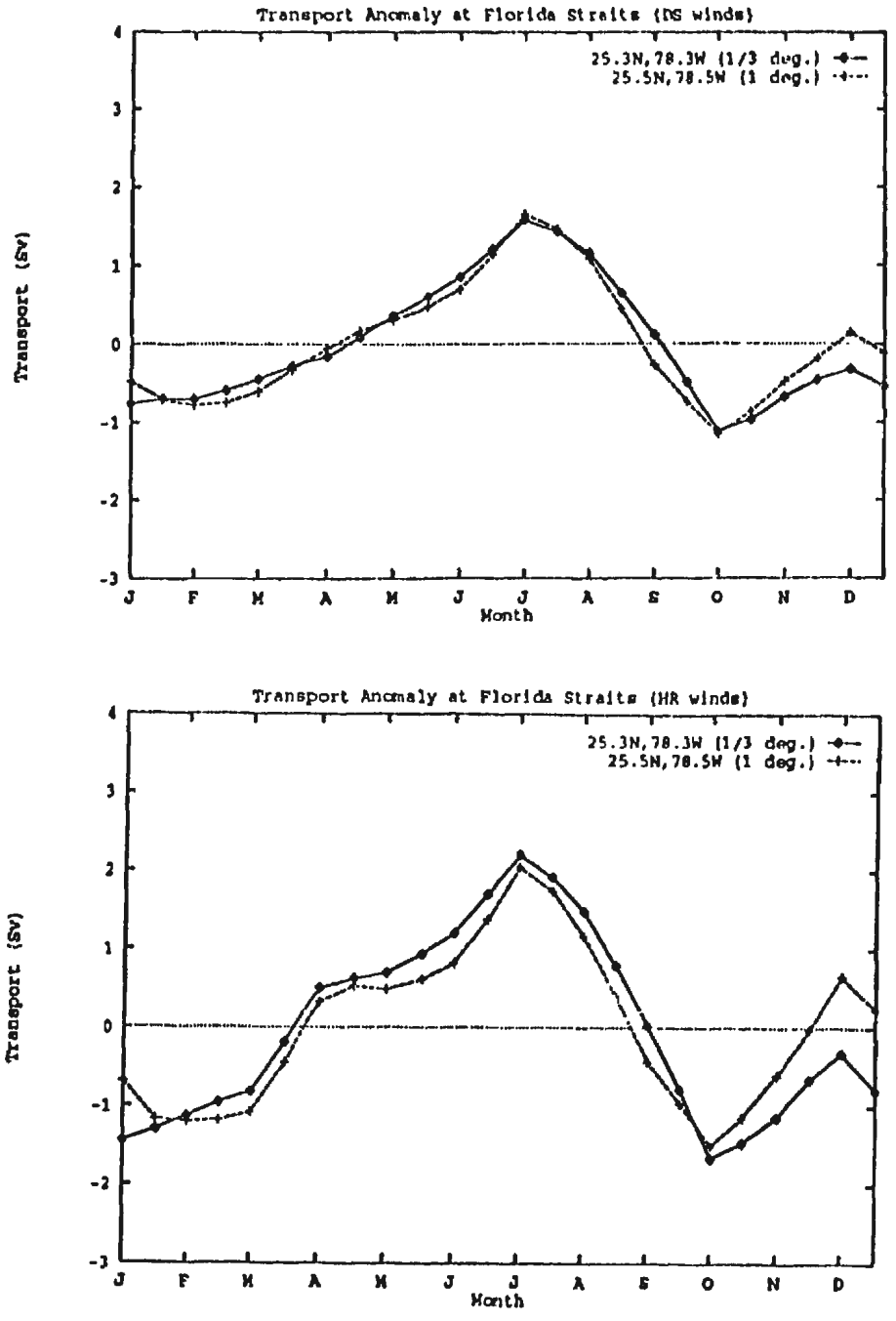

Figure 7.4: *Comparison of the 1° × 1° resolution model-calculated seasonal cycle of transport (Sv) with that of 1/3° × 1/3° resolution seasonal cycle of transport at the corresponding location, for each of the seasonal climatologies of (a) DS; (b) HR; (c) HI; and (d) TR.*

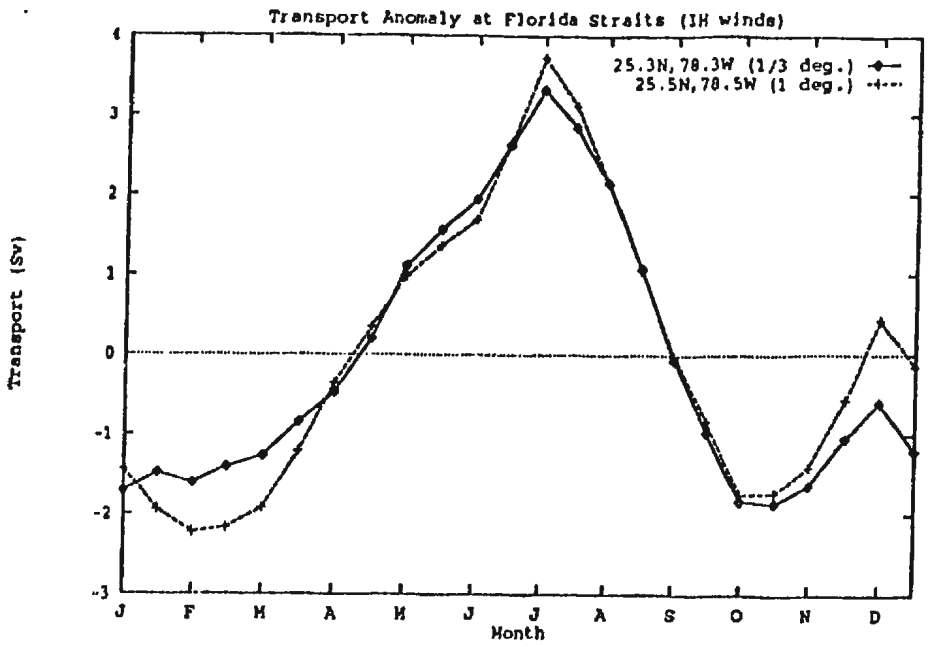

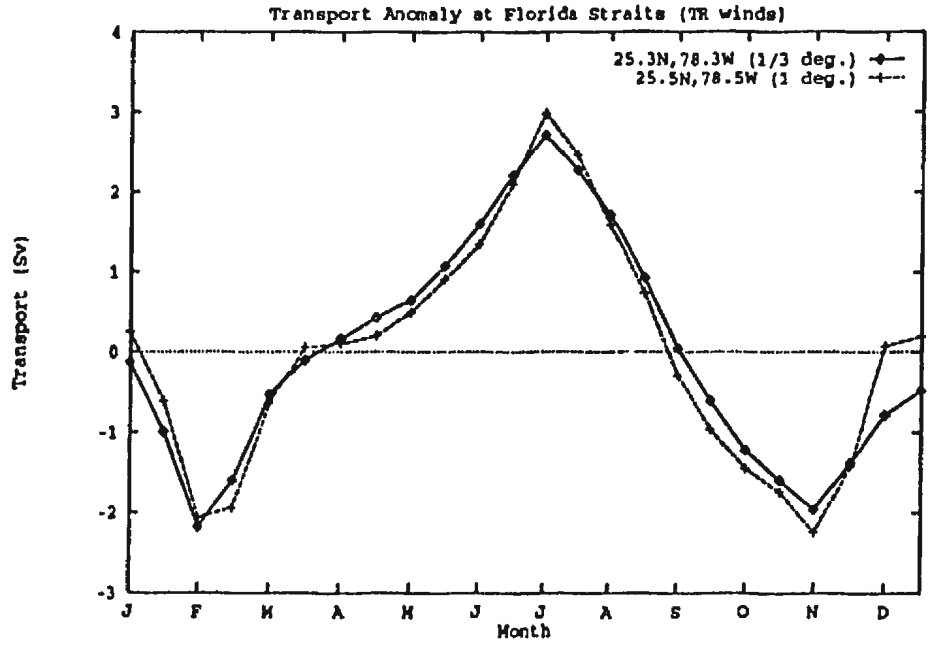

Figure 7.4: *continued*

anomaly extends along the slope with a cyclonic anomaly existing off-shore, this feature is virtually non-existant in the "no inflow" case (Fig. C.3b) and indicates the enhanced flow at this time of year in our model is again a result of forcing to the north and east of the limited-area domain, consistant with our earlier findings.

The fact that f/H contours are constrained to follow topography (the continental slope in this case) explains why the values of Ψ offshore in deep water in Figs.C.1a-C.3a fail to penetrate across the continental slope and influence the model response at the Flroida Straits. As we noted when discussing (2.1.7), in the absence of forcing, the topographic Sverdrup balance reduces to

$$\nabla\Psi \times \nabla\frac{f}{H} = 0$$

indicating that streamlines are confined to follow lines of planetary potential vorticity, which as we have just pointed out are dominated by the continental shelf/slope in the North Atlantic. In this sense, not only is the information from deeper waters offshore excluded from having a dominant effect (the inclusion of friction does allow diffusion across these contours to some extent), but also the existence of the tongue of streamfunction anomaly in Figs.C.1a-C.3a can be seen as being guided along the continental slope to the Florida Straits, consistent with the linear, barotropic dynamics employed in our model. This is because, as was noted earlier when discussing (2.1.5), and the CME, information in our model propagates in the direction of long, topographic wave propagation which in this case, is southward along the continental slope (cf. Csanady, 1978).

CHAPTER 8: SUMMARY AND CONCLUSIONS

In this thesis, the wind-forced response of the North Atlantic is evaluated. In order to accomplish this task, we have developed two of the simplest possible numerical models that can be used for this purpose; namely, a linear, single layer, barotropic model, and a linear two-density layered model. The models extend from 10^0S to 65^0N and 100^0W to 15^0E and have been utilized to study the seasonal variability of the Florida Straits transport. The models are driven with the seasonal anomalies (monthly means with the annual mean removed) of wind stress as derived by each of da Silva et al. (1993a; hereafter DS), Hellerman and Rosenstein (1983; hereafter HR), Isemer and Hasse (1987; hereafter IH) and Trenberth et al. (1990; hereafter TR). In particular, we study the effect each of these different wind stress climatologies has on the model-calculated seasonal transport variation.

Forcing the models with each climatology leads to a model-calculated, seasonal transport variation at the Florida Straits similar to that observed, with maximum northward transport in the summer and minima in the fall and late winter. However, each climatology produces differing ranges (that is maximum minus minimum transport). In the barotropic model with $1^o \times 1^o$ resolution, the HR wind stress field gives an annual range of $3.6Sv$, DS $2.8Sv$, IH $5.9Sv$, and TR $5.2Sv$. By comparison, Larsen's (1992) cable-derived transport for the Florida Straits indicates an annual range of 4.6 ± 0.4 Sv. This indicates that compared to Larsen, the amplitudes of the HR and DS cases are too small, while IH and TR are too large. We find that whereas the meridional component of the wind stress is the most important for determining the overall cycle of transport calculated by the model, differences in the zonal component play an important role in determining the differences between each

case. We have also seen that the forcing term due to the meridional component of the wind, in combination with the east-west gradient of topography, is very important for determining our model response. Furthermore, forcing through this component is particularly significant along the continental slope region to the north of the Straits. This contrasts with Böning et al.(1991b) who concluded, using the Kiel version of the WOCE-CME, that wind forcing north of 35^0N played little role in their results. We suggest that this may be because of advection (e.g. of the density field) by the mean flow in the CME experiments. On the other hand, our simple, linear models can account for the increase in the amplitude of the model-calculated seasonal signal found by Böning et al.(1991b) when using III wind forcing rather than HR. Indeed, the ranges calculated by our model using HR and III wind forcing agree well with the CME results.

It is disappointing that the DS wind stress fields give the smallest amplitude of all our cases. We believe the DS wind stress climatology to be the most representative of the actual wind stress over the ocean of all the climatologies used here. This is because of the way the DS climatology has been constructed; taking account of the scientific Beaufort scale (Kaufeld, 1981) and a correction for ship anemometer height, before calculating the stress. Furthermore, unlike IH, these corrections were made to the individual ship observations, in an effort to reduce bias in the calculated momentum fluxes. One possible reason for the discrepancy is that the wind stress climatology is compiled from data collected over a different time period (actually 1945-89) than the cable data. We have checked this and run the $1^o \times 1^o$ model with a modified DS wind stress climatology that uses data only from the months for which there is cable data. The result is shown in Figure 8.1. The range of the

model-calculated solution is increased slightly over the standard barotropic DS case ($3.0Sv$, as against $2.8Sv$ before), but is still less than the range found in Larsen's data. Perhaps

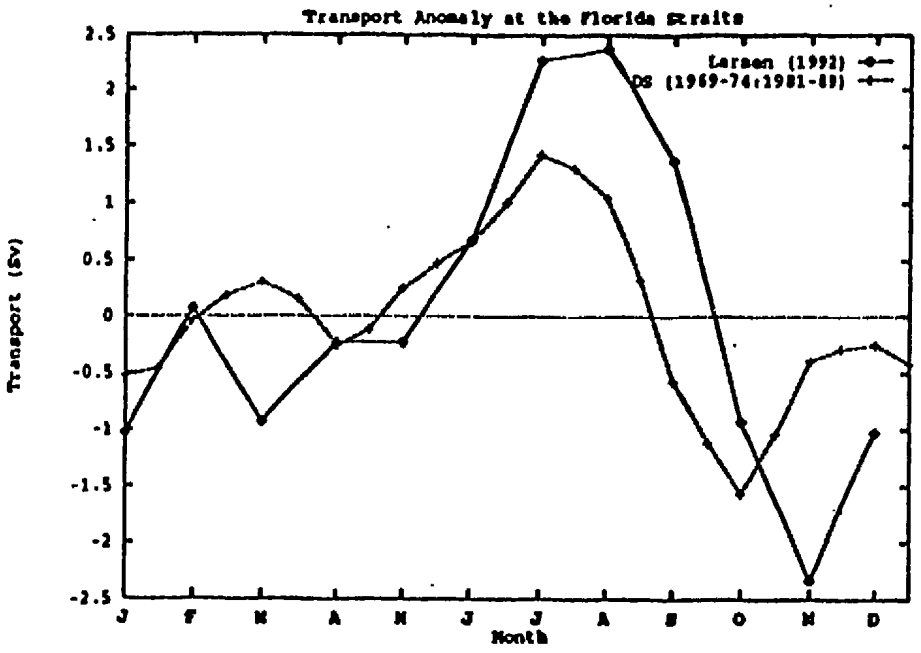

Figure 8.1: *A comparison between the DS ($1^\circ \times 1^\circ$) case and Larsen's cable data, but when the data used to compile the wind stress climatology is taken only from those months for which there is cable data.*

the discrepancy is saying that linear, barotropic dynamics is not enough to explain the observed seasonal variation of transport through the Straits ? Certainly, the wide range in the amplitude of our model response, which is dependent only on the wind stress climatology used to drive the model, suggests that obtaining agreement between a model and observations is not enough in itself to determine the essential dynamics responsible for the observations. Rather, intercomparisons between experiments using models of differing complexity are required, e.g. the intercomparison we have made between our linear, barotropic

model and the WOCE-CME. Indeed, it seems likely that much is to be gained by explaining the discrepancies between results obtained using models based on different dynamics.

In addition to the barotropic results previously discussed, we have also run cases with a linear, two-density layer model at $1^{\circ} \times 1^{\circ}$ resolution, similar to that of Anderson and Corry(1985b). The results do not differ greatly from those of the barotropic model. When the JEBAR (Joint Effect of Baroclinicity And Relief) forced transport is also considered the amplitude of the model-calculated response changes slightly in each case, with ranges of $6.1Sv$, $5.8Sv$, $3.9Sv$ and $3.3Sv$ for each of IH, TR, HR and DS, respectively. The range in the DS and HR cases come into closer agreement with the cable data, but still much lower than the other climatologies.

Experiments using a $1/3^{\circ} \times 1/3^{\circ}$ version of the model applied to the region bounded by 5^0N, to 42^0N, and 100^0W to 70^0W generally confirms our earlier analysis that wind forcing exterior to the Florida Straits is important for our model results. When the eastern boundary is closed, the model-calculated ranges between Grand Bahama Island and the coast are; 0.6 Sv, 2.0 Sv, 1.4 Sv and 0.6 Sv for each of DS, HR, IH, and TR. When flow through the eastern boundary is specified from our $1^{\circ} \times 1^{\circ}$ resolution model results, the model-calculated ranges between Grand Bahama Island and the coast are; 1.3 Sv, 2.8 Sv, 3.1 Sv and 3.0 Sv for each of DS, HR, IH, and TR. Again, these results are inconsistent with Böning et al.(1991b) who concluded, using the Kiel version of the WOCE-CME, that wind forcing north of 35^0N played little role in their results.

The details of the model-calculated amplitude in the $1/3^{\circ} \times 1/3^{\circ}$ resolution results are particularily sensitive to the precise choice of which grid point is used to represent the

Florida Straits. If we choose the Grand Bahama Islands, the cases with transport specified on the eastern boundary yield ranges of $1.3Sv$, $2.8Sv$, $3.0Sv$ and $3.1Sv$ for each of DS, HR, TR, and III respectively. If instead, we choose a region between the Grand Bahama Island, and Andros Island (the Providence Channel area) the $1/3^o \times 1/3^o$ model-calculated results agree quite well with our $1^o \times 1^o$ results. This would appear to be a consequence of the fact that even at $1/3^o \times 1/3^o$ resolution, we still do not properly resolve the Florida Straits. The $1/3^o \times 1/3^o$ resolution Florida Straits essentially do not receive as much information along f/H contours as in the 1^0 x 1^0 case, or as the grid-point in the vicinity of the Providence Channel because, as a result of smoothing the topography, the model Straits are too shallow in the 1^0 x 1^0 case. Future work will have to address the problem of using high resolution, smoothed topography, while maintaining a realistic depth for the Florida Straits.

The general agreement between the barotropic and two-density layer model, and their failure to reproduce some, but not all of the CME results points to the possible importance of non-linearity and, in particular, advection by the mean flow in determining the observed seasonal transport variations at the Florida Straits. We noted, when discussing this problem in Chapter 6, that advection by the mean flow can carry information in the direction opposite to that of long, topographic wave propagation. Indeed, Greatbatch and Goulding(1992) give an example of this effect in which the important process is advection of the density field (and subsequent forcing of the barotropic flow field via JEBAR - the Joint Effect of Baroclinicity And Relief). It remains to be seen if this process is important in the case of the Florida Straits (and also similar advective effects found in the idealised calculations of Greatbatch and Li, 1990), a topic for future research. Advection is, nonetheless, one

way that information could be carried from the Caribbean to the Straits. Schott and Zantopp (1985) noted that the seasonal variation of the wind stress curl over the Caribbean is similar to that of transport through the Straits, but offer no physical explanation for any connection between the two. Also, Schott et al.(1988) have shown that a frictional model based only on the along-Straits wind stress can reproduce the observed transport variations provided a different dissipation time is used for different time scales of variability (a similar "local" model has been described by Lee and Williams, 1988). This contradicts our finding that remote wind forcing, north of $35^0 N$, plays a role in determining our model-calculated transport variations.

APPENDIX A:

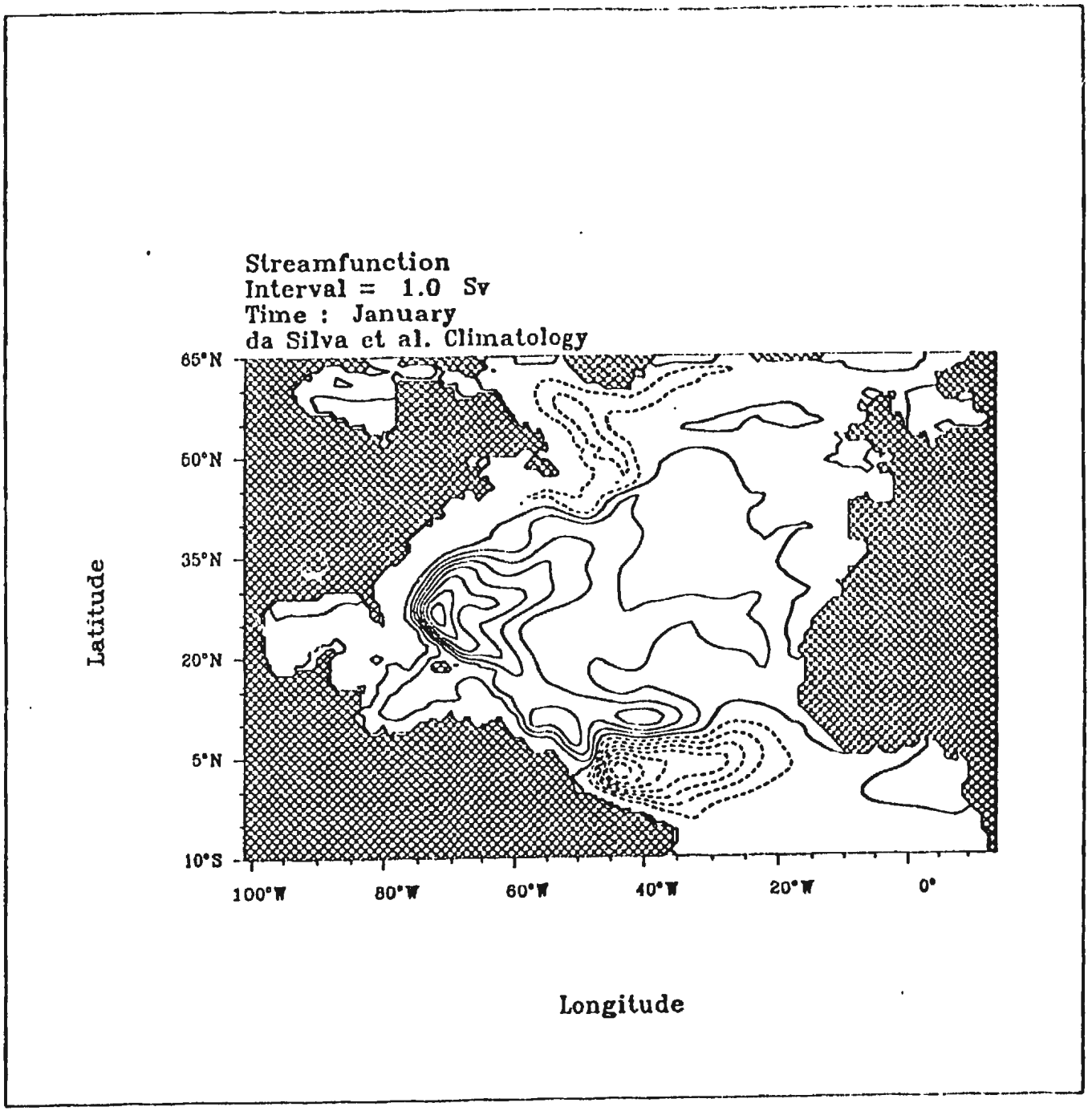

Figure A.1: *Plan views of the anomalous monthly mean transport streamfunction, Ψ, produced by the barotropic model, and corresponding to DS wind forcing. The contour interval is 1.0Sv, dashed contours indicate negative values, solid contours positive values.*

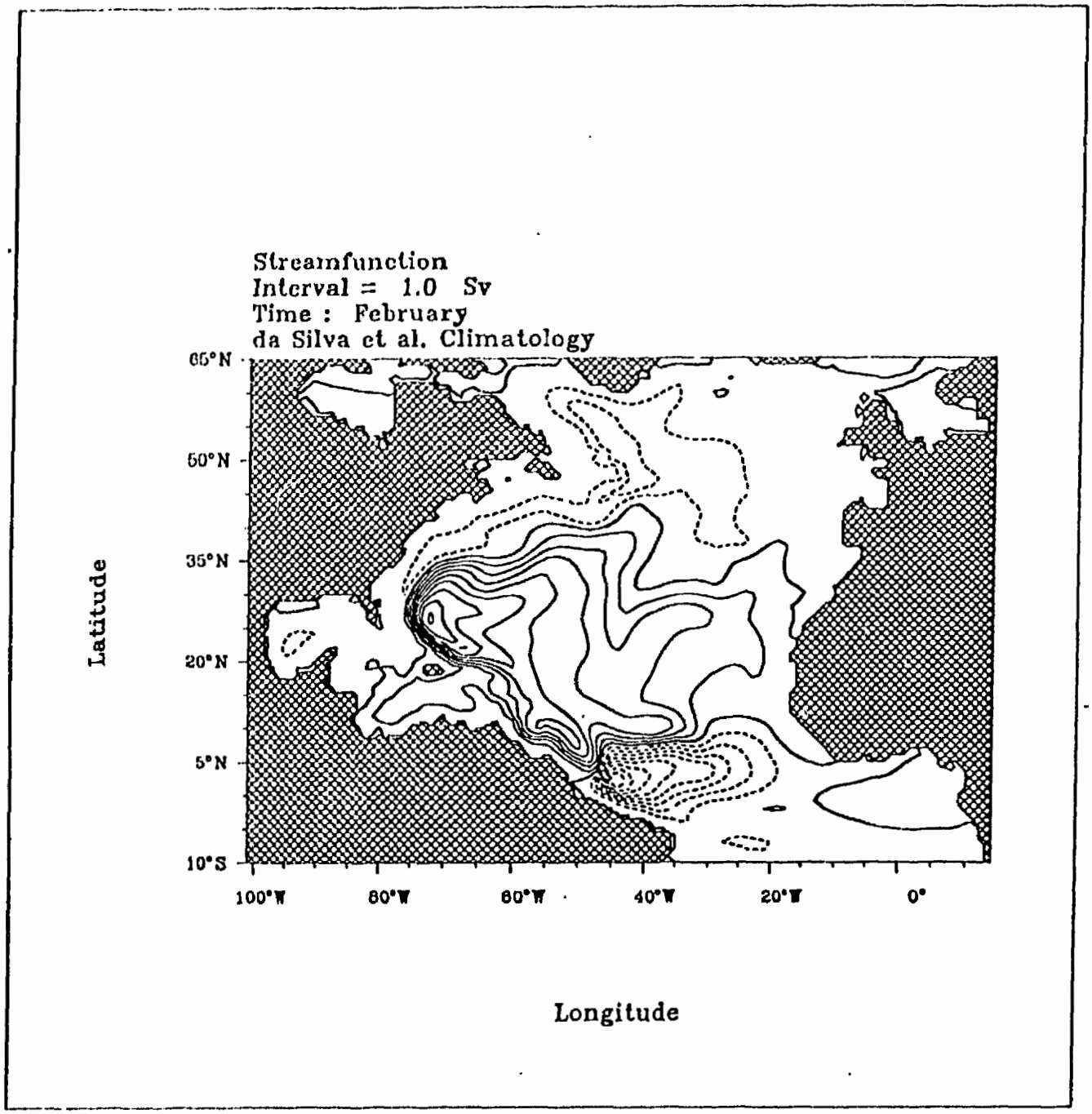

Figure A.1: *continued*

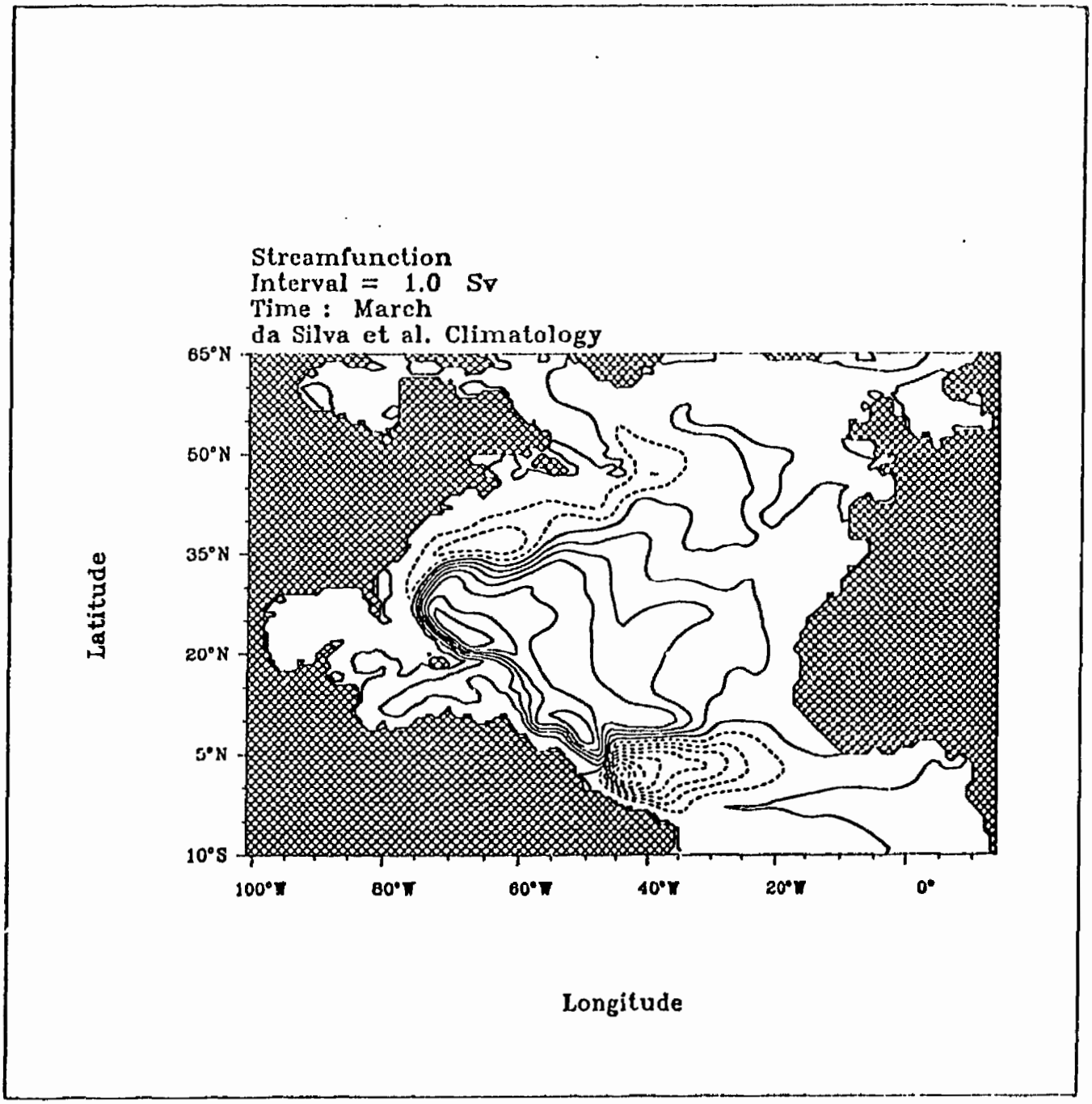

Figure A.1: *continued*

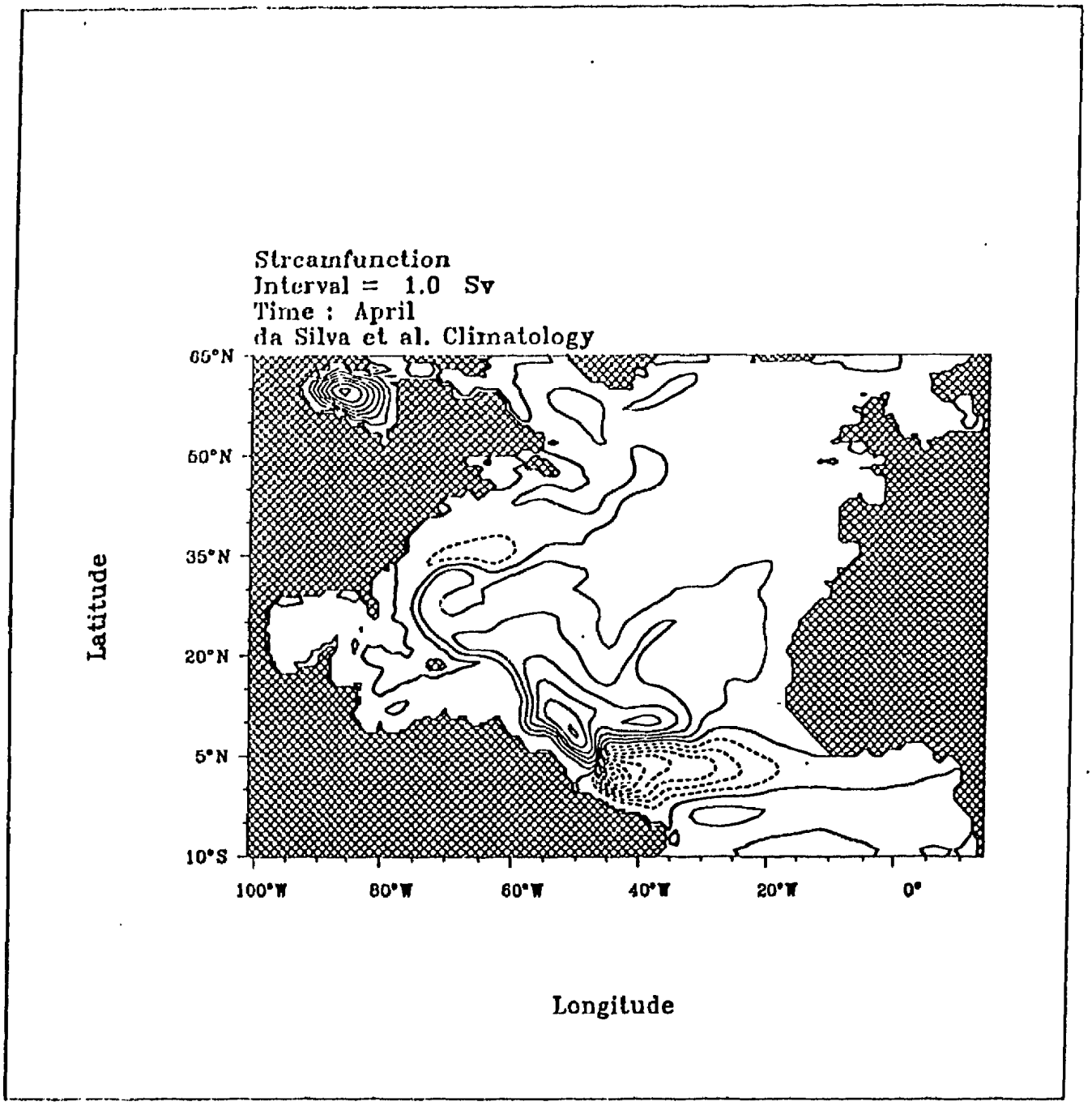

Figure A.1: *continued*

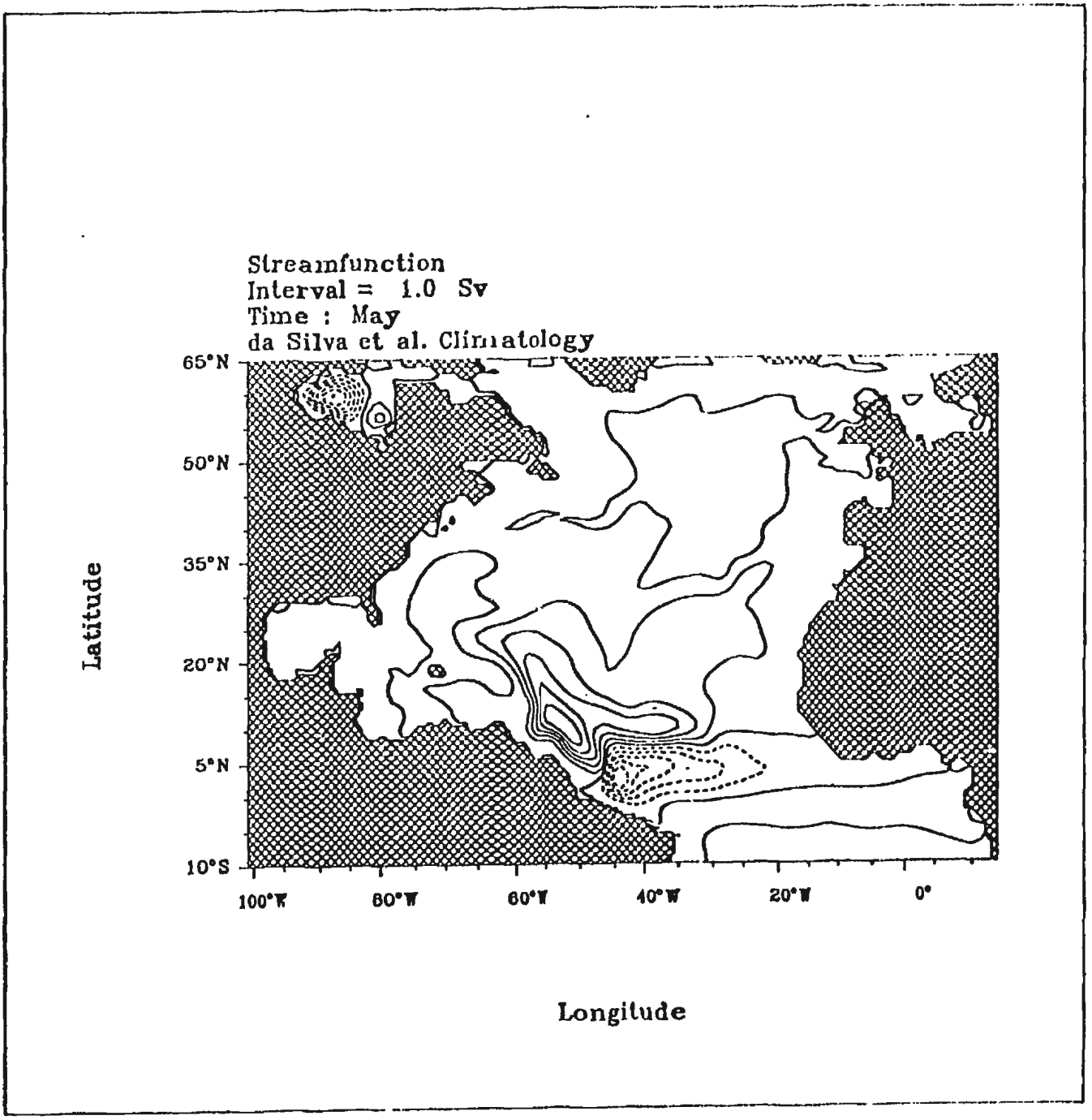

Figure A.1: *continued*

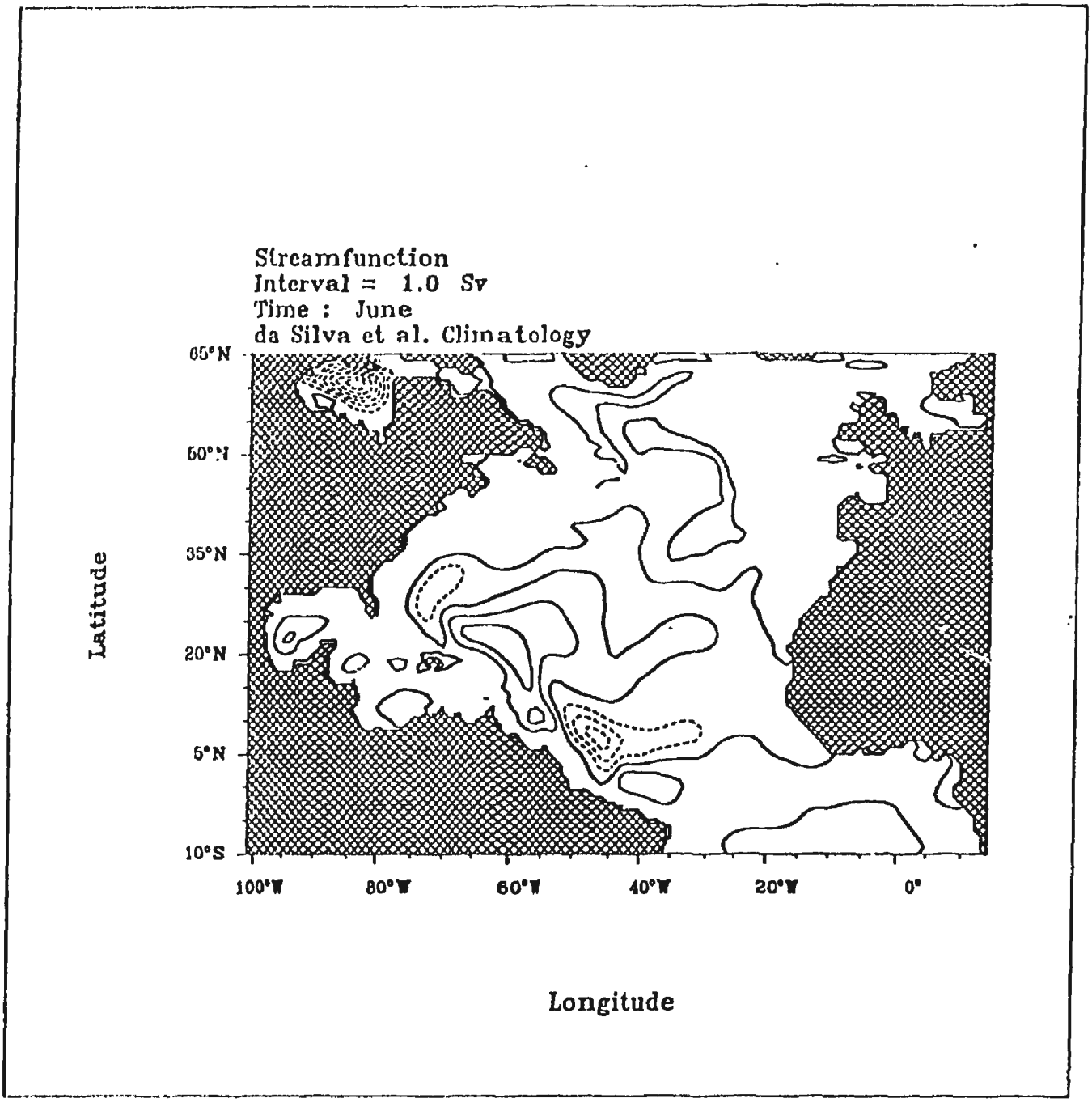

Figure A.1: *continued*

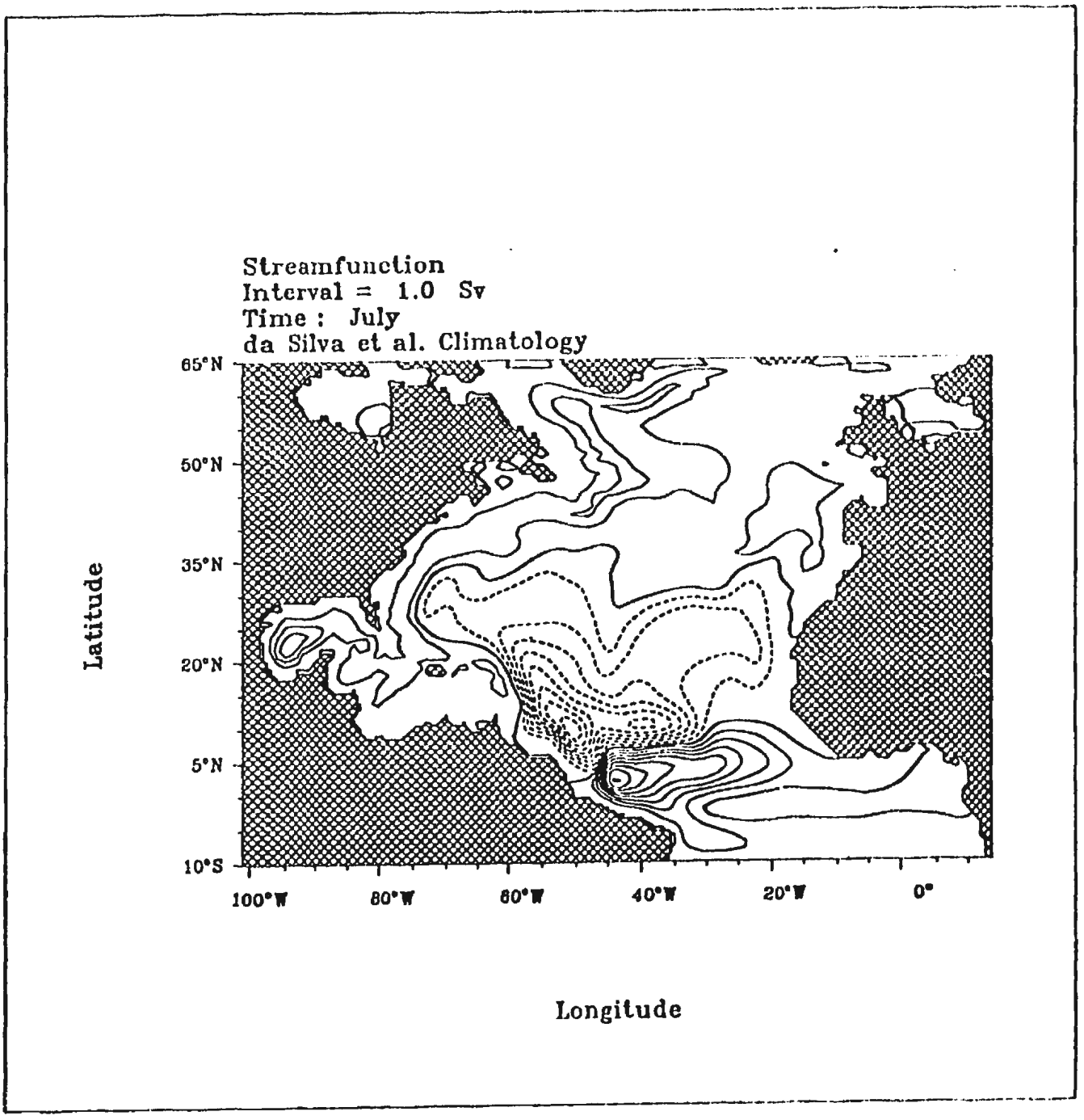

Figure A.1: *continued*

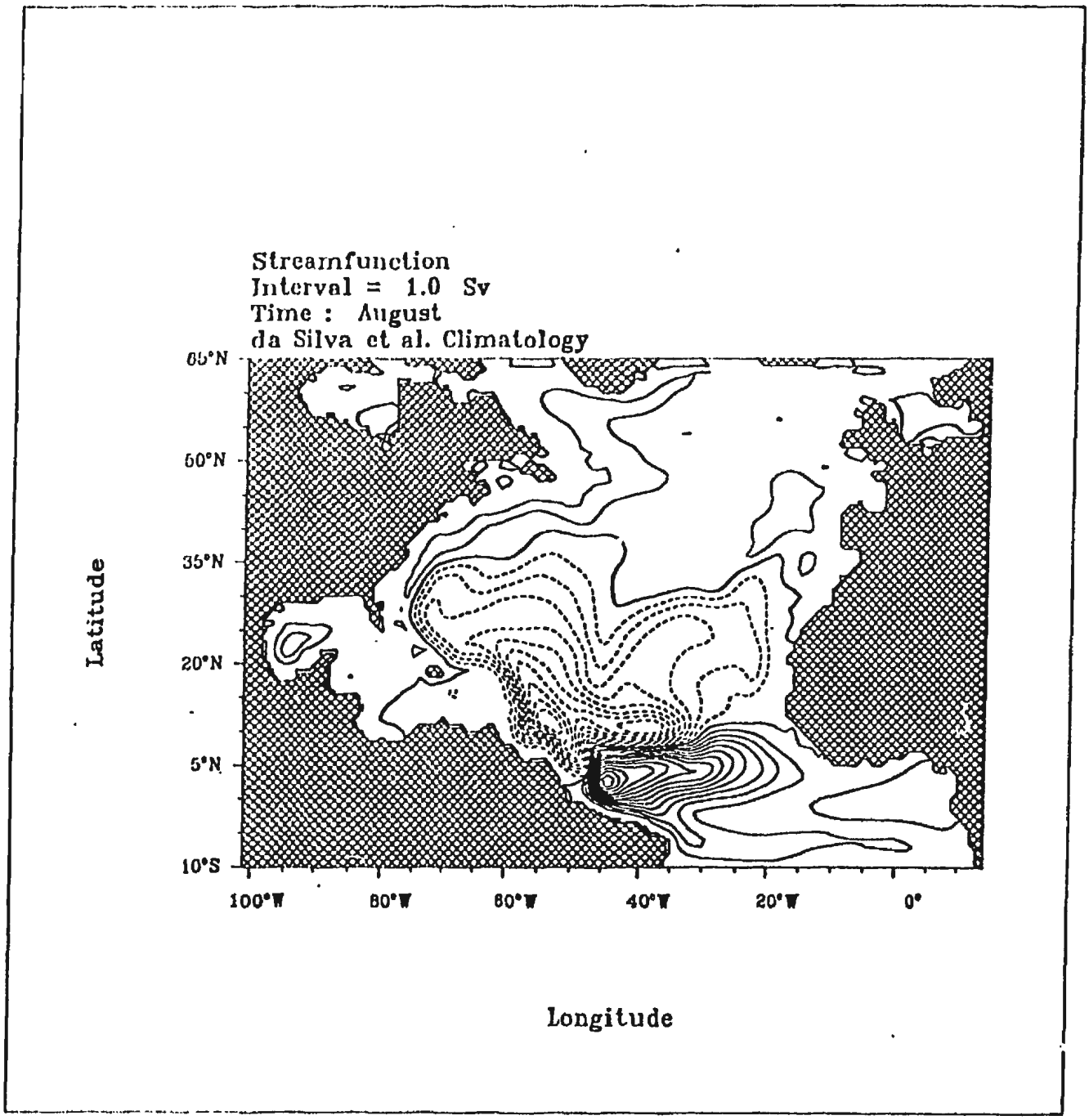

Figure A.1: *continued*

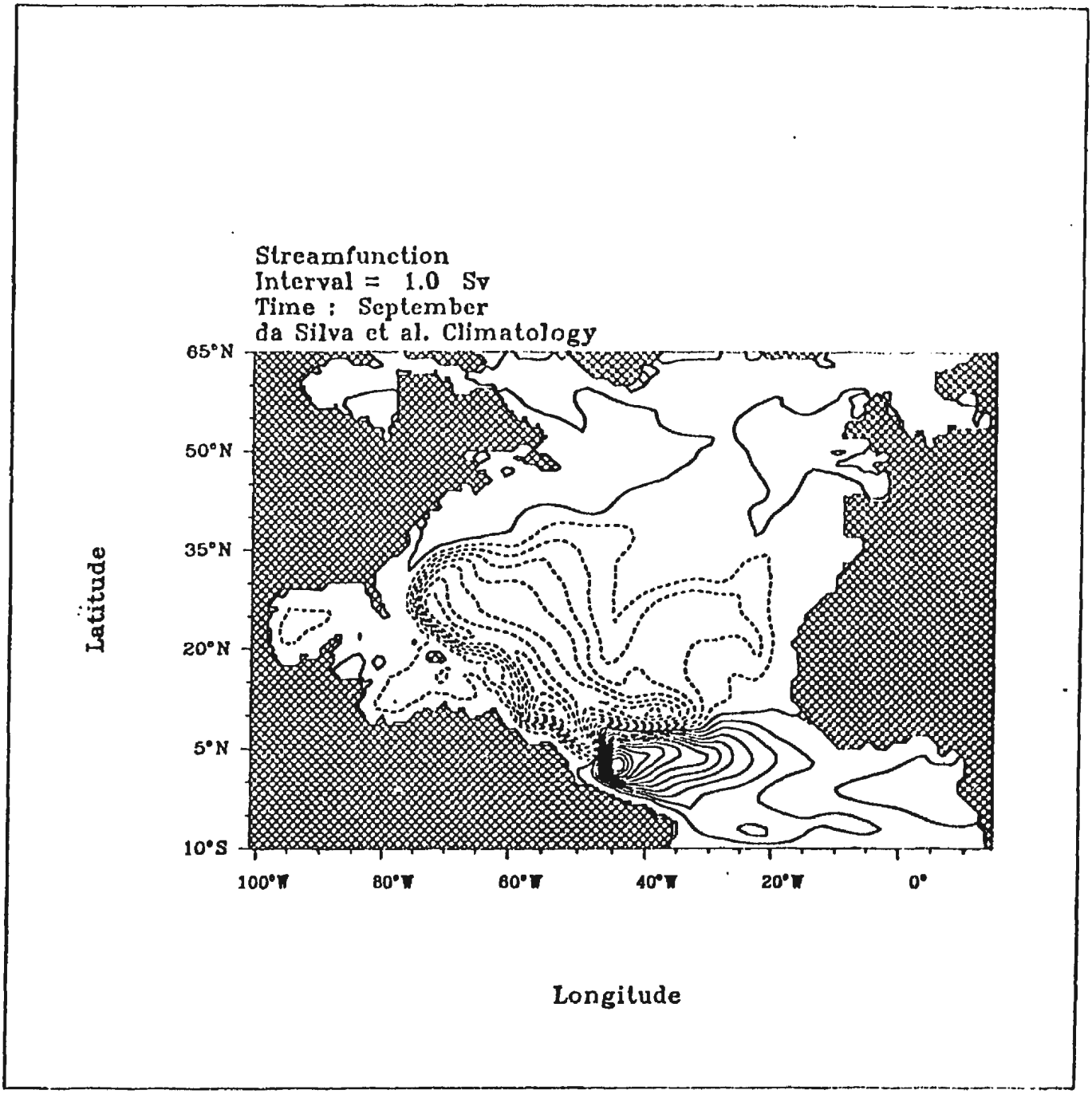

Figure A.1: *continued*

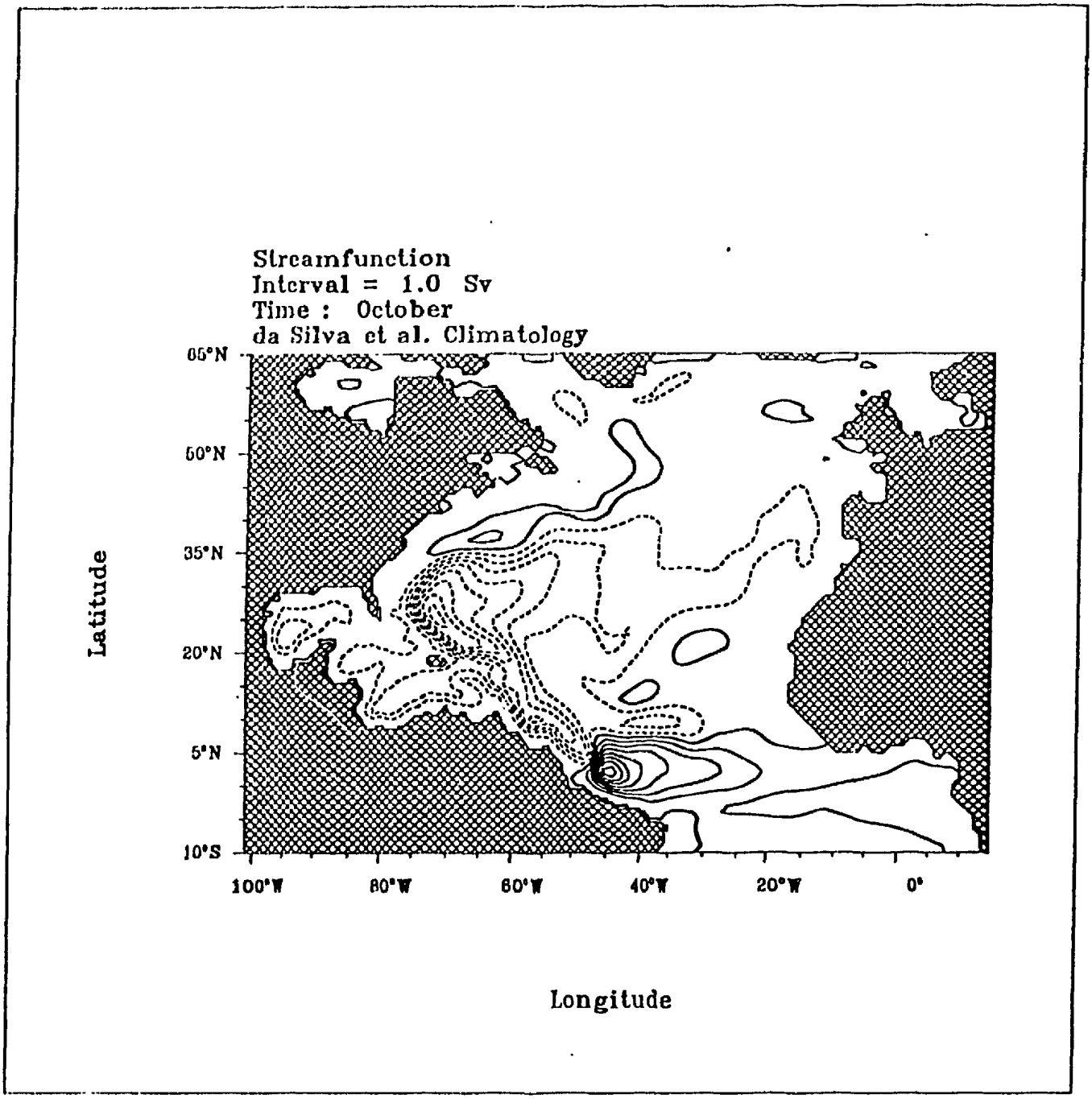

Figure A.1: *continued*

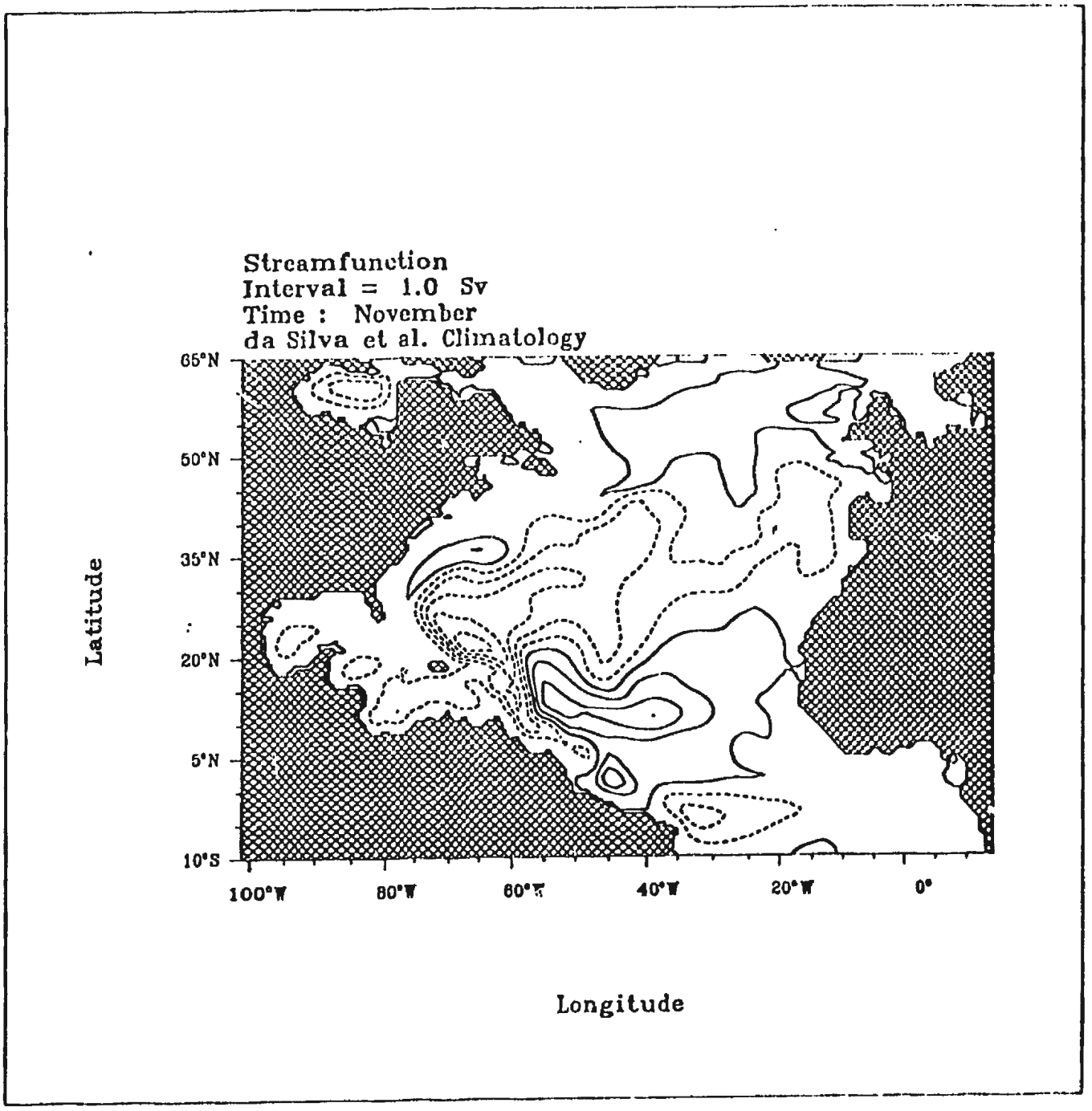

Figure A.1: *continued*

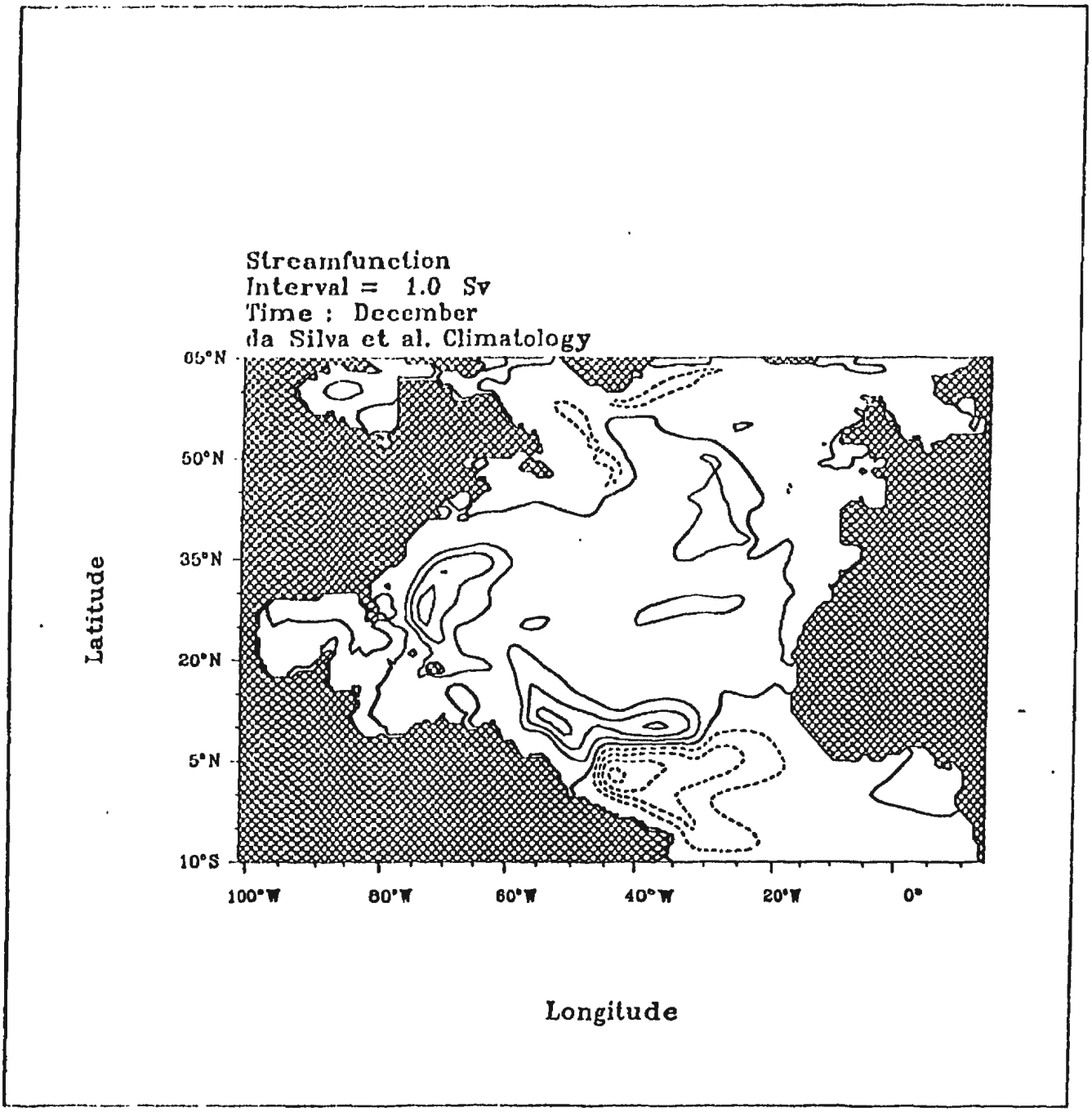

Figure A.1: *continued*

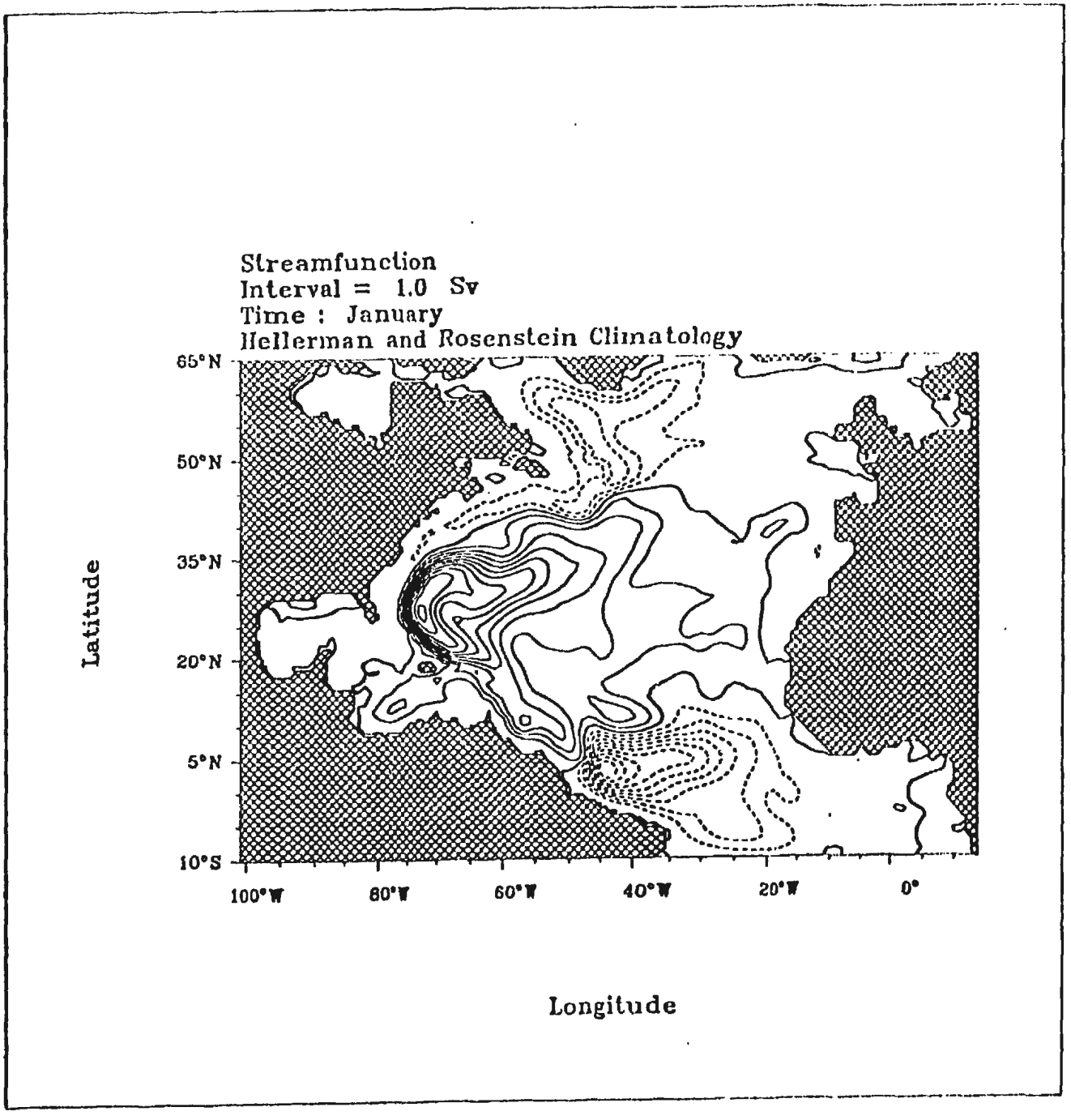

Figure A.2: As Figure A.1, but for HR wind forcing

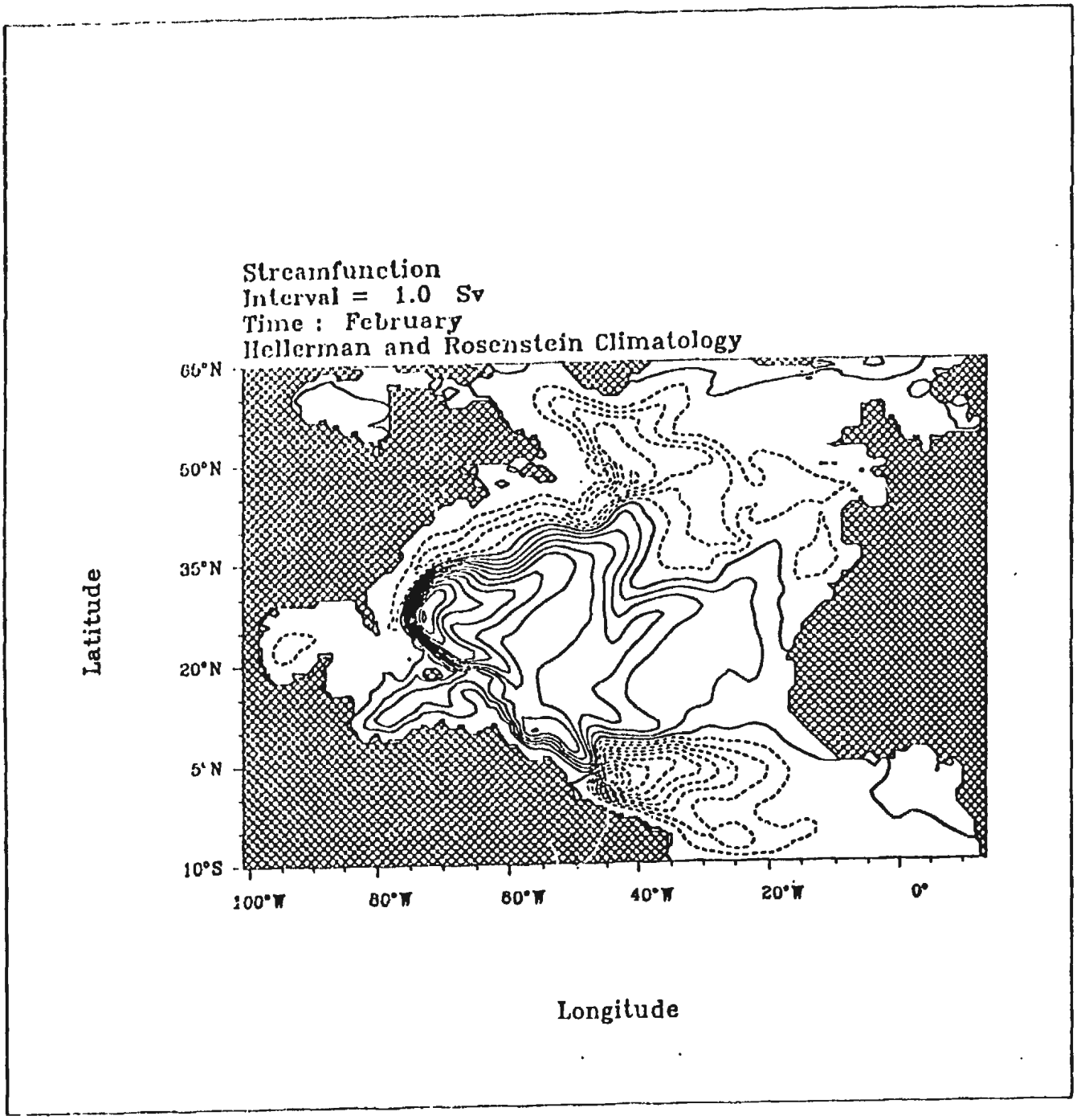

Figure A.2: *continued*

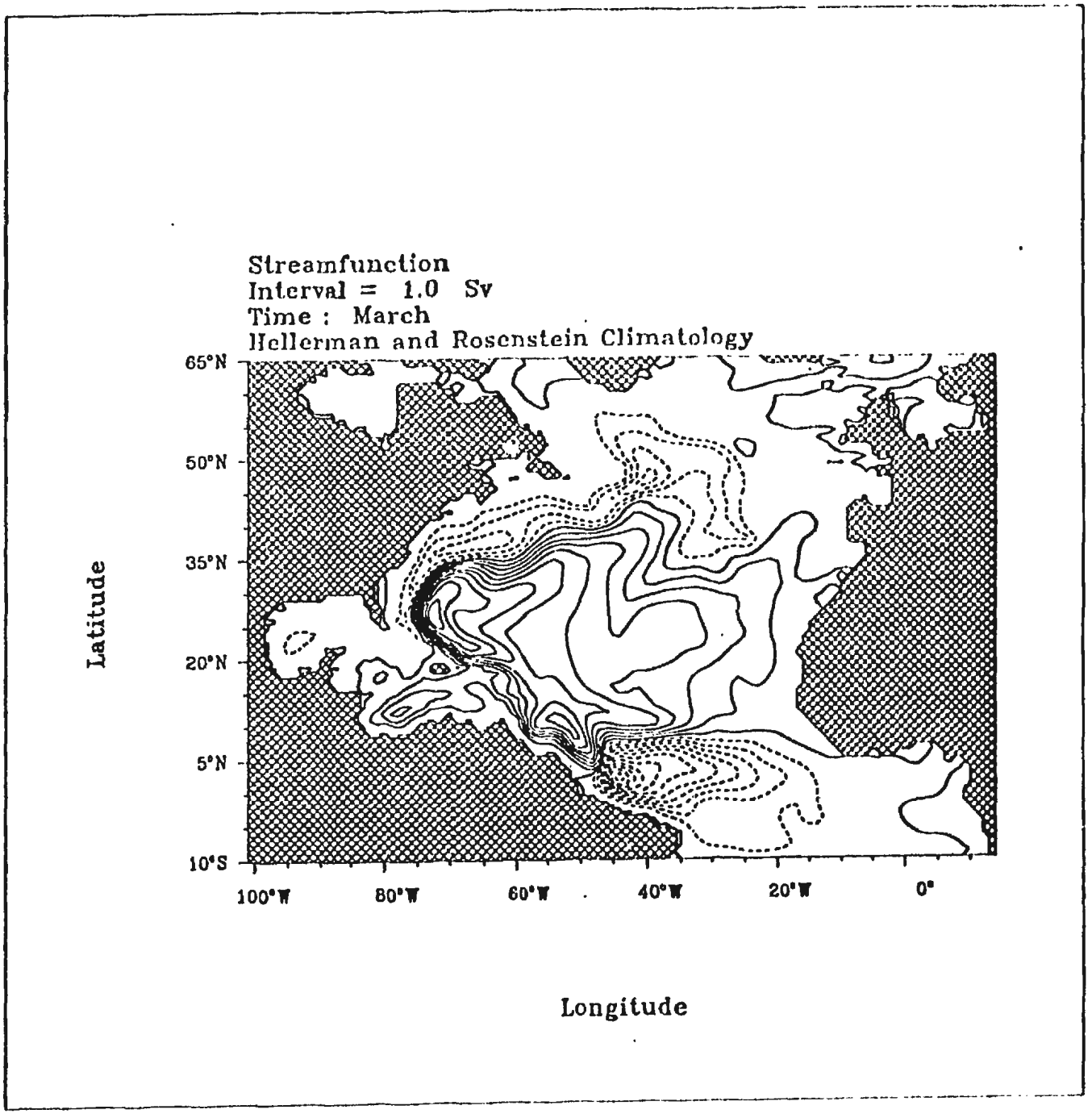

Figure A.2: *continued*

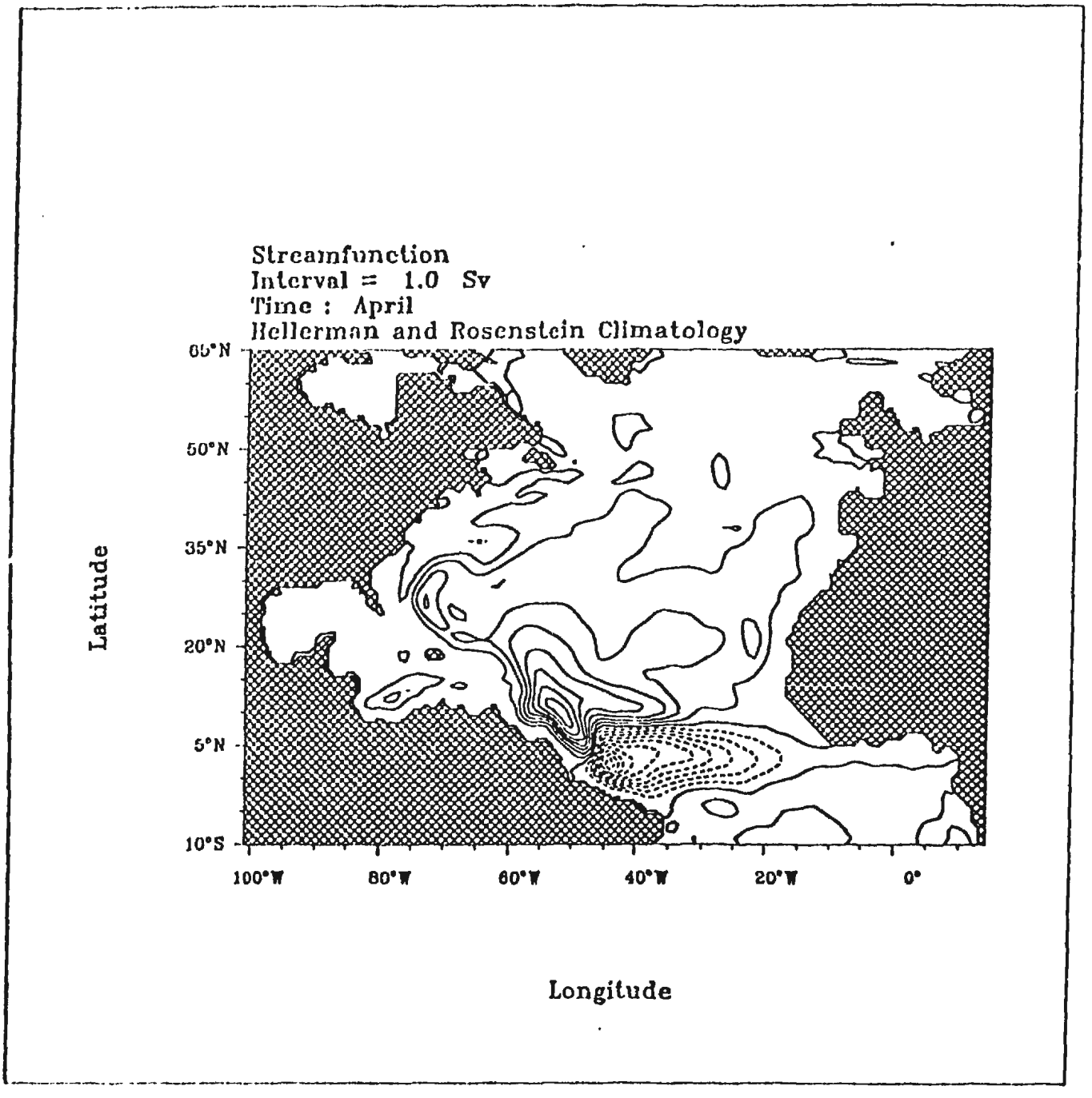

Figure A.2: *continued*

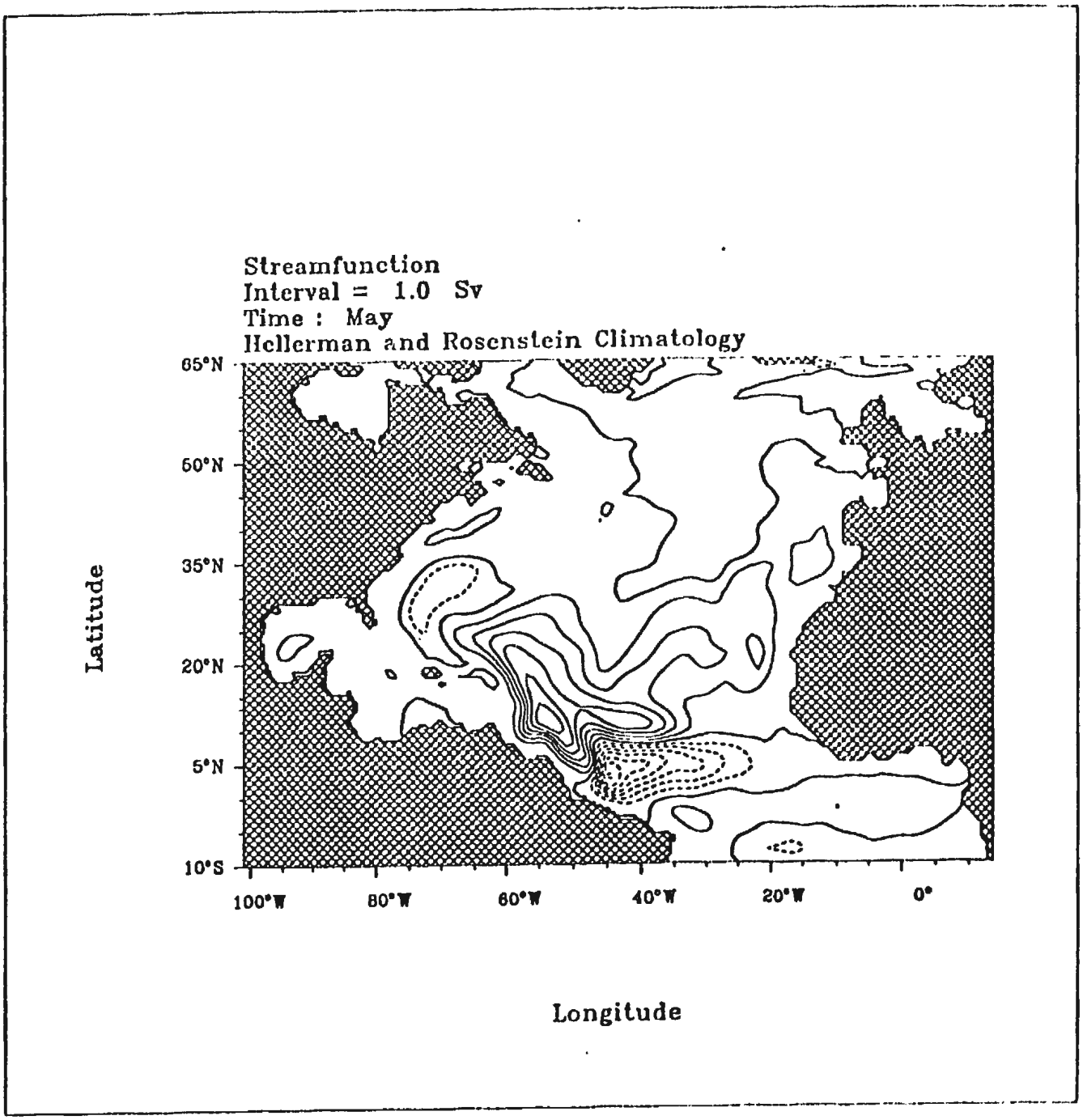

Figure A.2: *continued*

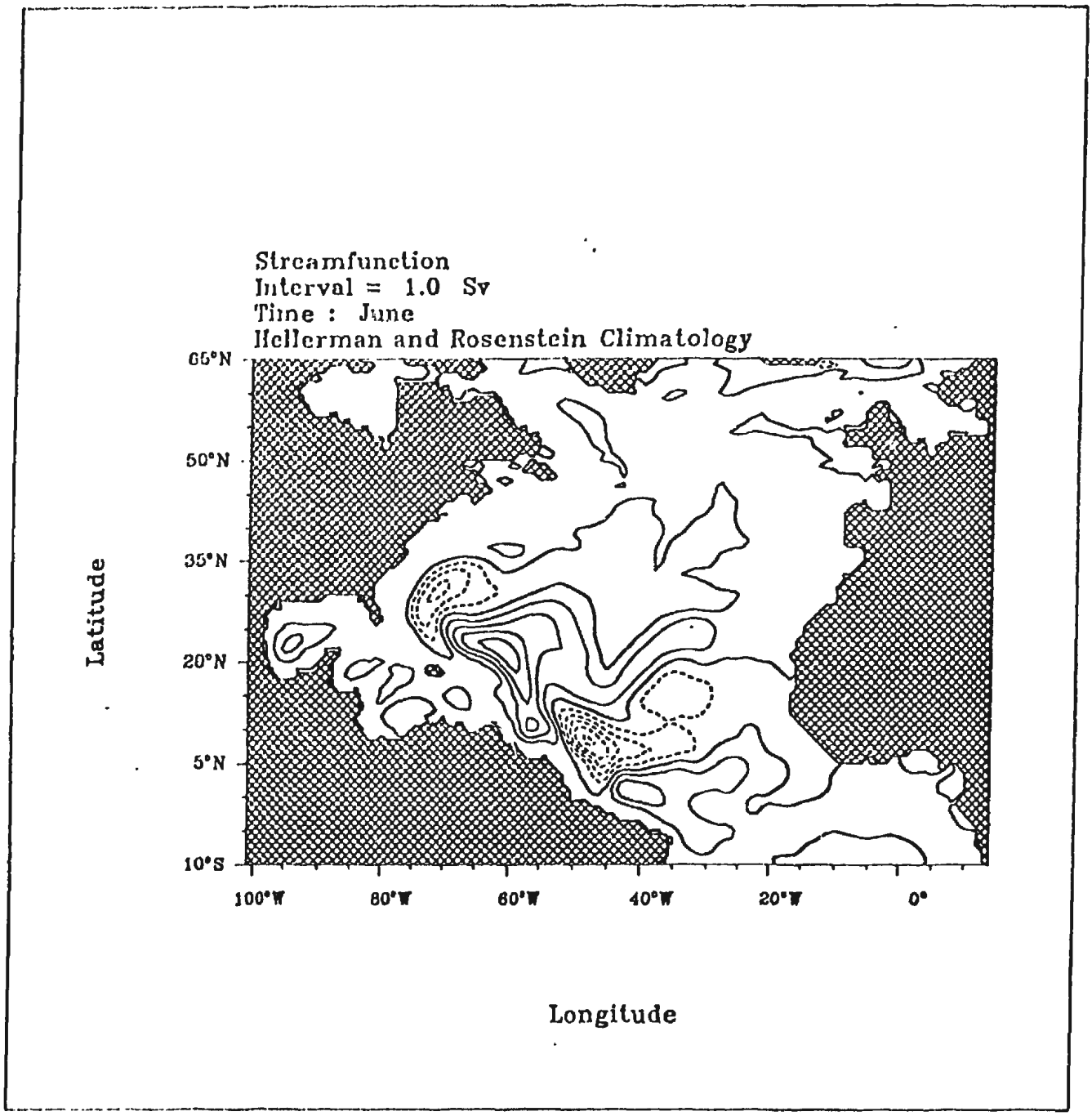

Figure A.2: *continued*

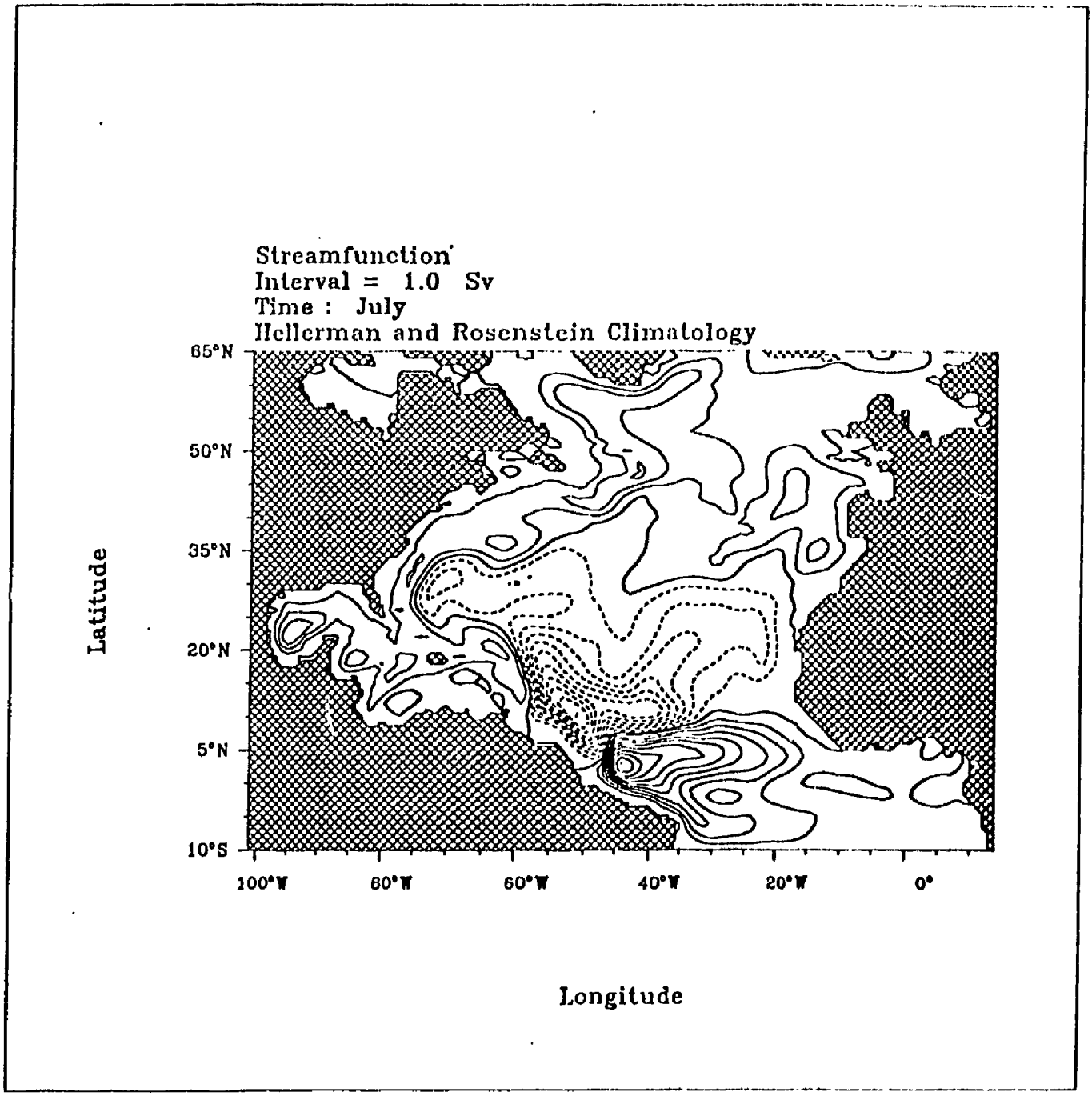

Figure A.2: *continued*

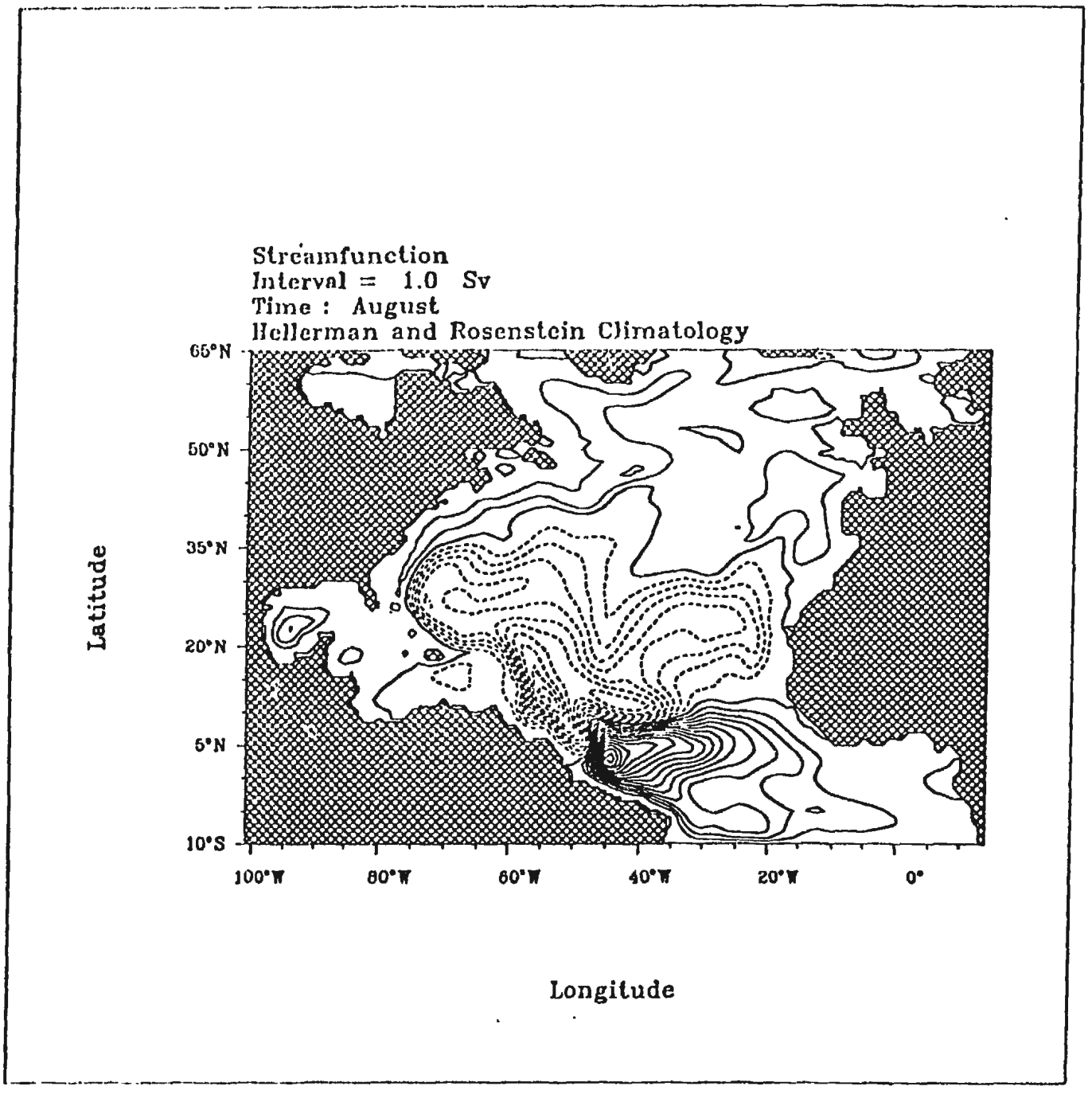

Figure A.2: *continued*

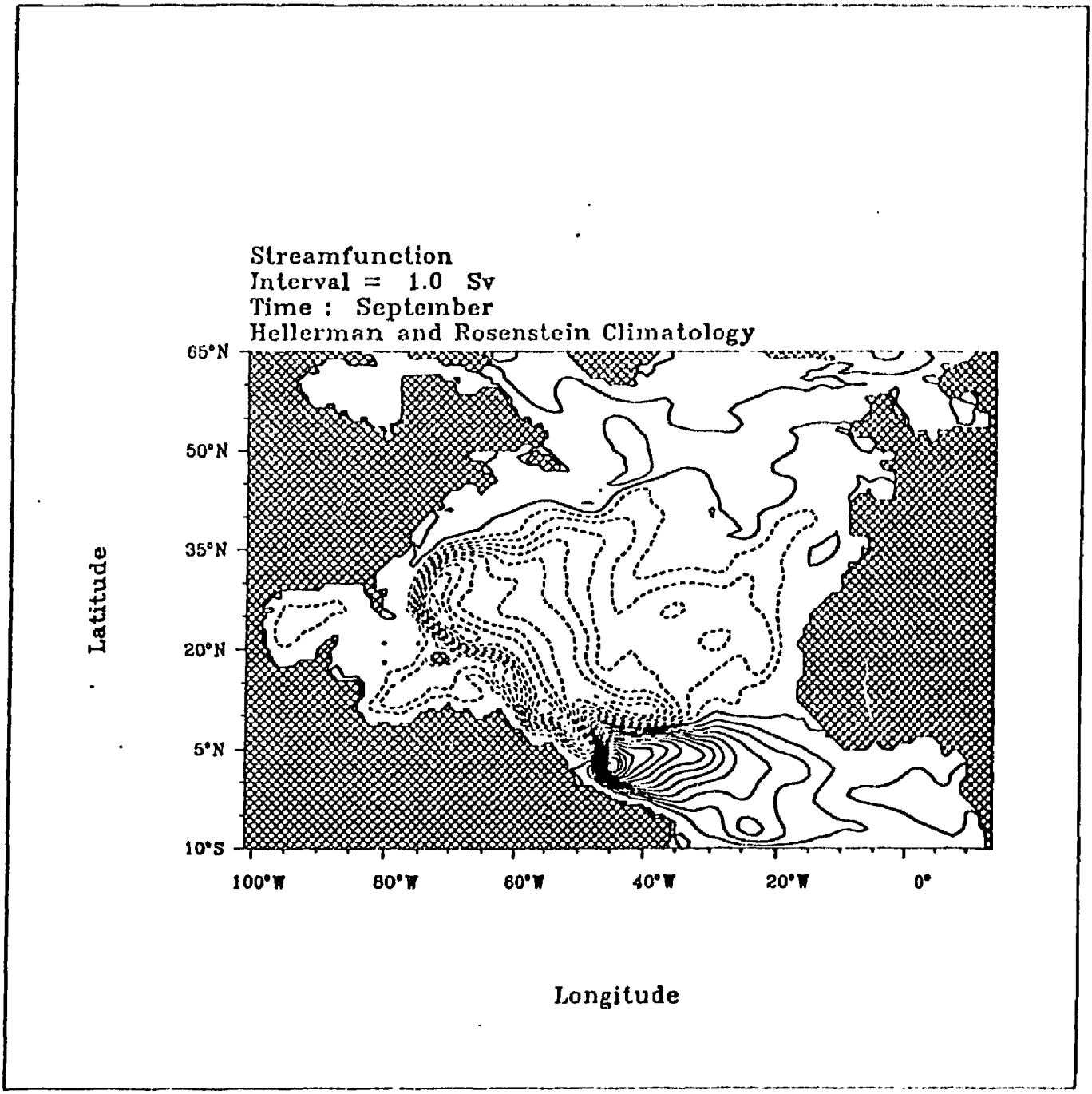

Figure A.2: *continued*

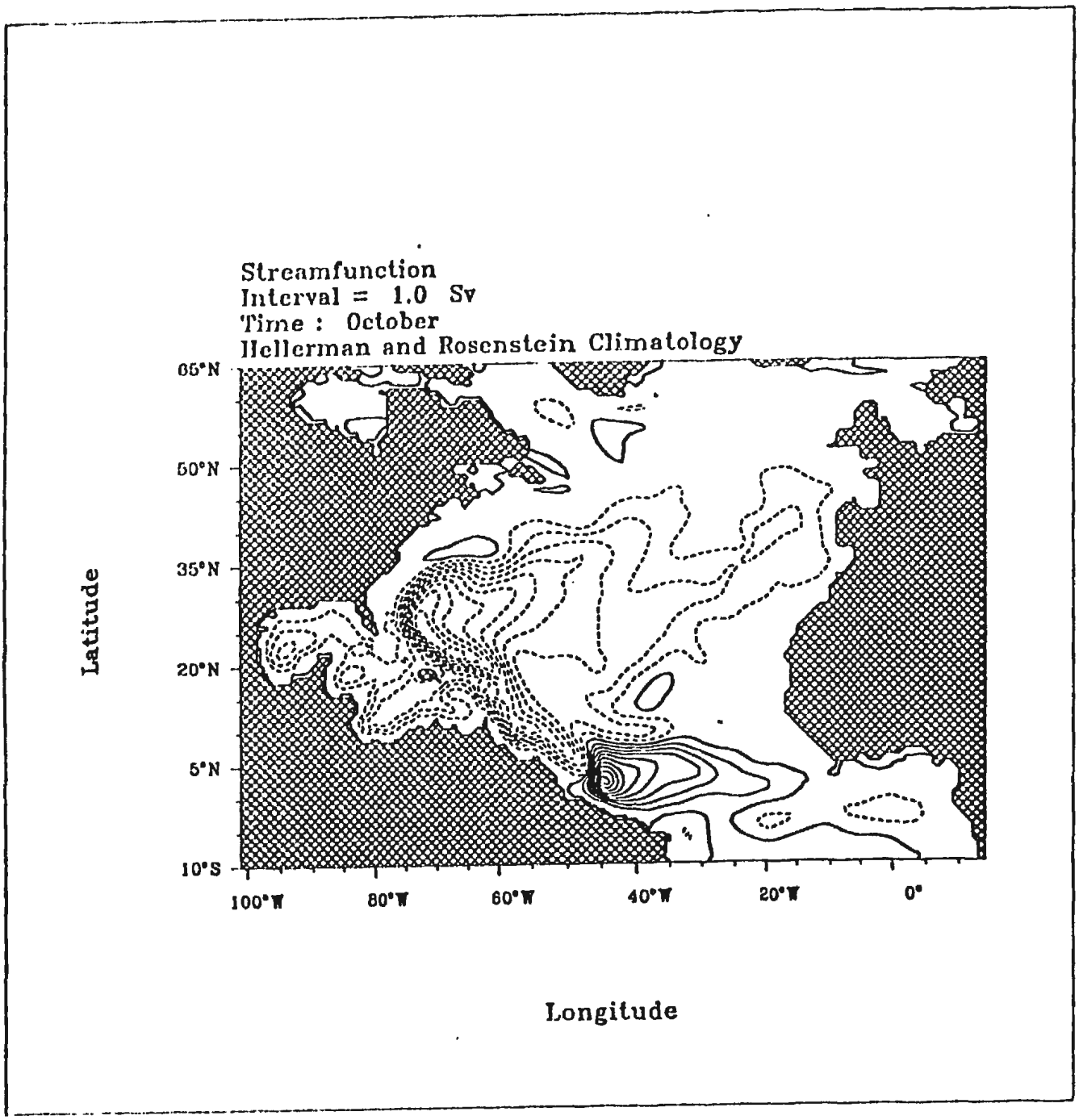

Figure A.2: *continued*

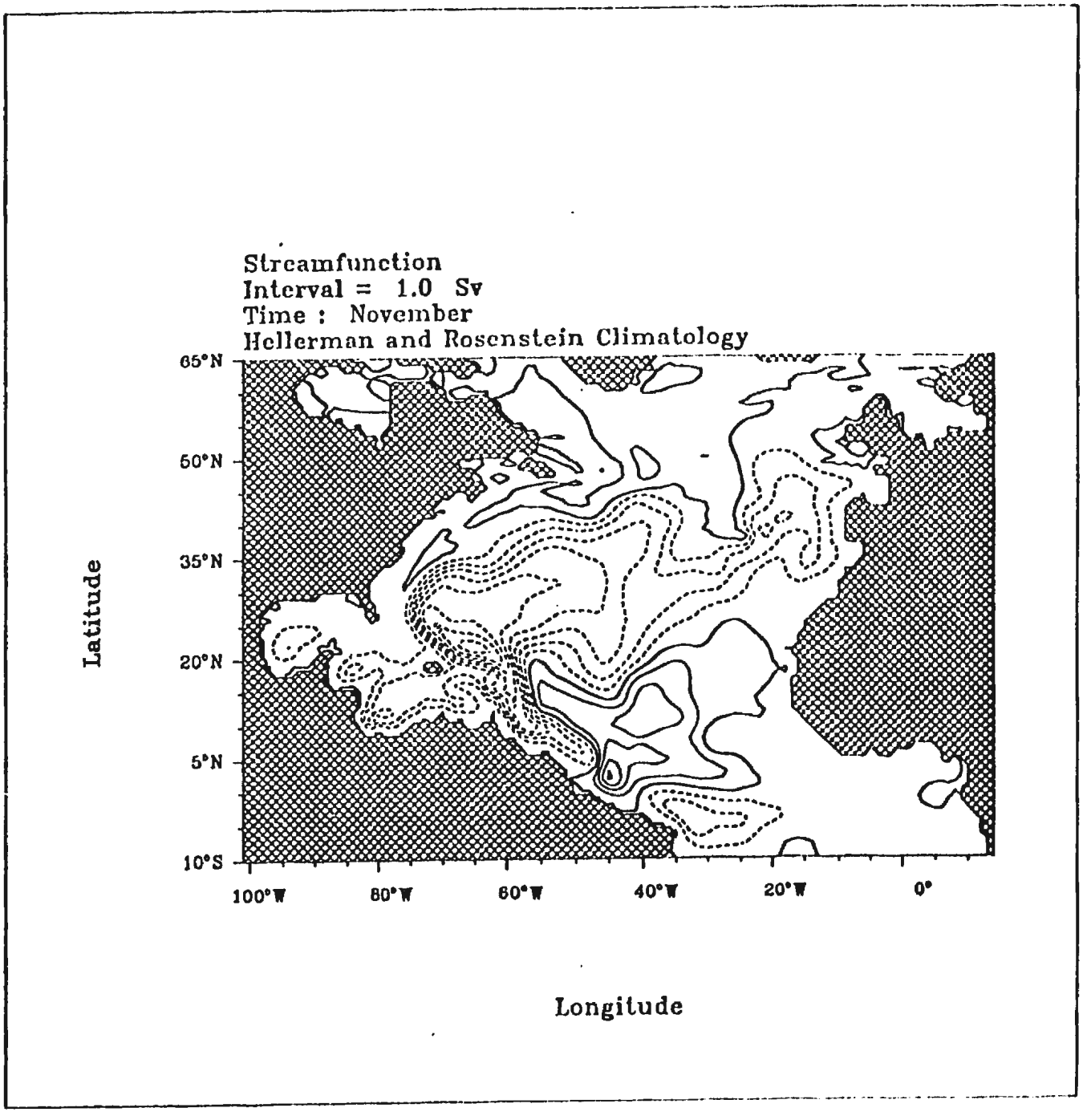

Figure A.2: *continued*

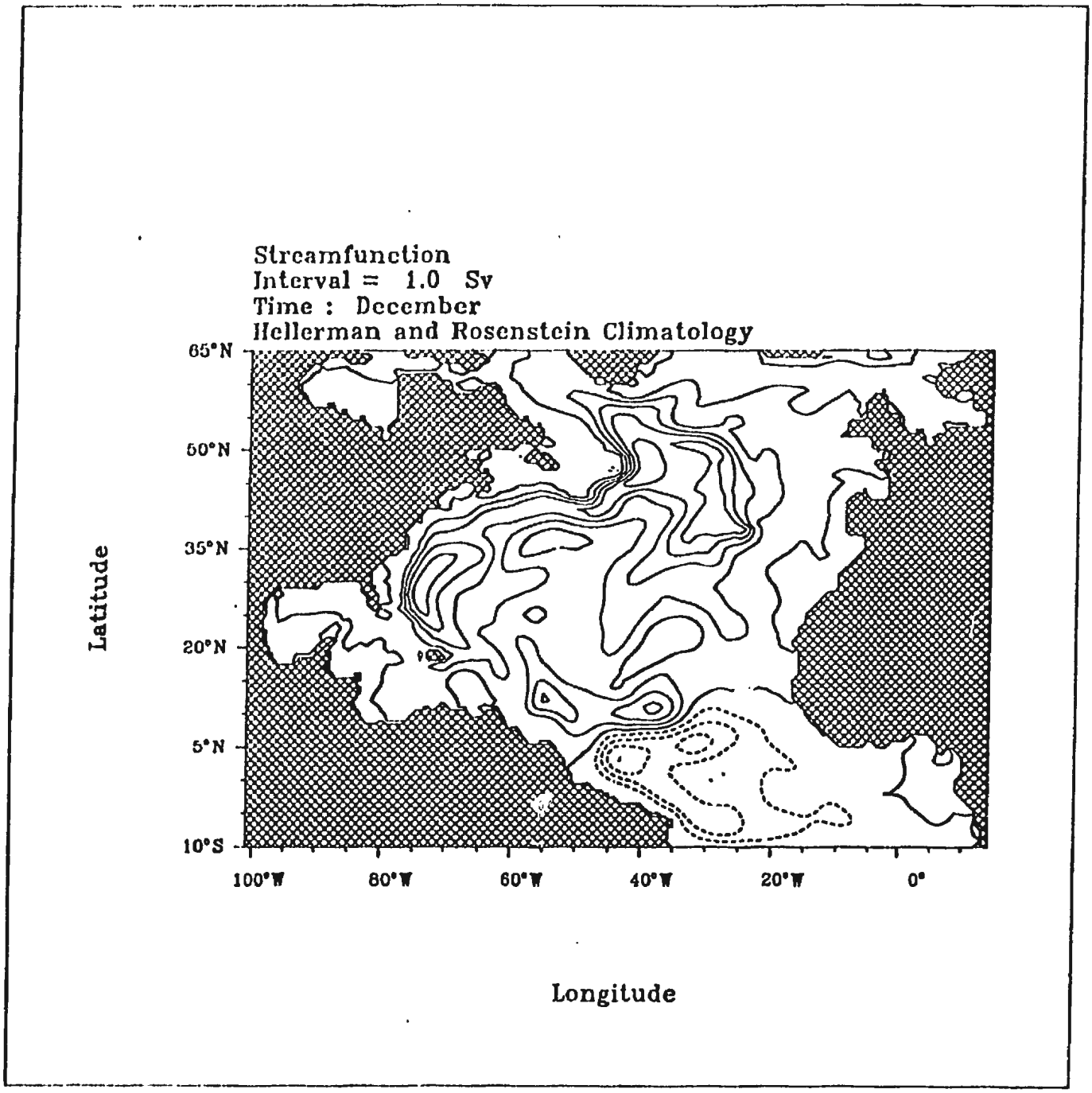

Figure A.2: *continued*

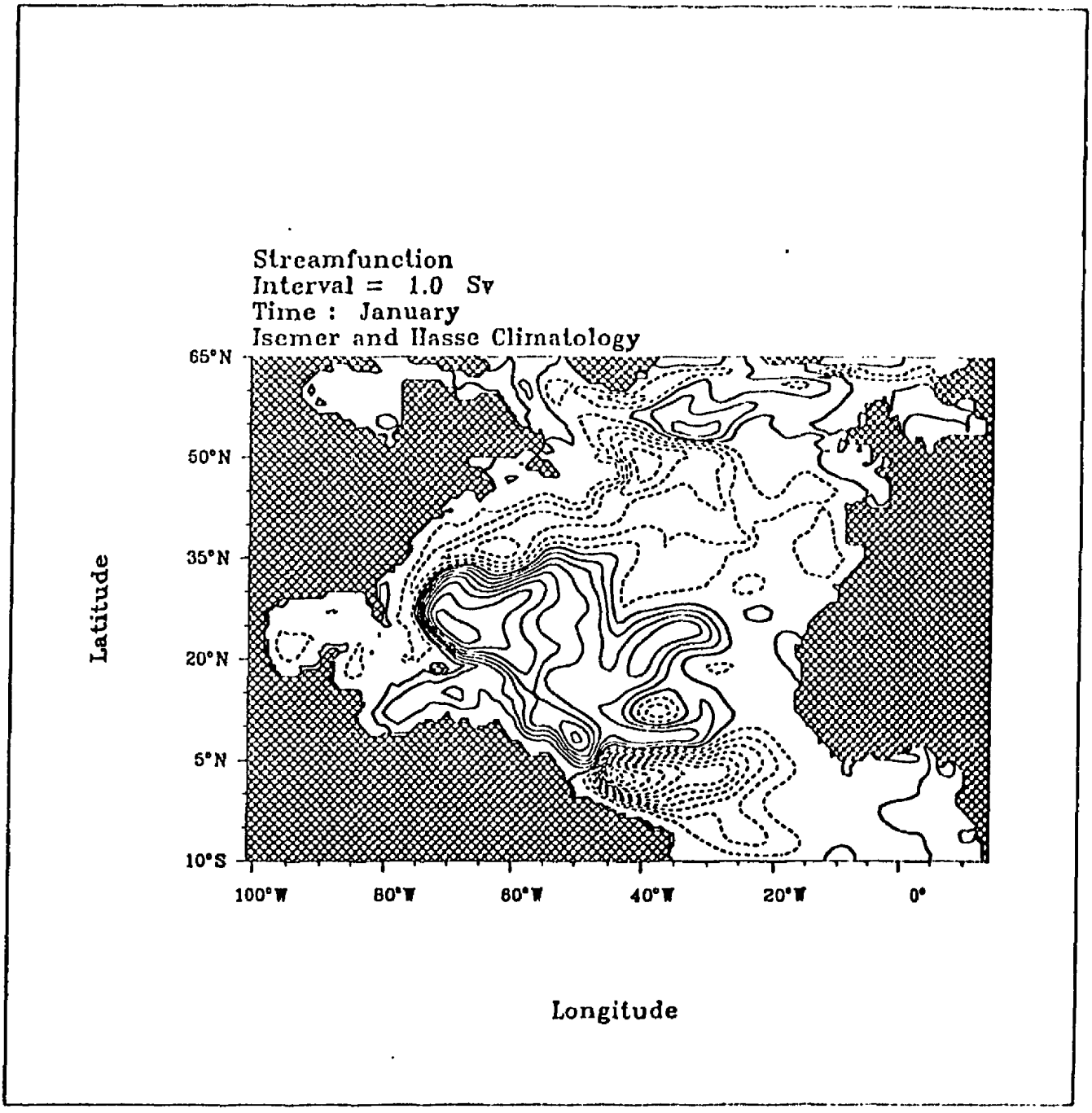

Figure A.3: As Figure A.1, but for III wind forcing

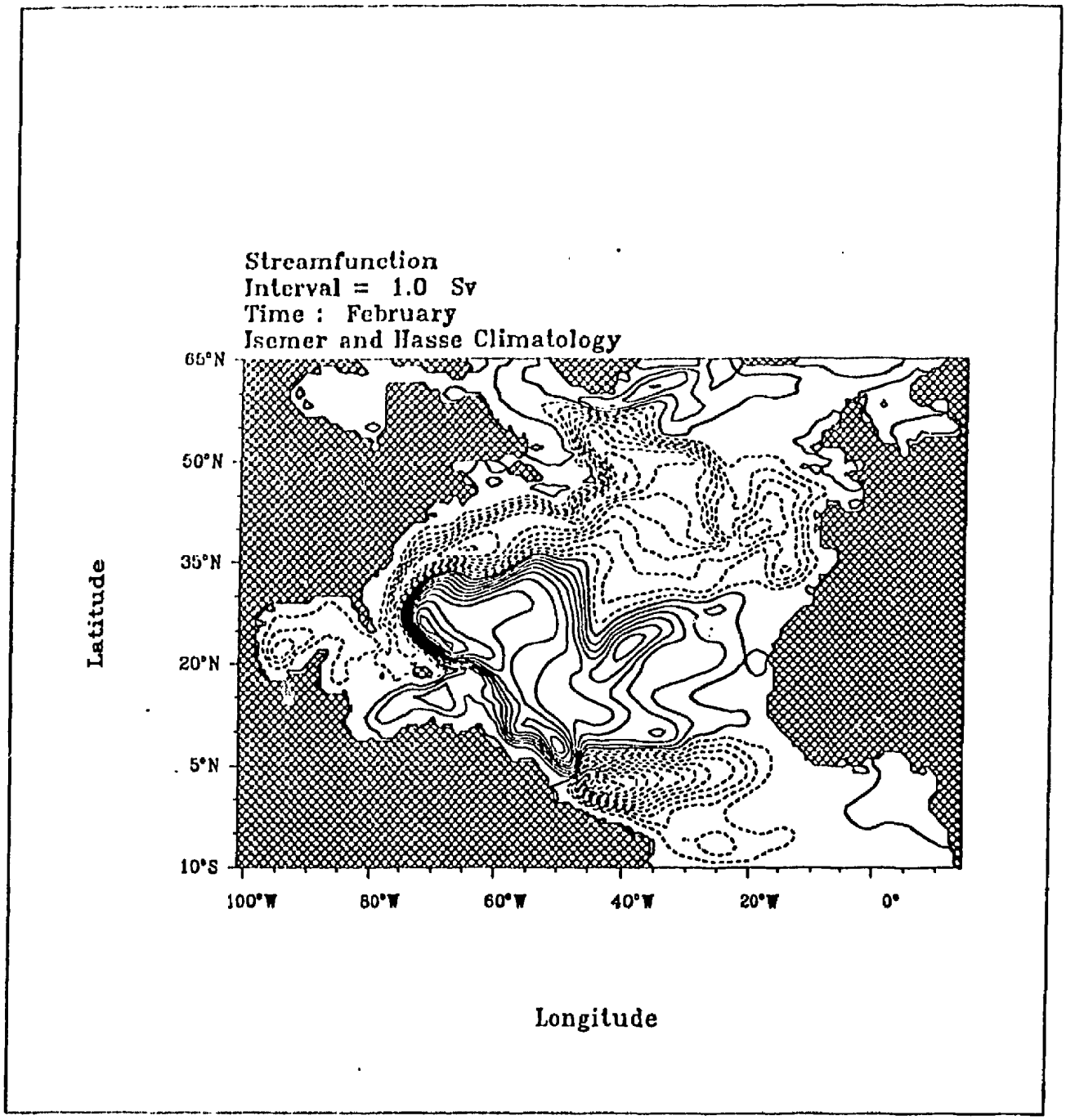

Figure A.3: *continued*

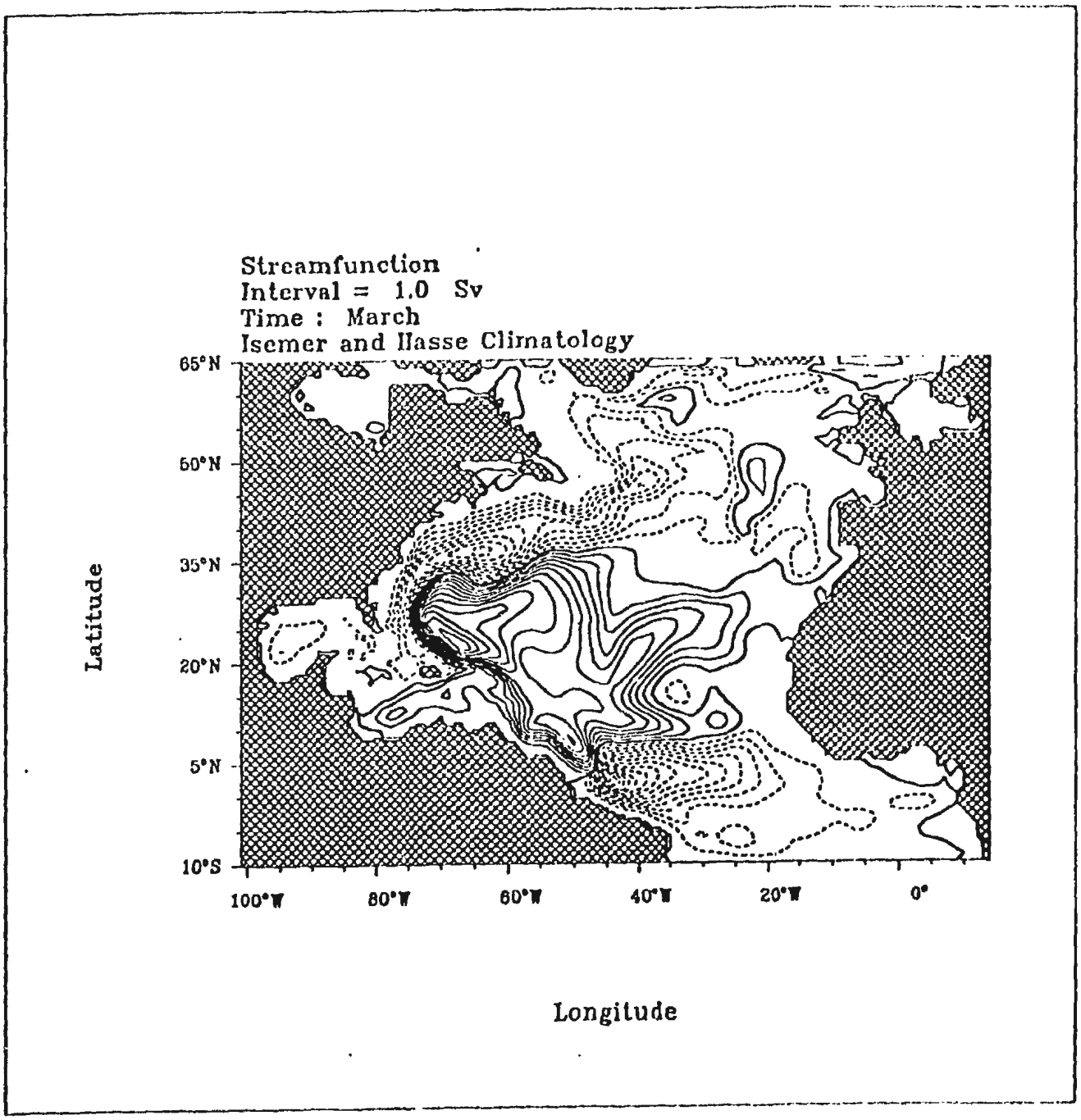

Figure A.3: *continued*

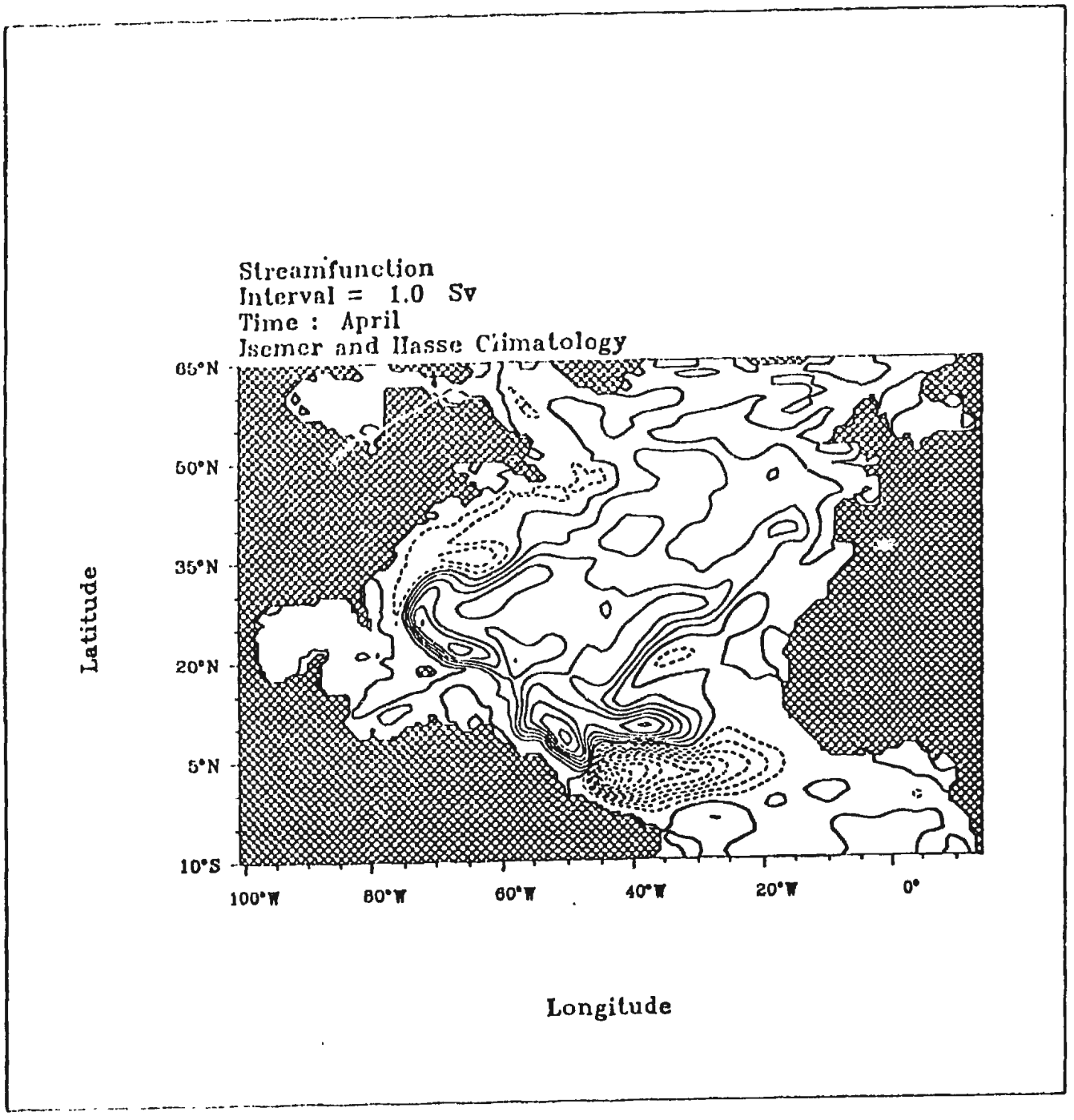

Figure A.3: *continued*

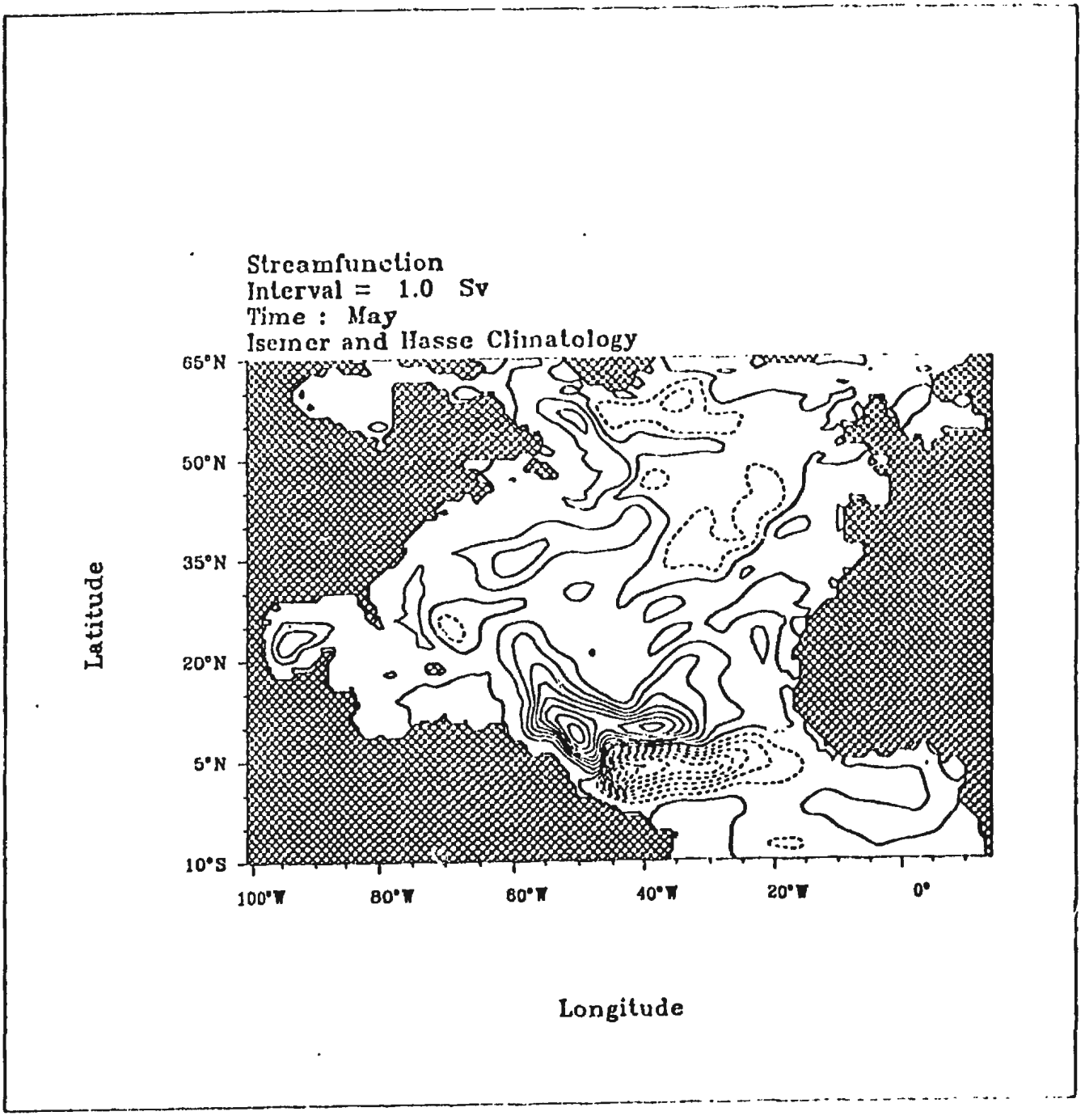

Figure A.3: *continued*

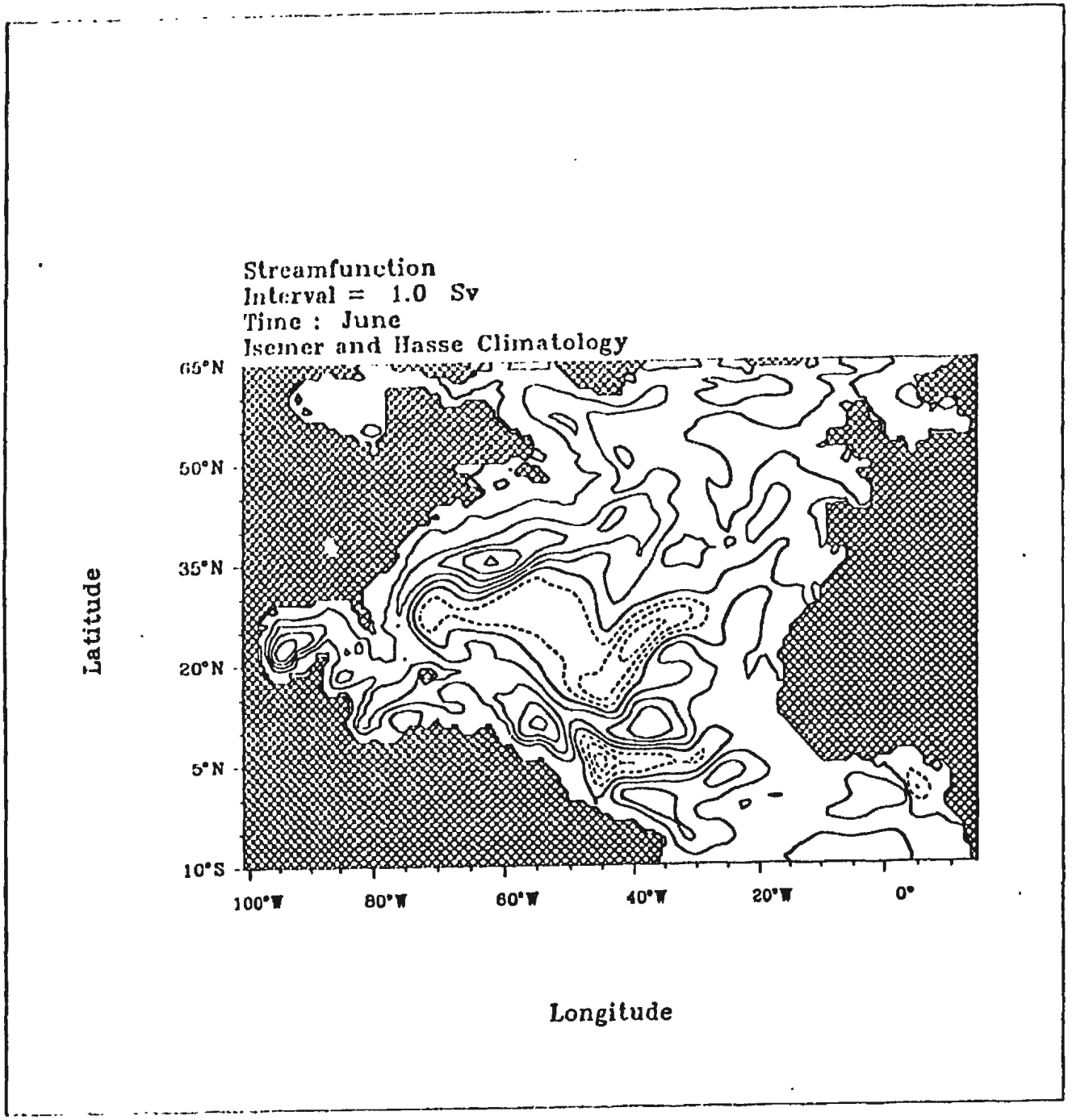

Figure A.3: *continued*

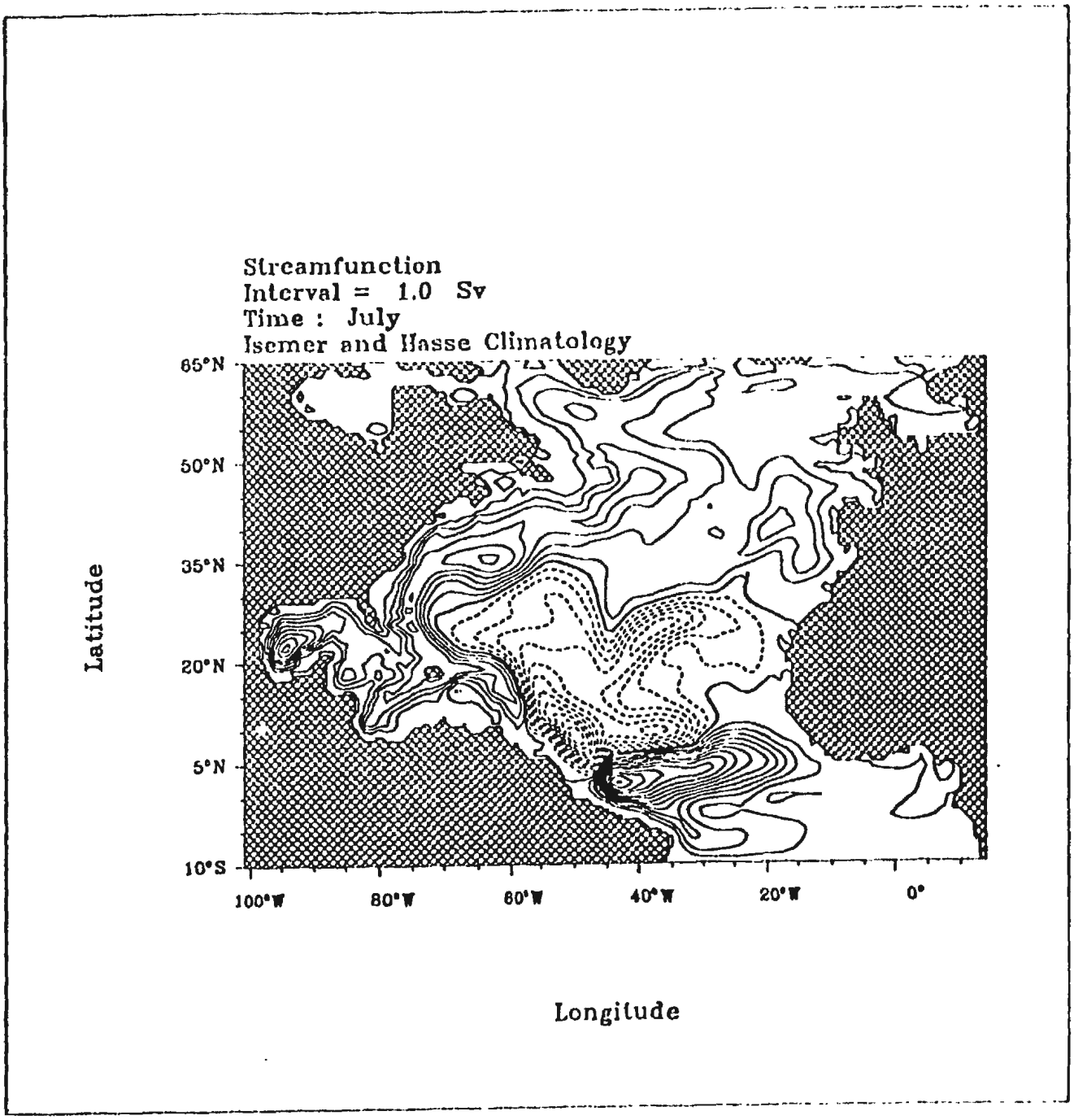

Figure A.3: *continued*

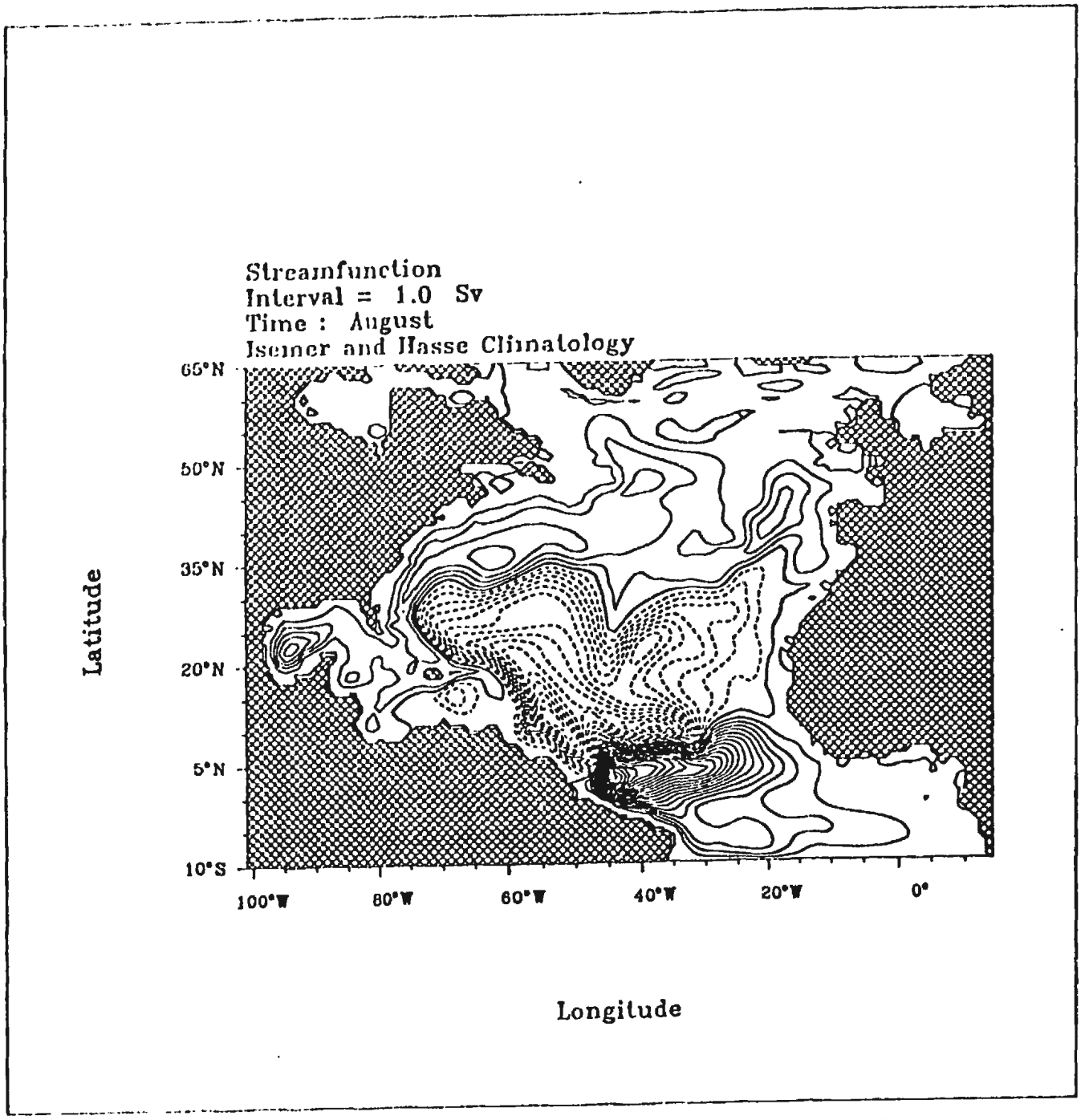

Figure A.3: *continued*

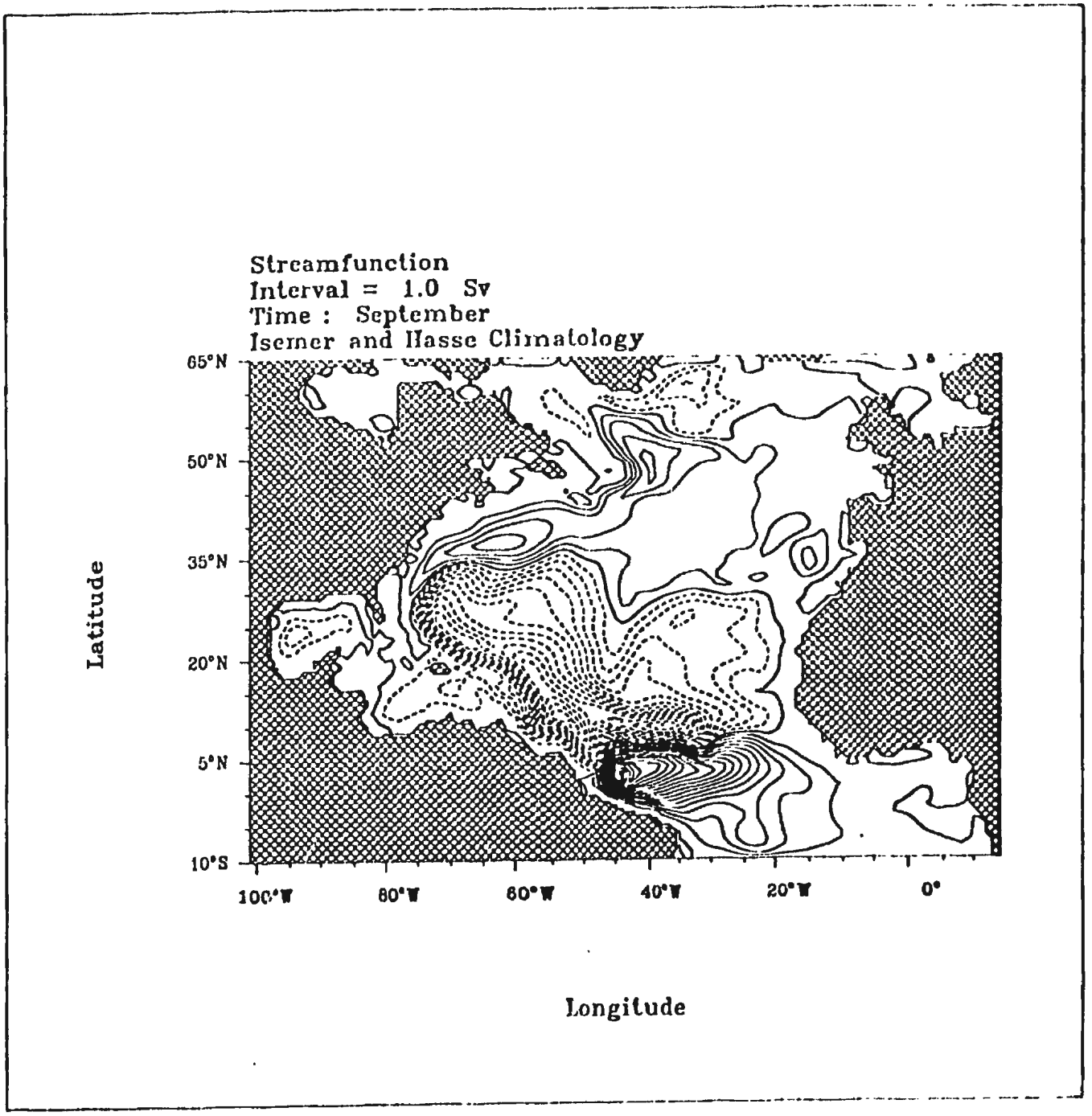

Figure A.3: *continued*

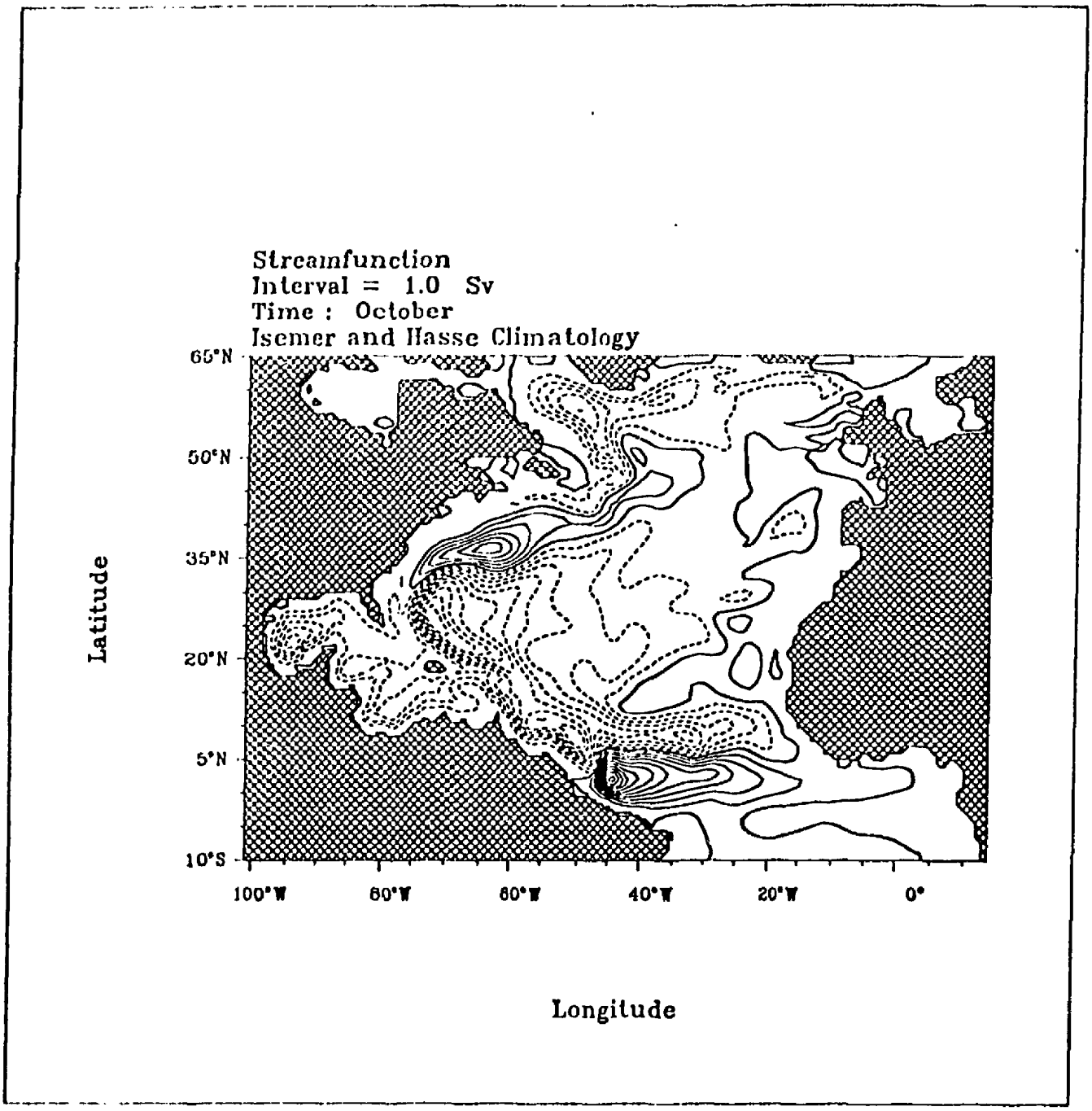

Figure A.3: *continued*

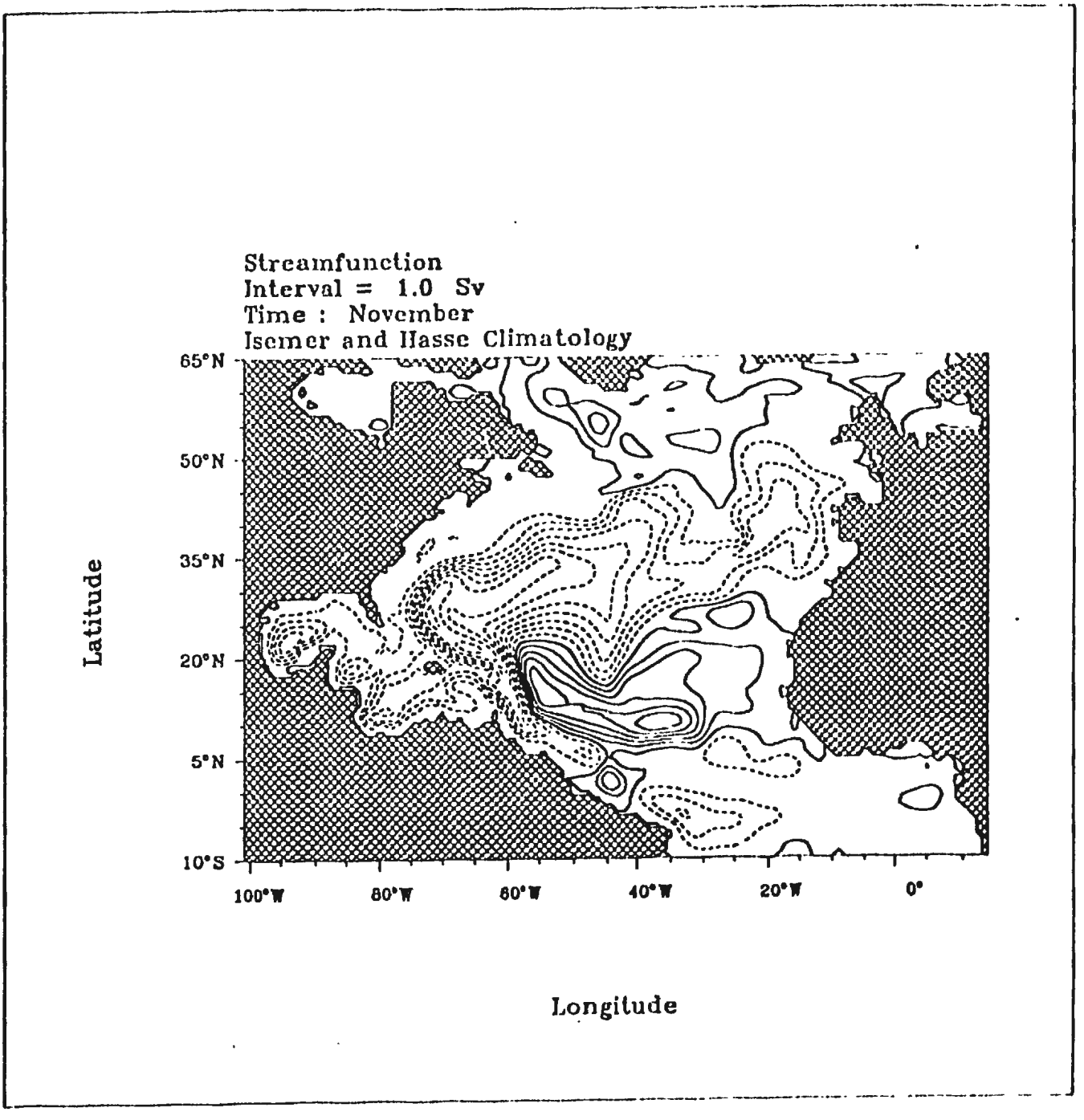

Figure A.3: *continued*

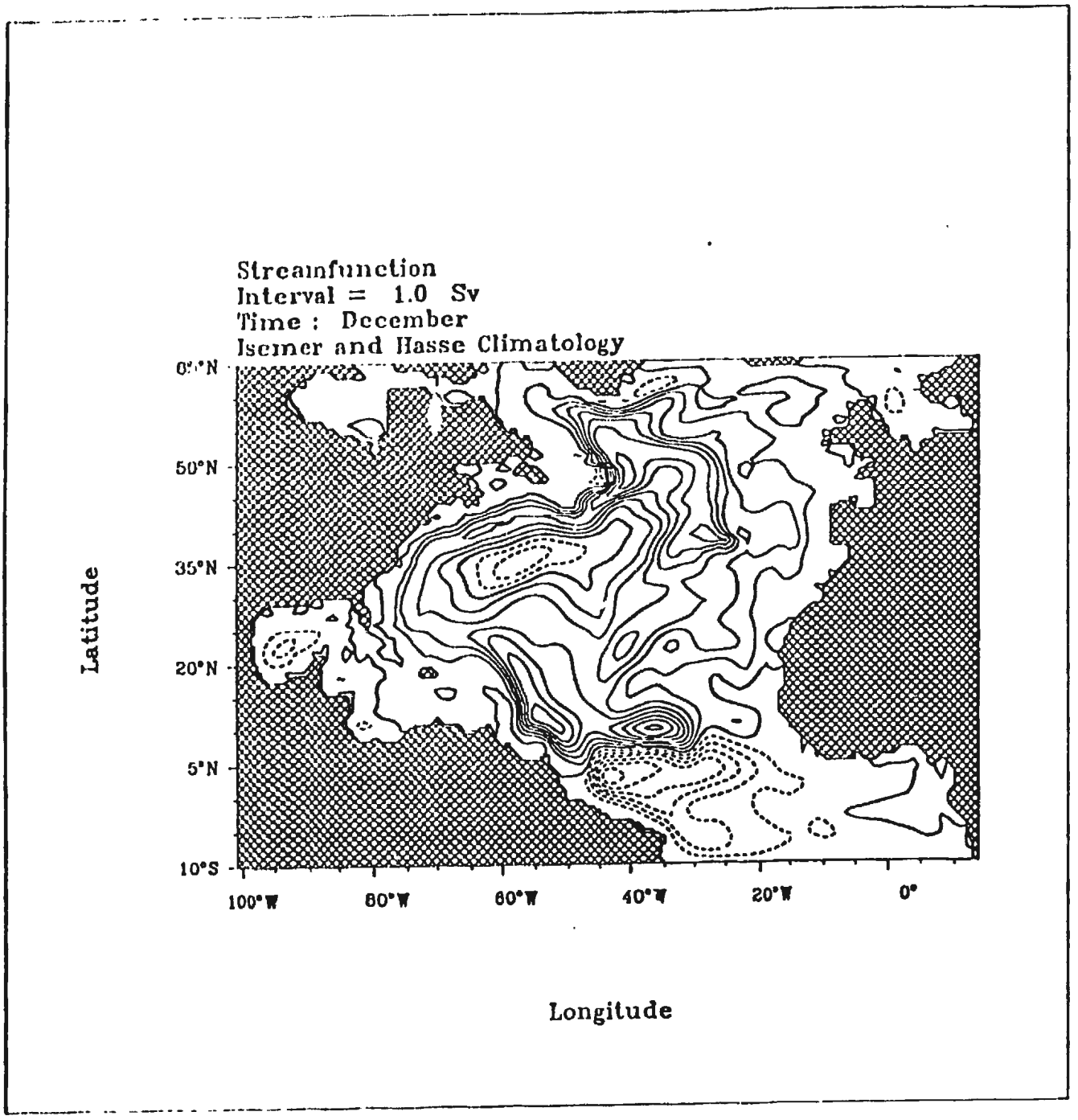

Figure A.3: *continued*

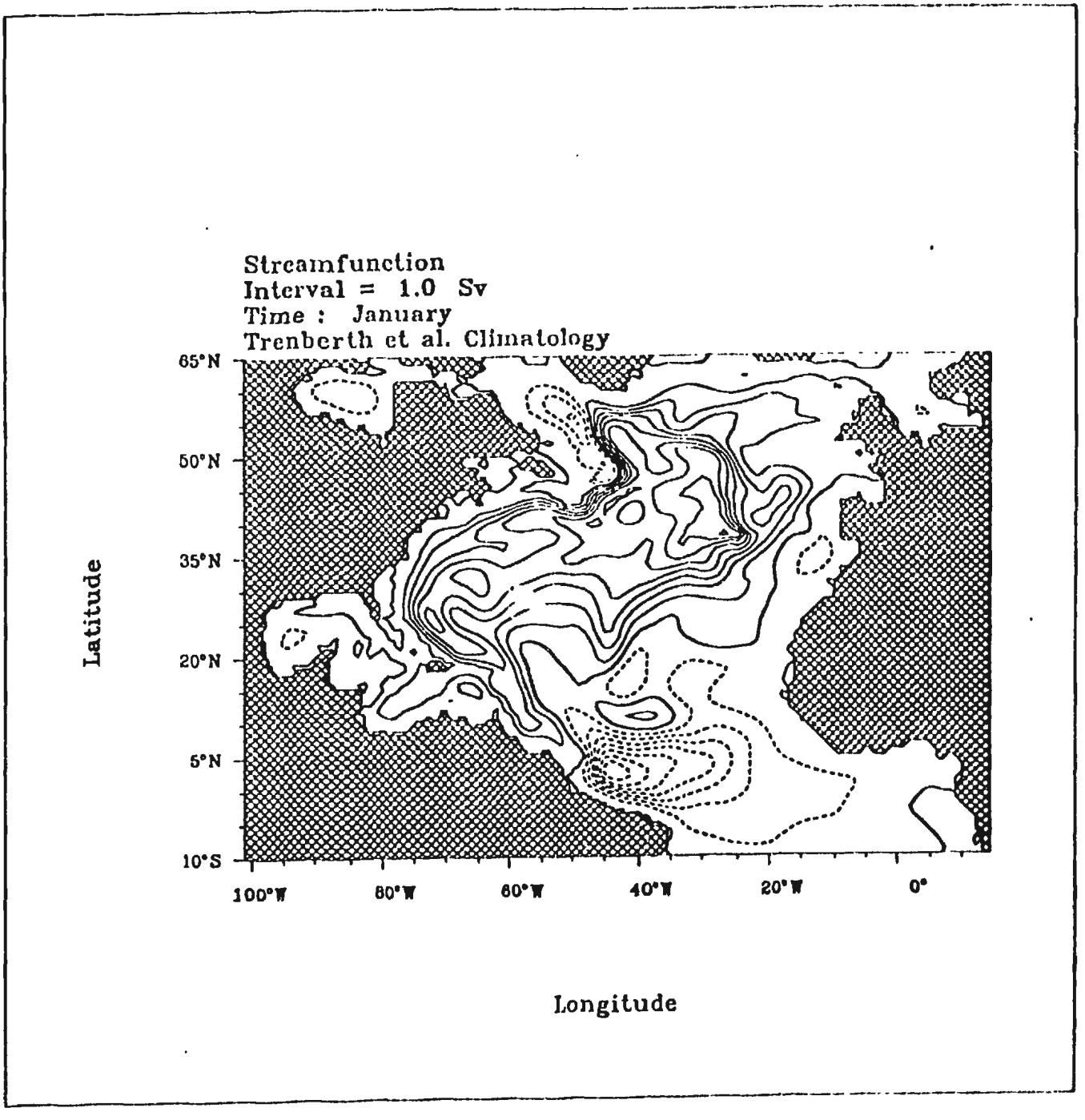

Figure A.4: As Figure A.1, but for TR wind forcing

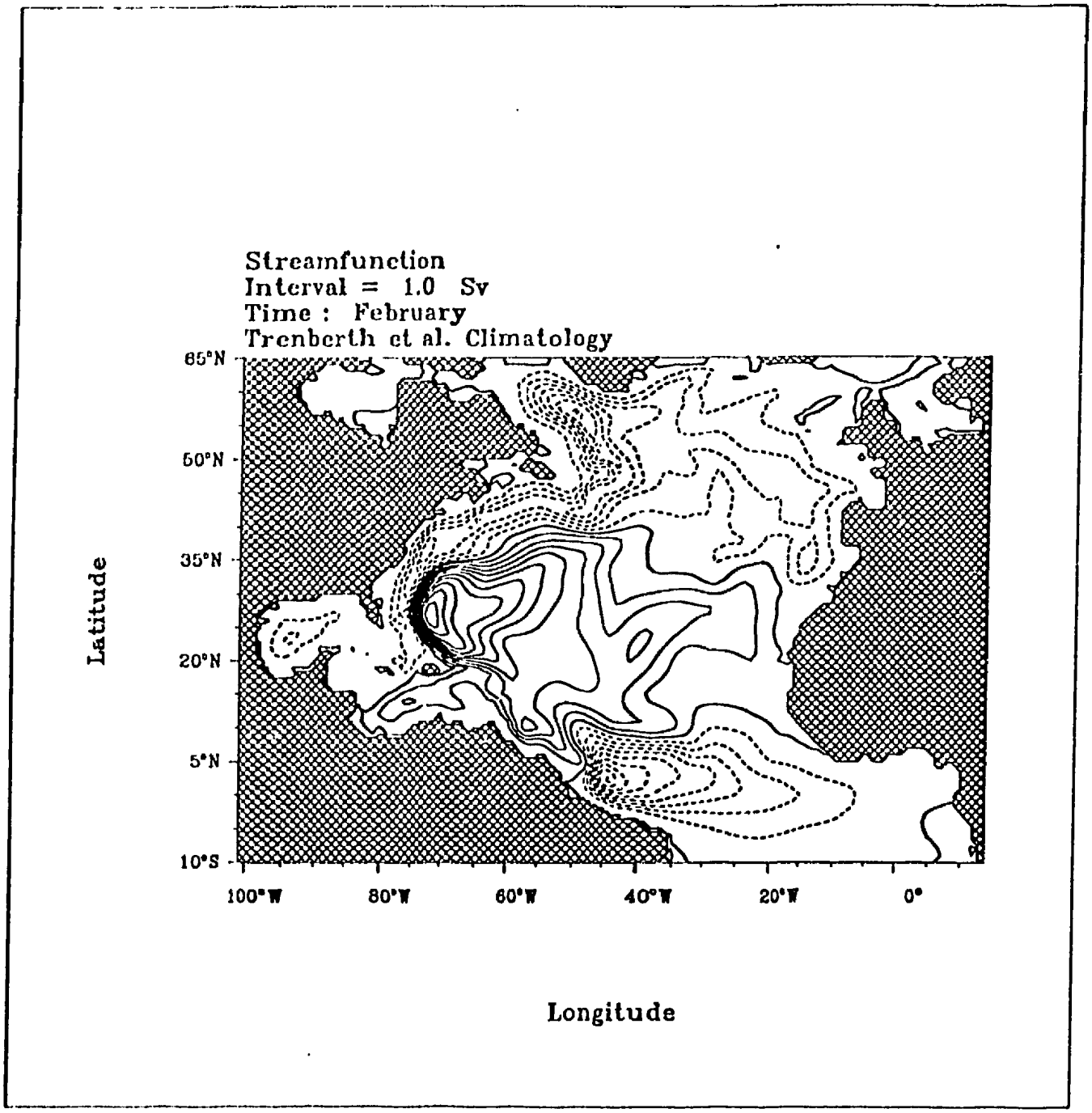

Figure A.4: *continued*

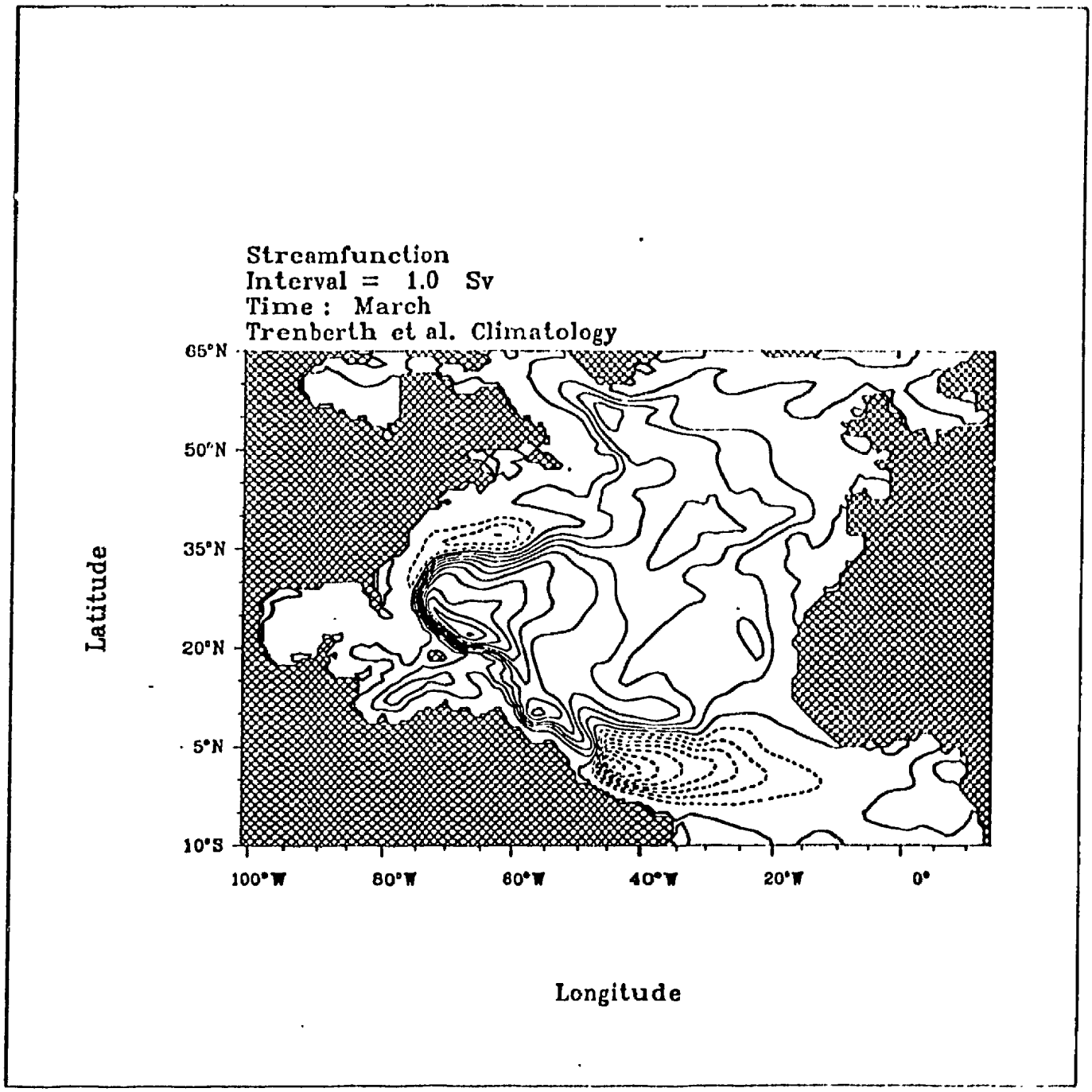

Figure A.4: *continued*

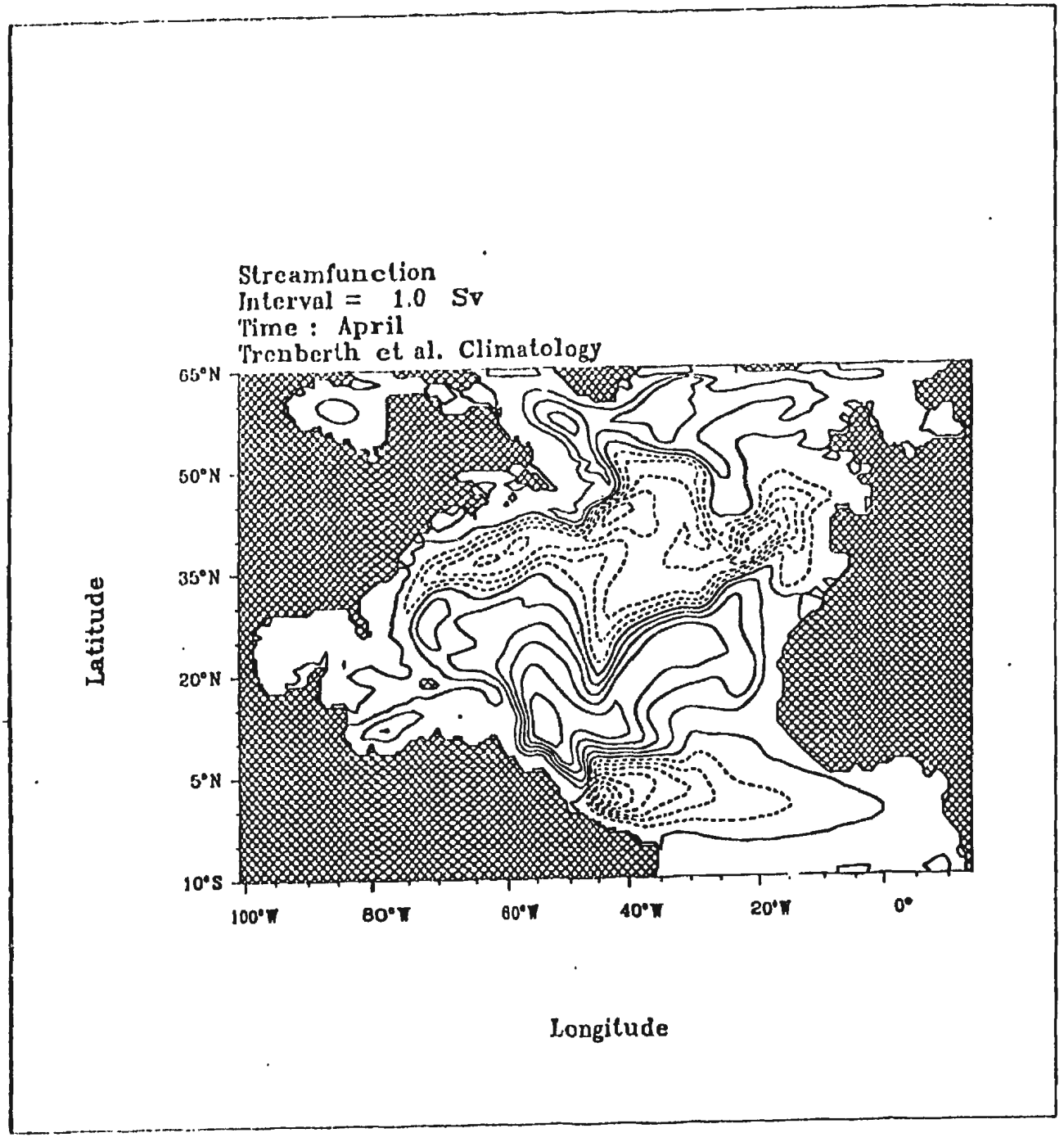

Figure A.4: *continued*

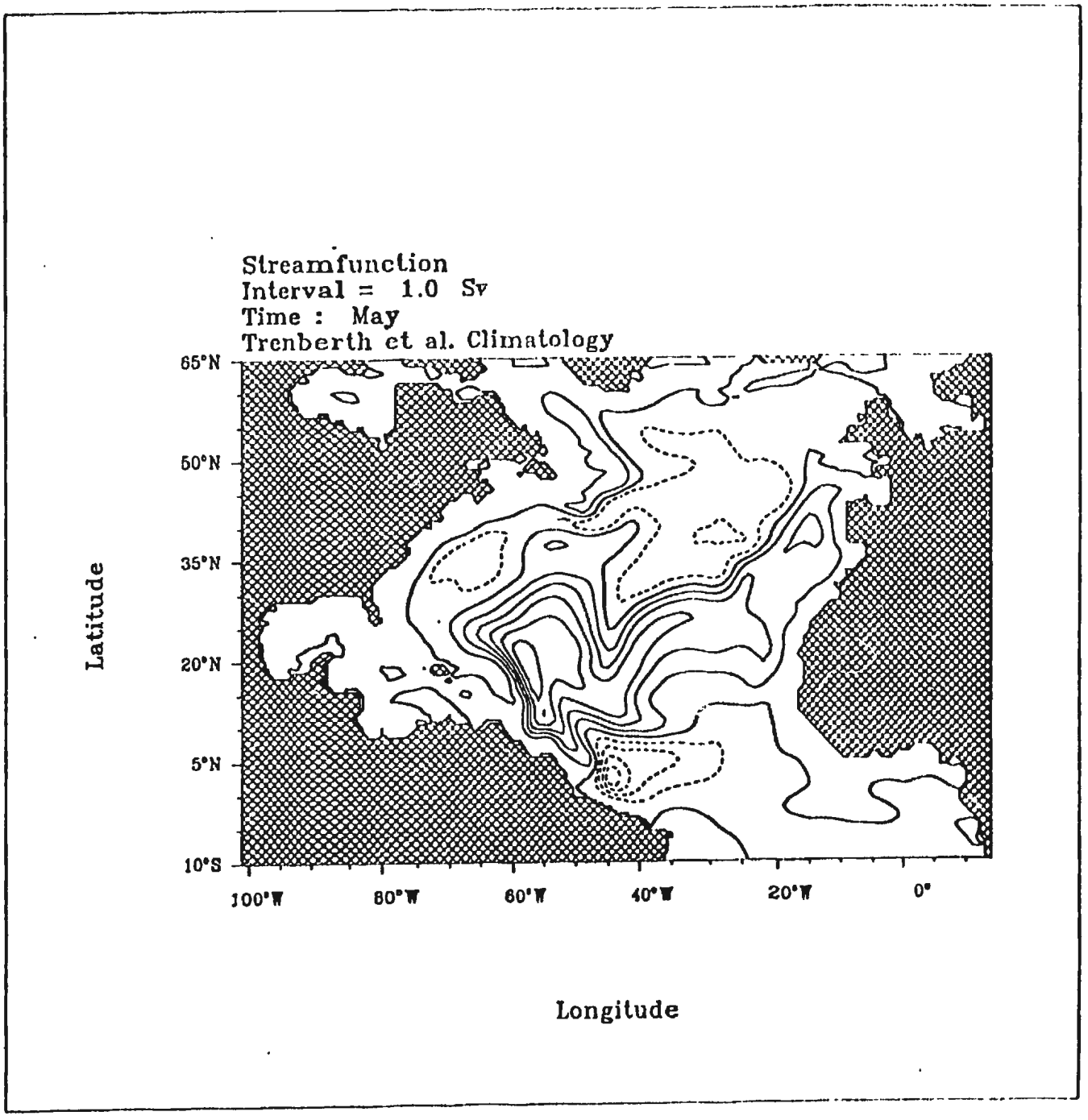

Figure A.4: *continued*

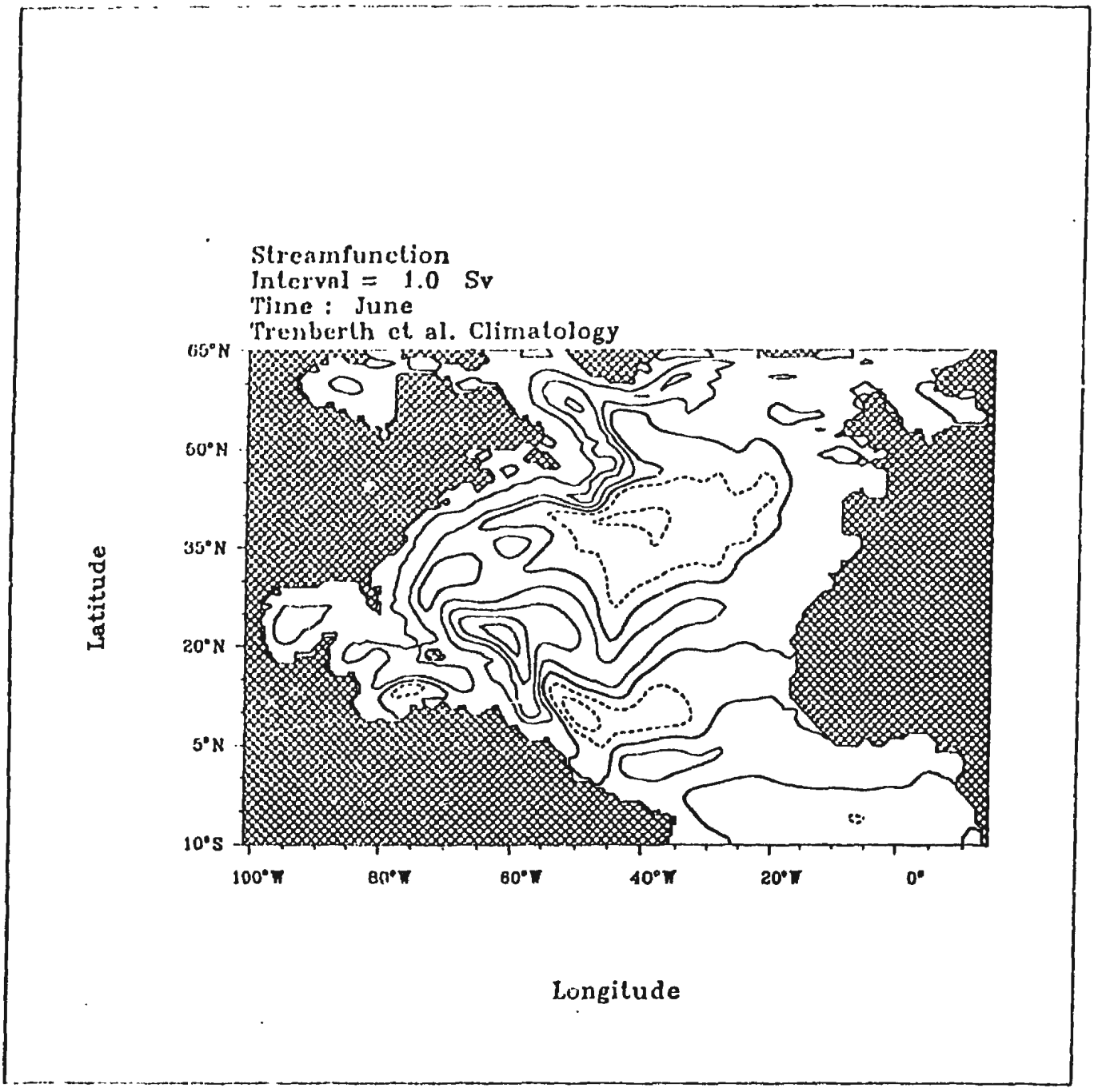

Figure A.4: *continued*

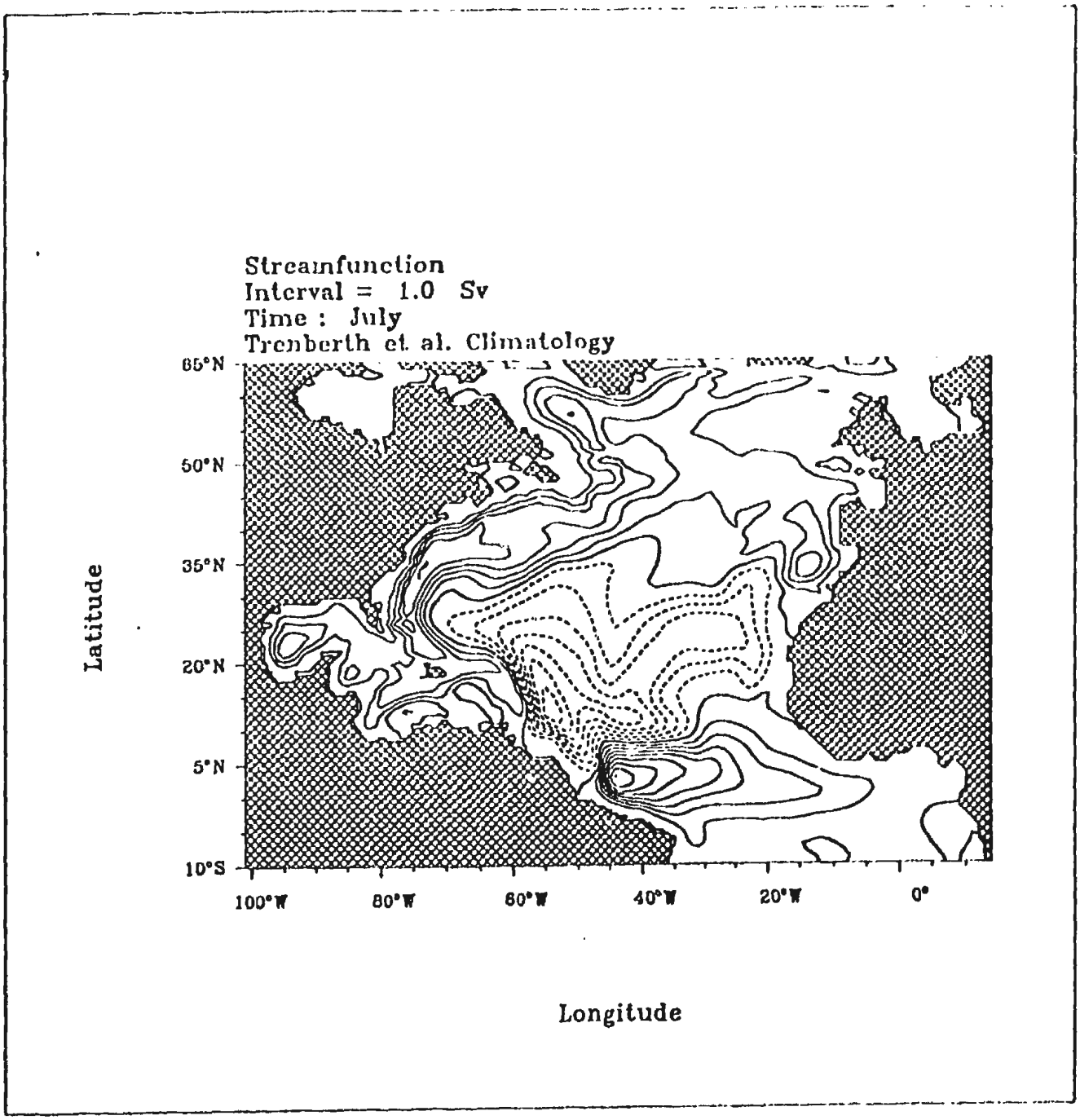

Figure A.4: *continued*

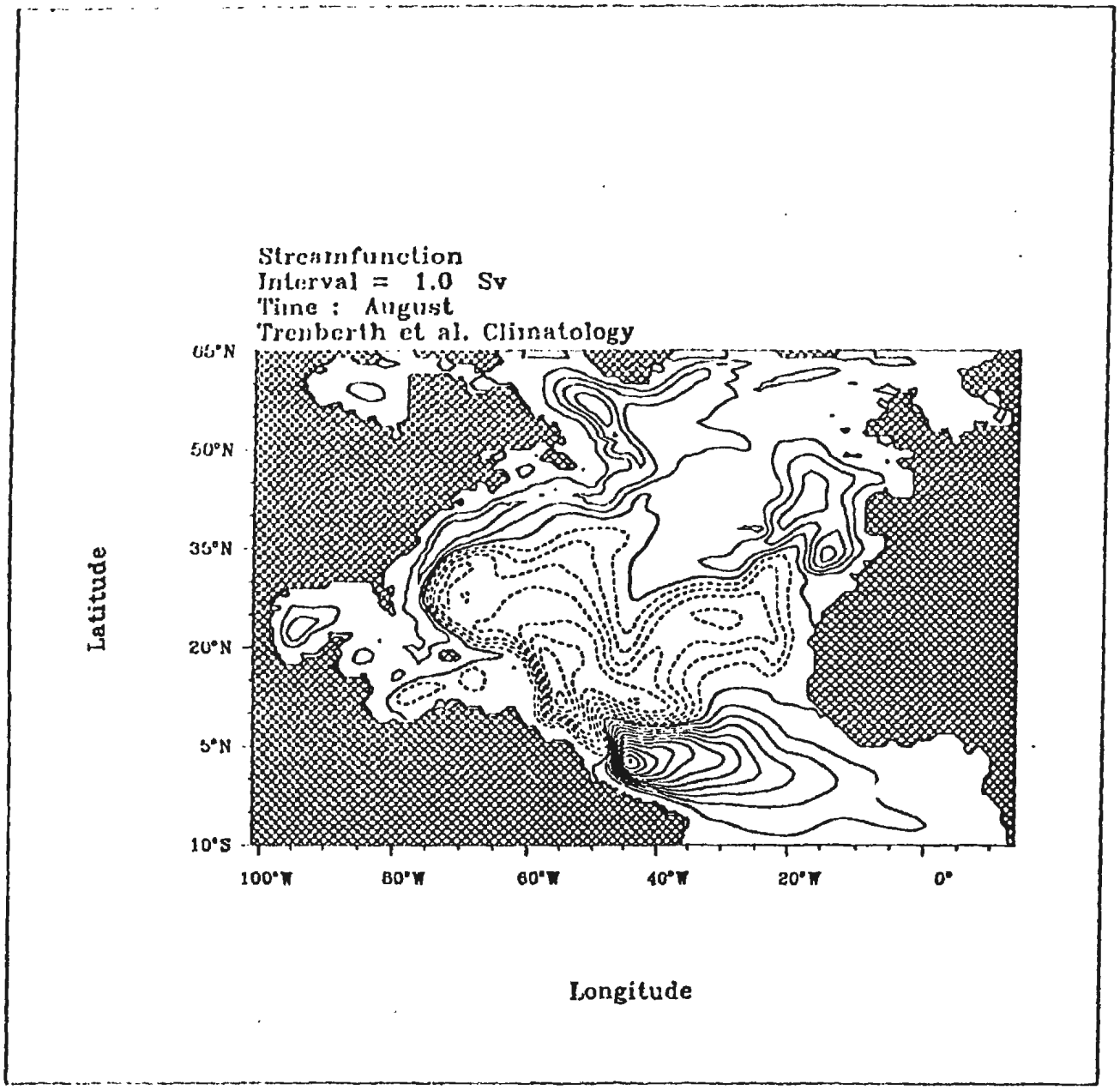

Figure A.4: *continued*

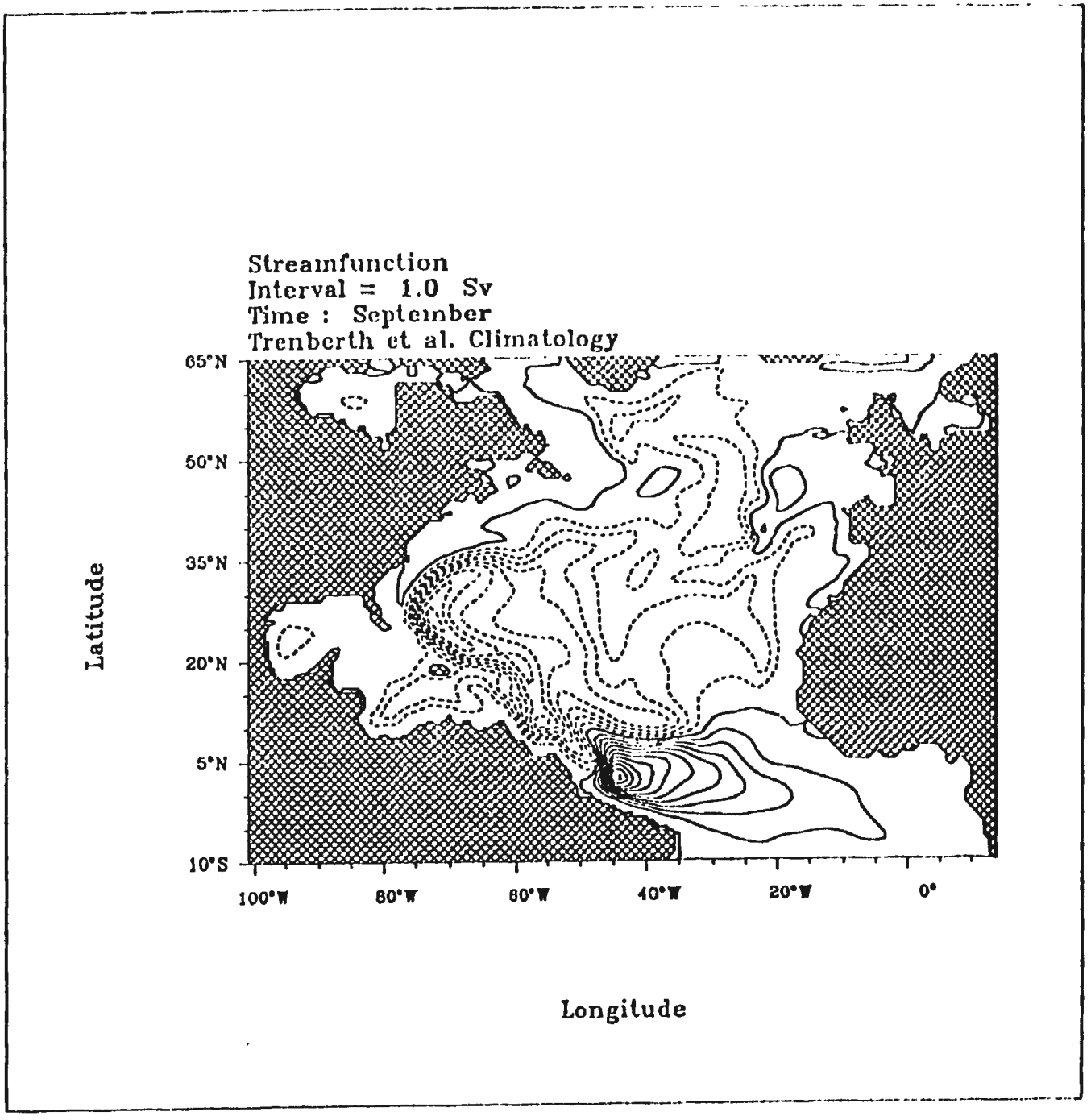

Figure A.4: *continued*

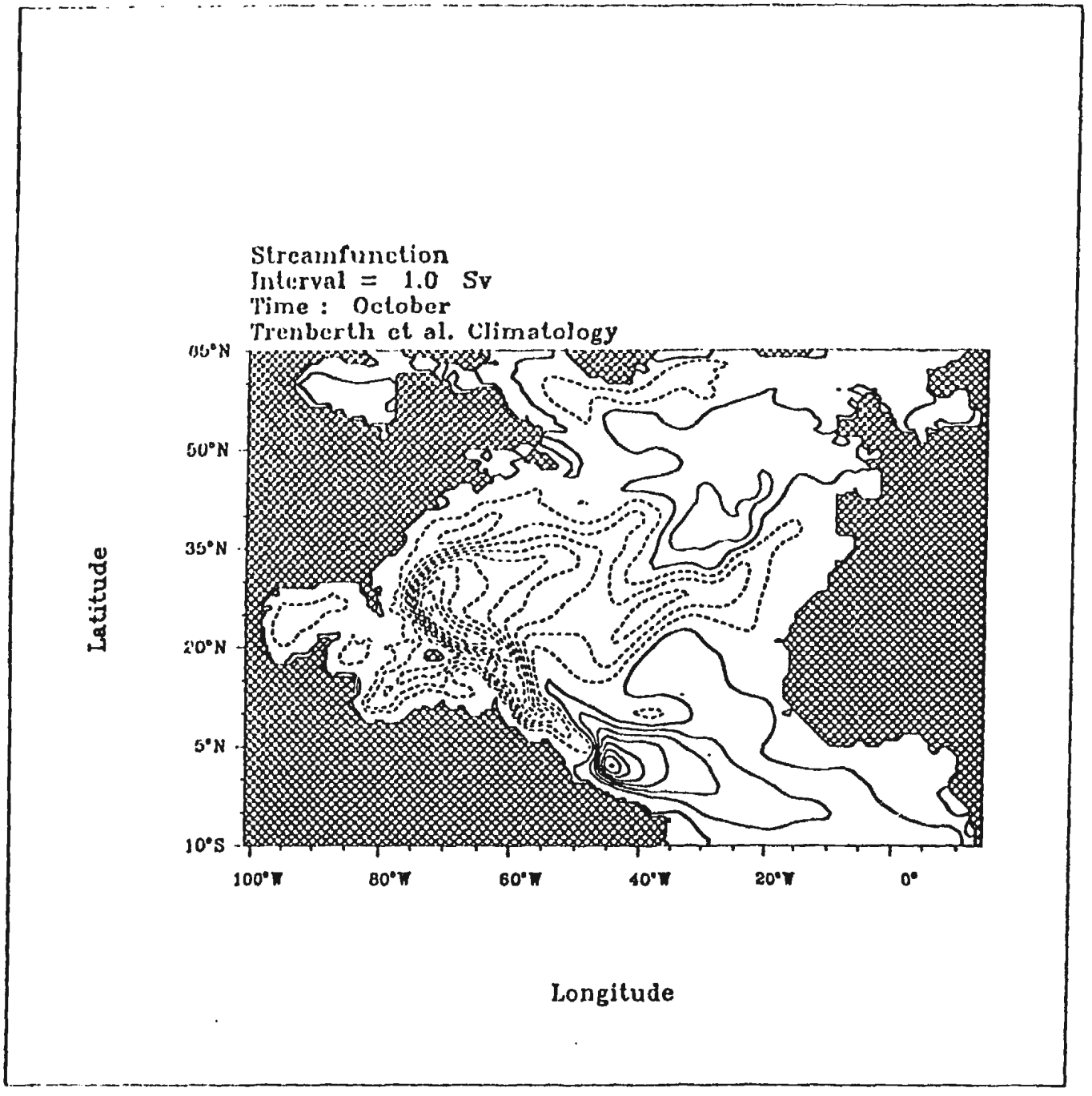

Figure A.4: *continued*

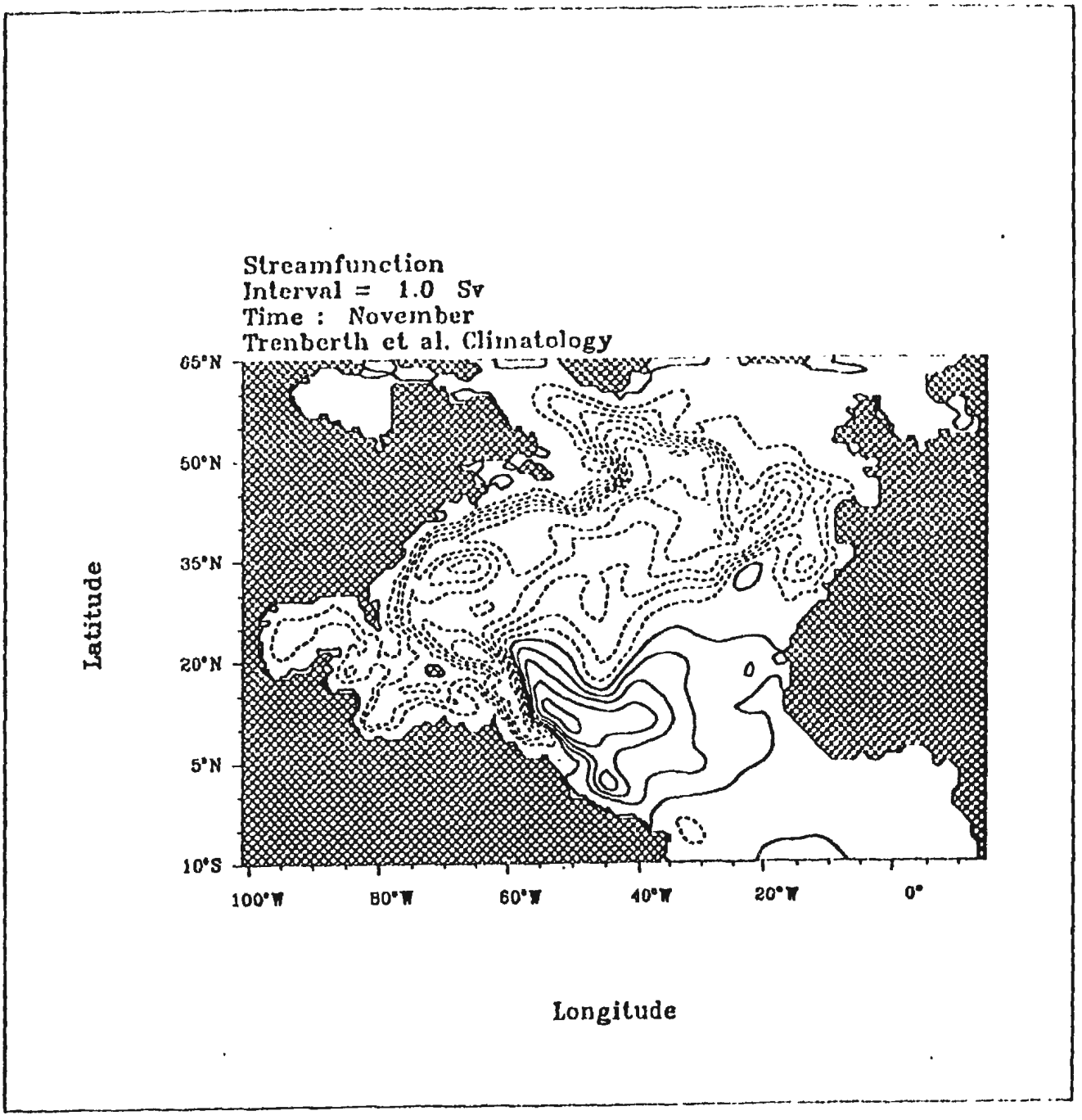

Figure A.4: *continued*

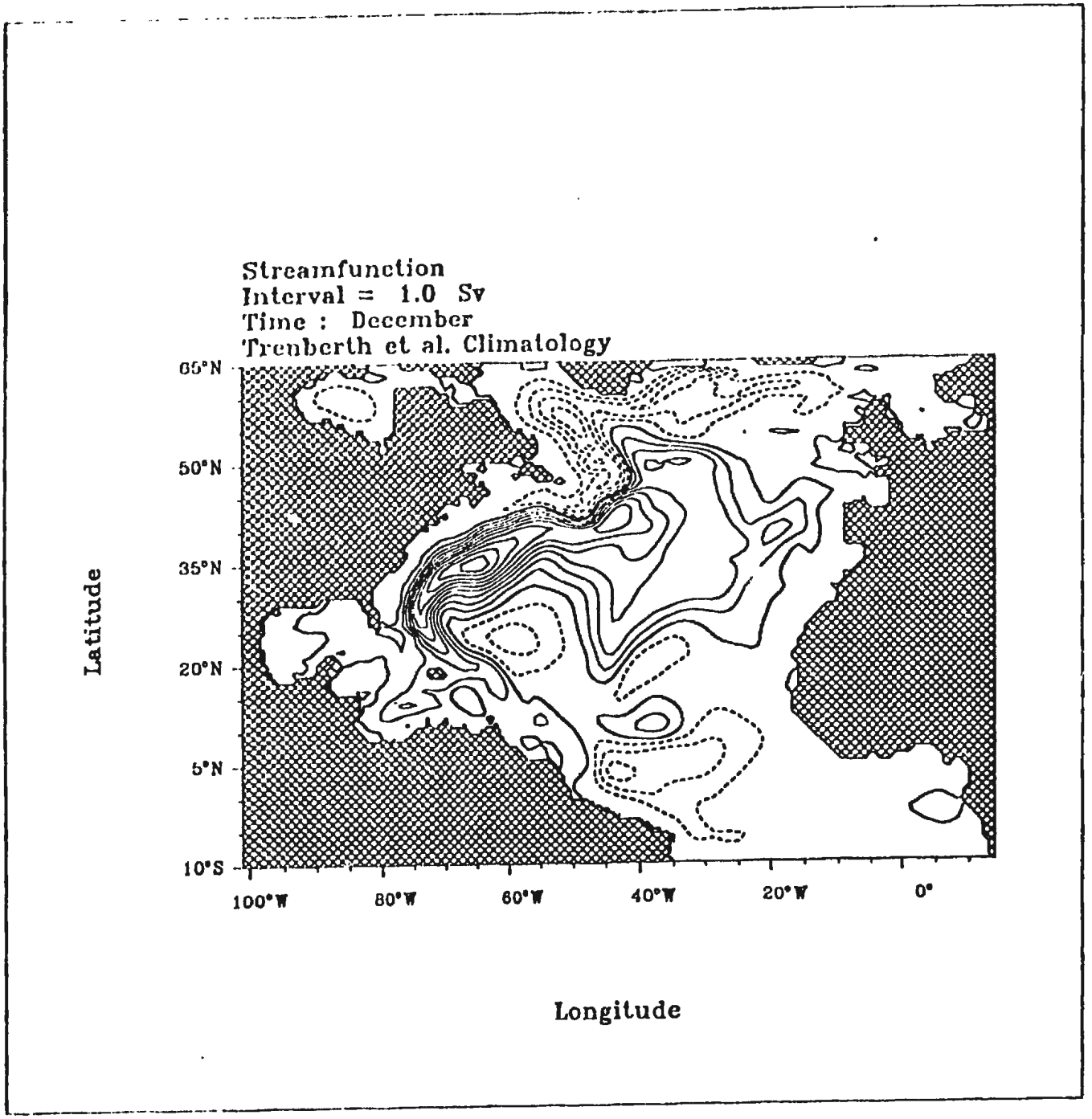

Figure A.4: *continued*

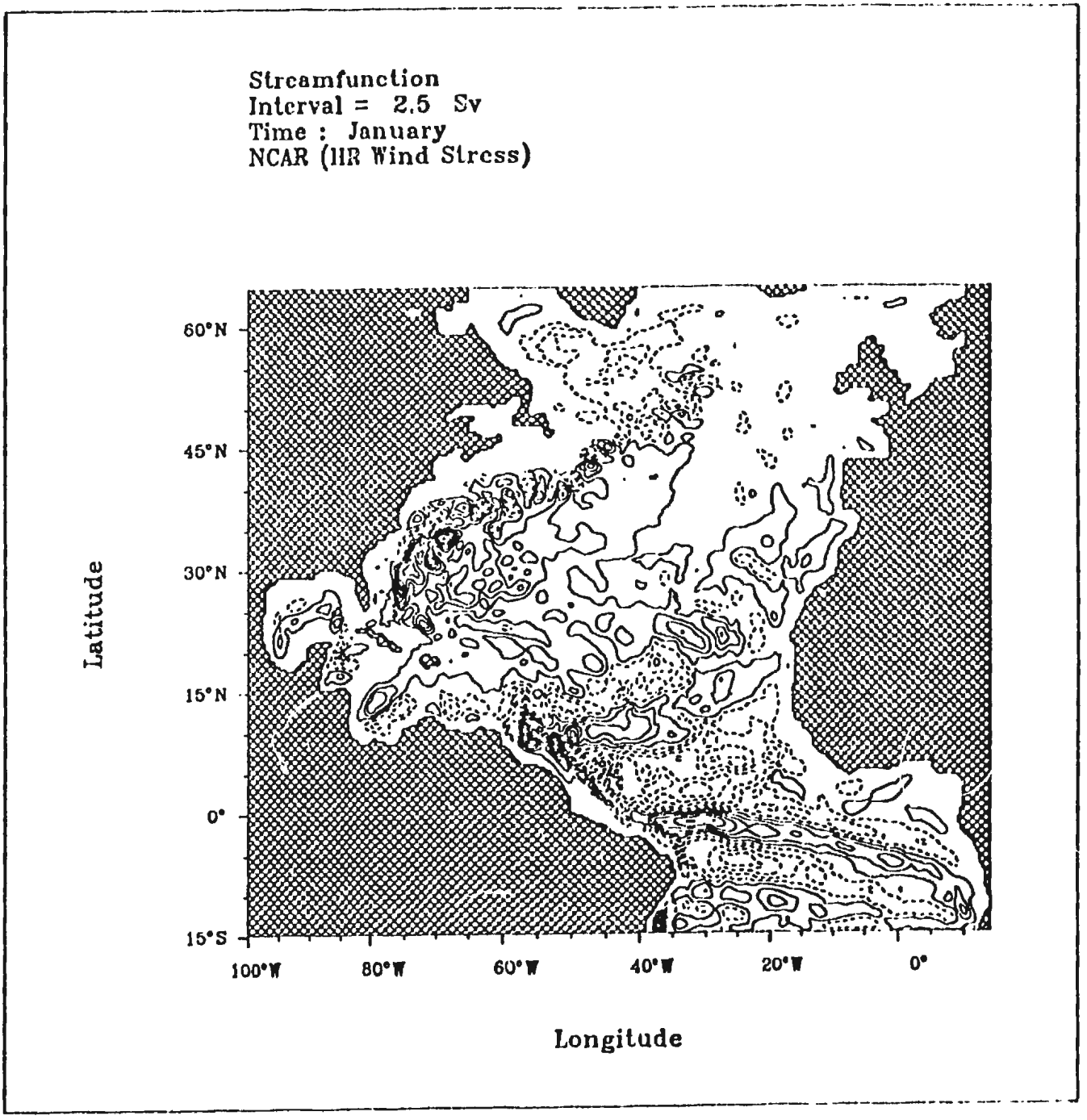

Figure A.5: Plan views of the anomalous monthly mean transport streamfunction, Ψ, using 5 years of output from the NCAR version of the WOCE-CME under HR wind forcing. The contour interval is 2.5 *Sv*, dashed contours indicate negative values, solid contours positive values.

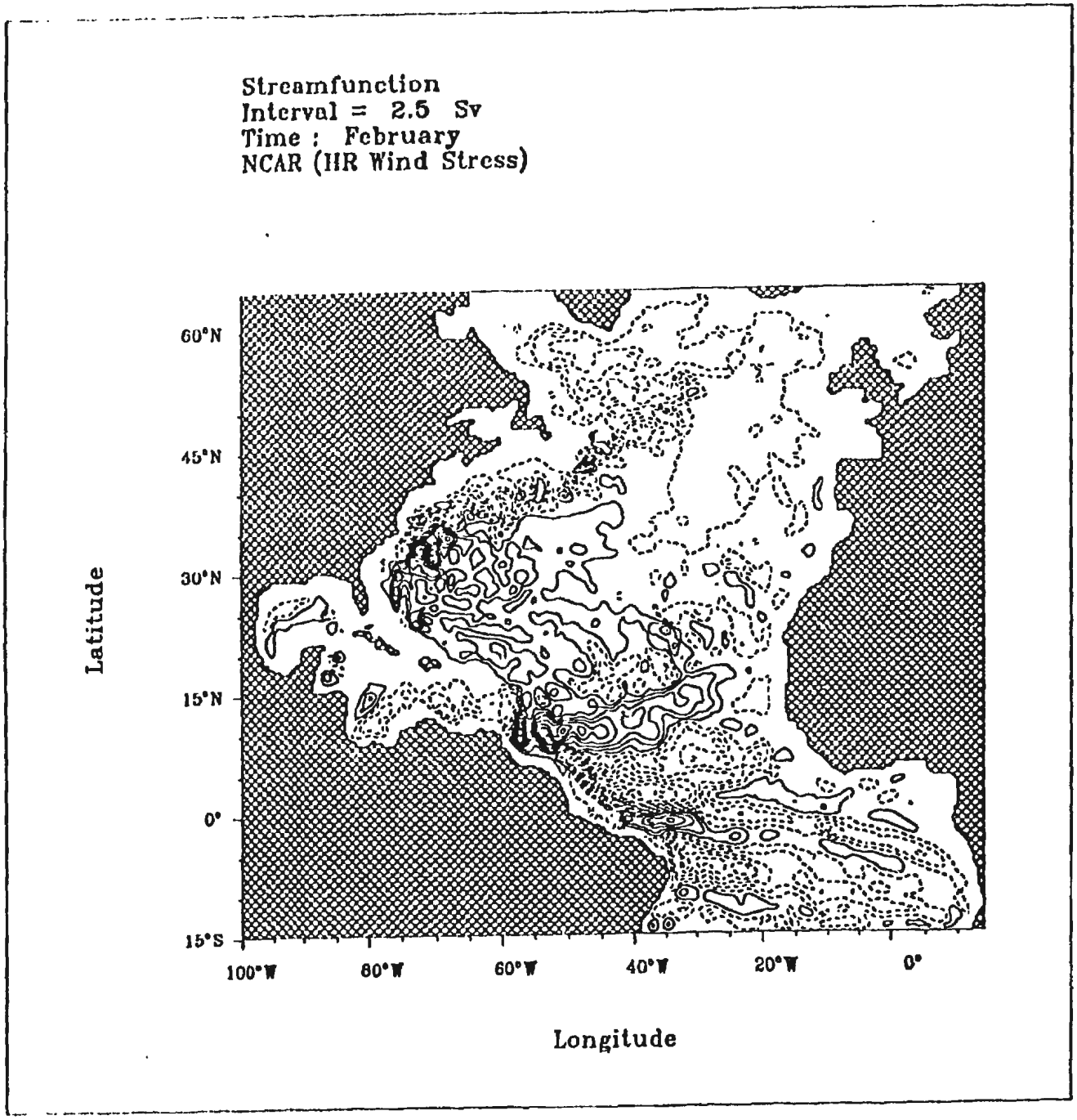

Figure A.5: *continued*

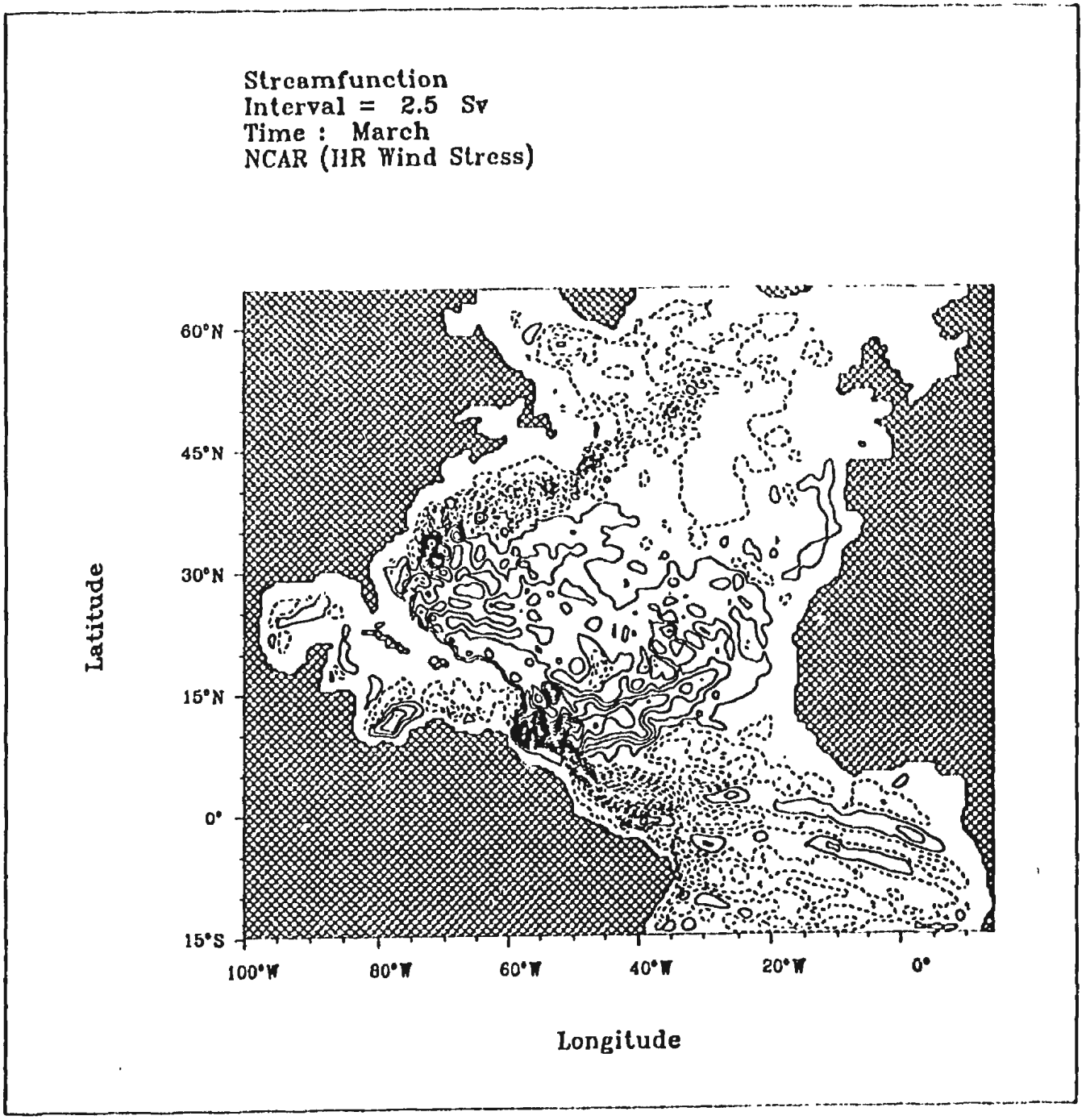

Figure A.5: *continued*

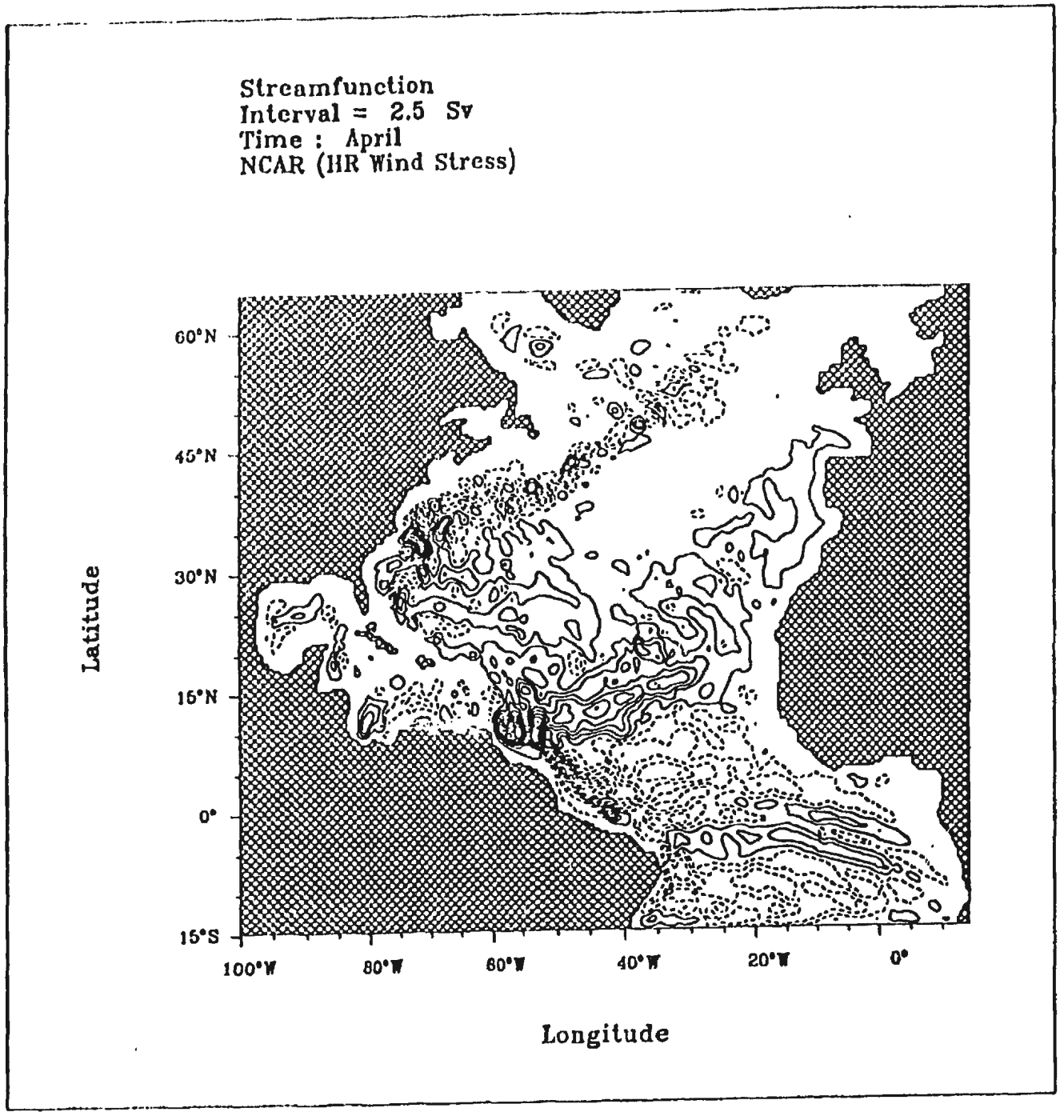

Figure A.5: *continued*

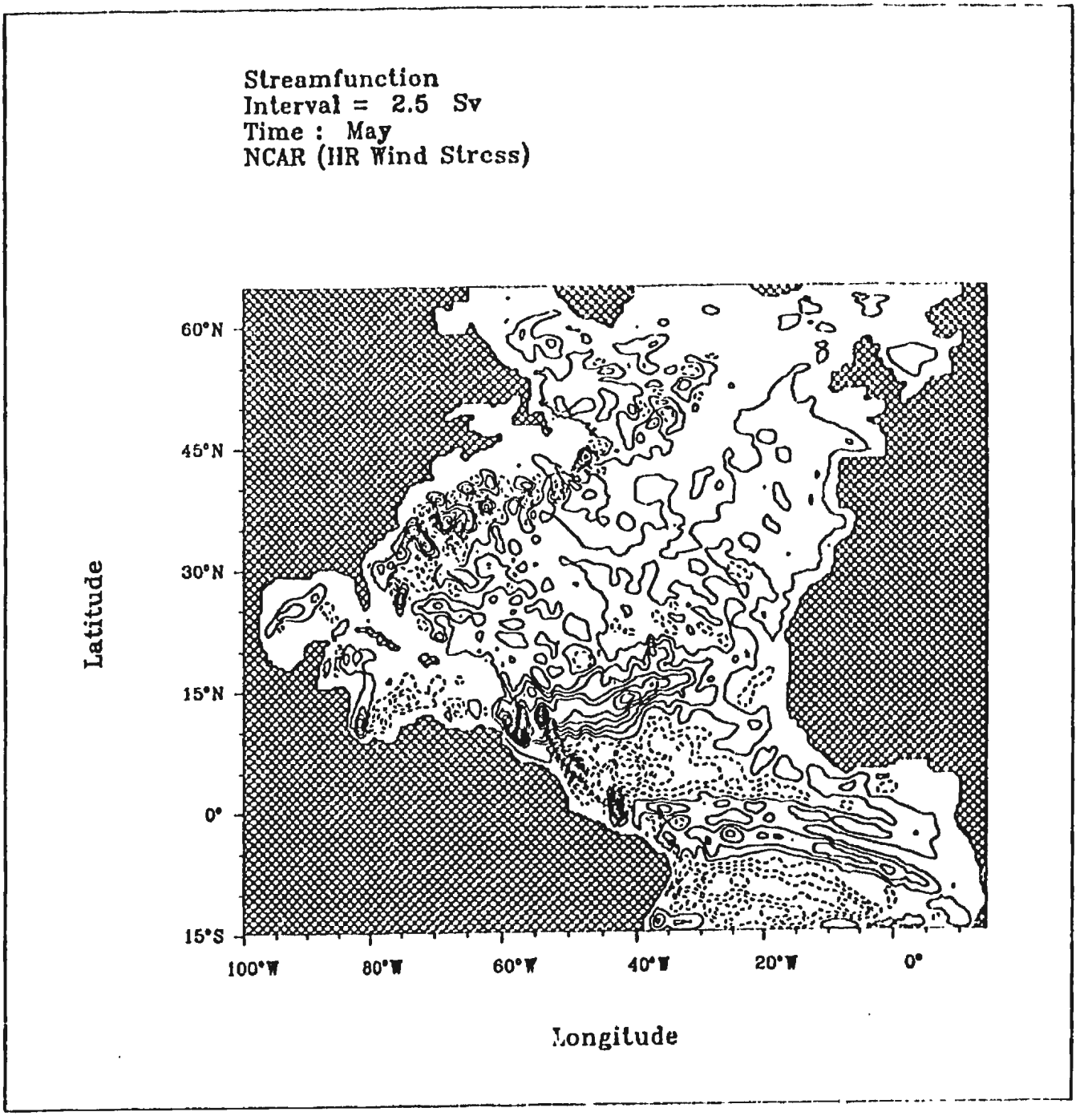

Figure A.5: *continued*

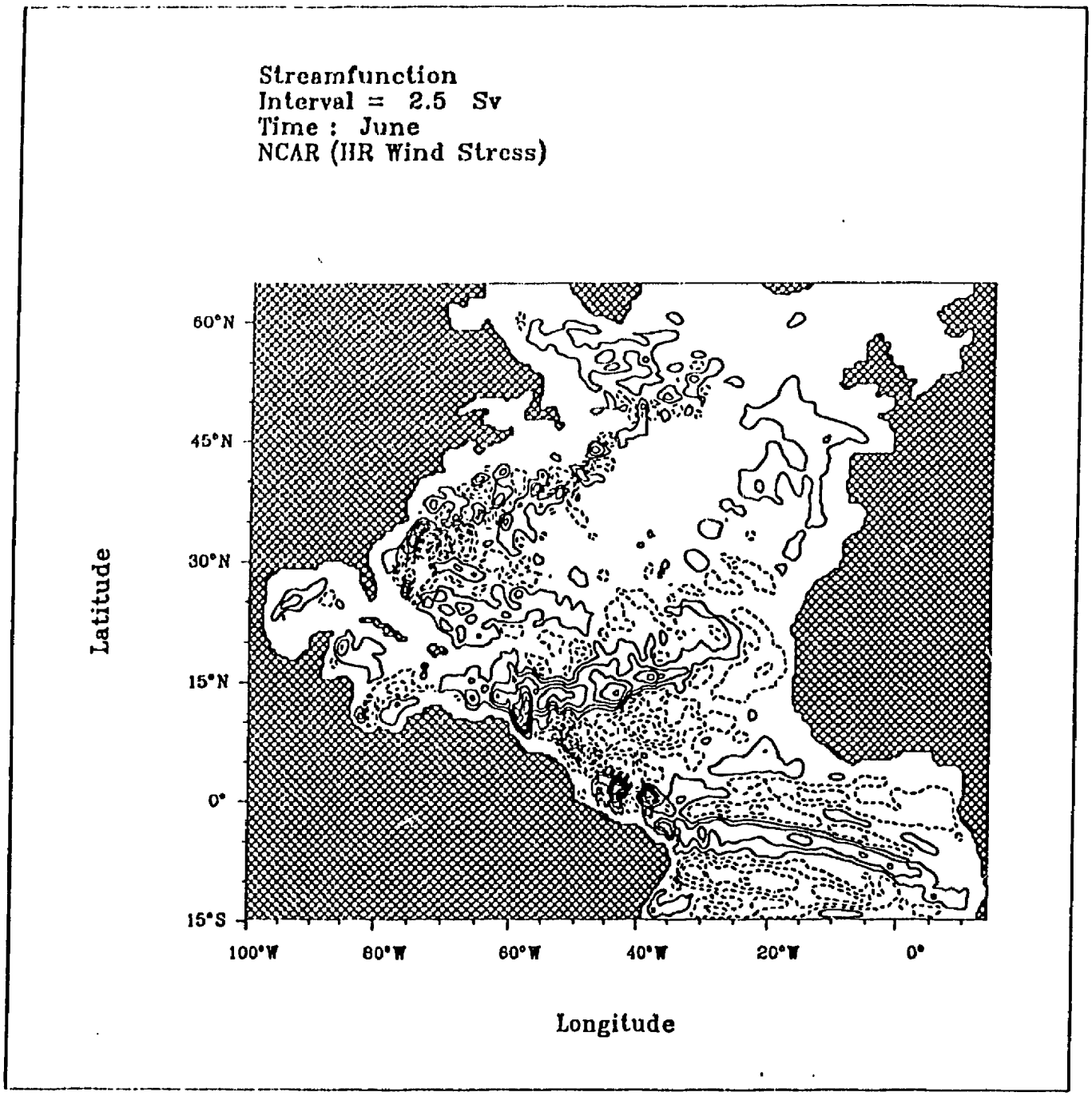

Figure A.5: *continued*

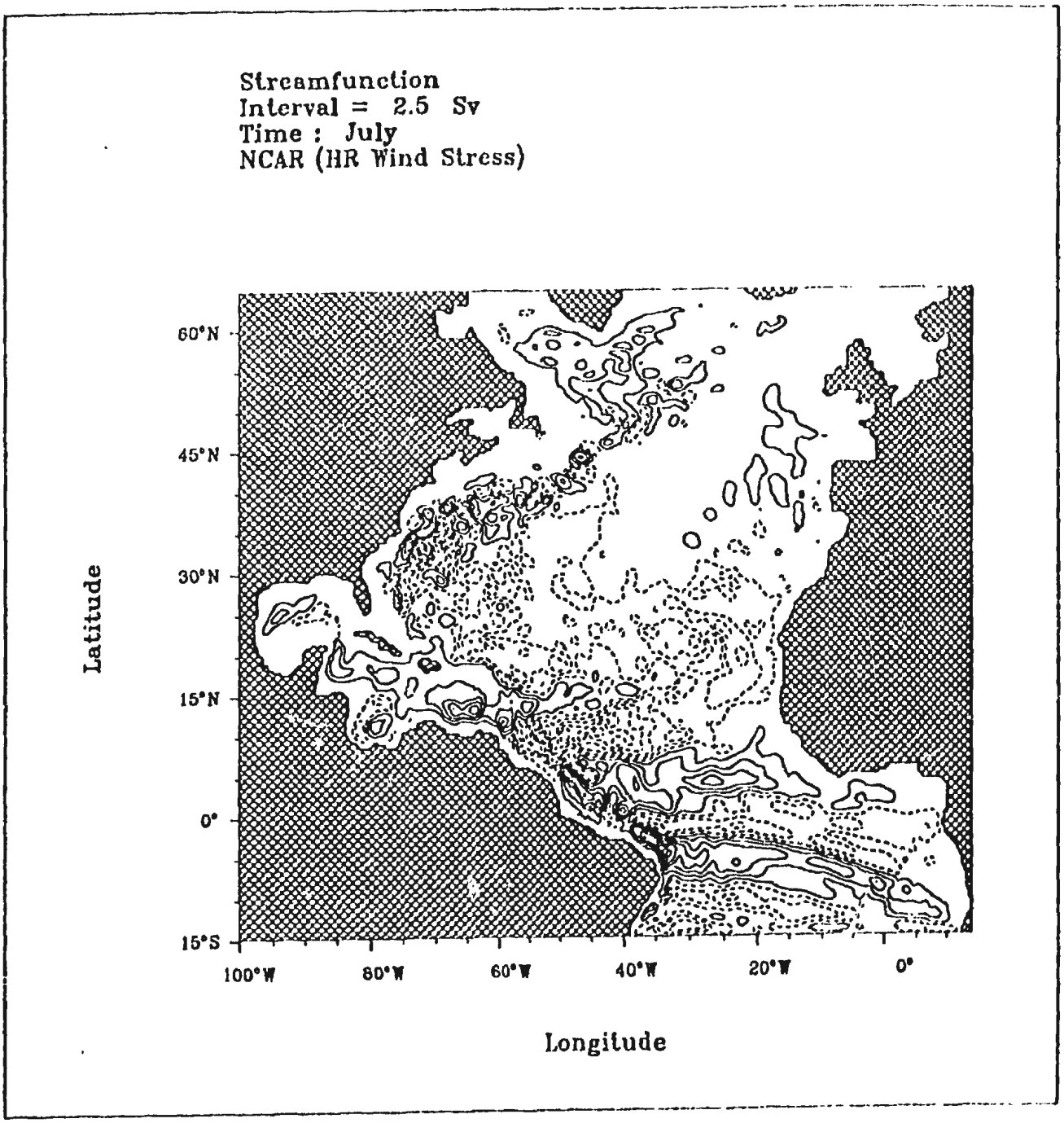

Figure A.5: *continued*

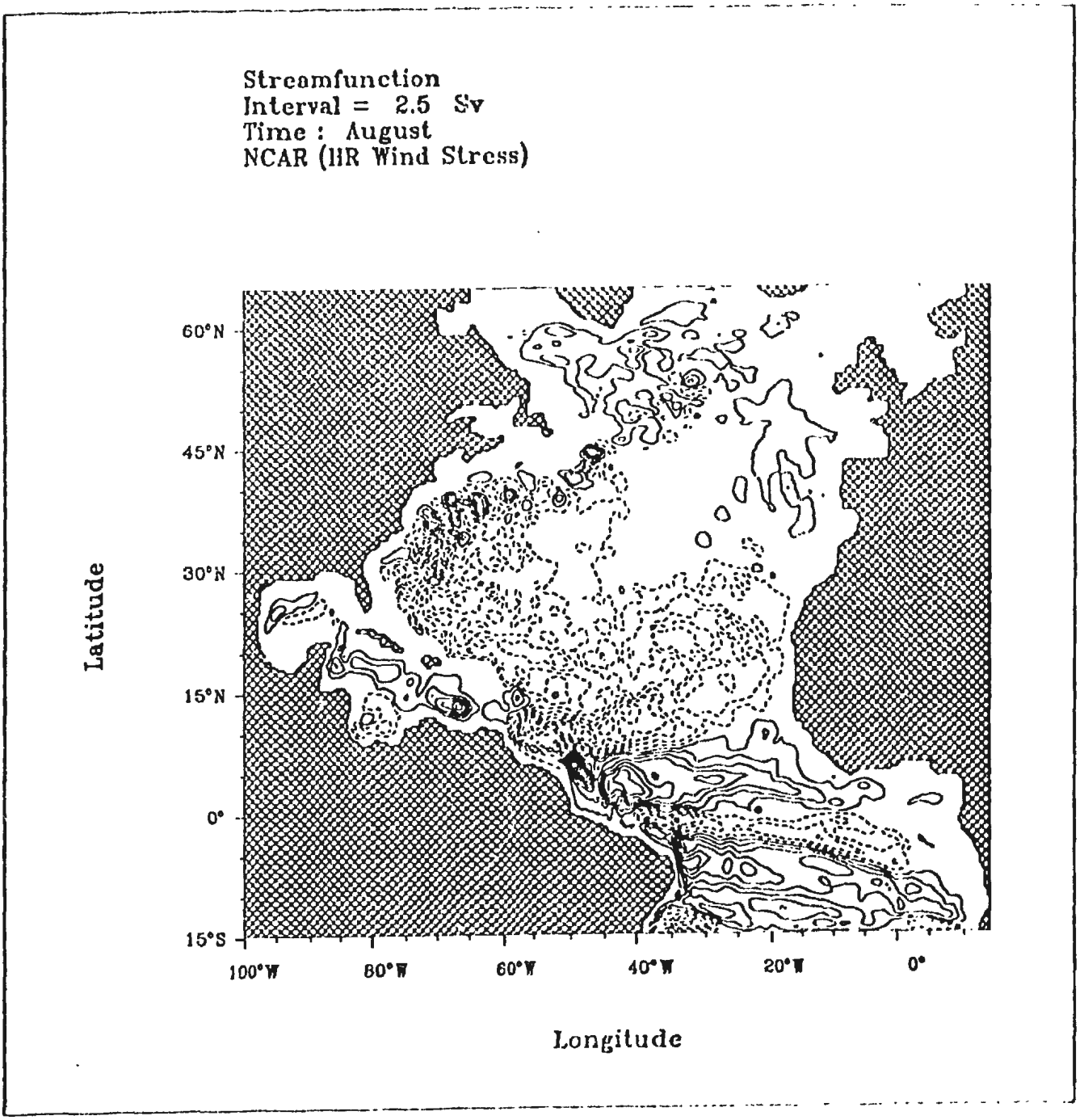

Figure A.5: *continued*

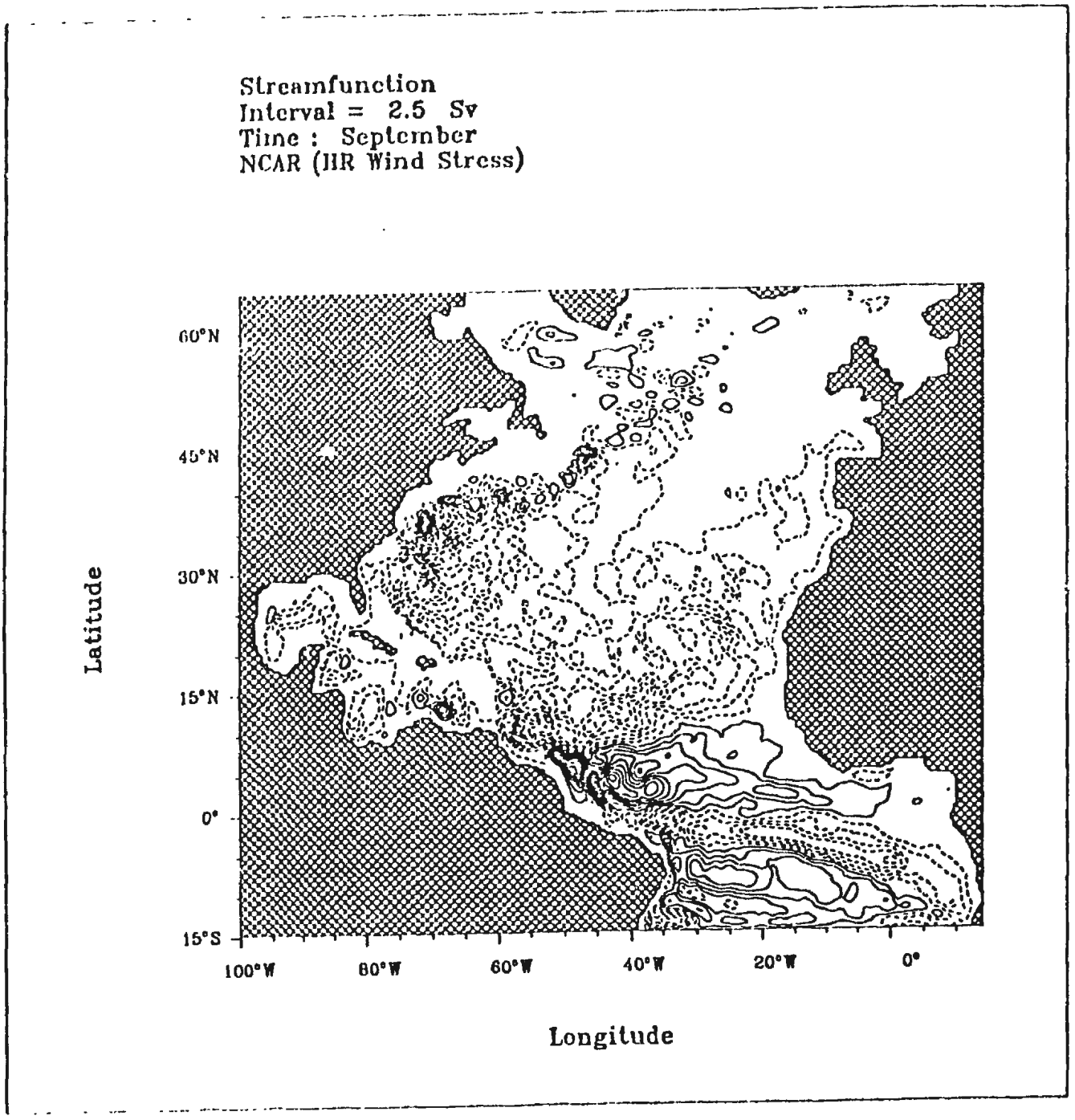

Figure A.5: *continued*

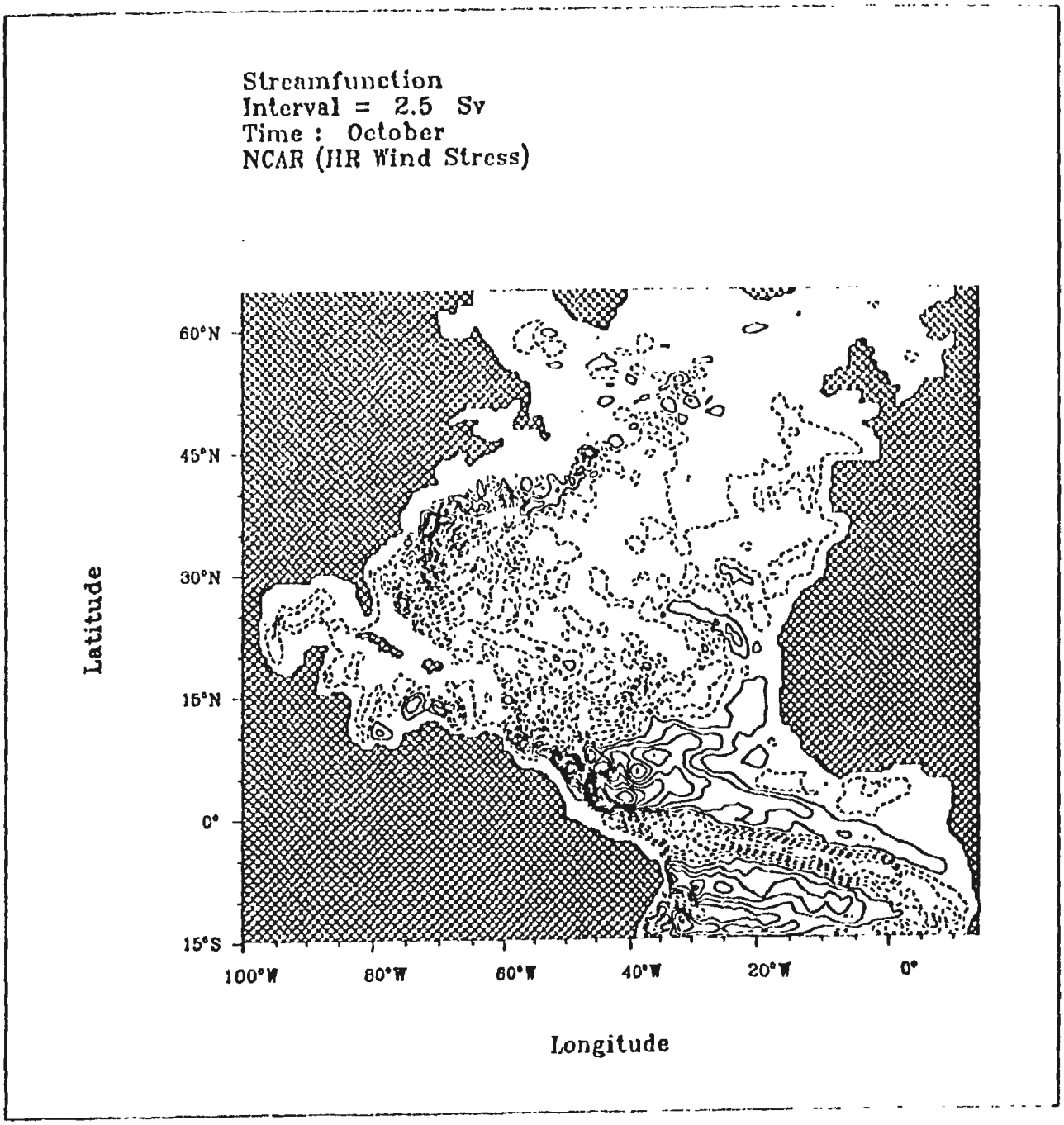

Figure A.5: *continued*

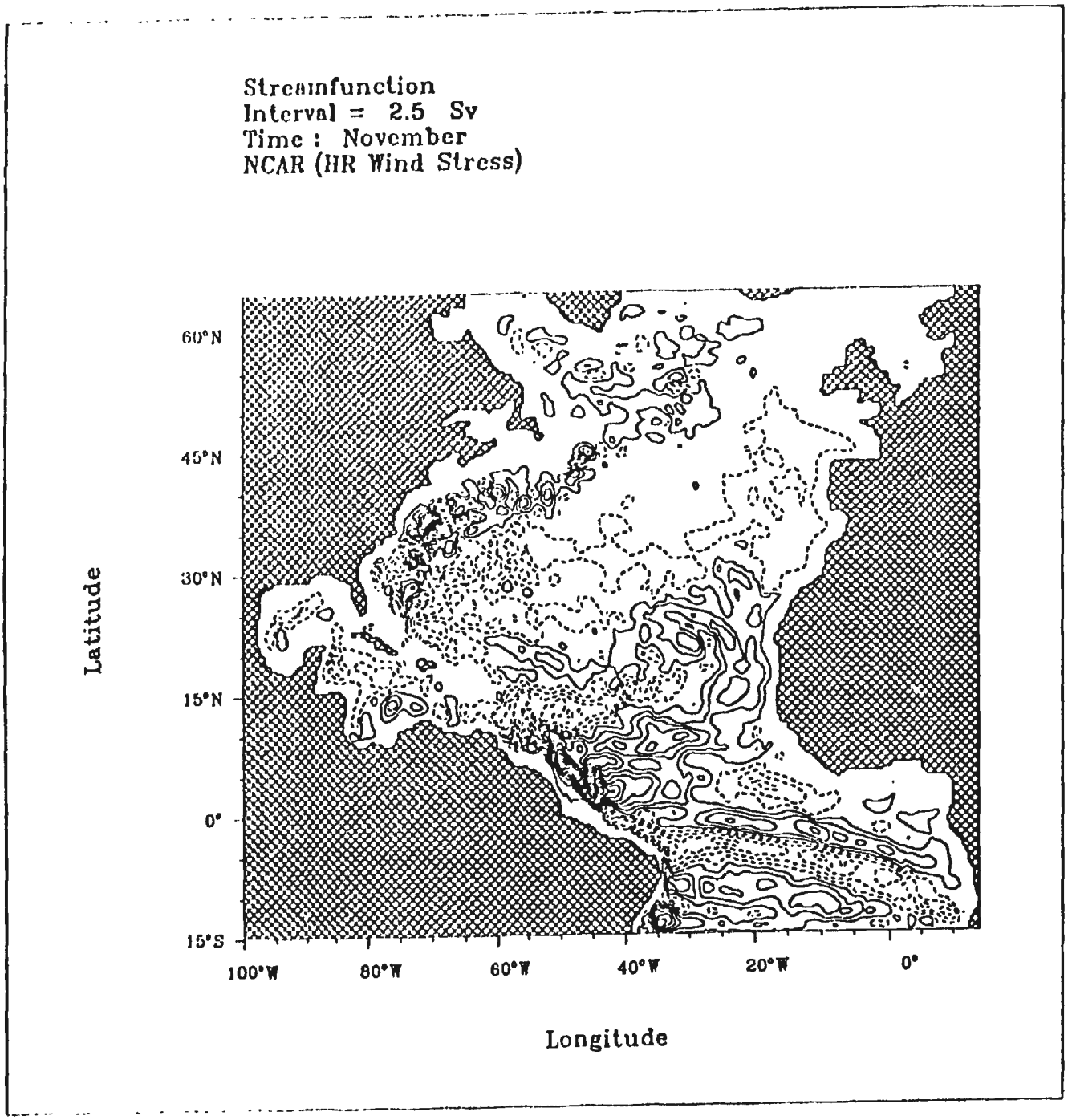

Figure A.5: *continued*

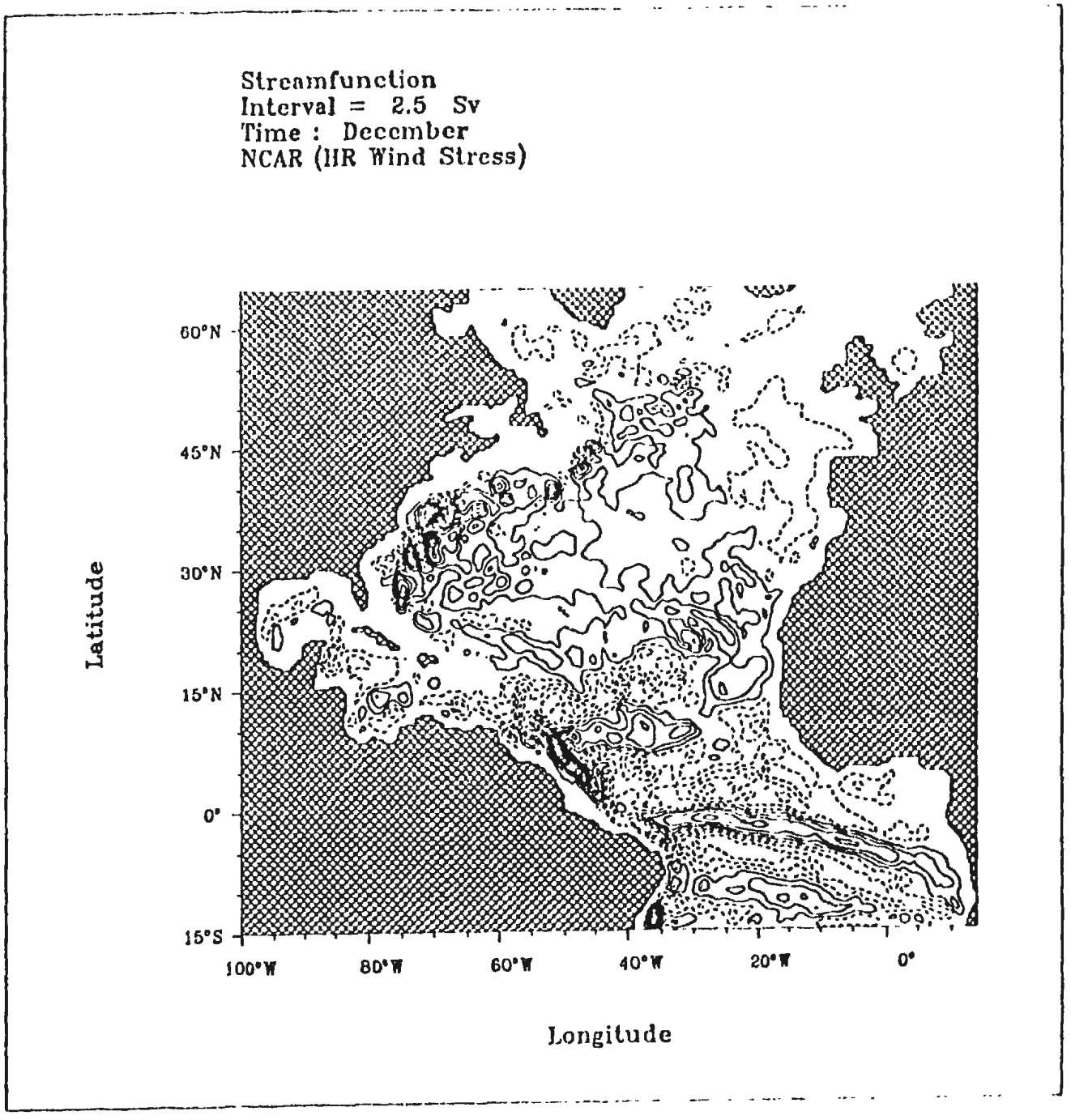

Figure A.5: *continued*

APPENDIX B:

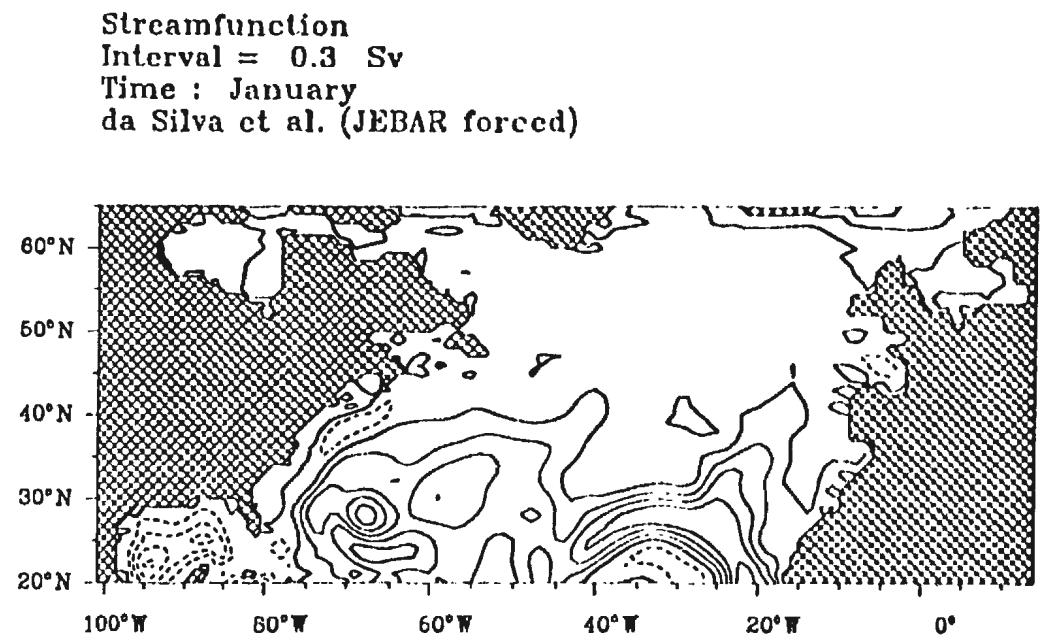

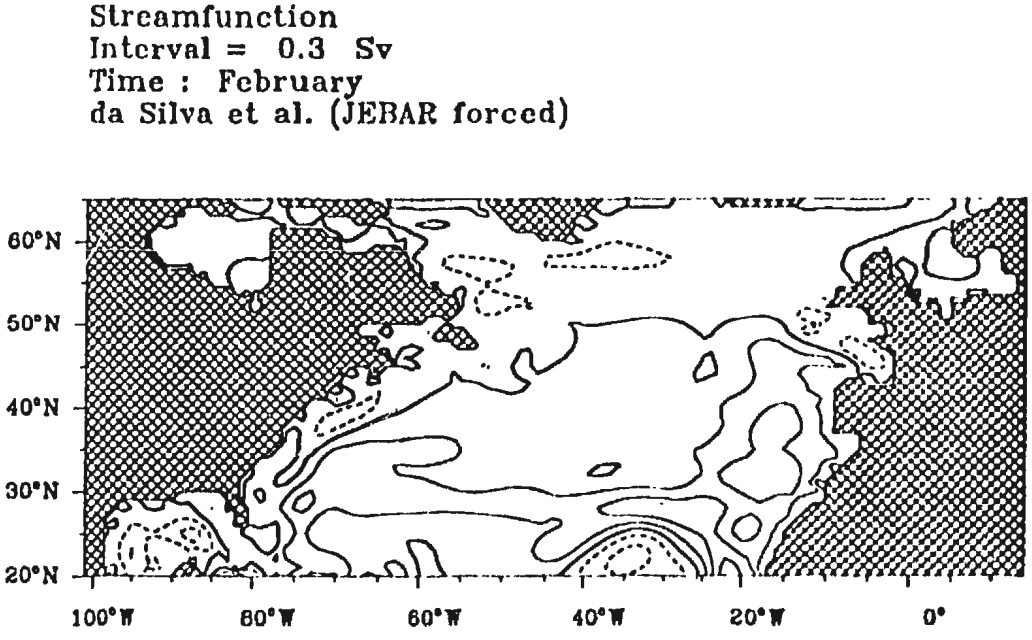

Figure B.1: *Plan views of the anomalous monthly mean transport streamfunction, Ψ, corresponding to the DS wind forced baroclinic response. The contour interval is 0.3 Sv, dashed contours indicate negative values, solid contours positive values.*

Streamfunction
Interval = 0.3 Sv
Time : March
da Silva et al. (JEBAR forced)

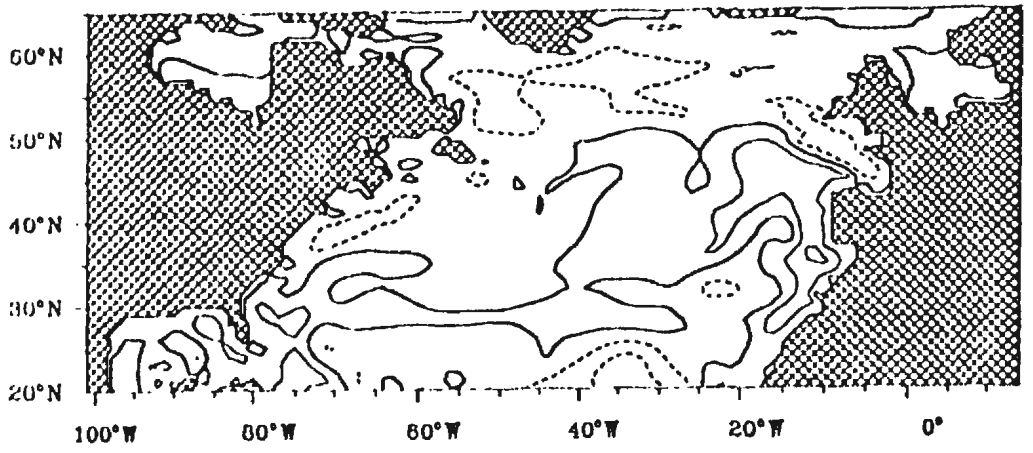

Streamfunction
Interval = 0.3 Sv
Time : April
da Silva et al. (JEBAR forced)

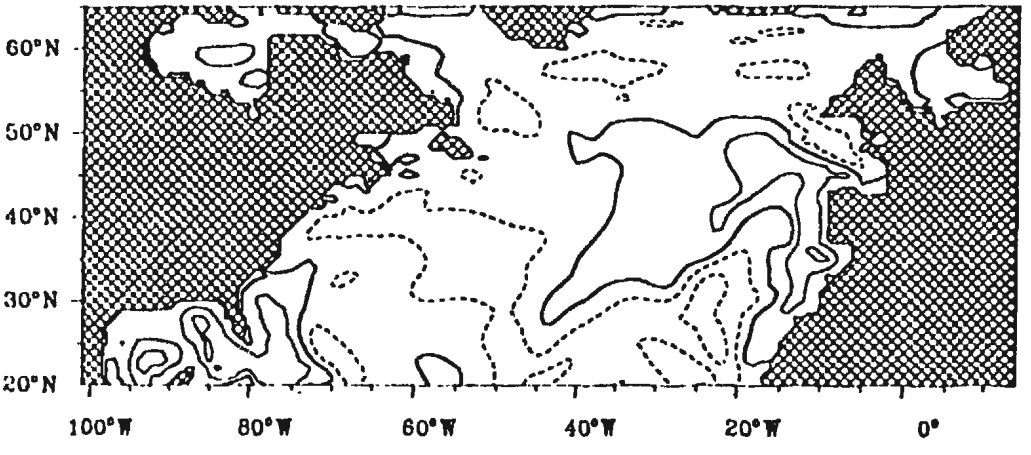

Figure B.1: *continued*

Streamfunction
Interval = 0.3 Sv
Time : May
da Silva et al. (JEBAR forced)

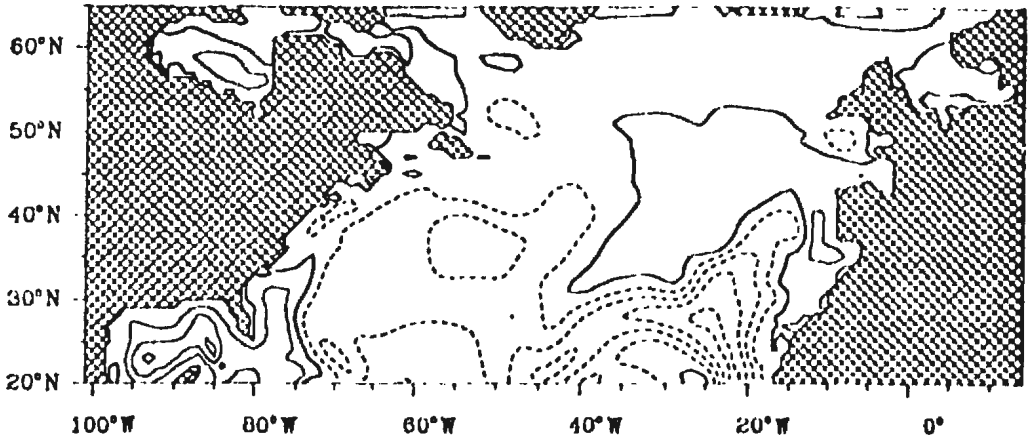

Streamfunction
Interval = 0.3 Sv
Time : June
da Silva et al. (JEBAR forced)

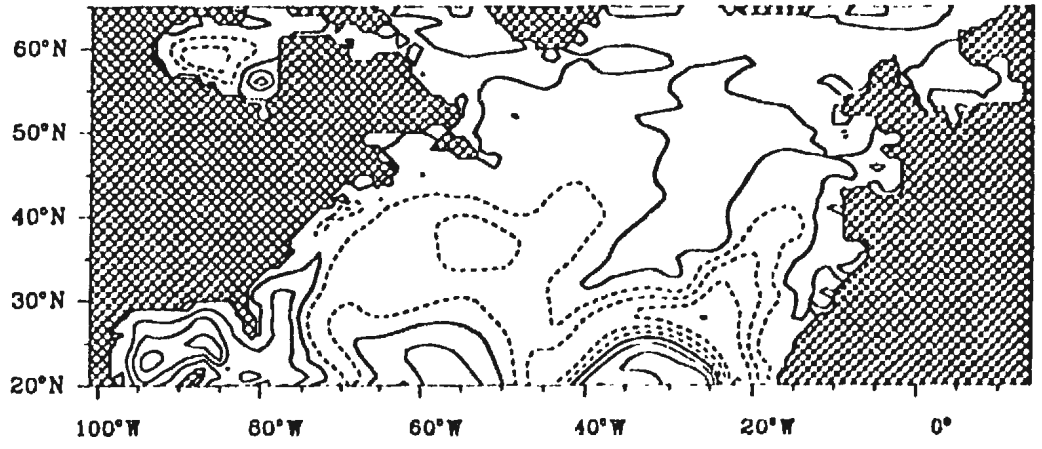

Figure B.1: *continued*

Streamfunction
Interval = 0.3 Sv
Time : July
da Silva et al. (JEBAR forced)

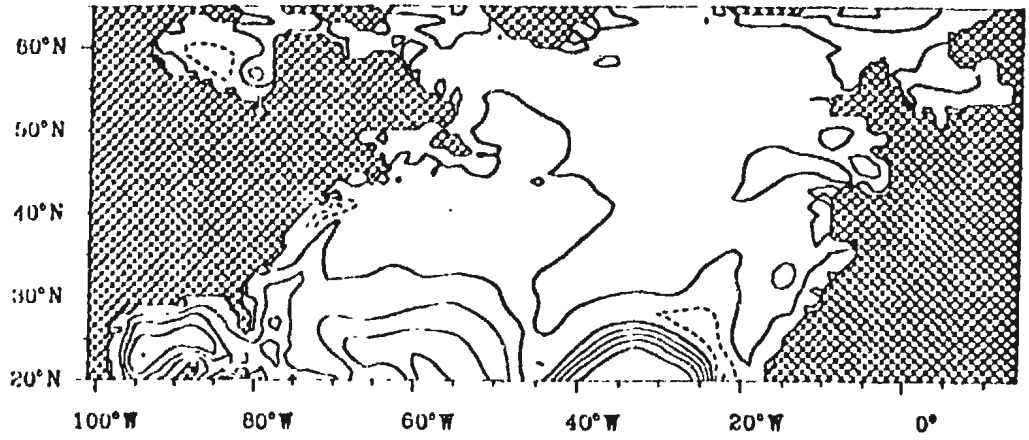

Streamfunction
Interval = 0.3 Sv
Time : August
da Silva et al. (JEBAR forced)

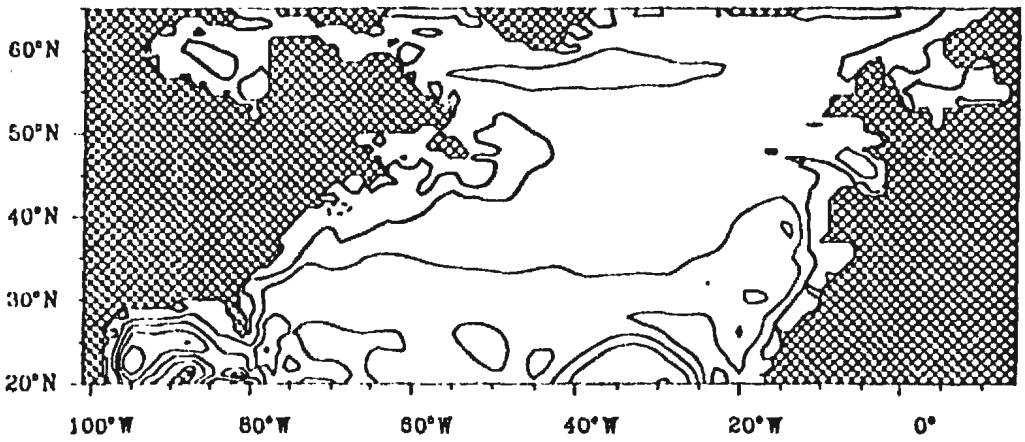

Figure B.1: *continued*

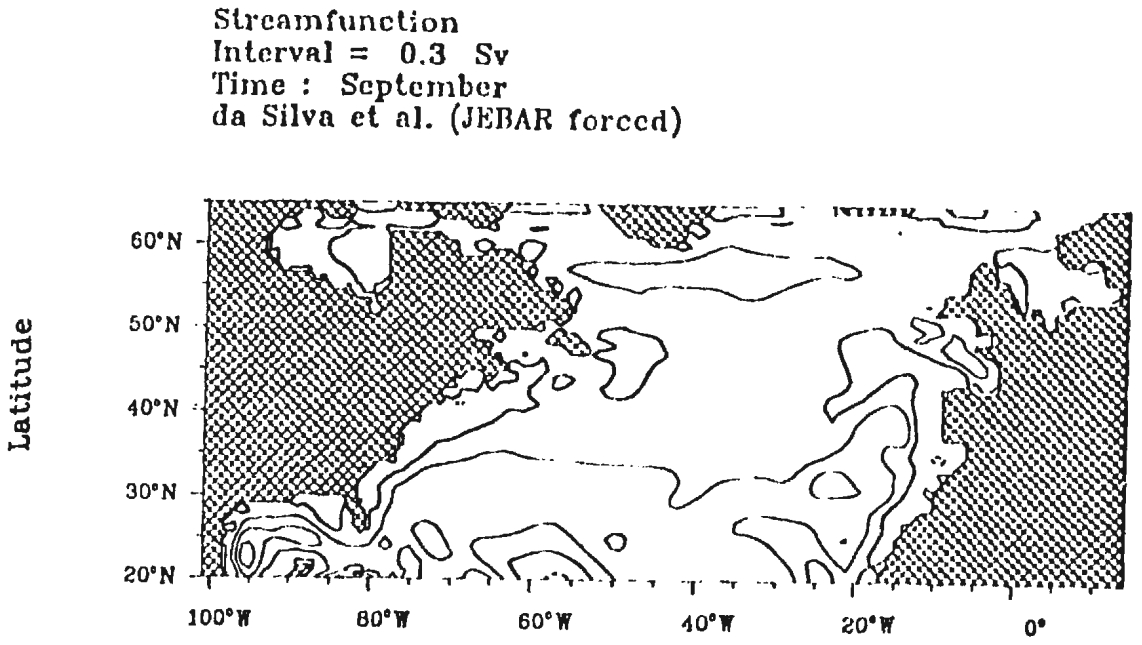

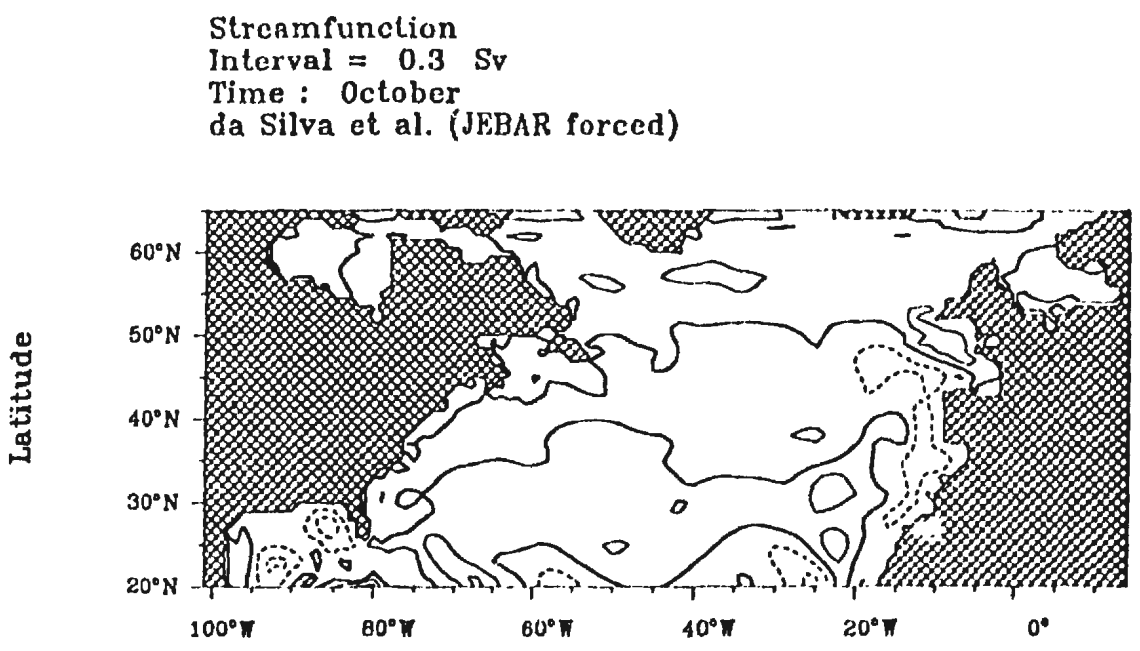

Figure B.1: *continued*

Streamfunction
Interval = 0.3 Sv
Time : November
da Silva et al. (JEBAR forced)

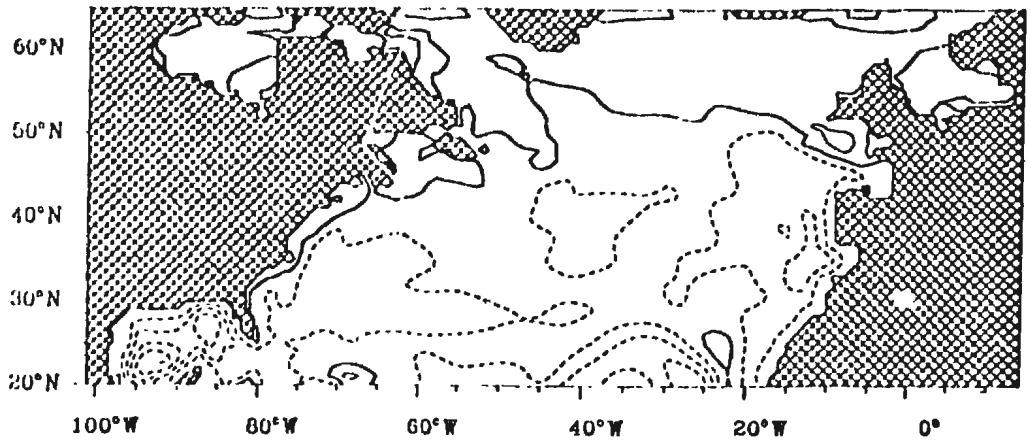

Streamfunction
Interval = 0.3 Sv
Time : December
da Silva et al. (JEBAR forced)

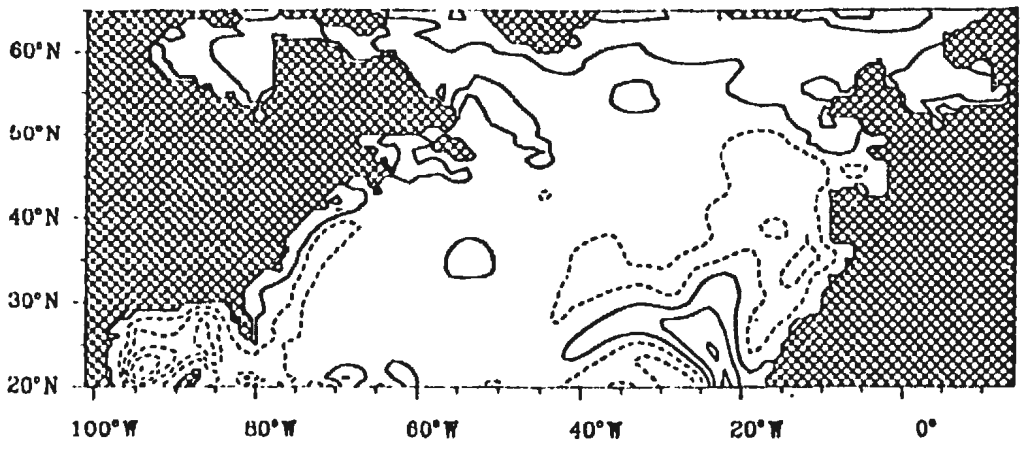

Figure B.1: *continued*

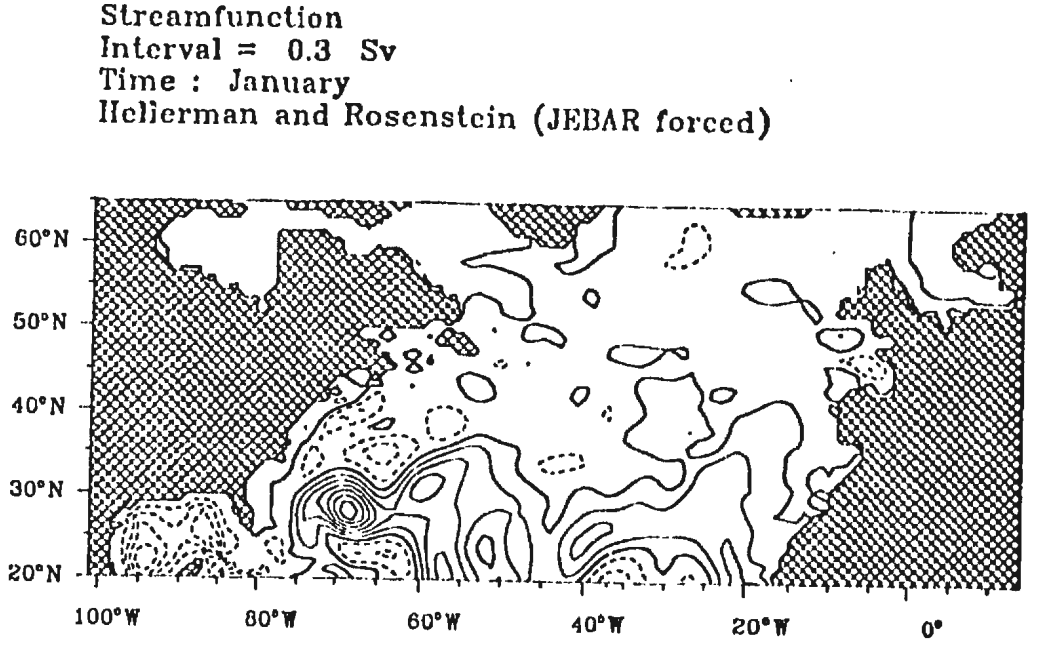

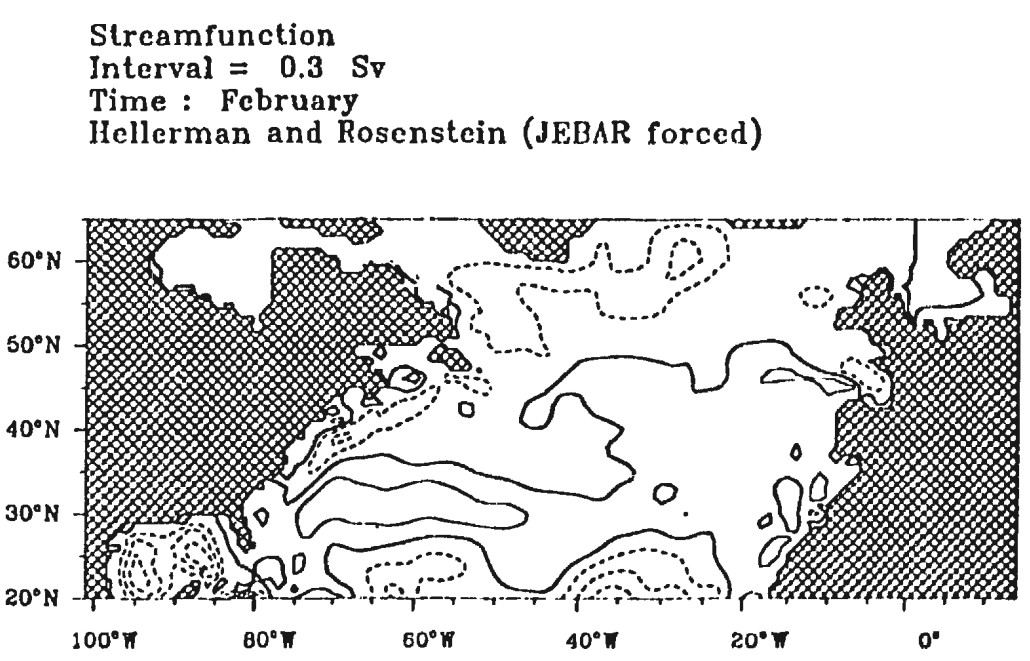

Figure B.2: *As Figure B.1, but for HR wind forcing*

Streamfunction
Interval = 0.3 Sv
Time : March
Hellerman and Rosenstein (JEBAR forced)

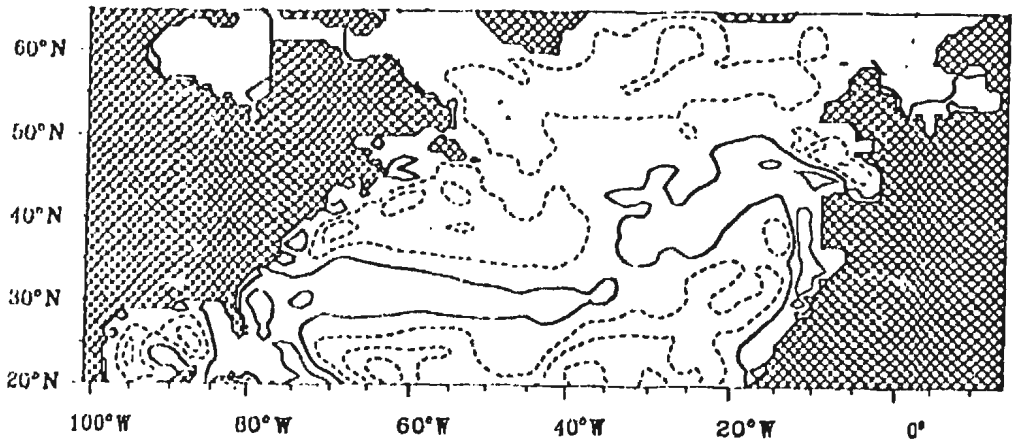

Streamfunction
Interval = 0.3 Sv
Time : April
Hellerman and Rosenstein (JEBAR forced)

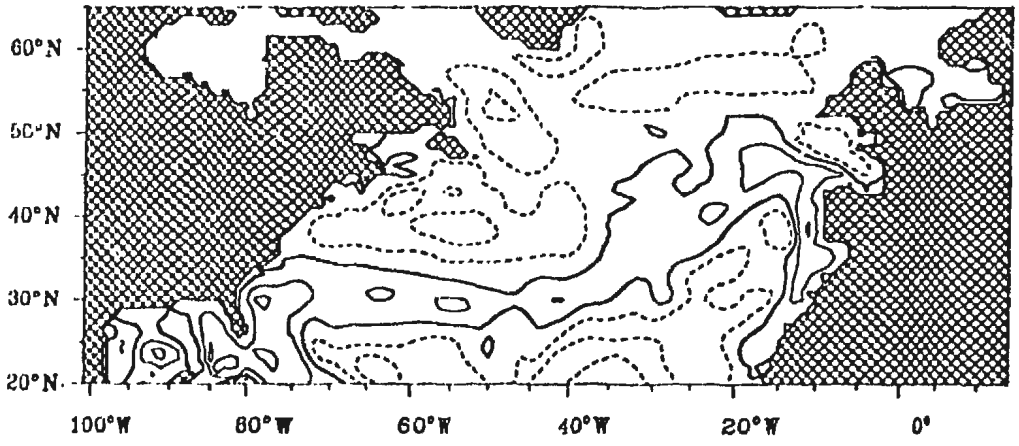

Figure B.2: *continued*

Streamfunction
Interval = 0.3 Sv
Time : May
Hellerman and Rosenstein (JEBAR forced)

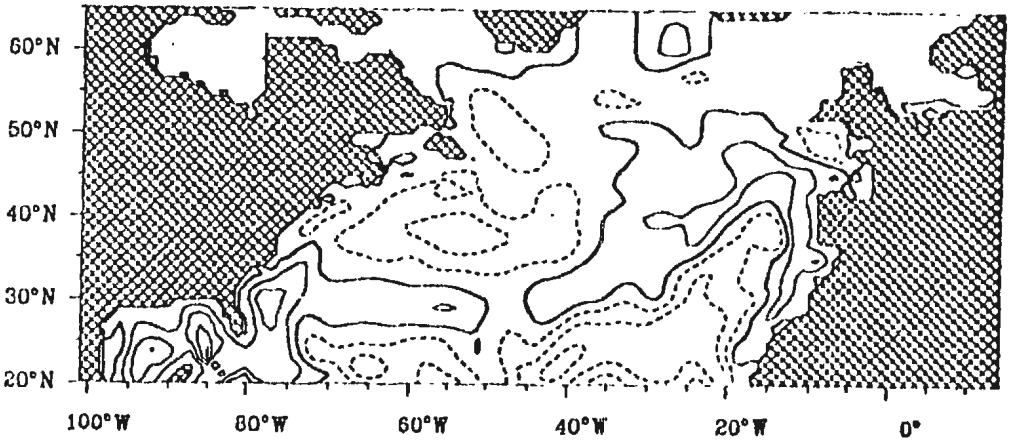

Streamfunction
Interval = 0.3 Sv
Time : June
Hellerman and Rosenstein (JEBAR forced)

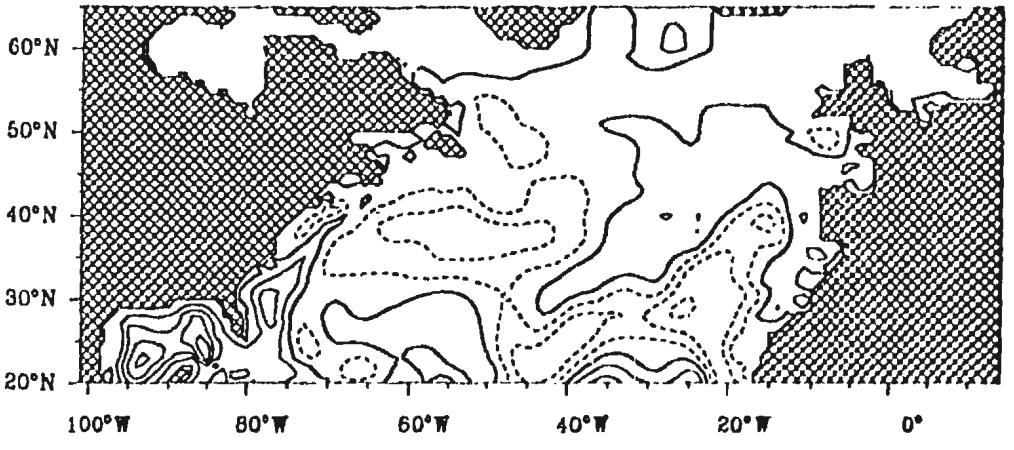

Figure B.2: *continued*

Streamfunction
Interval = 0.3 Sv
Time : July
Hellerman and Rosenstein (JEBAR forced)

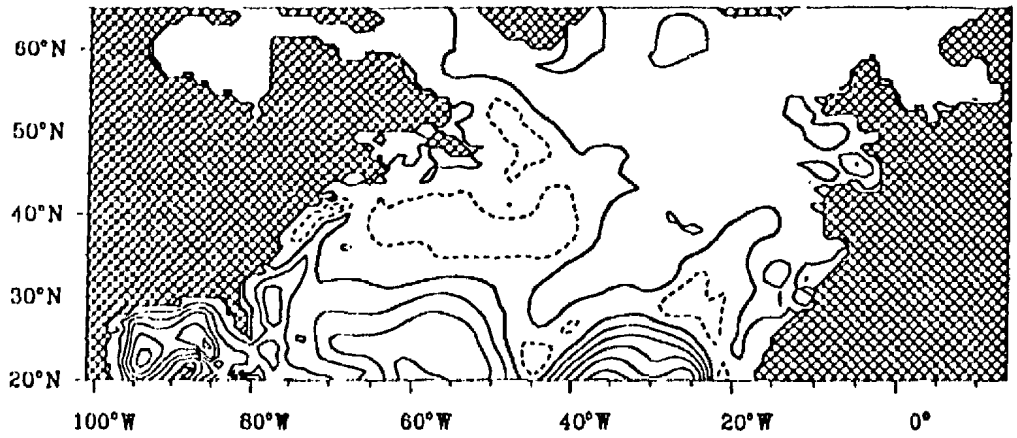

Streamfunction
Interval = 0.3 Sv
Time : August
Hellerman and Rosenstein (JEBAR forced)

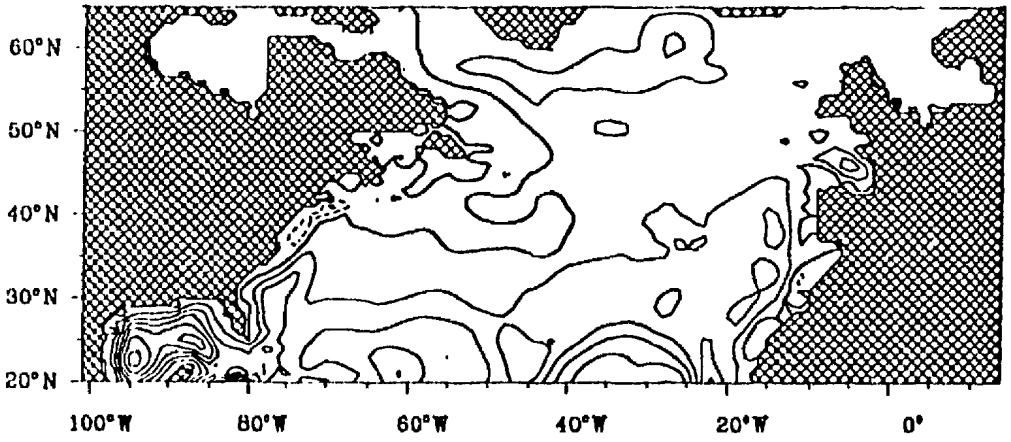

Figure B.2: *continued*

Streamfunction
Interval = 0.3 Sv
Time : September
Hellerman and Rosenstein (JEBAR forced)

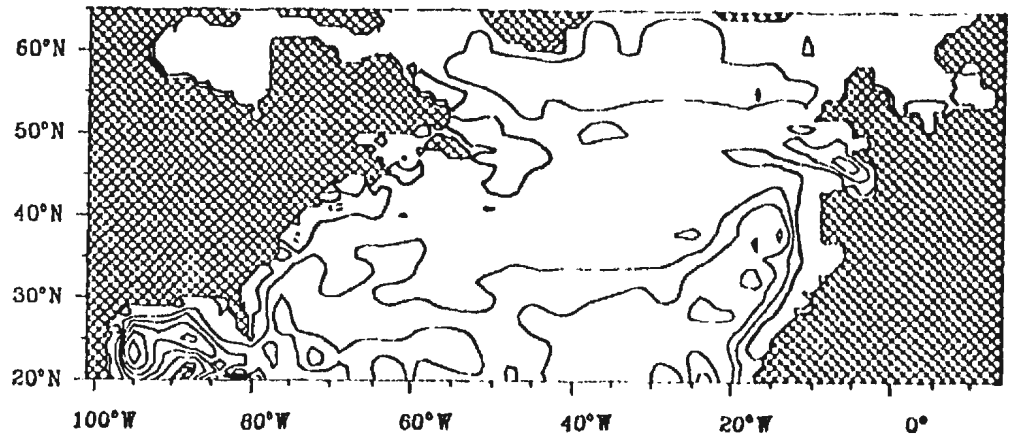

Streamfunction
Interval = 0.3 Sv
Time : October
Hellerman and Rosenstein (JEBAR forced)

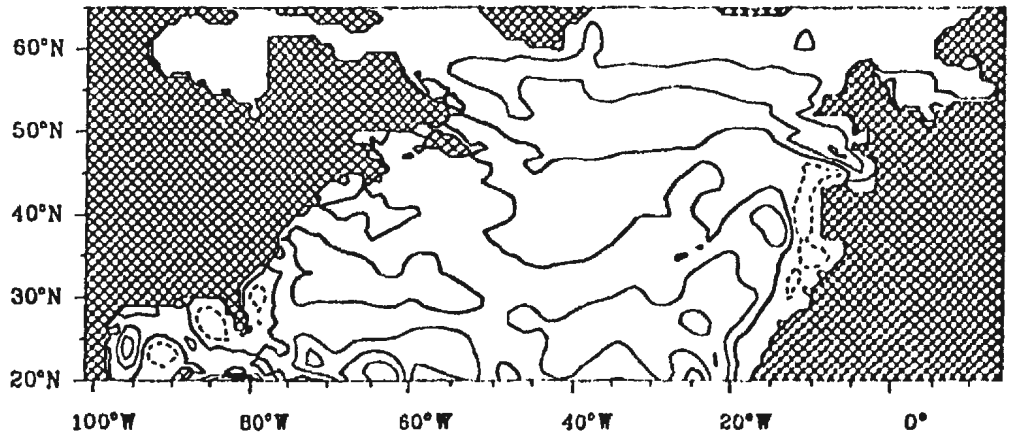

Figure B.2: *continued*

Streamfunction
Interval = 0.3 Sv
Time : November
Hellerman and Rosenstein (JEBAR forced)

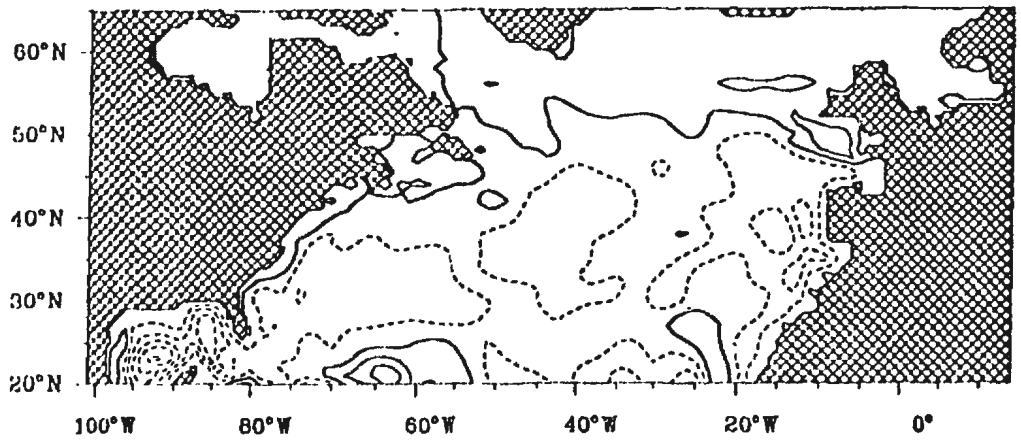

Streamfunction
Interval = 0.3 Sv
Time : December
Hellerman and Rosenstein (JEBAR forced)

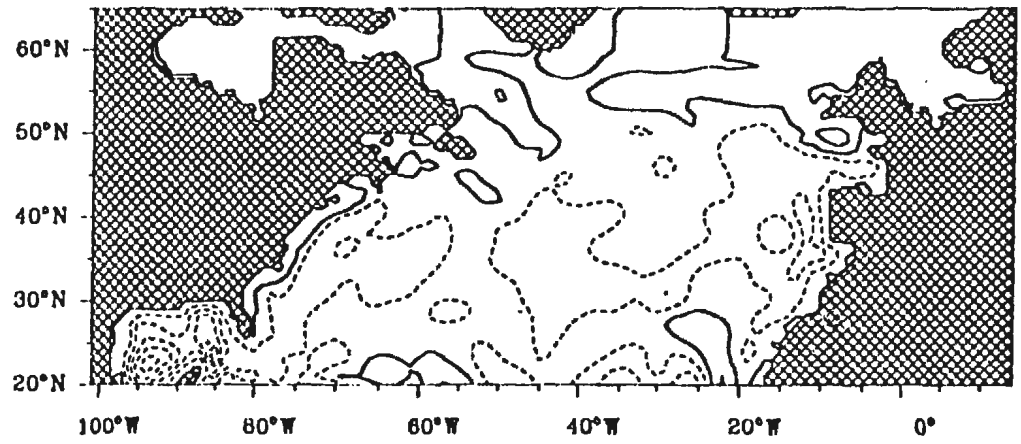

Figure B.2: *continued*

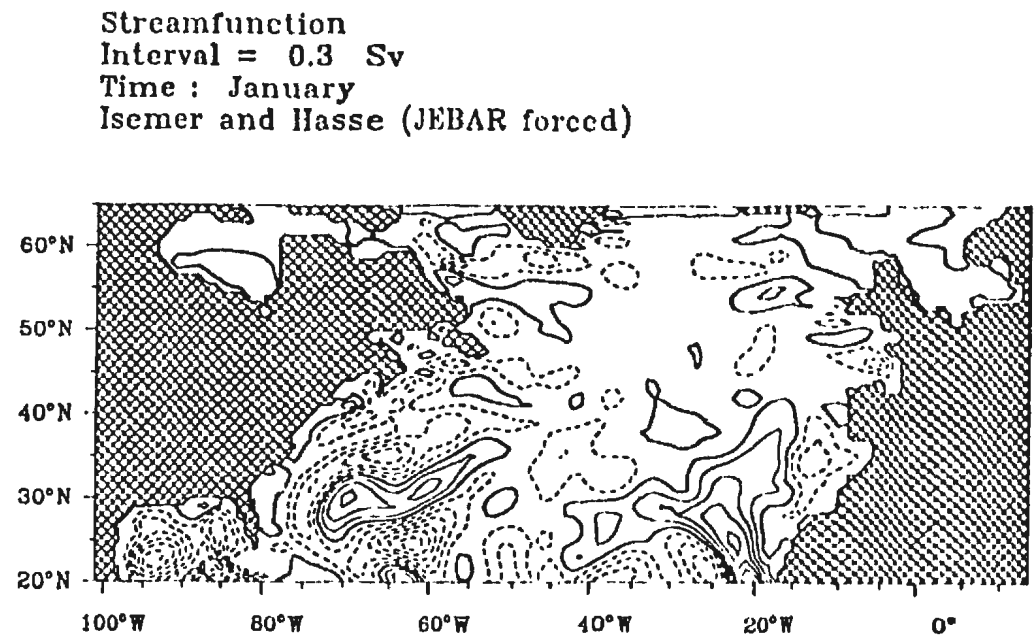

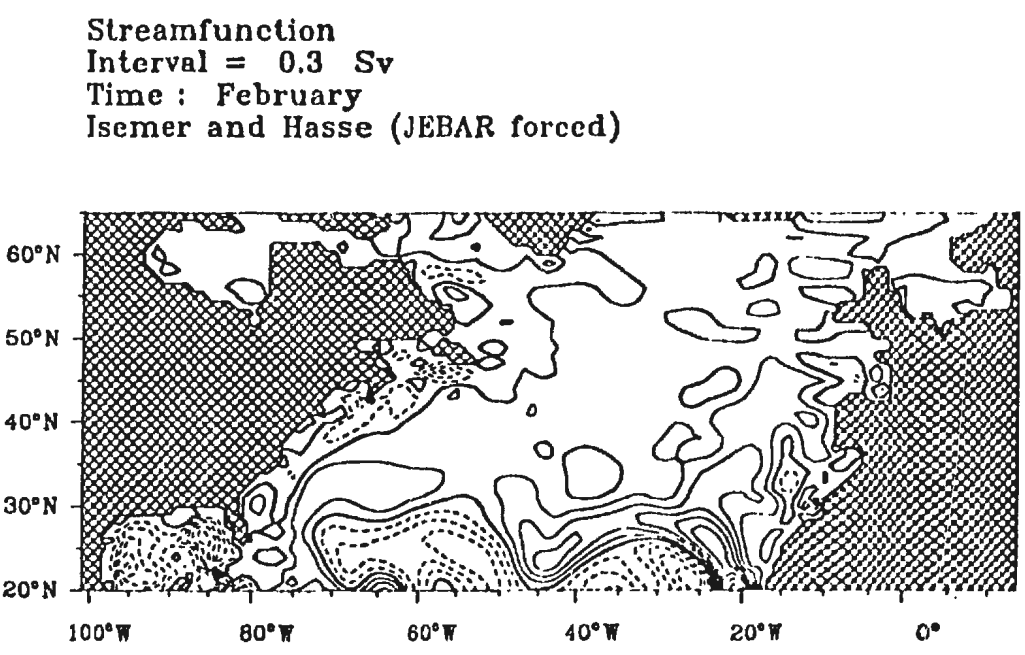

Figure B.3: *As Figure B.1, but for III wind forcing*

Streamfunction
Interval = 0.3 Sv
Time : March
Isemer and Hasse (JEBAR forced)

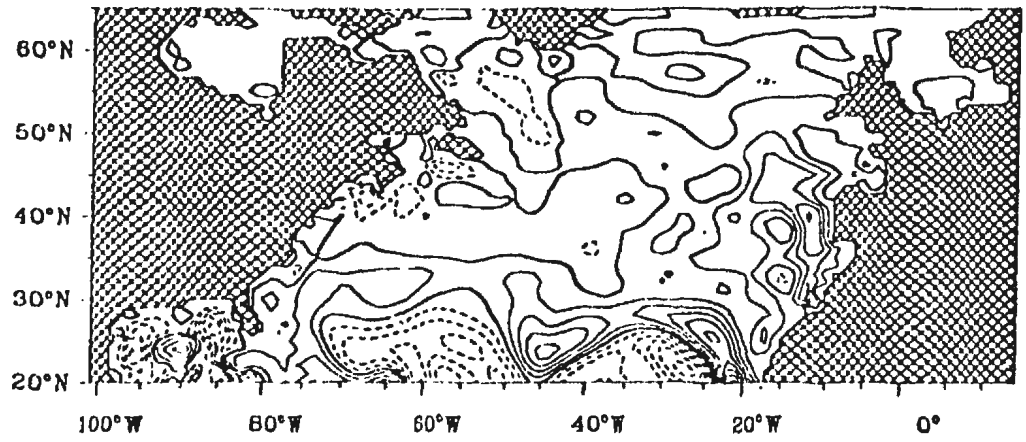

Streamfunction
Interval = 0.3 Sv
Time : April
Isemer and Hasse (JEBAR forced)

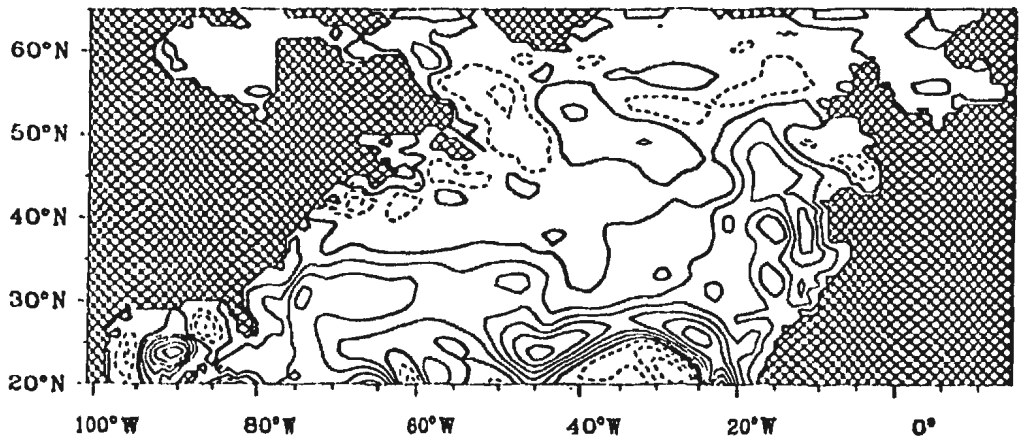

Figure B.3: *continued*

Streamfunction
Interval = 0.3 Sv
Time : May
Isemer and Hasse (JEBAR forced)

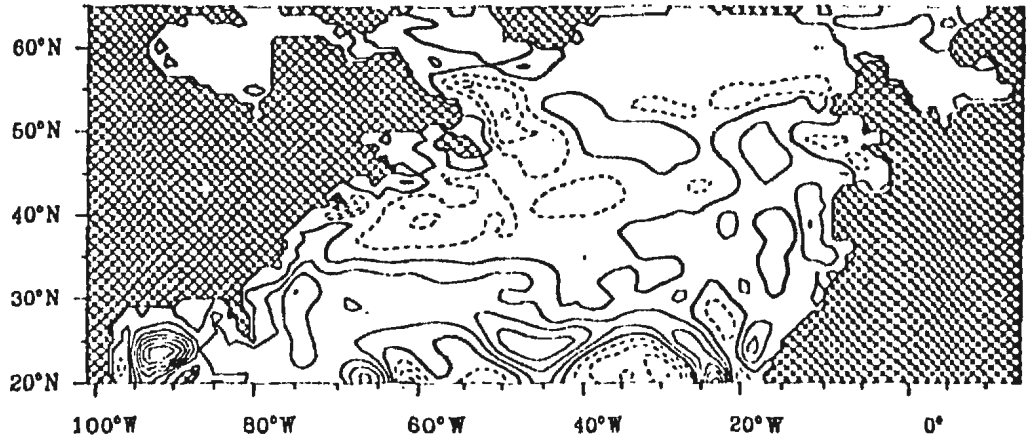

Streamfunction
Interval = 0.3 Sv
Time : June
Isemer and Hasse (JEBAR forced)

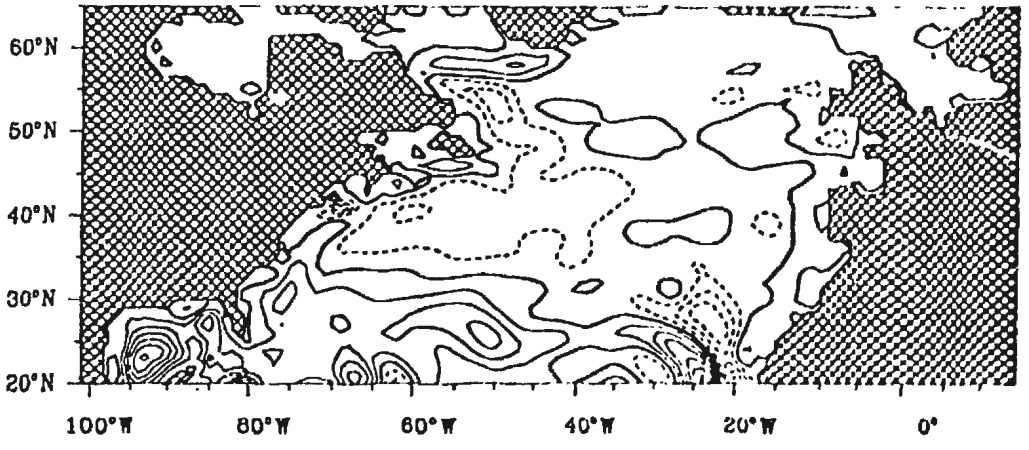

Figure B.3: *continued*

Streamfunction
Interval = 0.3 Sv
Time : July
Isemer and Hasse (JEBAR forced)

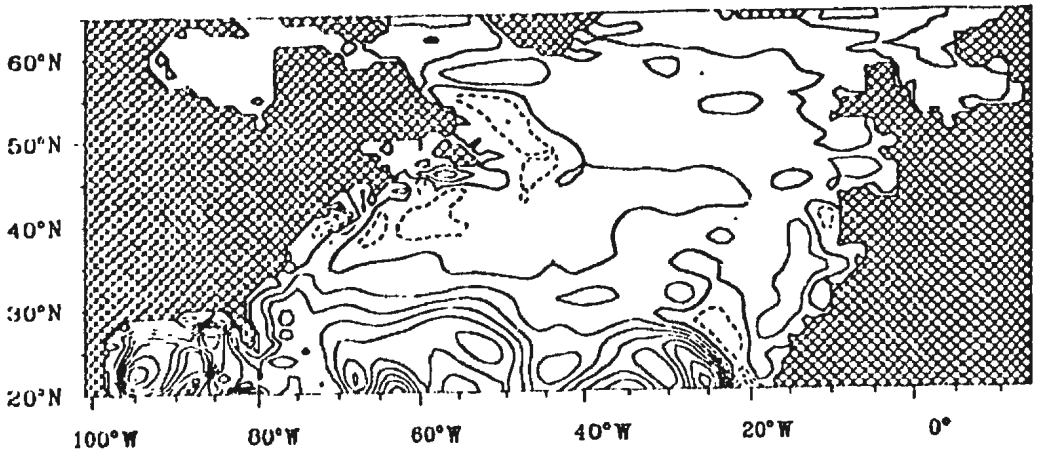

Streamfunction
Interval = 0.3 Sv
Time : August
Isemer and Hasse (JEBAR forced)

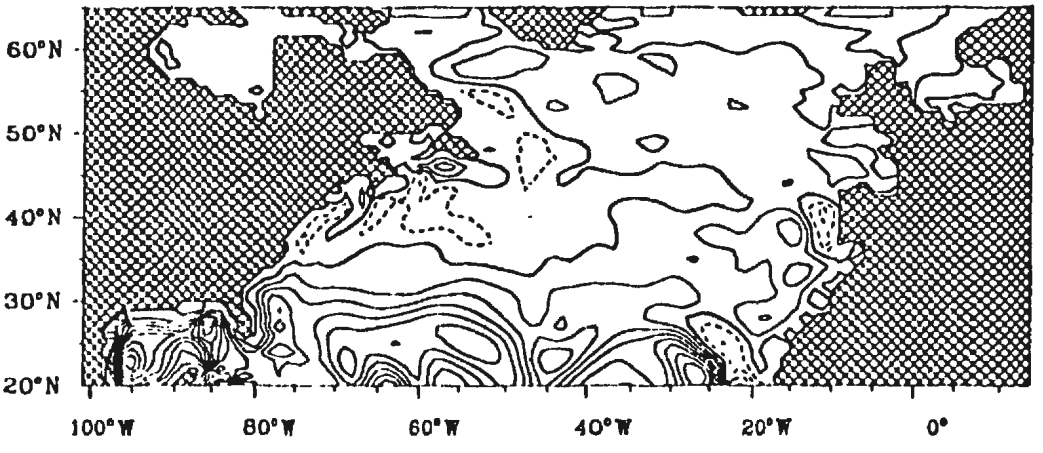

Figure B.3: *continued*

Streamfunction
Interval = 0.3 Sv
Time : September
Isemer and Hasse (JEBAR forced)

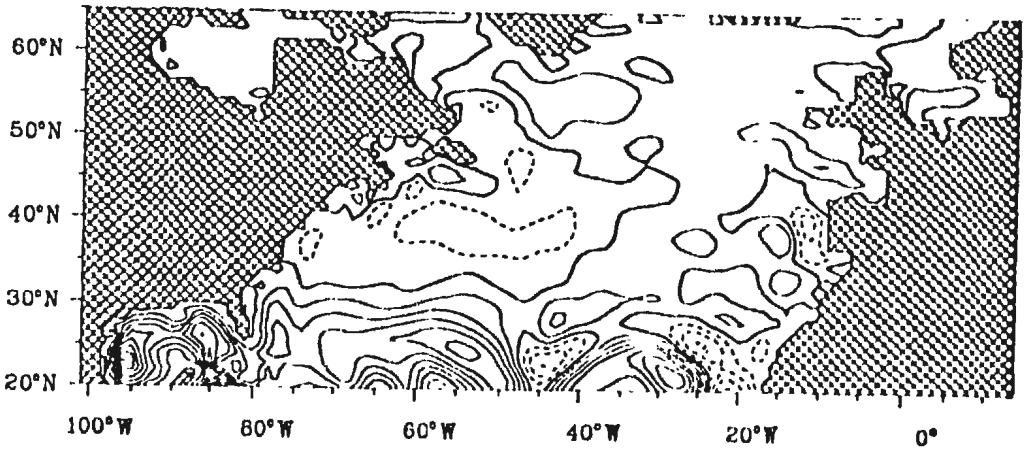

Streamfunction
Interval = 0.3 Sv
Time : October
Isemer and Hasse (JEBAR forced)

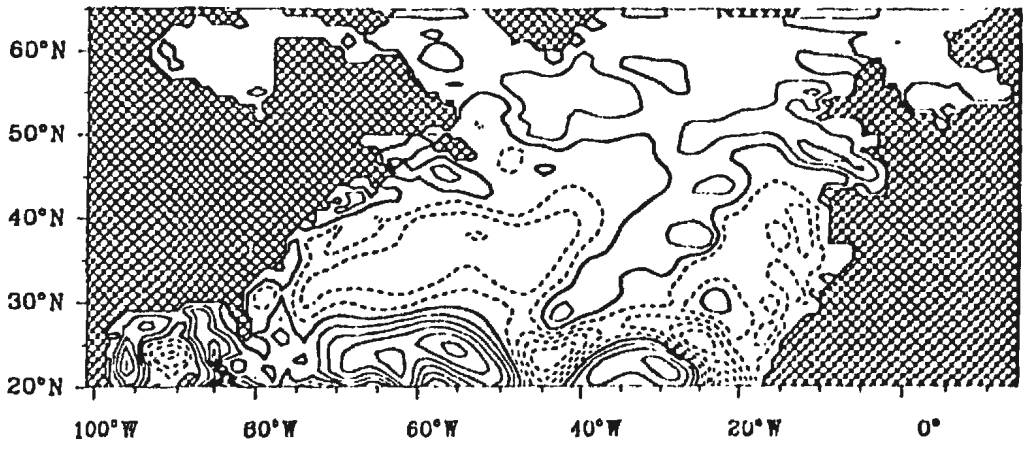

Figure B.3: *continued*

Streamfunction
Interval = 0.3 Sv
Time : November
Isemer and Hasse (JEBAR forced)

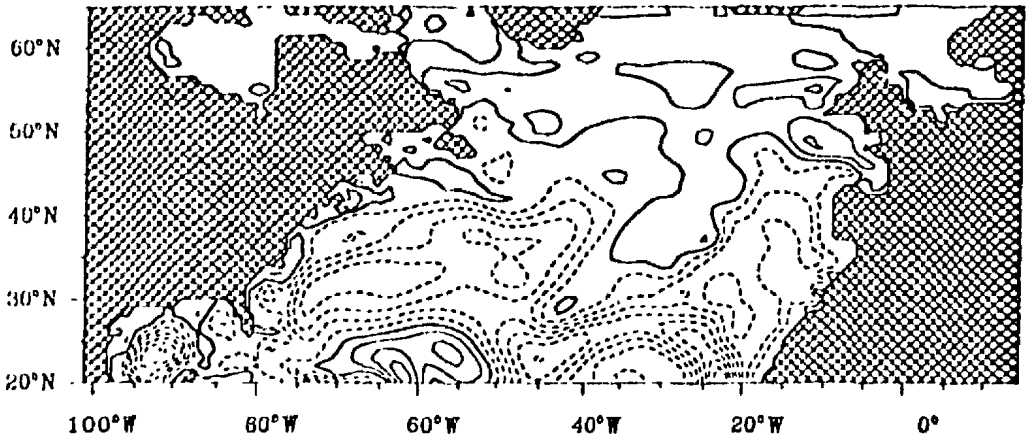

Streamfunction
Interval = 0.3 Sv
Time : December
Isemer and Hasse (JEBAR forced)

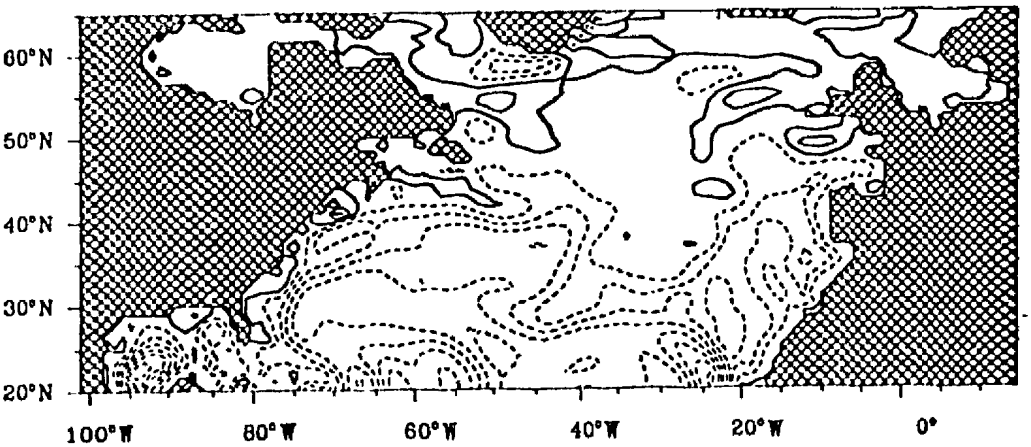

Figure B.3: *continued*

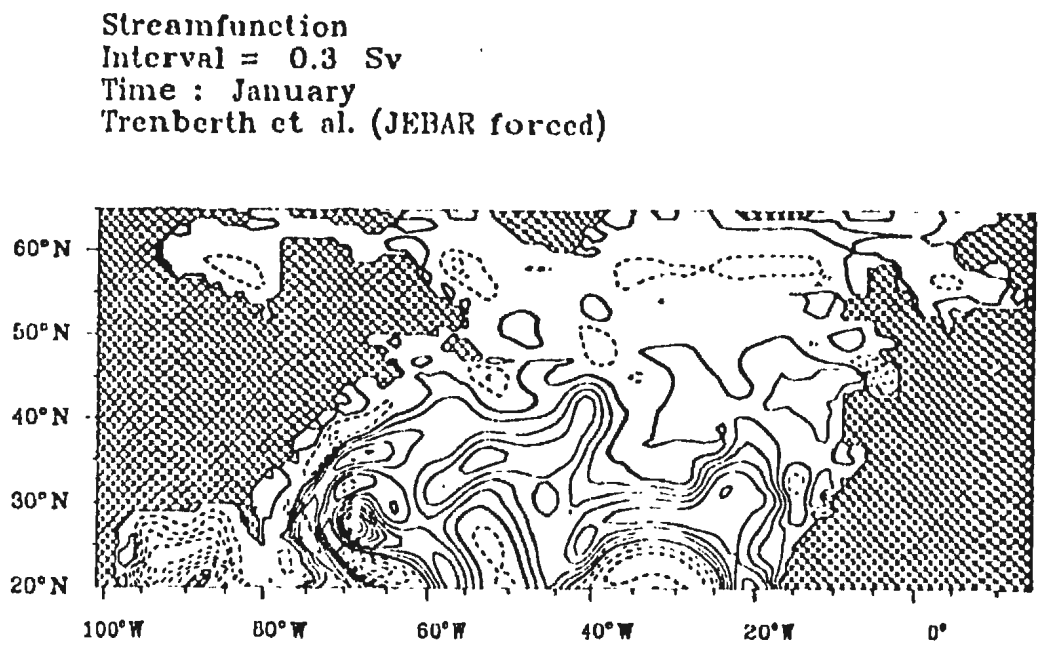

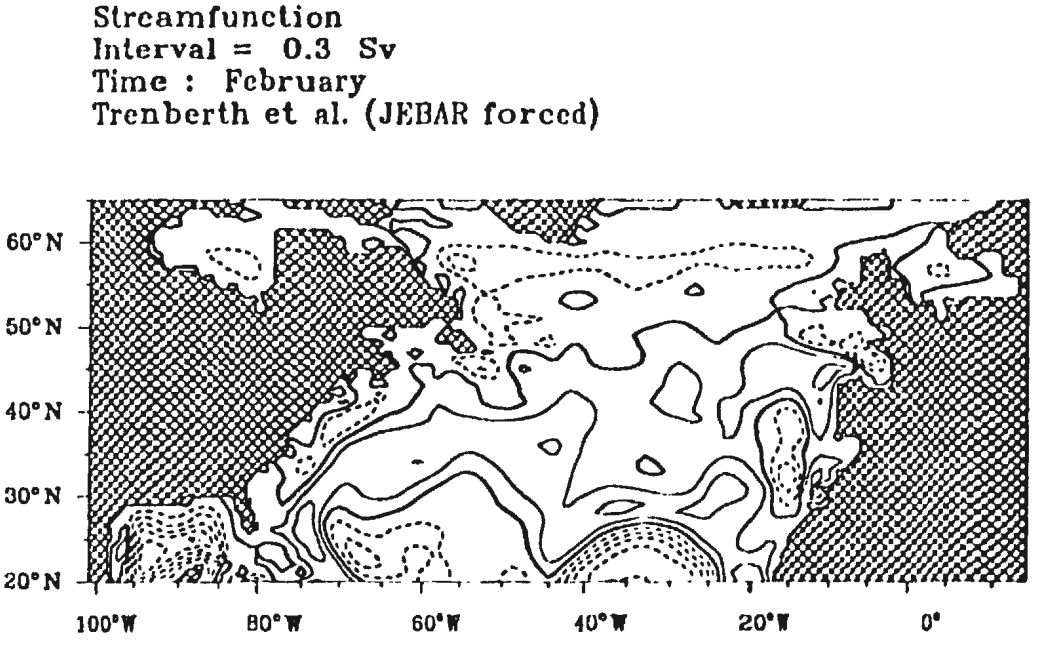

Figure B.4: *As Figure B.1, but for TR wind forcing*

Streamfunction
Interval = 0.3 Sv
Time : March
Trenberth et al. (JEBAR forced)

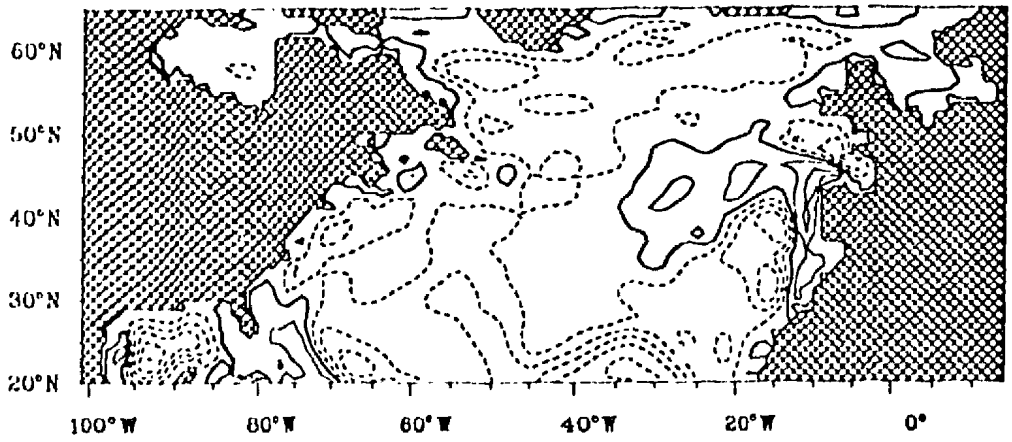

Streamfunction
Interval = 0.3 Sv
Time : April
Trenberth et al. (JEBAR forced)

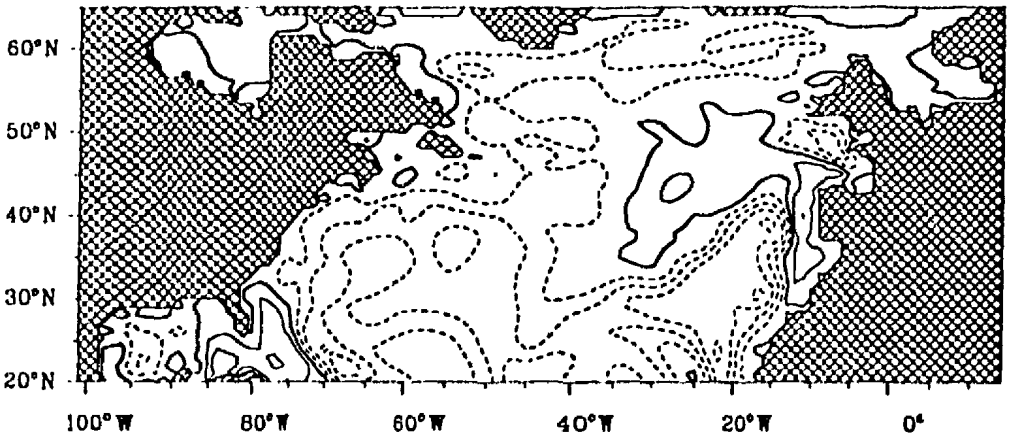

Figure B.4: *continued*

Streamfunction
Interval = 0.3 Sv
Time : May
Trenberth et al. (JEBAR forced)

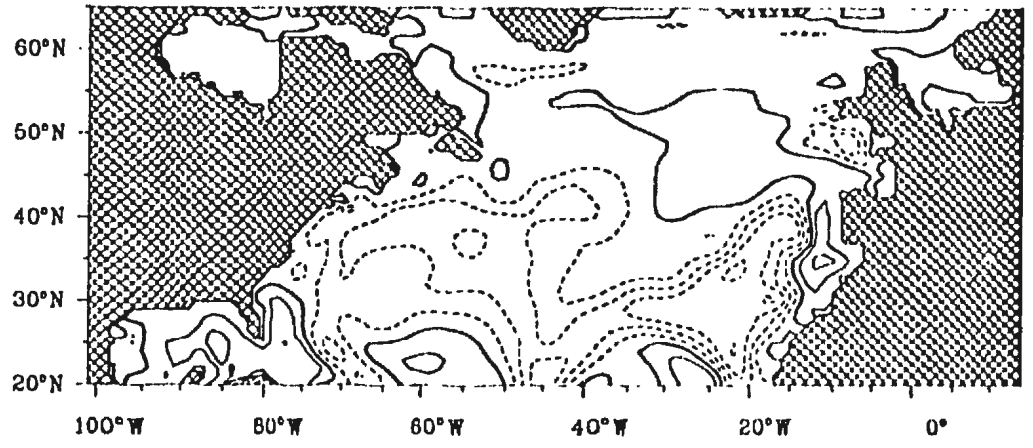

Streamfunction
Interval = 0.3 Sv
Time : June
Trenberth et al. (JEBAR forced)

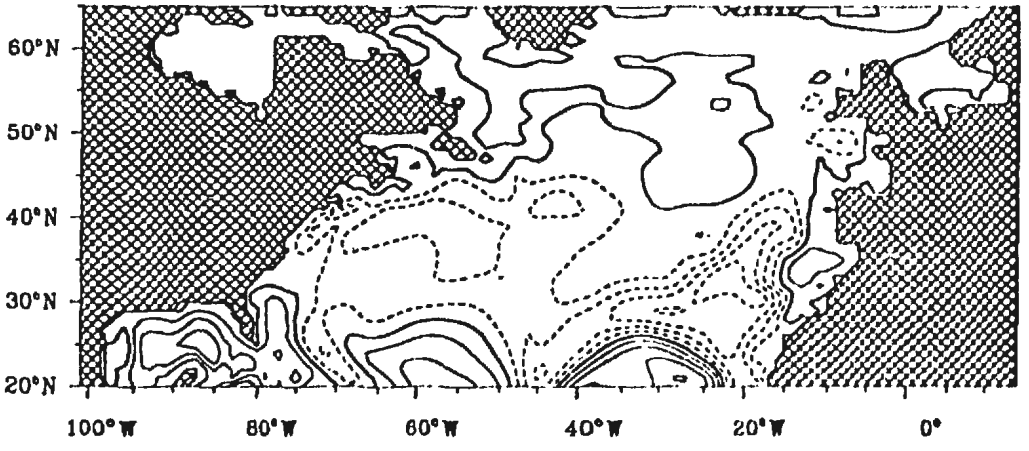

Figure B.4: *continued*

Streamfunction
Interval = 0.3 Sv
Time : July
Trenberth et al. (JEBAR forced)

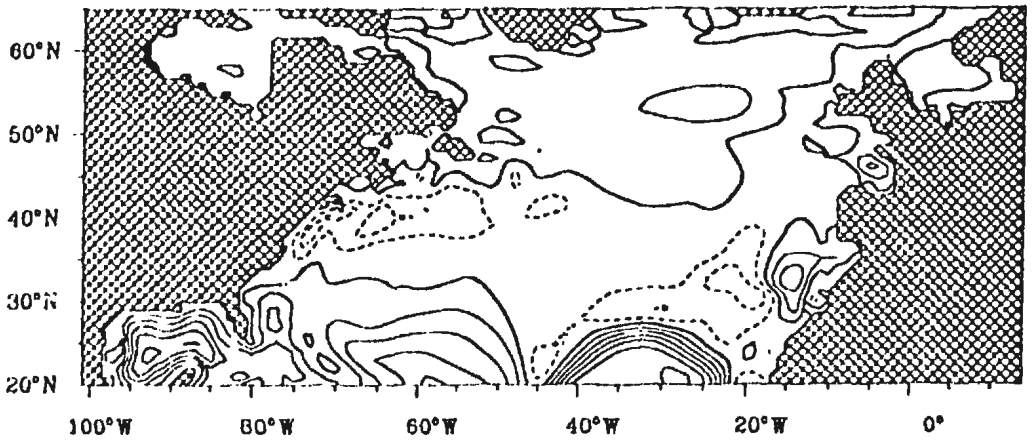

Streamfunction
Interval = 0.3 Sv
Time : August
Trenberth et al. (JEBAR forced)

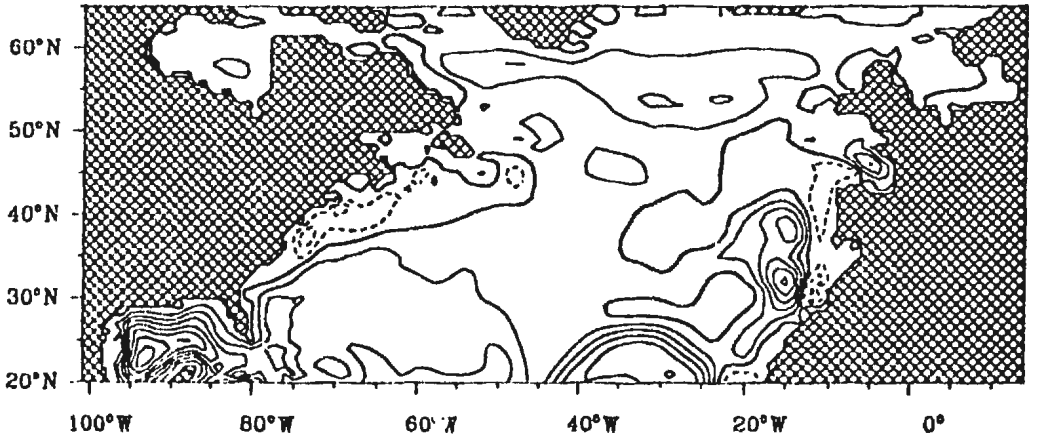

Figure B.4: *continued*

Streamfunction
Interval = 0.3 Sv
Time : September
Trenberth et al. (JEBAR forced)

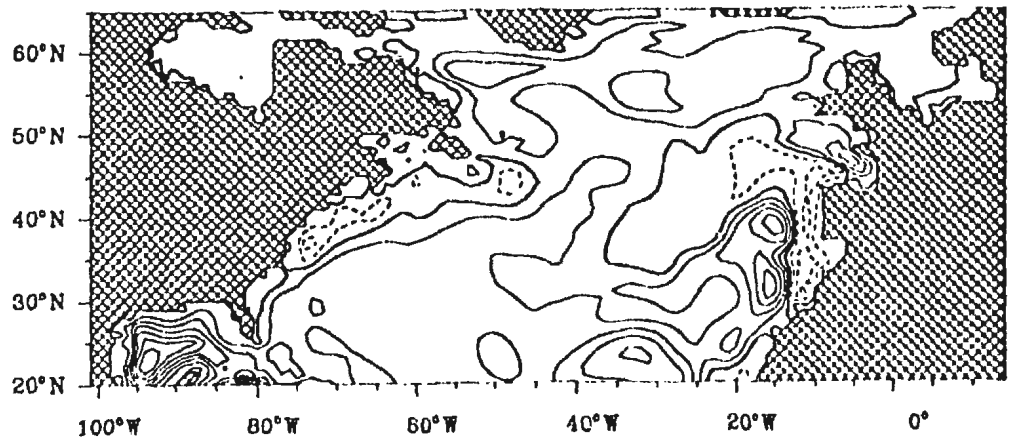

Streamfunction
Interval = 0.3 Sv
Time : October
Trenberth et al. (JEBAR forced)

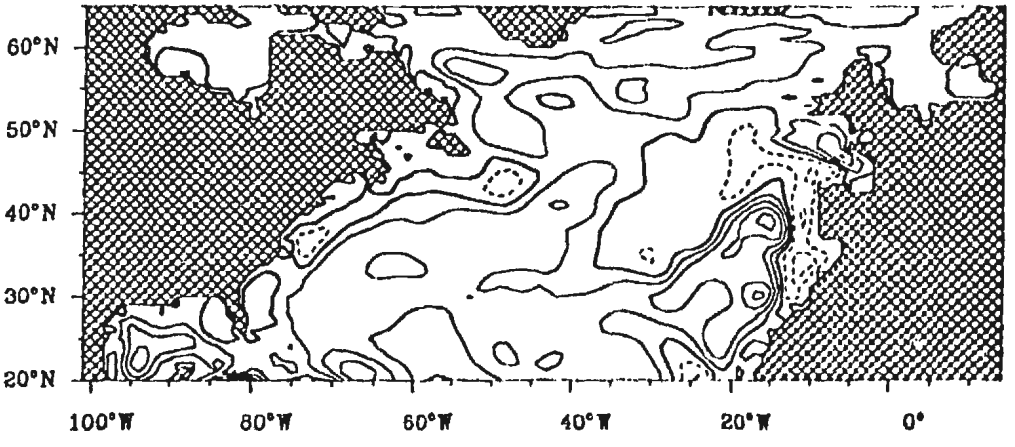

Figure B.4: *continued*

Streamfunction
Interval = 0.3 Sv
Time : November
Trenberth et al. (JEBAR forced)

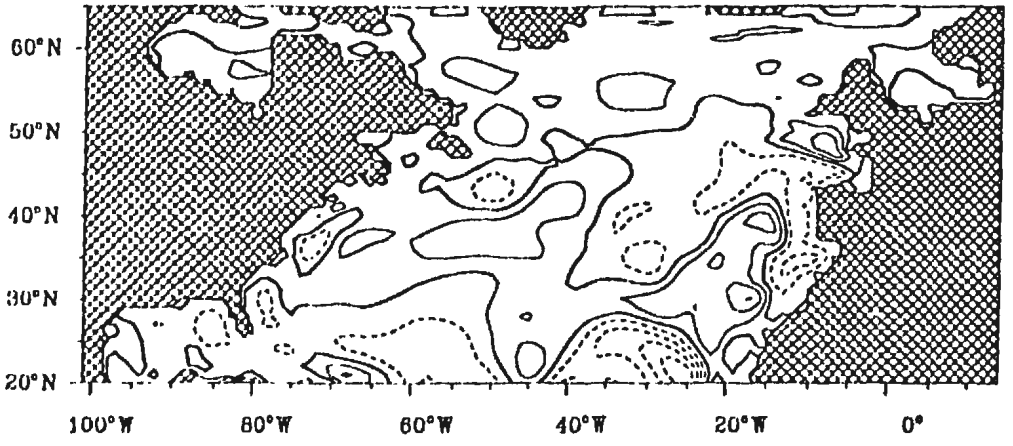

Streamfunction
Interval = 0.3 Sv
Time : December
Trenberth et al. (JEBAR forced)

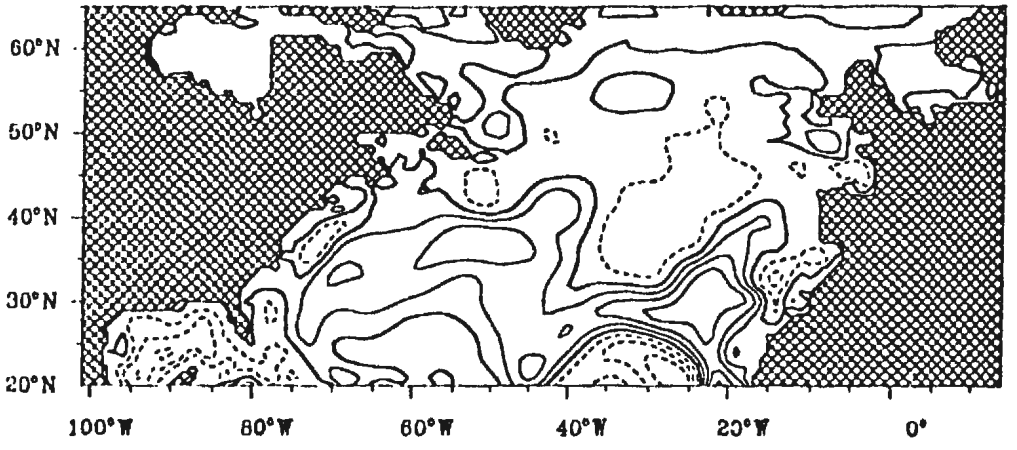

Figure B.4: *continued*

APPENDIX C:

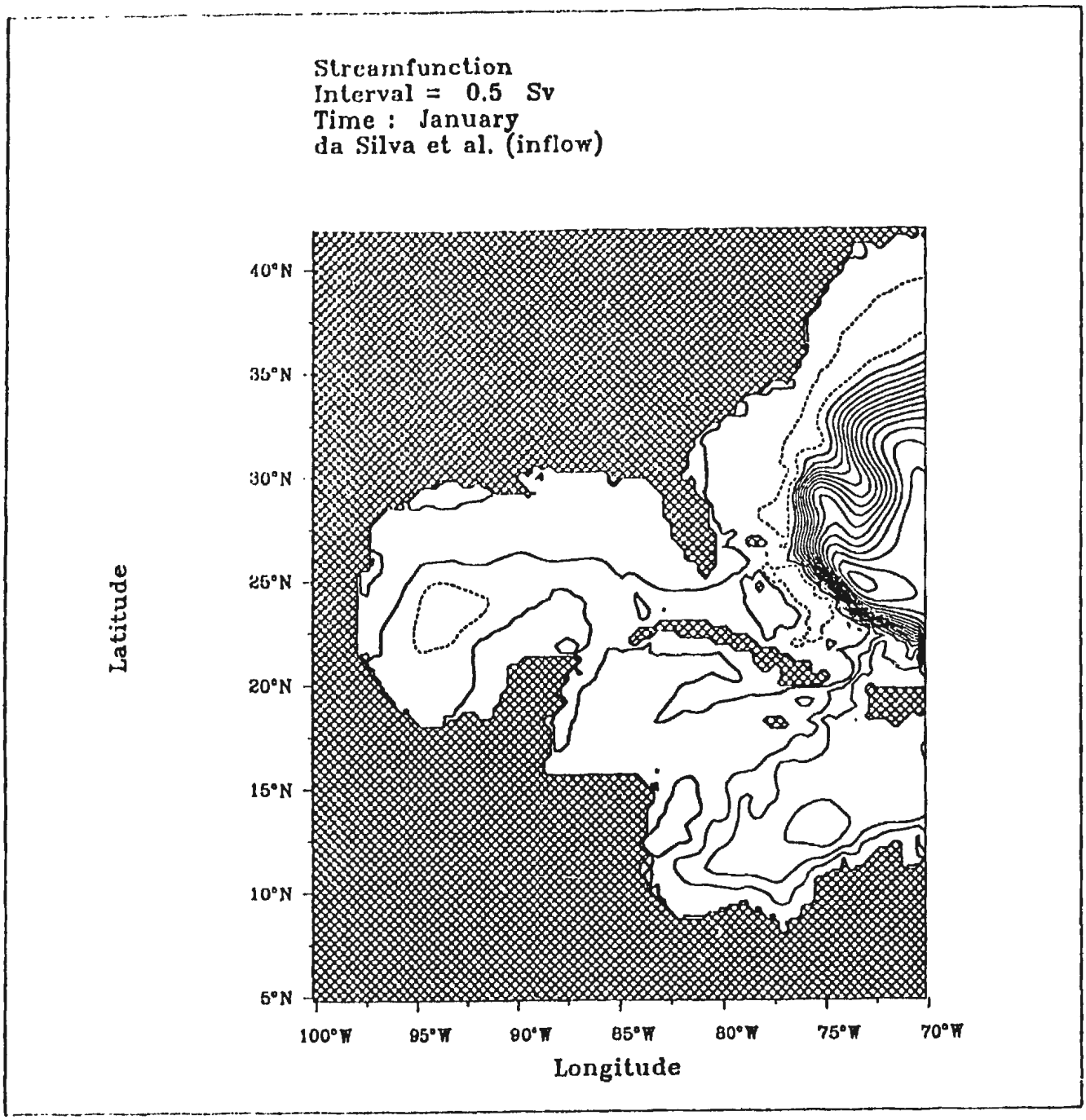

Figure C.1: *Plan-view of the model-calculated transport (Sv) in January, for the (a) "inflow" and (b) "no inlfow" cases for each of the seasonal climatologies of DS; IIR; III; and TR (see text for details).*

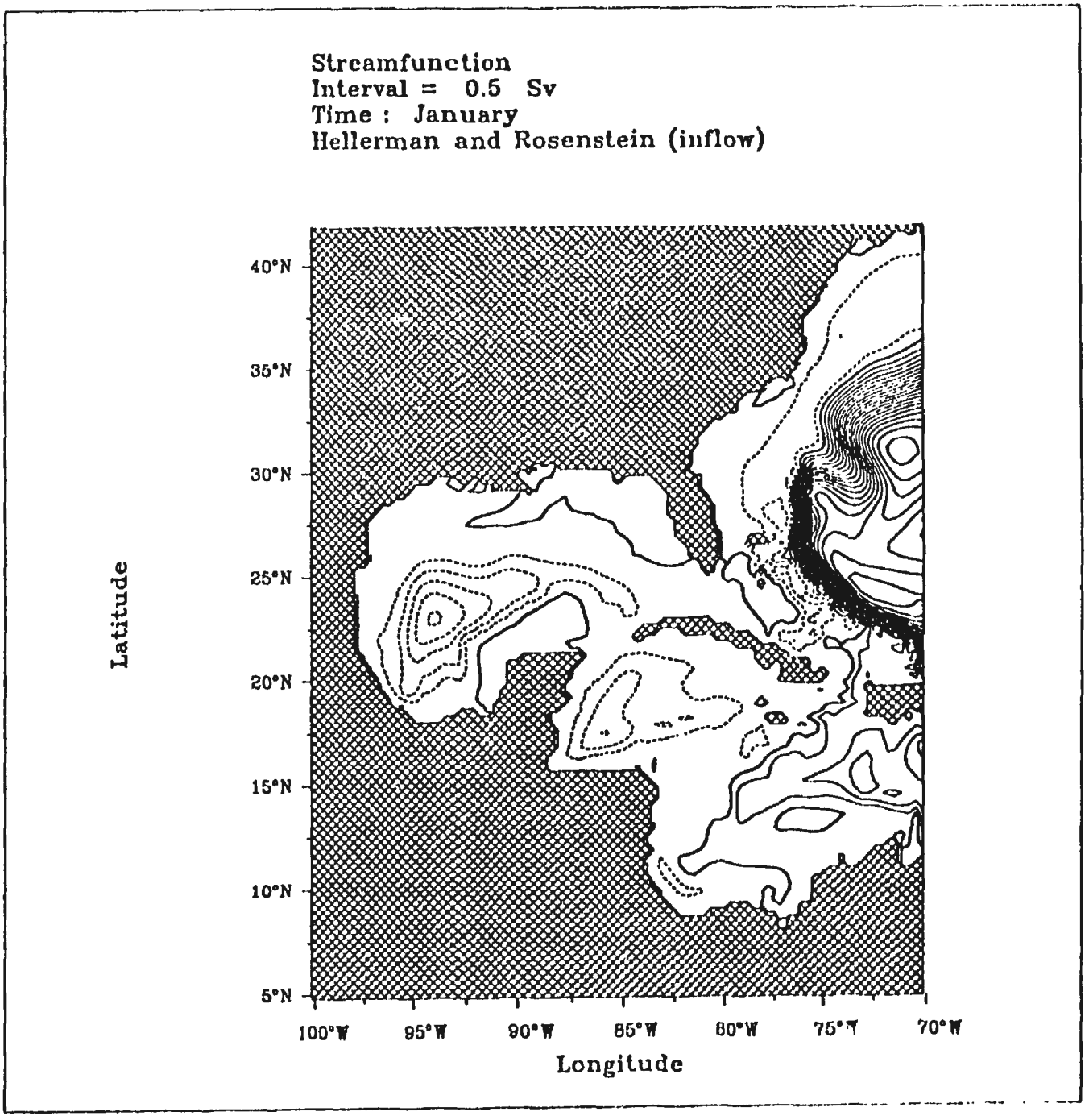

Figure C.1(a): *continued*

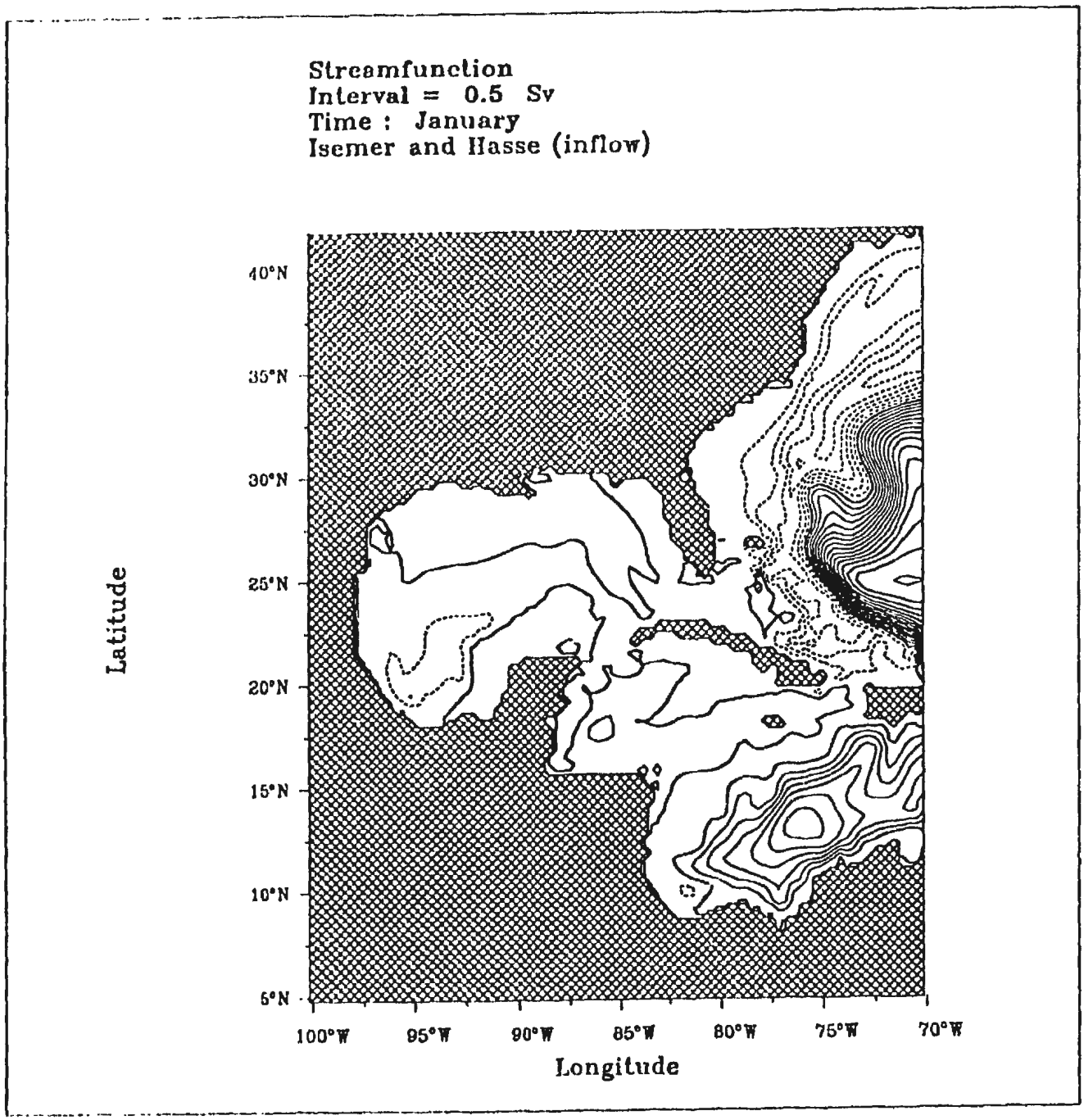

Figure C.1(a): *continued*

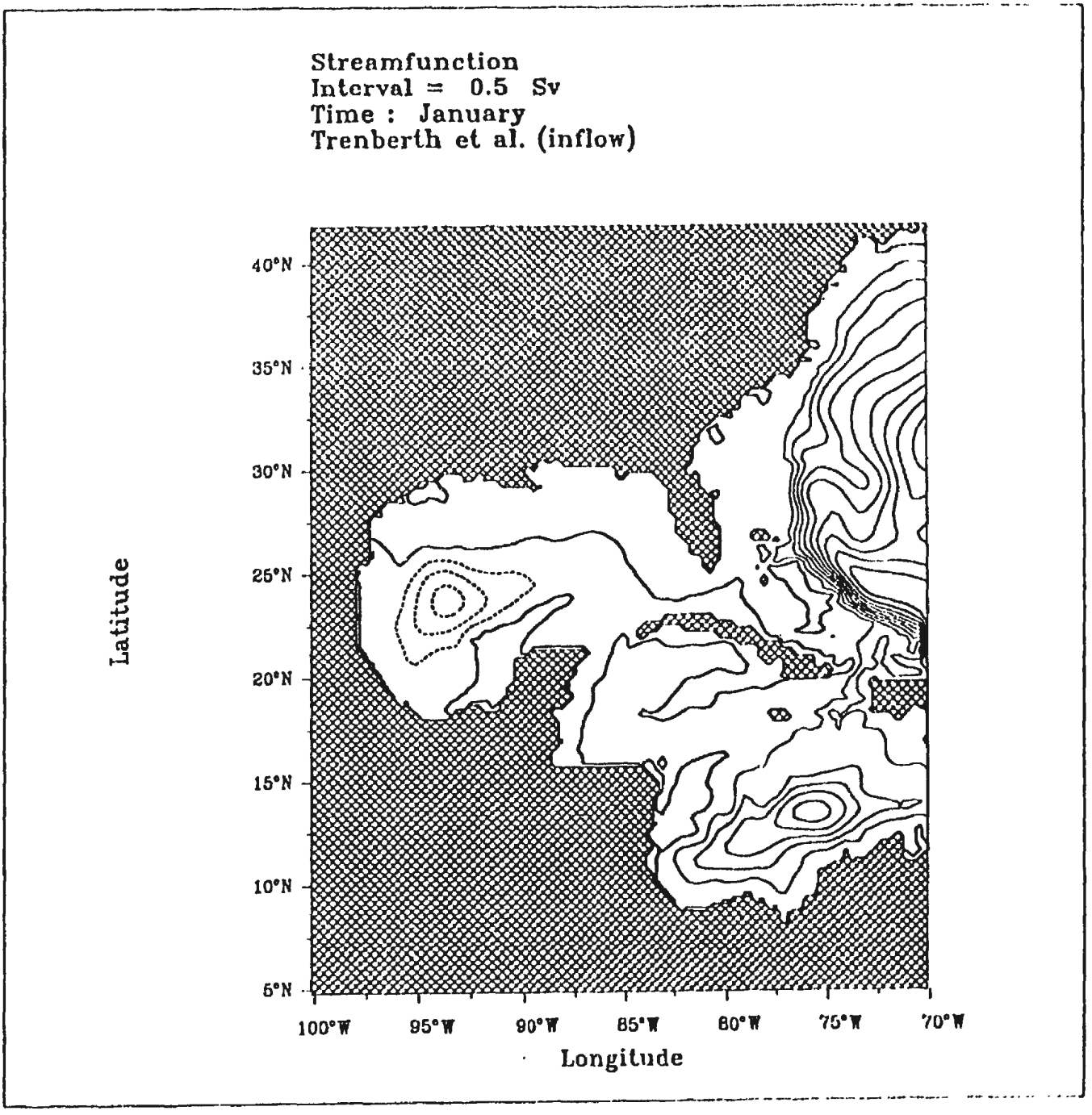

Figure C.1(a): *continued*

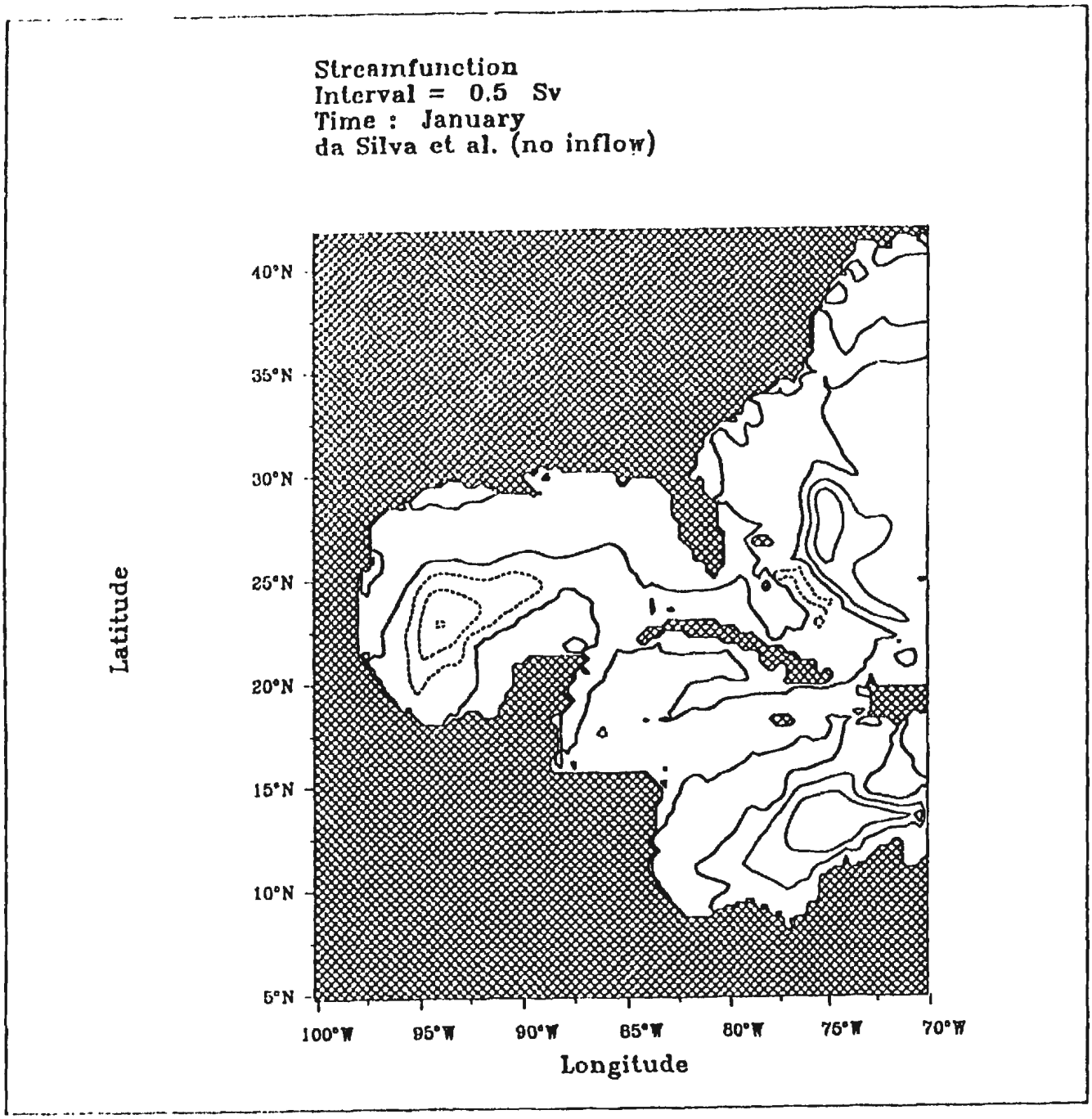

Figure C.1(b): *continued*

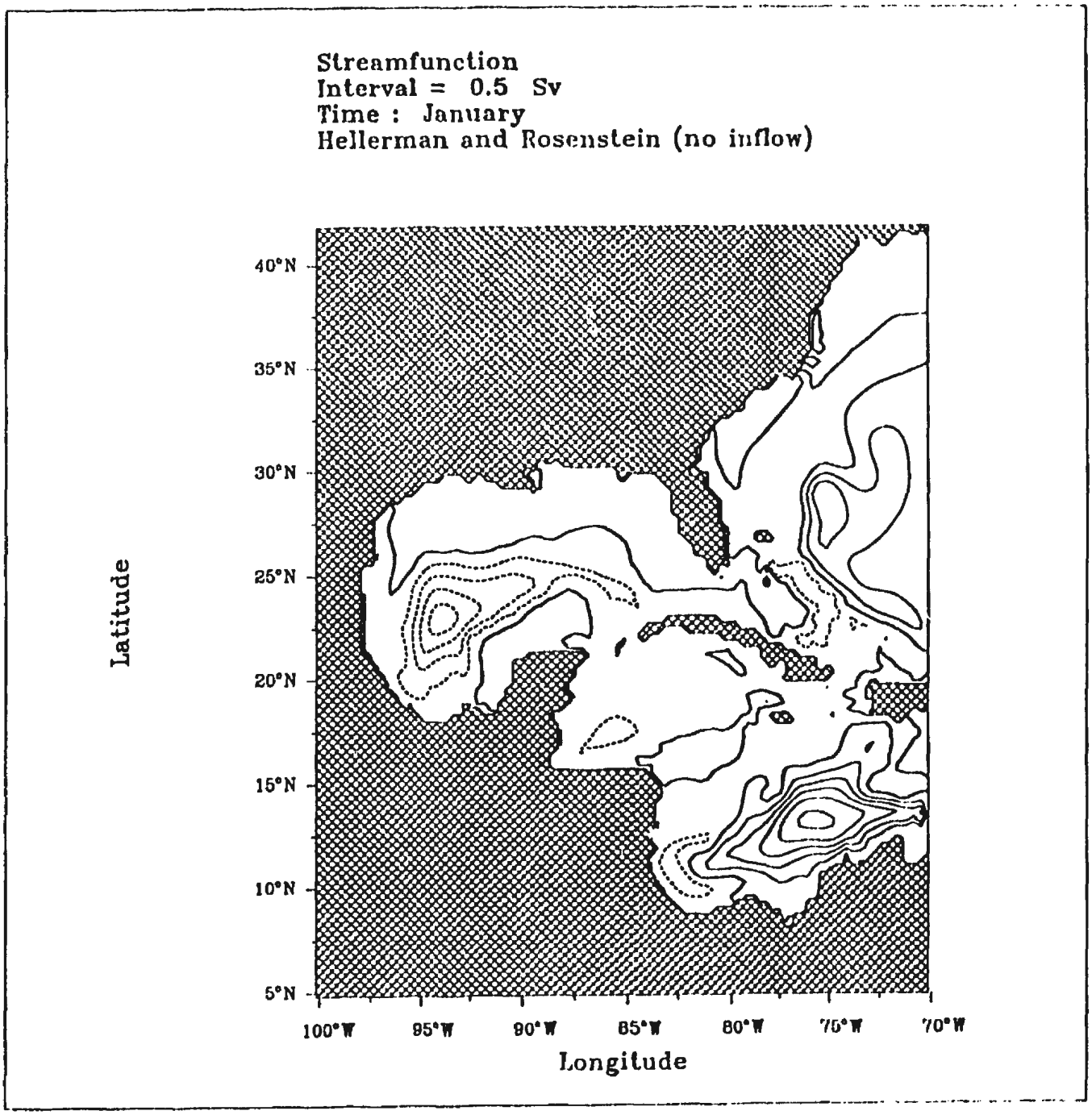

Figure C.1(b): *continued*

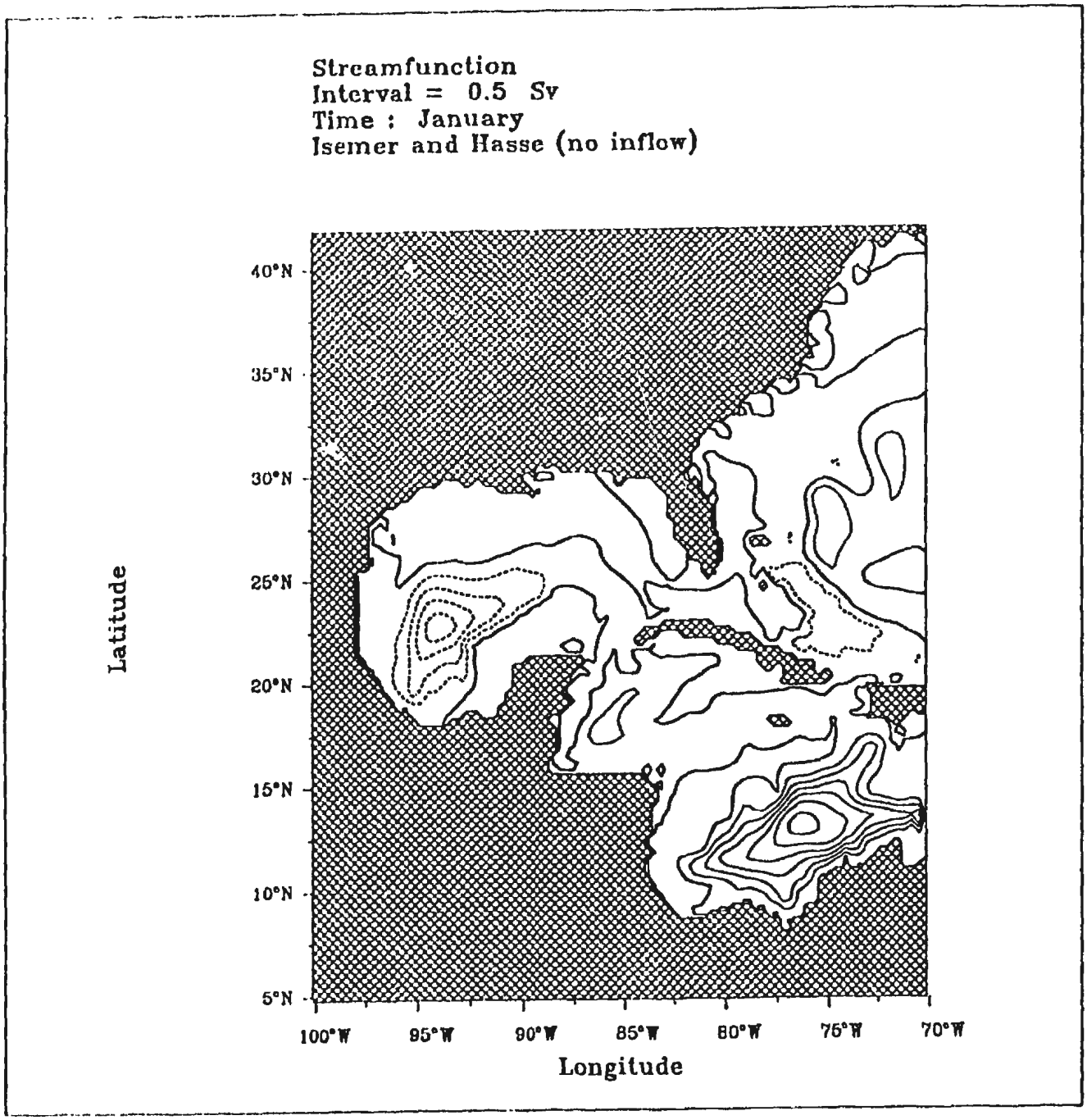

Figure C.1(b): *continued*

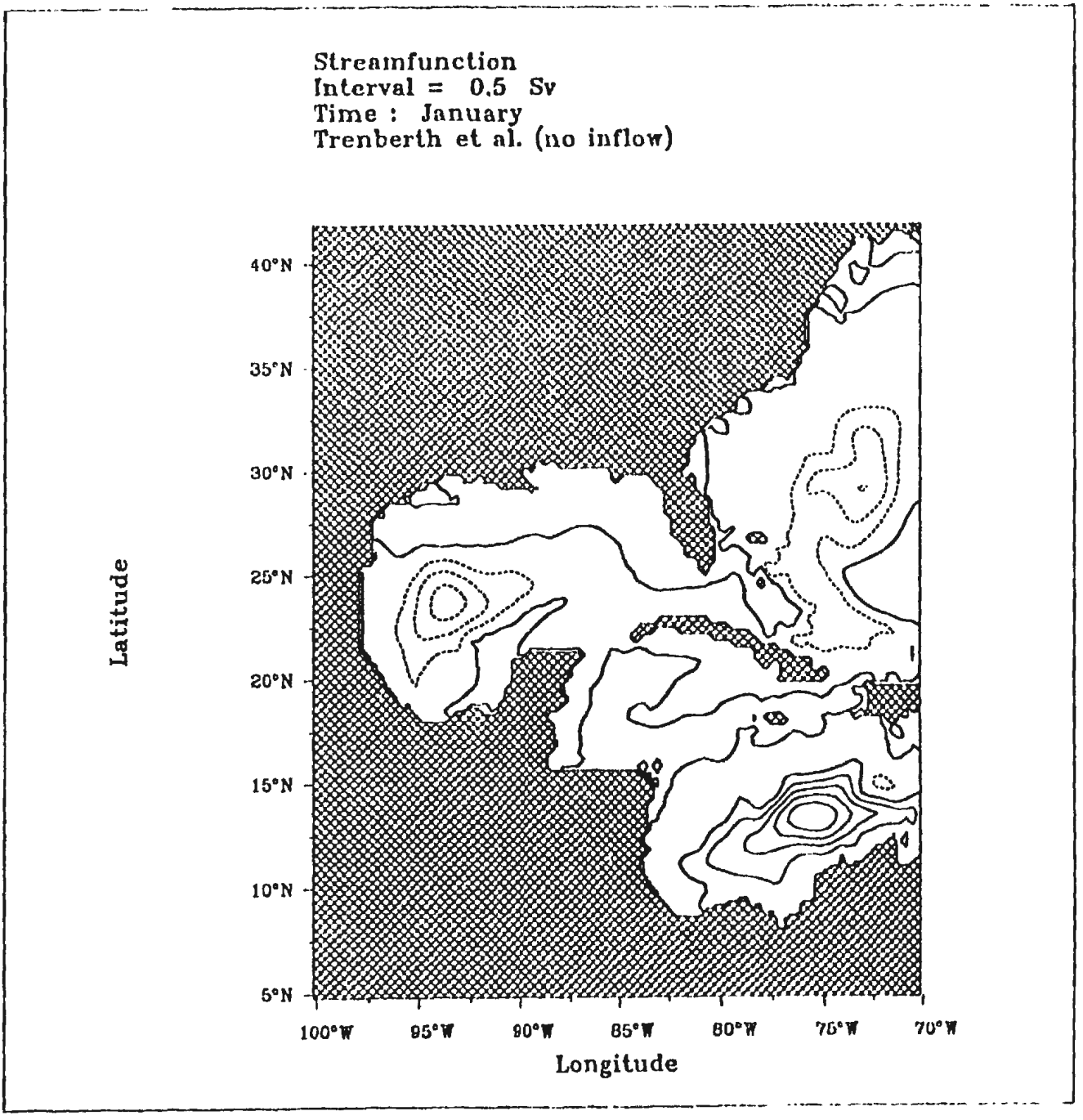

Figure C.1(b): *continued*

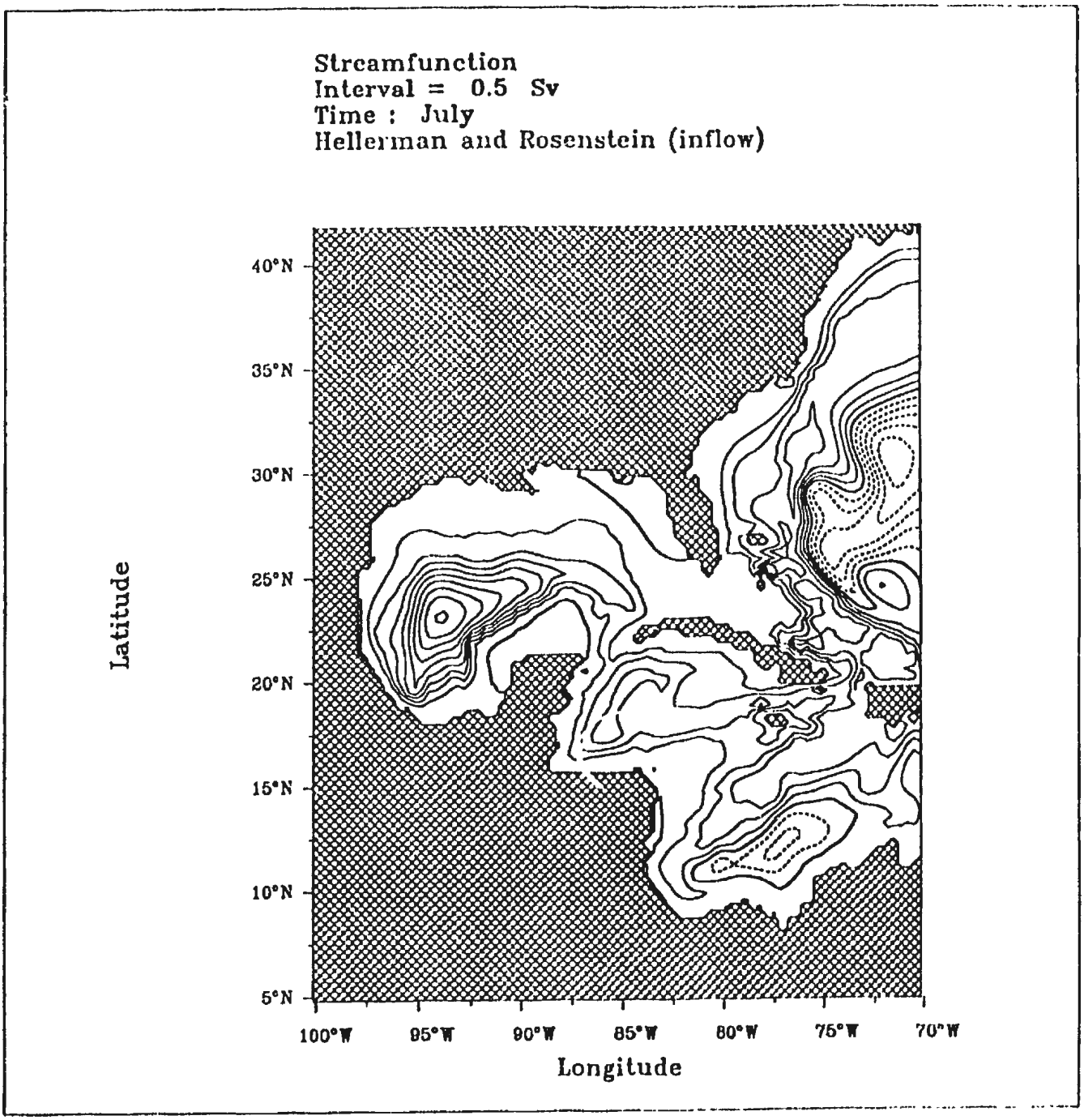

Figure C.2(a): *continued*

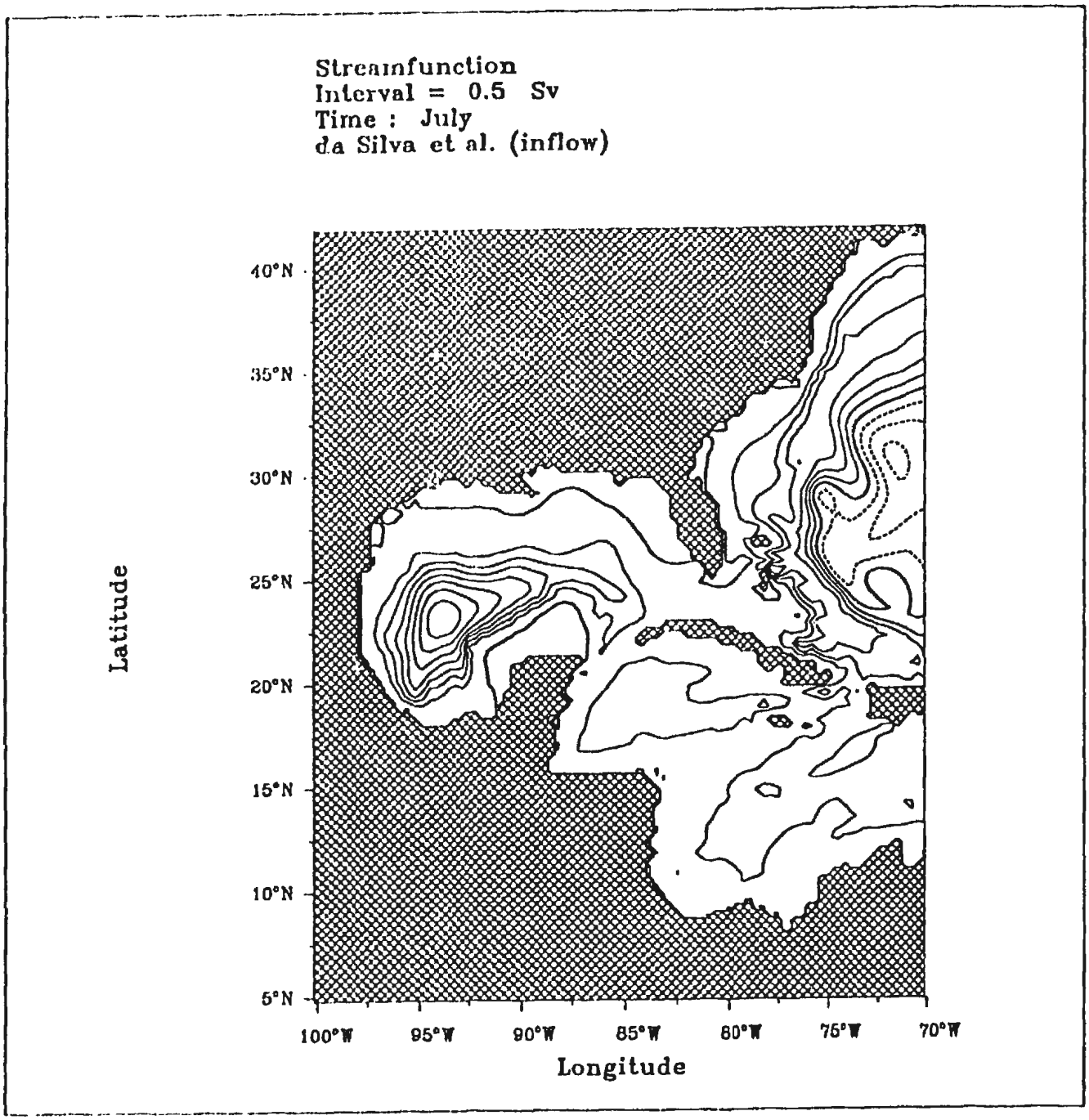

Figure C.2: *As Figure C.1, but for July.*

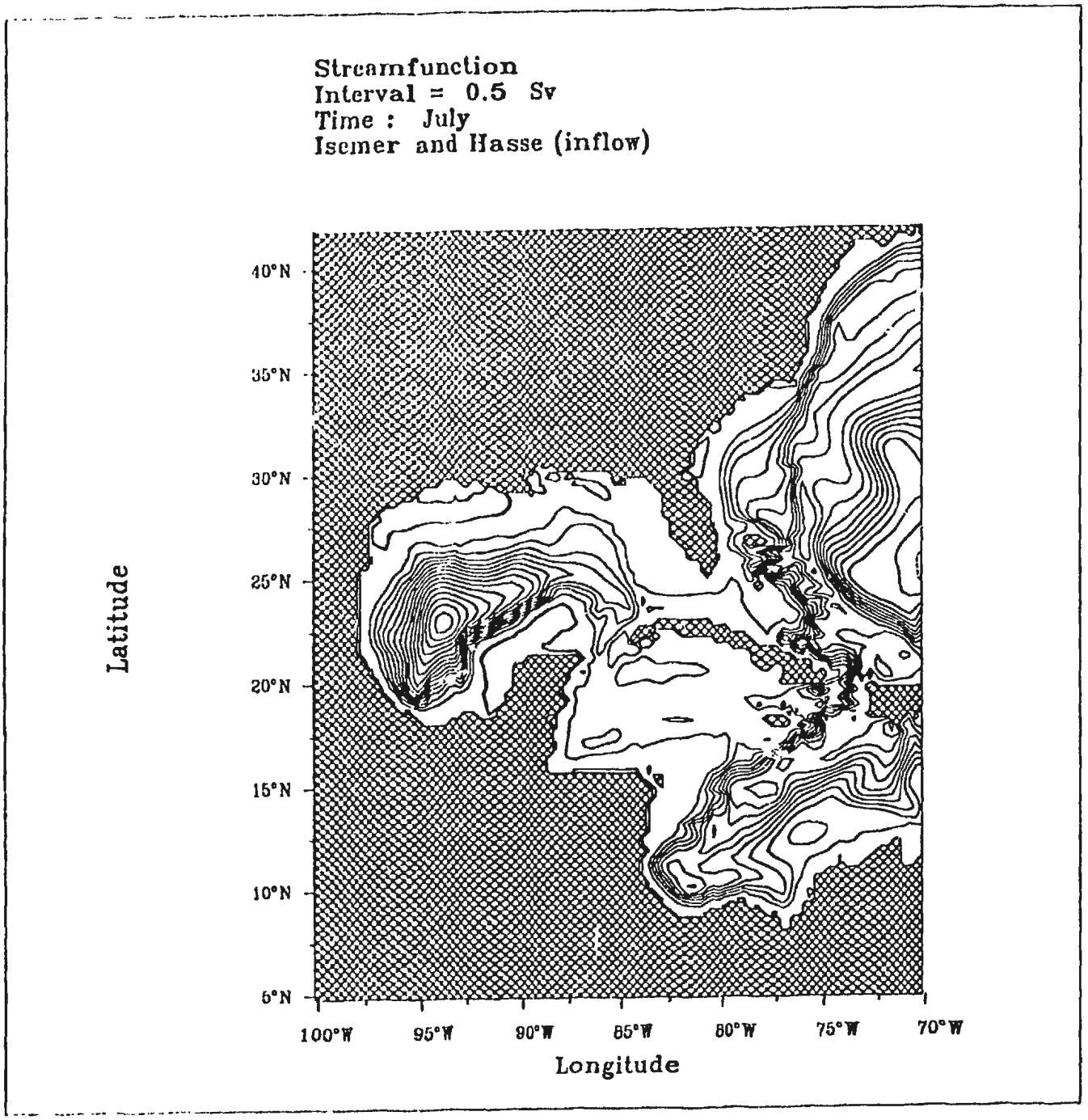

Figure C.2(a): *continued*

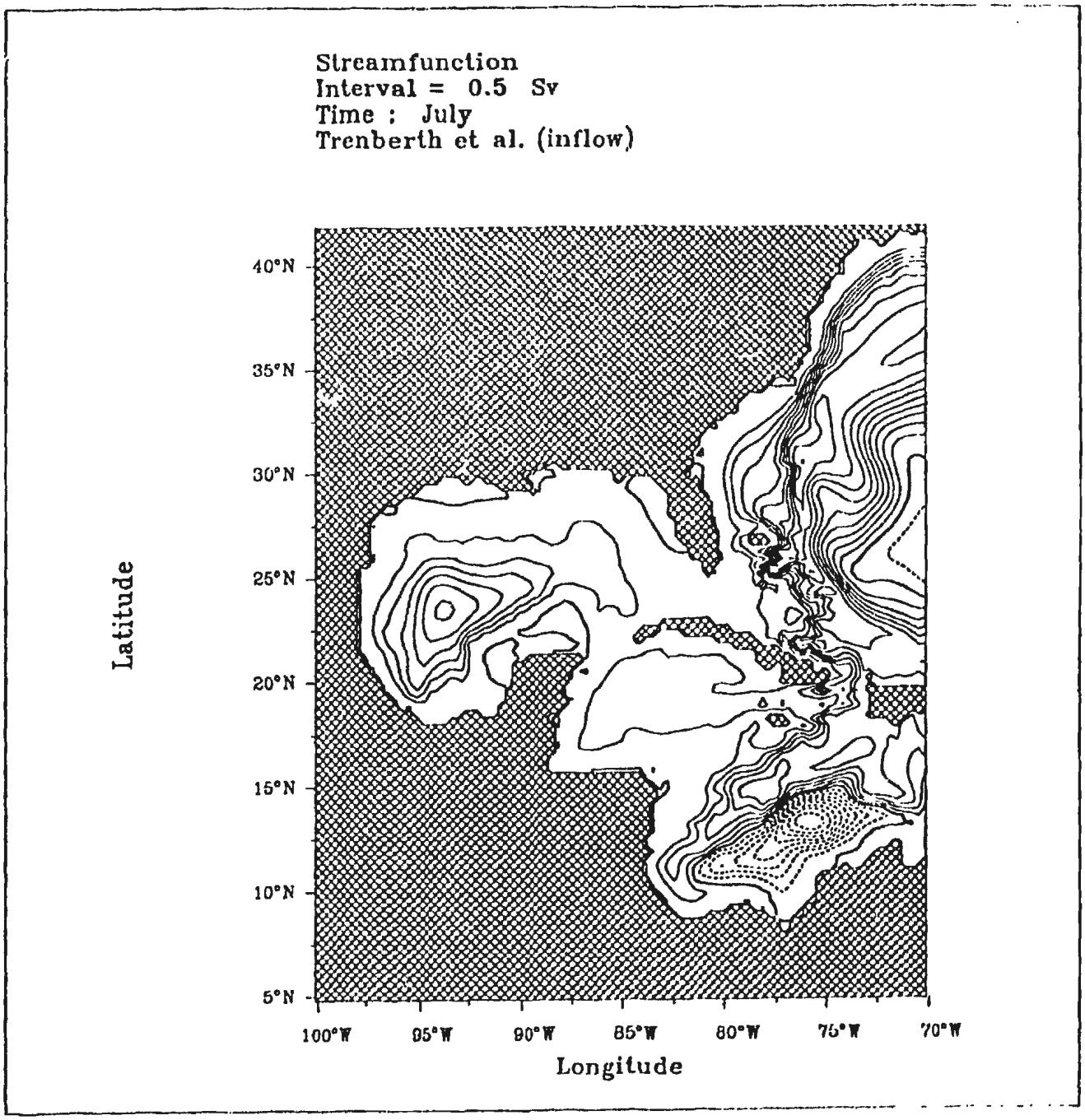

Figure C.2(a): *continued*

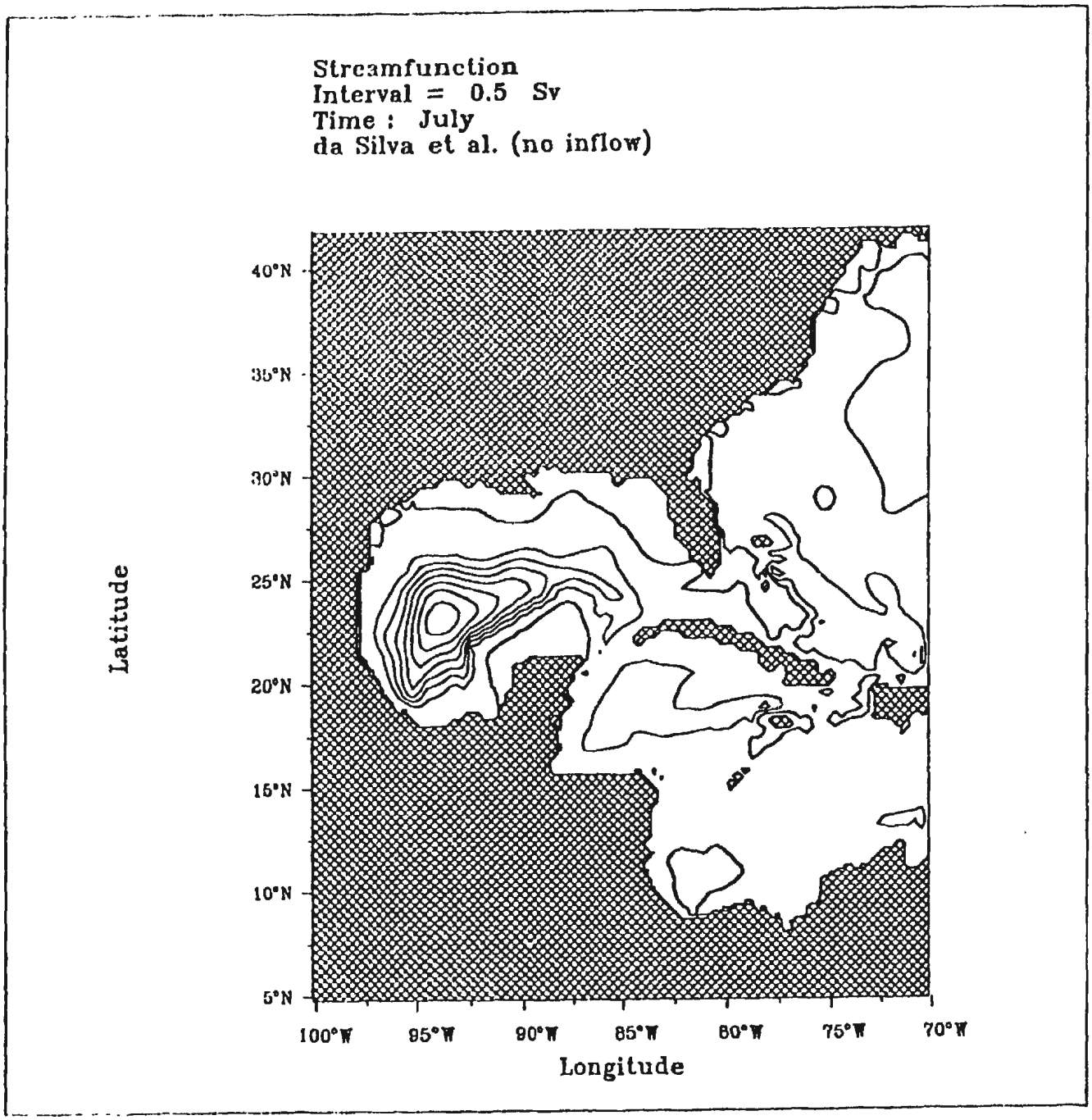

Figure C.2(b): *continued*

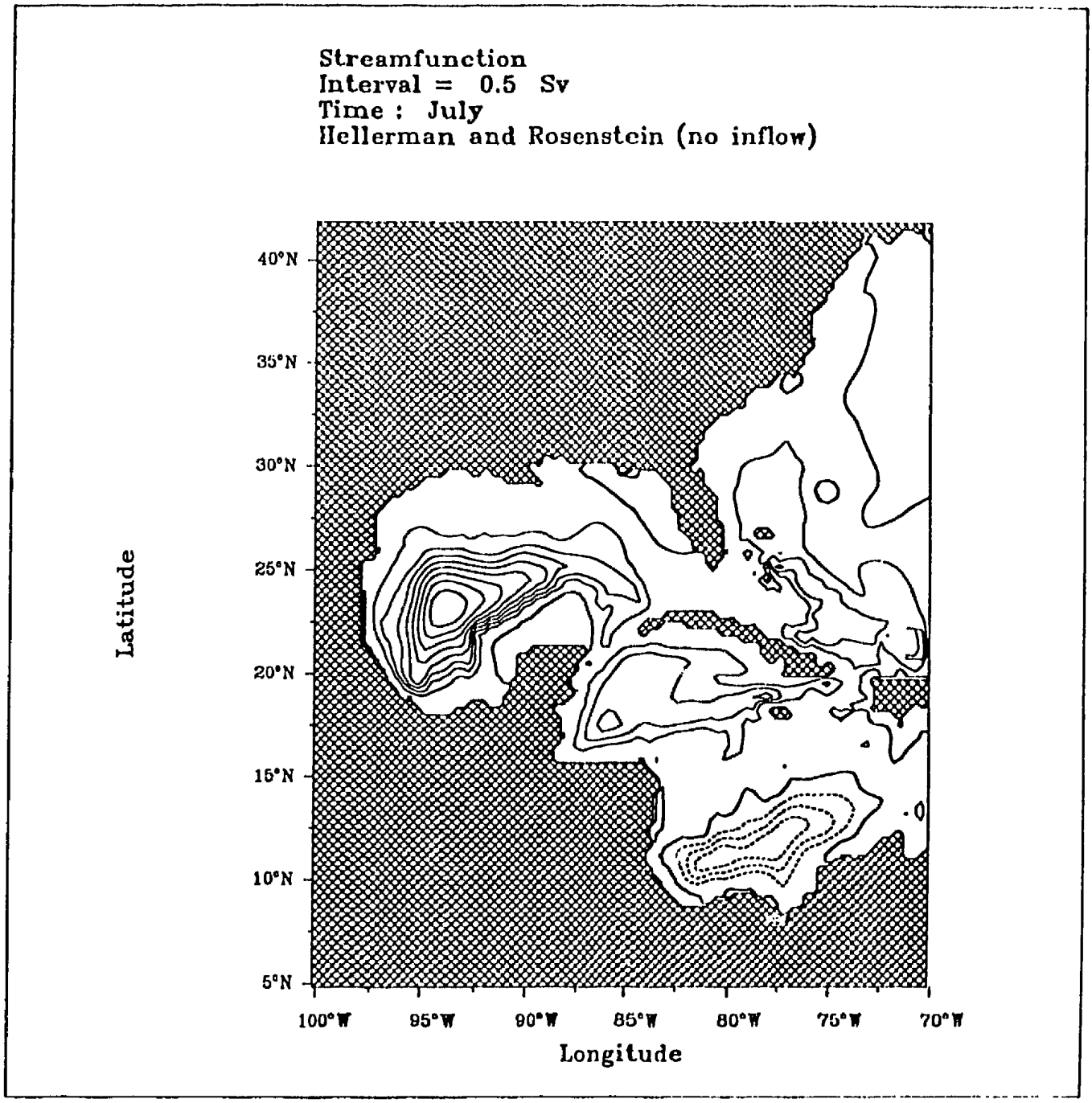

Figure C.2(b): *continued*

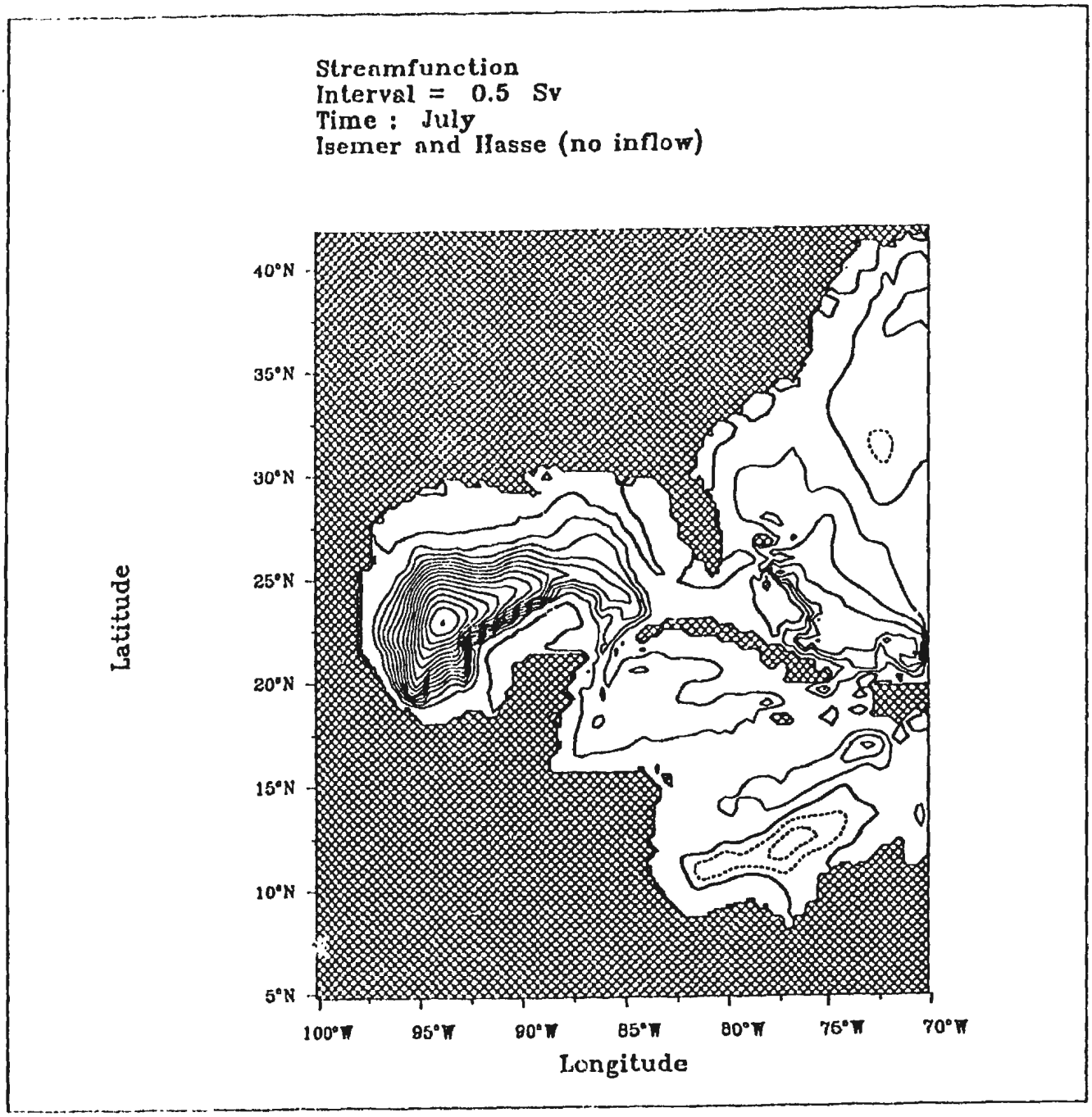

Figure C.2(b): *continued*

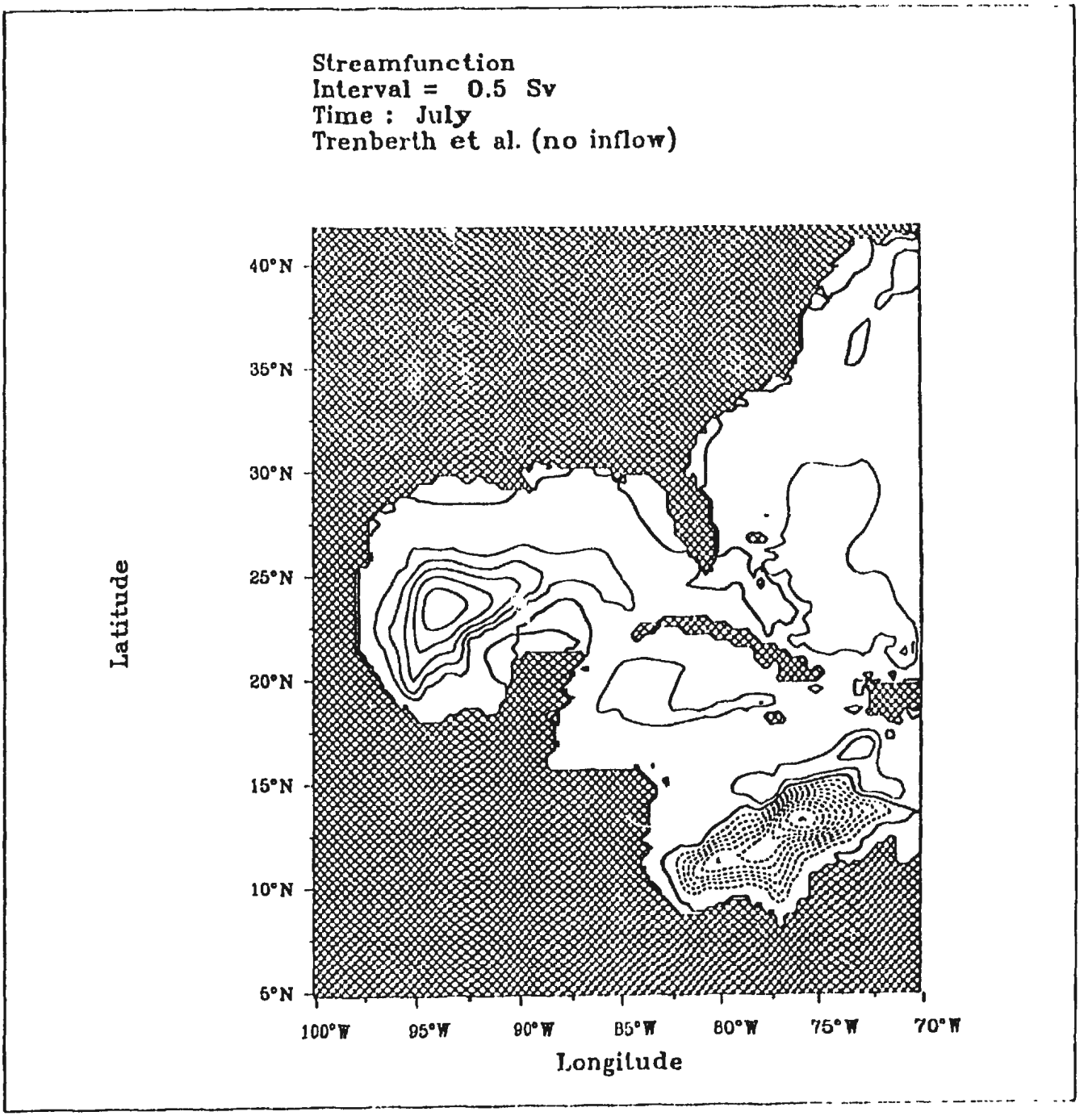

Figure C.2(b): *continued*

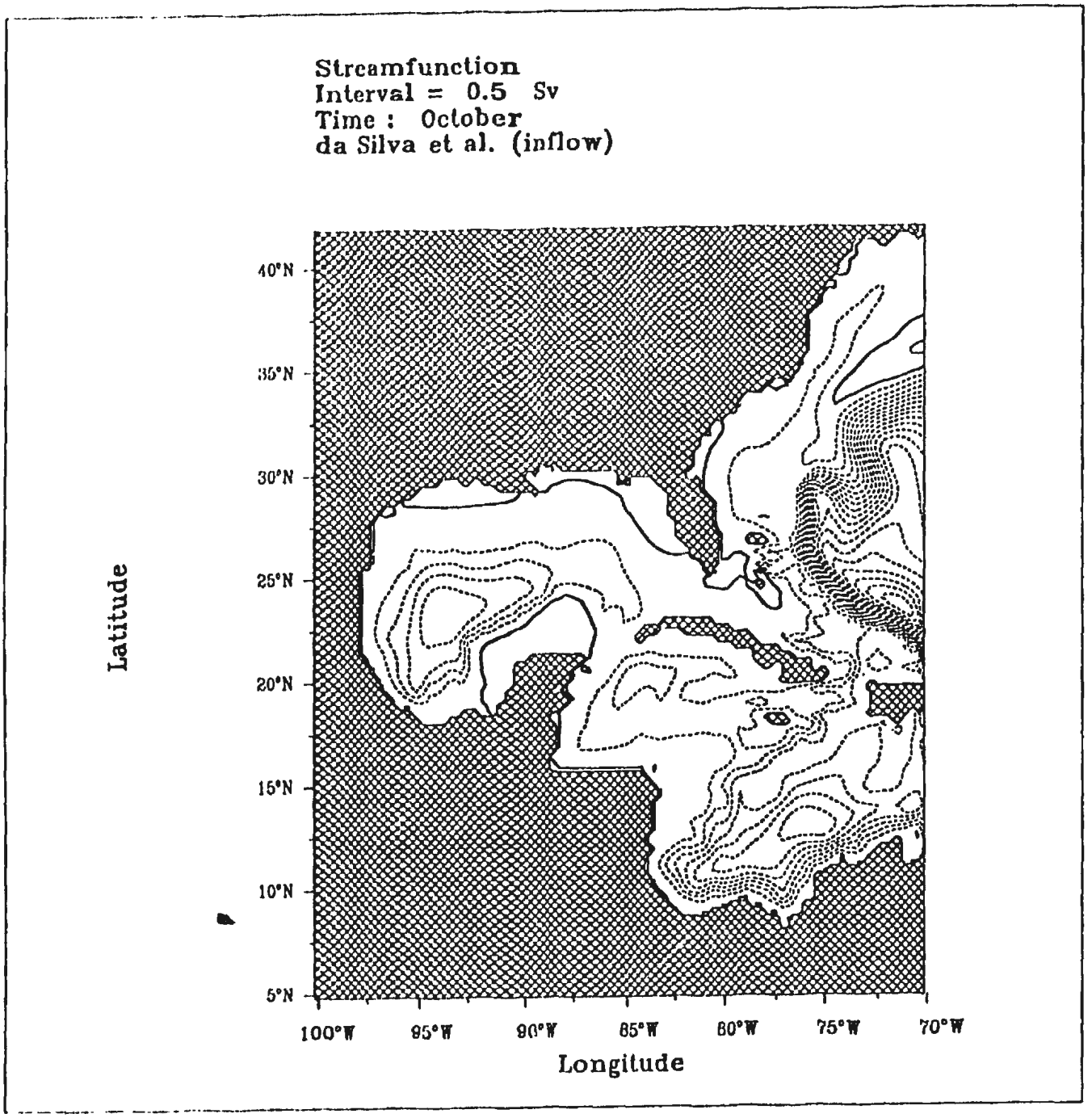

Figure C.3: *As Figure C.1, but for October.*

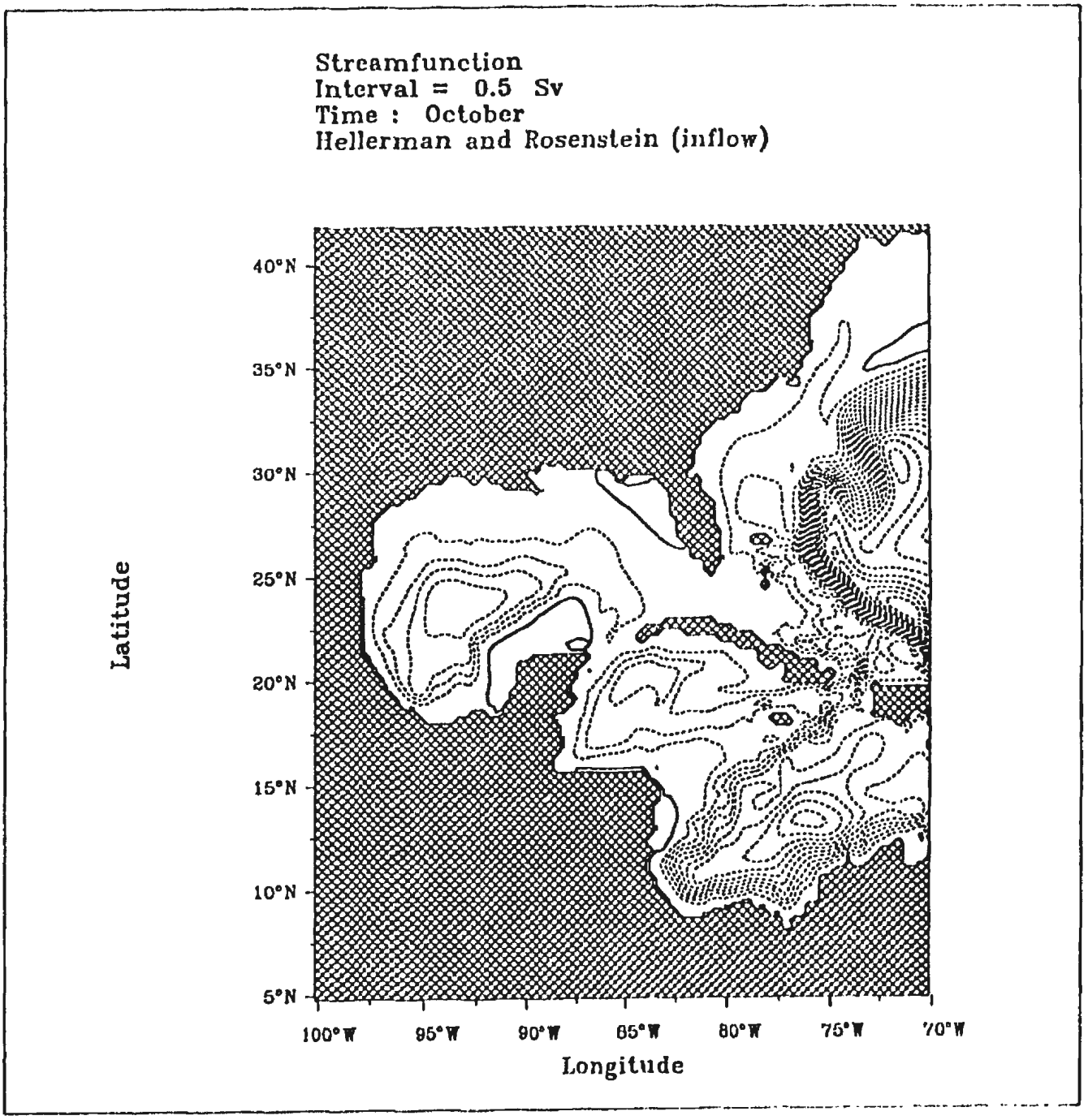

Figure C.3(a): *continued*

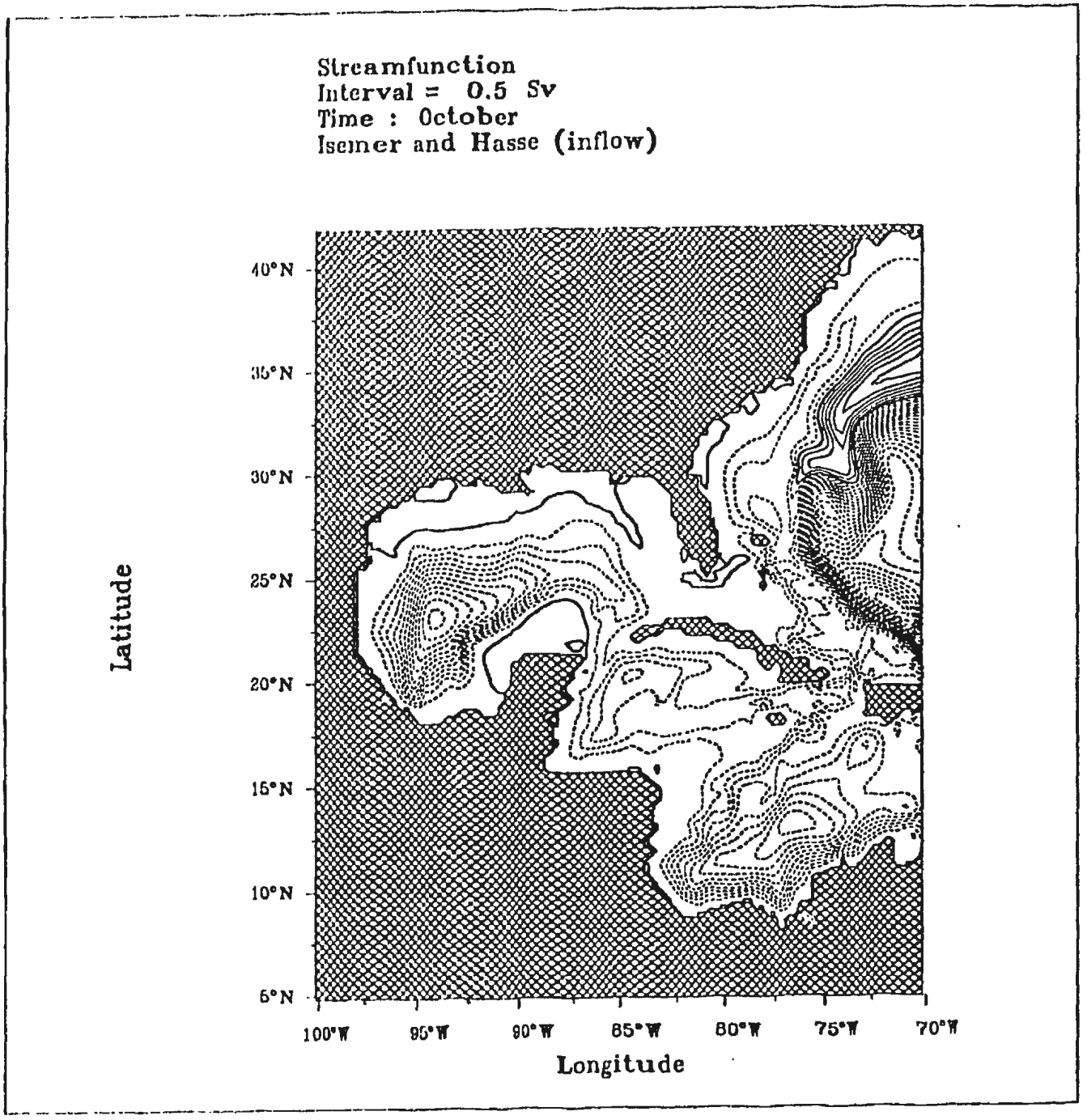

Figure C.3(a): *continued*

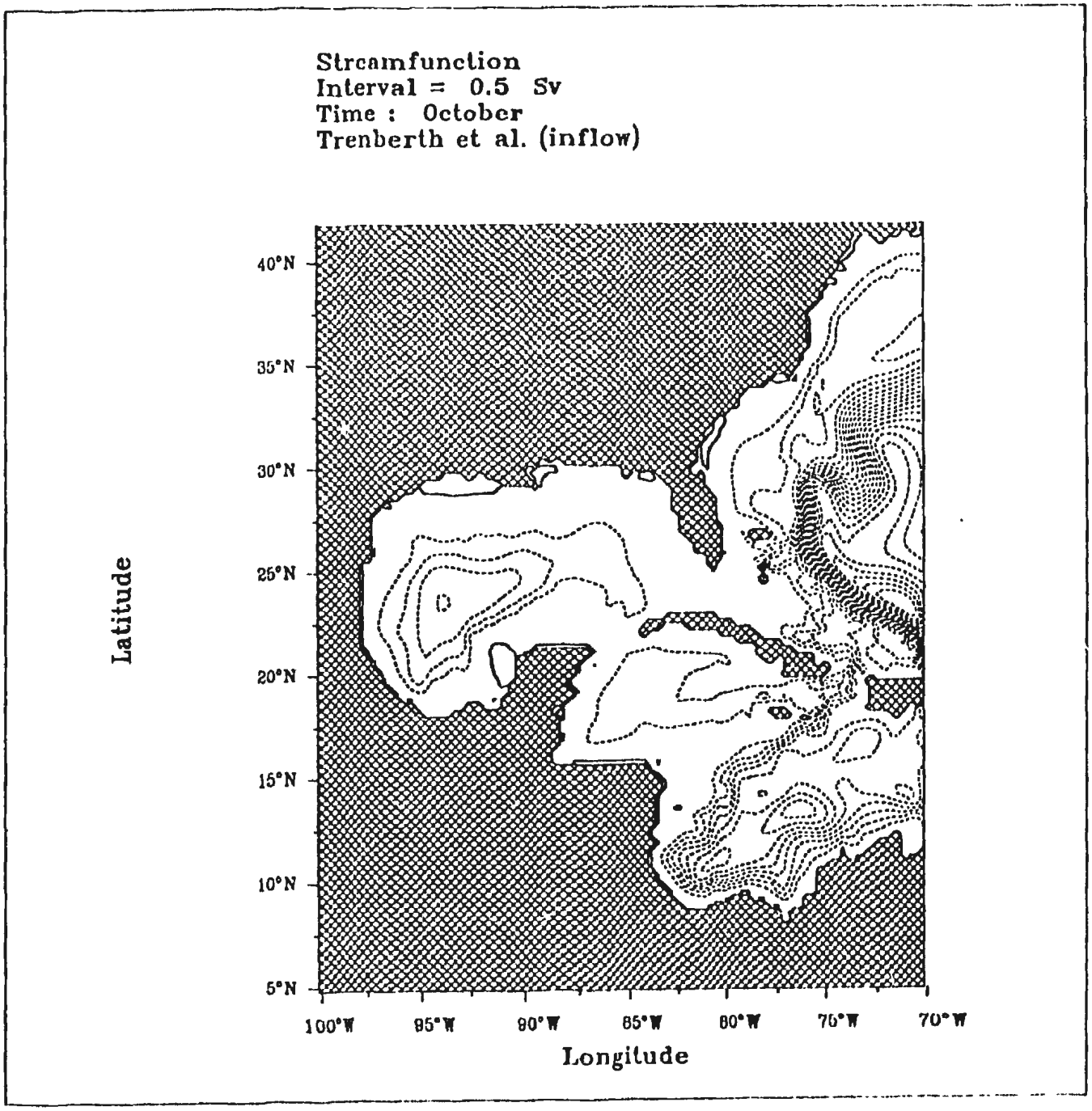

Figure C.3(a): *continued*

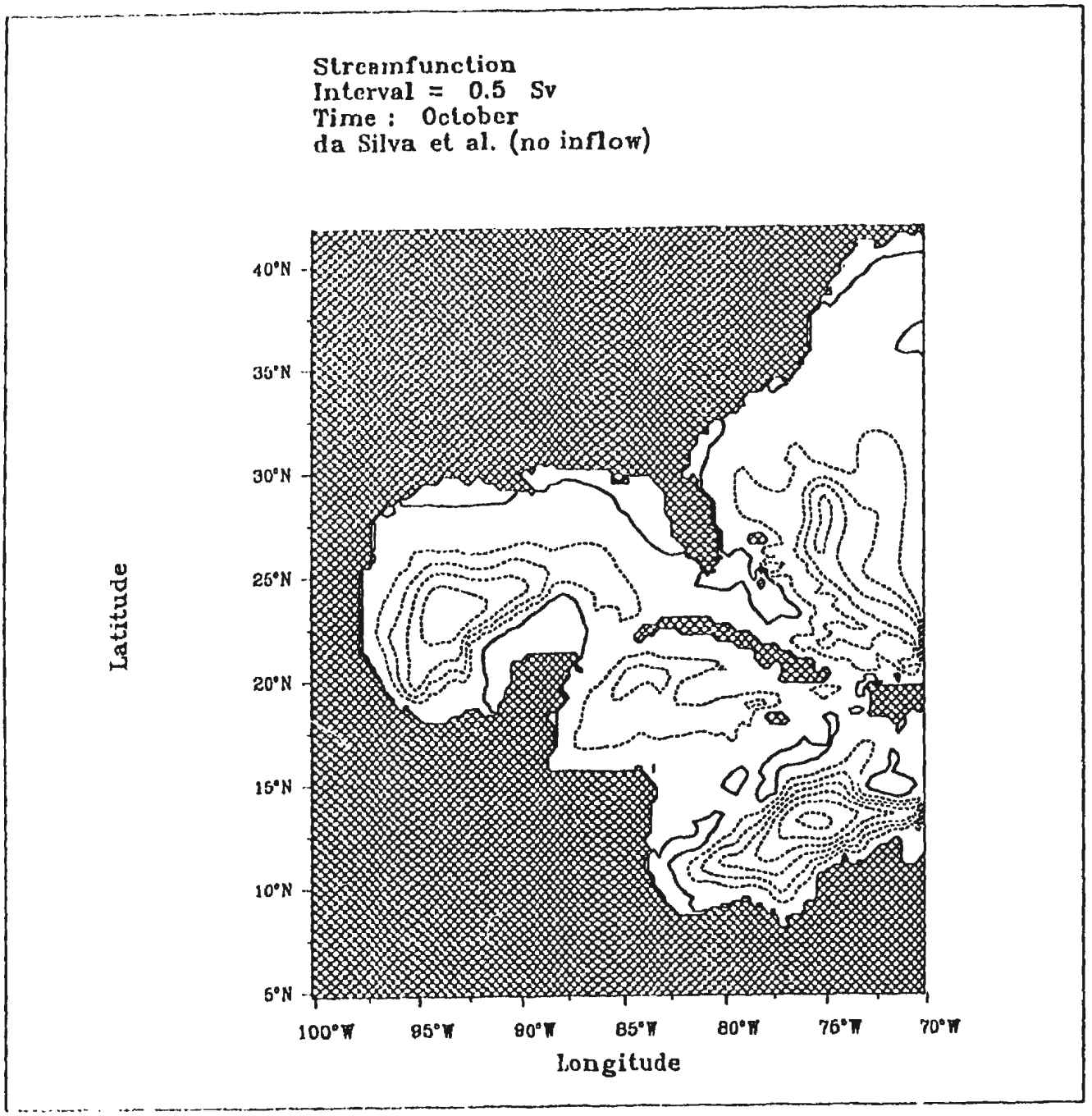

Figure C.3(b): *continued*

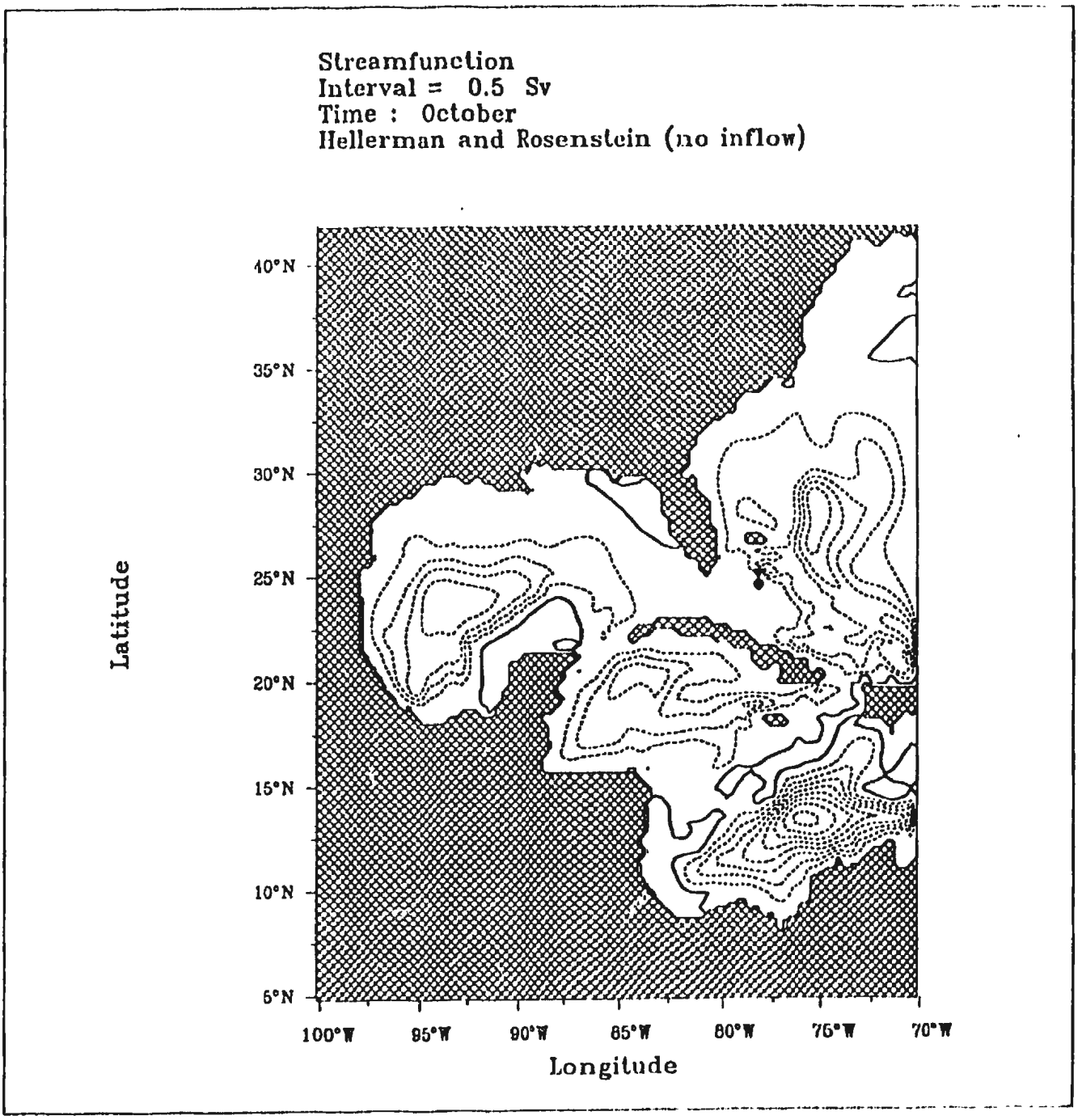

Figure C.3(b): *continued*

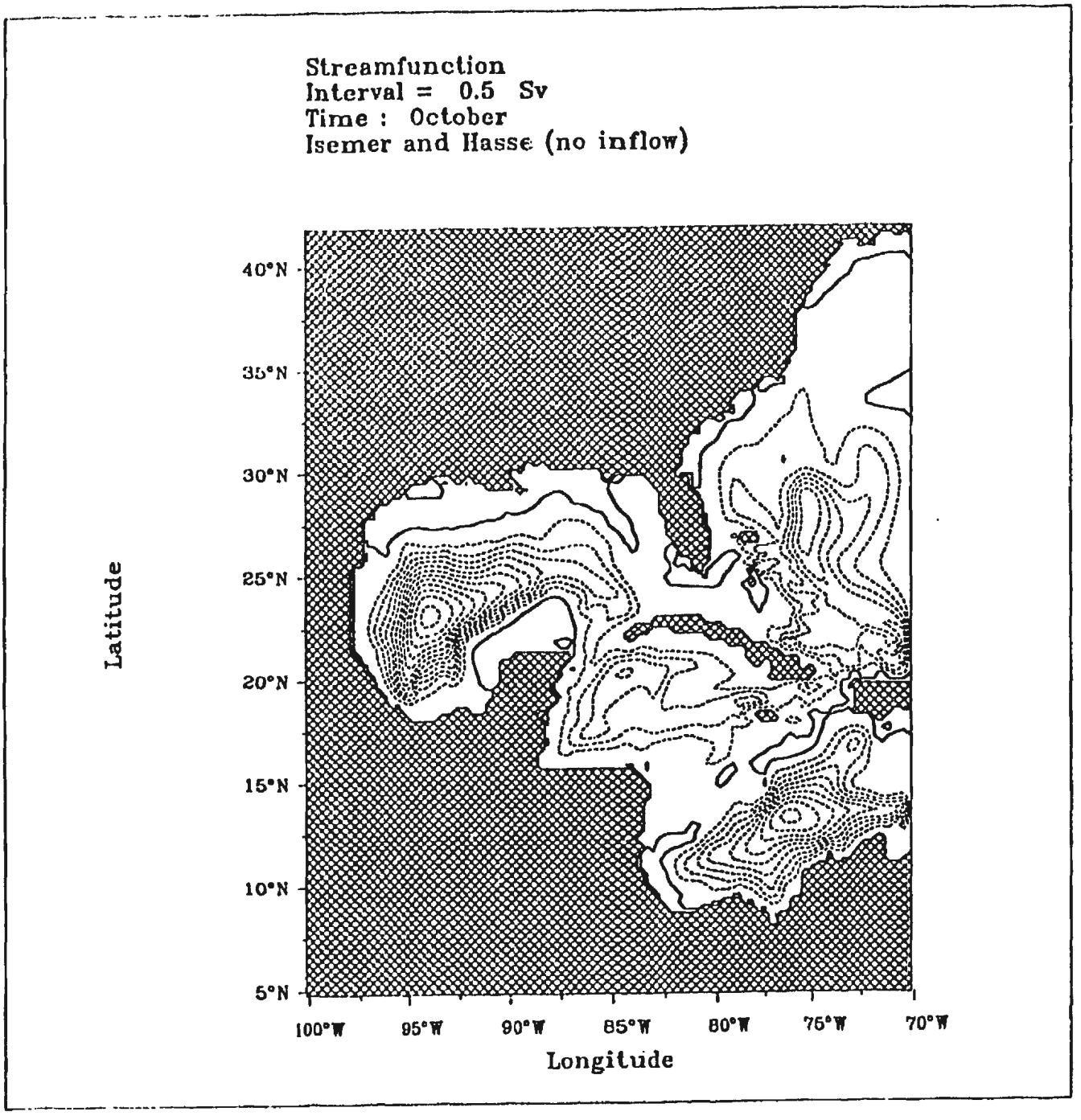

Figure C.3(b): *continued*

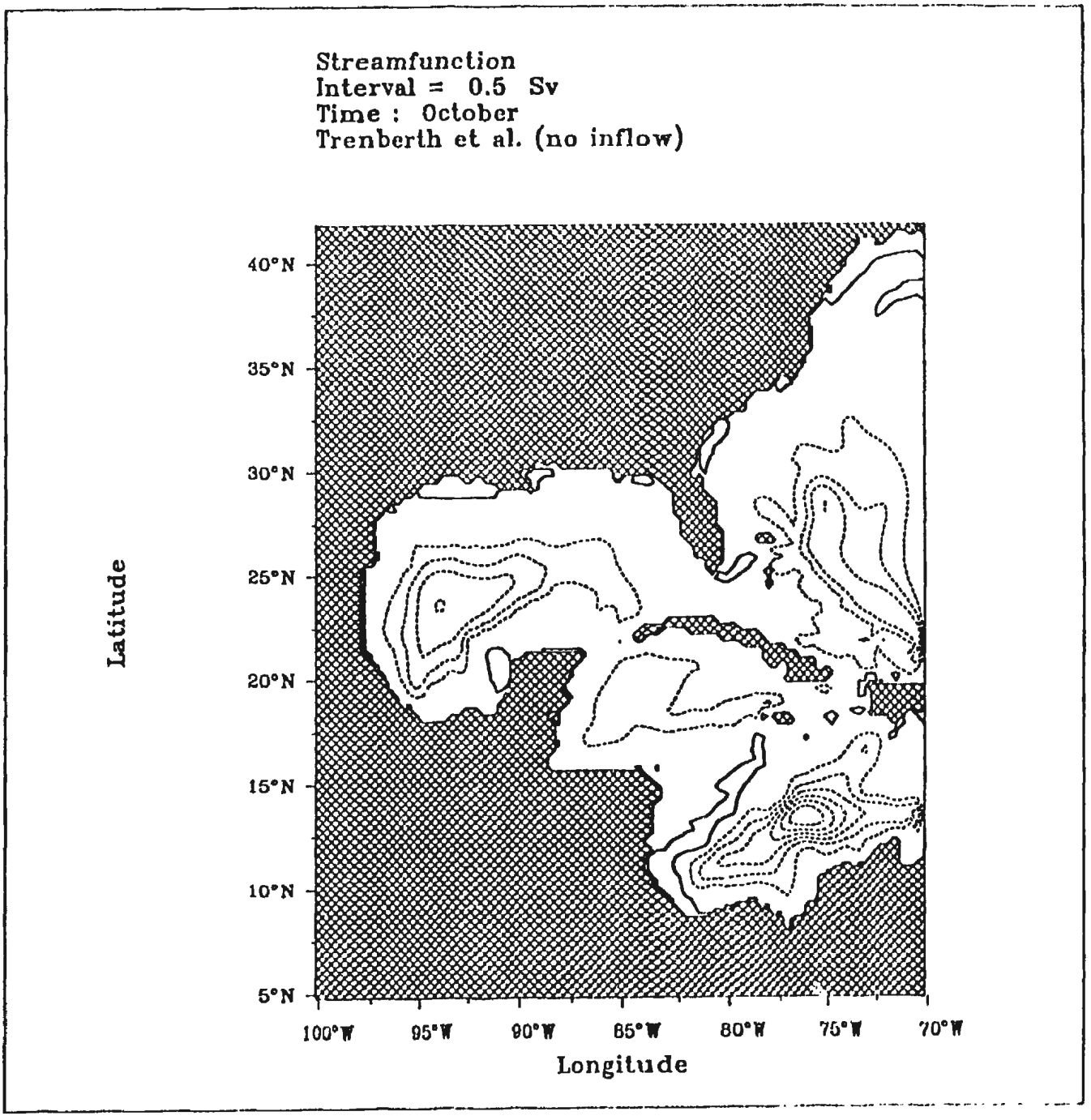

Figure C.3(b): *continued*

REFERENCES:

Akima, H., 1978: A method of bivariate interpolation and smooth surface fitting for irregularly distributed data points. *ACM Transactions on Mathematical Software*, **4(2)**, 148-159.

Anderson, D. L. T., and R. A. Corry, 1985a: Ocean response to low frequency wind forcing with application to the seasonal variation in the Florida Straits - Gulf Stream transport *Prog. Oceanog.*, **14**, 7-40.

, and , 1985b: Seasonal transport variations in the Florida Straits: A model study. *J. Phys. Oceanog.*, **15**, 773-786.

, and P. D. Killworth, 1977: Spin up of a stratified ocean, with topography. *Deep-Sea Res.*, **24**, 709-732.

, K. Bryan, A. E. Gill, and R. C. Pacanowski, 1979: The transient response of the North Atlantic: Some model studies. *J. Geophys. Res.*, **84, C8,** 4795-4815.

, and P. B. Rowlands, 1976: The role of inertia-gravity and planetary waves in the response of a tropical ocean to the incidence of an equatorial Kelvin wave on a meridional boundary. *J. Mar. Res.* **34**, 295-312.

Böning, C. W., R. Döscher and H. -J. Isemer, 1991a: Monthly mean wind stress and Sverdrup Transports in the North Atlantic: A comparison of the Hellerman -Rosenstein and Isemer-Hasse climatologies. *J. Phys. Oceanog.*, **21**, 221-235

, , and R. G. Budich, 1991b: Seasonal transport variation in the western subtropical North Atlantic: Experiments with an eddy-resolving model. *J. Phys. Oceanog.* **21(9)**, 1271-1289.

Brooks, I. H., 1979: Fluctuations in the transport of the Florida Current at periods between tidal and two weeks. *J. Phys. Oceanog.*, **9**, 1048-1053.

Bryan, F. O. and W. R. Holland, 1989: A high resolution simulation of the wind- and thermohaline driven circulation in the North Atlantic Ocean. *Parameterization of Small-Scale Processes. Proc. 'Aha Huliko'a, Hawaiian Winter Workshop*, P. Müller, D. Henderson, Eds., University of Hawaii at Manoa, 99-115.

Bunker, A. F., 1976: Computations of surface energy flux and annual air-sea interaction cycles of the North Atlantic Ocean. *Mon. Wea. Rev.*, **104**, 1127-1140.

———————, and R.A. Goldsmith, 1979: Archived time-series of Atlantic Ocean meteorological variables and surface fluxes.
Woods Hole Oceanographic Institution Tech. Rep. WHOI 79-3, 27pp.

Cardone, V.J., J.G.Greenwood and M.Cane, 1990: On trends in historical marine wind data. *J. Climate*, **3**, 113-127.

Clarke, R. A., 1984: Transport through the Cape Farewell-Flemish Cap section *Rapp. P. -v. Reun. Cons. int. Explor. Mer.*, **185**: 120-130.

Courant, R., K. Friedrichs, and H. Lewy, 1928: *Über die partiellen Differenzengleichungen der mathematischen Physik.* Math. Annalen, **100**, 32-74.

Csanady, G.T., 1978: The arrested topographic wave. *J. Phys. Oceanog.*, **8**, 47-62.

——— , 1982: *Circulation in the coastal ocean.* D.Reidel, Hingham, MA., U.S.A., 279pp.

Emery, W.J., W.G. Lee, L. Magaard, 1984: Geographic and seasonal distribution of Brunt-Väisälä frequency and Rossby radii in the North Pacific and North Atlantic. *J. Phys. Oceanog.*, **14**, 294-317.

Fanning, A.F., 1991: Diagnostic calculations of the circulation in the North Atlantic and North Pacific including the role of baroclinic effects over realistic topography (JEBAR). BSc. Honours Thesis, Memorial University of Newfoundland.

Faraday, M., 1832: Bakerian Lecture-Experimental researches in electricity. *Philosophical Transactions, Royal Society of London*, Part 1, 163-177

Gill, A.E., 1982: *Atmosphere-ocean dynamics*. Academic Press, 662 pp.

-, and P. P. Niiler, 1973: The theory of the seasonal variability in the ocean. *Deep Sea Res.*, **20**, 141-177.

Greatbatch, R. J., and A. Goulding, 1989: Seasonal variations in a linear barotropic model of the North Atlantic driven by the Hellerman and Rosenstein wind stress field. *J. Phys. Oceanog.*, **19(5)**, 572-595.

, and , 1992: A long-time-scale, density-stratified shelf circulation model *Cont. Shelf. Res.*, **12(1)**, 115-141.

, and J. Li, 1990: Barotropic variability in the presence of an ocean gyre. *J. Mar. Res.*, **48**, 37-53

, and T. Otterson, 1991: On the formulation of open boundary conditions at the mouth of a bay. *J. Geophys. Res.*, **96, C10**, 18431-18445.

, A. F. Fanning, A. D. Goulding, and S. Levitus, 1991: A diagnosis of interpentadal circulation changes in the North Atlantic. *J. Phys. Oceanog.*, **19(5)**, 572-595.

Halkin, D. and T. Rossby, 1985: The structure and transport of the Gulf Stream at 73^0W. *J. Phys. Oceanogr.*, **15** 1439-1452.

Heaps, N. S., 1971: On the numerical solution of the three-dimensional hydrodynamic equations for tides and storm surges. *Mem. Soc. R. Sci. Liege*, Ser.6, **1**, 143-180.

Hellerman, S., and M. Rosenstein, 1983: Normal monthly wind stress over the World Ocean with error estimates. *J. Phys. Oceanogr.*, **13**, 1093-1104.

Holland, W.R., 1973: Baroclinic and topographic influences on the transport in western boundary currents. *Geophys. Fluid Dyn.*, **4**, 187-210.

Hsieh, W. W., M. K. Davey and R. C. Wajsowicz, 1983: The free Kelvin wave in finite difference numerical models. *J. Phys. Oceanogr.*, **13**, 1383-1397.

Isemer, H. -J. , and L. Hasse, 1987: The BUNKER Climate Atlas of the North Atlantic Ocean, Vol. 2: Air-Sea Interactions. Springer-Verlag, 256 pp.

———————, and ———, 1991: The scientific Beaufort equivalent scale: effects on wind statistics and climatological air-sea flux estimates in the North Atlantic Ocean. *J. Climate*, **4**, 819-836.

Johnson, M.A. and J.J. O'Brien, 1990: The role of coastal Kelvin waves on the Northeast Pacific Ocean. *J. Mar. Syst.*, **1**, 29-38.

Kaufeld, L. 1981: The developement of a new Beaufort equivalent scale. *Meteor. Rundsch*, **34**, 17-23.

Large, W. G. and S. Pond, 1981: Open ocean momentum flux measurements in moderate to strong winds. *J. Phys. Oceanogr.*, **11**, 324-336.

Larsen, J. C., 1992: Transport and heat flux of the Florida Current at $27^0 N$ derived from cross-stream voltages and profiling data: theory and observations. *Phil. Trans. R. Soc. Lond. A*, **338**, 169-236.

Leaman, K. D., R. L. Molinari, and P. S. Vertes, 1987: Structure and Variability of the Florida Current at 27°*N*: April 1982-July 1984. *J. Phys. Oceanogr.*, **17**, 565-583.

Lee, T. N. and E. Williams, 1988: Wind forced transport fluctuations of the Florida Current. *J. Phys. Oceanogr.*, **18**, 937-946.

Leetmaa, A. and A. F. Bunker, 1978: Updated charts of the mean annual wind stress, convervgences in the Ekman layers, and Sverdrup transports in the North Atlantic. *J. Mar. Res.*, **36**, 311-322.

. P. Niiler and H. Stommel, 1977: Does the Sverdrup relation account for the Mid-Atlantic circulation ? *J. Mar. Res.*, **35(1)**, 1-10.

Levitus, S. 1982: Climatological Atlas of the World Ocean. *NOAA* Prof. Paper, **3**.

-, 1989a: Interpentadal variability of temperature and salinity at intermediate depths of the North Atlantic Ocean, 1970-1974 versus 1955-1959. *J. Geophys. Res.*, **94(C5)**, 6091-6131.

-, 1989b: Interpentadal variability of salinity in the upper 150m of the North Atlantic Ocean, 1970-1974 versus 1955-1959. *J. Geophys. Res.*, **94(C7)**, 9679-9685.

-, 1989c: Interpentadal variability of temperature and salinity in the deep North Atlantic, 1970-1974 versus 1955-1959. *J. Geophys. Res.*, **94(C11)**, 16125-16131.

-, 1990: Interpentadal variability of steric sea level and geopotential thickness of the North Atlantic Ocean, 1970-1974 versus 1955-1959. *J. Geophys. Res.*, **95(C4)**, 5233-5238.

Mellor, G.L., C.R. Mechoso and E. Keto, 1982: A Diagnostic calculation of the general circulation of the Atlantic Ocean. *Deep Sea Res.*, **29 (10a)**, 1171-1192.

Mesinger, F., and A. Arakawa, 1976: *Numerical methods used in atmospheric models*, GARP Publ. Ser. No. 17, Vol. 1. World Meteorol. Organ. Int. Counc. Sci. Unions, Geneva.

Meyers, G., 1979: On the annual Rossby wave in the subtropical North Pacific Ocean. *J. Phys. Oceanogr.*, **9**, 664-673.

Moore, D. W., and S. G. H. Philander, 1977: Modeling of the tropical oceanic circulation. *The Sea*, Vol.6, E. Goldberg *et al.*, Eds., Wiley-Interscience, 319-361.

Munk, W. H., 1950: On the wind driven ocean circulation. *Journal of Meteorology*, **7**, 79-93.

Mysak, L., 1983: Generation of annual Rossby waves in the North Pacific. *J. Phys. Oceanogr.*, **13**, 1909-1923.

Niiler, P. P. and W. S. Richardson 1973: Seasonal variability of the Florida Current. *J. Mar. Res.* **31(3)**, 144-167.

Richardson, P.L., 1985: Average velocity and transport of the Gulf Stream near 55^0W. *J. Mar. Res.*, **43**, 83-111.

Roemmich, D. and C. Wunsch, 1985: Two transatlantic sections: Meridional circulation and heat flux in the subtropical North Atlantic Ocean. *Deep Sea Res.*, **32**, 619-664.

Rosenfeld, L. K., R. L. Molinari and K. D. Leaman 1989: Observed and modeled annual cycle of the transport in the Straits of Florida and east of Abaco Island, the Bahamas (26.5^0N). *J. Geophys. Res.*, **94, C4,** 4867-4878.

Sarkisyan, A. S., and V. F. Ivanov, 1971: Joint effect of baroclinicity and bottom relief as an important factor in the dynamics of sea currents. *Izv. Atmospheric and Oceanic Physics*, **7(2)**, 173-188.

Schmitz, W. J. Jr., J. D. Thompson, and J. R. Luyten, 1992: The Sverdrup Circulation for the Atlantic along 24^0N. *J. Geophys. Res.*, **97, C5,** 7251-7256.

Schott, F. and R. Zantopp, 1985: Florida Current: Seasonal and Interannual Variability. *Science*, **227,** 308-311.

-, T. N. Lee, and R. Zantopp, 1988: Variability of structure and transport of the Florida Current in the period range from days to seasonal. *J. Phys. Oceanogr.*, **18**, 1209-1230.

Sielecki, A., 1968: An energy conserving difference scheme for storm surge equations. *Mon. Weather Rev.*, **96**, 150-156.

da Silva, A. M., C. C. Young, and S. Levitus, 1993a: Revised wind stress over the global oceans with bias corrections: climatology and anomalies for 1945-1989. *J. Phys. Oceanogr.*, to be submitted.

, , and -, 1993b: A Note on the effect of scientific Beaufort scales on climatological wind statistics. Submitted to *J. Climate*.

Slutz, R.J., S.J. Lubker, J.D. Hiscox, S.D. Woodruff, R.L. Jenne, D.H. Joseph, P.M. Steurer and J.D. Elms, 1985: COADS, Comprehensive Ocean-Atmosphere Data Set, Release 1. Climate Research Program, Environmental Research Laboratory, Boulder, CO, 262 pp.

Stommel, H. 1948: The westward intensification of wind-driven ocean currents. *Trans. Am. Geophys. Union*, **29(2)**, 202-206.

Trenberth, K. E., W. G. Large, and J. G. Olson, 1990: The mean annual cycle in global ocean wind stress. *J. Phys. Oceanogr.*, **20**, 1742-1760.

UNESCO, 1980: Background papers and supporting data on the International Equation of State of Seawater 1980, *UNESCO Technical Papers in Marine Science*, **38**.

Weaver, A.J., and E.S. Sarachik, 1991: Evidence for decadal variability in an ocean general circulation model: an advective mechanism.

Atmosphere-Ocean, **29(2)**, 197-231.

Webster, P., 1965: Measurements of eddy fluxes of momentum in the surface layer of the Gulf Stream. *Tellus*, **17** 239-245.

White, W.B. 1977: Annual forcing of baroclinic long waves in the tropical North Pacific Ocean. *J. Phys. Oceanogr.*, **7**, 50-61.

--------, and J.F.T Saur, 1981: A source of annual baroclinic waves in the eastern subtropical North Pacific. *J. Phys. Oceanogr.*, **11**, 1452-1462.

World Meteorological Organization, 1970: Reports on marine science affairs. Rep. No. 3: The Beaufort scale of wind force. WMO, Geneva, Switzerland, 22 pp.

Wunsch, C. and D. Roemmich, 1985: Is the North Atlantic in Sverdrup balance? *J. Phys. Oceanogr.*, **15**, 1876-1880.

Veronis, G. and H. Stommel, 1956: The action of variable wind stresses on a stratified ocean. *J. Mar. Res.*, **15**, 43-75.

Young, F. B., H. Gerard, and W. Jevons, 1920: On electrical disturbances due to tides and waves. *Philosophical Magazine*, Series 6, **40**, 149-159.